Microfluidic synthesis of multifunctional microgels for treatment of inflammatory bowel syndrome

Von der Fakultät für Mathematik, Informatik und Naturwissenschaften der RWTH Aachen University zur Erlangung des akademischen Grades einer Doktorin der Naturwissenschaften genehmigte Dissertation

vorgelegt von

Yonca Kittel (geb. Kayku), M. Sc.

aus

Stolberg (Rhld.), Deutschland

Berichter: Universitätsprofessorin Dr.-Ing. Laura De Laporte

Universitätsprofessor Dr. rer. nat. Alexander J. C. Kühne

Tag der mündlichen Prüfung: 04. Juni 2024

Diese Dissertation ist auf den Internetseiten der Universitätsbibliothek verfügbar.

"Hayatta en hakiki mürşit ilimdir"

"Our true mentor in life is science"

Mustafa Kemal Atatürk

Declaration of Authorship

I, Yonca Kittel

declare that this thesis and the work presented in it are my own and has been generated by me as the result of my own original research.

Hiermit erkläre ich an Eides statt / I do solemnly swear that:

1. This work was done wholly or mainly while in candidature for the doctoral degree at this faculty and university;

2. Where any part of this thesis has previously been submitted for a degree or any other qualification at this university or any other institution, this has been clearly stated;

3. Where I have consulted the published work of others or myself, this is always clearly attributed;

4. Where I have quoted from the work of others or myself, the source is always given. This thesis is entirely my own work, with the exception of such quotations;

5. I have acknowledged all major sources of assistance;

6. Where the thesis is based on work done by myself jointly with others, I have made clear exactly what was done by others and what I have contributed myself;

7. Parts of this work have been published before as:

   a.   Yonca Kittel, Alexander J. C. Kuehne, Laura De Laporte, Translating Therapeutic Microgels into Clinical Applications, Adv. Healthc. Mater., 2021, 11, 2101989.

   b.   Sarah Boesveld*, Yonca Kittel*, Yizhao Luo, Alexander Jans, Burak Oezcifci, Matthias Bartneck, Christian Preisinger, Dirk Rommel, Tamás Haraszti, Silvia P. Centeno, Arnold J. Boersma, Laura De Laporte, Christian Trautwein, Alexander J. C. Kuehne, Pavel Strnad, Adv. Healthc. Mater., 2023, 12, 2300695.

   c.   Yonca Kittel, Luis P. B. Guerzoni, Carolina Itzin, Dirk Rommel, Matthias Mork, Céline Bastard, Bernhard Häßel, Abdolrahman Omidinia-Anarkoli, Silvia P. Centeno, Tamás Haraszti, Kyoohyun Kim, Jochen Guck, Alexander J. C. Kuehne, Laura De Laporte, Angew. Chem. Int. Ed., 2023, 62, e202309779.

   * Equal contribution.

21.02.2024, Yonca Kittel

List of Publications

1. **Yonca Kittel**, Alexander J. C. Kuehne, Laura De Laporte, Translating Therapeutic Microgels into Clinical Applications, Adv. Healthc. Mater., 2021, 11, 2101989.

2. Dirk Rommel, Matthias Mork, Sitara Vedaraman, Céline Bastard, Luis P. B. Guerzoni, **Yonca Kittel**, Rostislav Vinokur, Nikolai Born, Tamás Haraszti, Laura De Laporte, Functionalized Microgel Rods Interlinked into Soft Macroporous Structures for 3D Cell Culture, Adv. Sci., 2021, 9, 2103554.

3. Lisa Chen, Mona Arnold, **Yonca Kittel**, Rémi Blinder, Fedor Jelezko, Alexander J. C. Kuehne, 2,7-Substituted N-Carbazole Donors on Tris(2,4,6-trichlorophenyl)methyl Radicals with High Quantum Yield, Adv. Optical Mater., 2022, 10, 2102101.

4. Susan Babu, I Chen, Sitara Vedaraman, José Gerardo-Nava, Christopher Licht, **Yonca Kittel**, Tamás Haraszti, Jacopo Di Russo, Laura De Laporte, How do the Local Physical, Biochemical, and Mechanical Properties of an Injectable Synthetic Anisotropic Hydrogel Affect Oriented Nerve Growth?, Adv. Funct. Mater., 2022, 32, 2202468.

5. Alisa C. Suturin, Andreas J. D. Krüger, Kathrin Neidig, Nina Klos, Nina Dolfen, Michelle Bund, Till Gronemann, Rebecca Sebers, Anna Manukanc, Ghazaleh Yazdani, **Yonca Kittel**, Dirk Rommel, Tamás Haraszti, Jens Köhler, Laura De Laporte, Annealing High Aspect Ratio Microgels into Macroporous 3D Scaffolds Allows for Higher Porosities and Effective Cell Migration, Adv. Healthc. Mater., 2022, 11, 2200989.

6. Sarah Boesveld*, **Yonca Kittel***, Yizhao Luo, Alexander Jans, Burak Oezcifci, Matthias Bartneck, Christian Preisinger, Dirk Rommel, Tamás Haraszti, Silvia P. Centeno, Arnold J. Boersma, Laura De Laporte, Christian Trautwein, Alexander J. C. Kuehne, Pavel Strnad, Microgels as Platforms for Antibody-Mediated Cytokine Scavenging, Adv. Healthc. Mater., 2023, 12, 2300695.

7. **Yonca Kittel**, Luis P. B. Guerzoni, Carolina Itzin, Dirk Rommel, Matthias Mork, Céline Bastard, Bernhard Häßel, Abdolrahman Omidinia-Anarkoli, Silvia P. Centeno, Tamás Haraszti, Kyoohyun Kim, Jochen Guck, Alexander J. C. Kuehne, Laura De Laporte, Varying the Stiffness and Diffusivity of Rod-Shaped Microgels Independently through Their Molecular Building Blocks, Angew. Chem. Int. Ed., 2023, 62, e202309779.

* Equal contribution.

Author's contributions

1. The published review article "Translating Therapeutic Microgels into Clinical Applications" in Advanced Healthcare Materials (2022, 11, 2101989) is partially incorporated into **Chapter 2**. Y. Kittel wrote the article. A. J. C. Kuehne and L. De Laporte corrected the manuscript.

2. **Chapter 3** was adapted with permission from the research article "Microgels as Platforms for Antibody-Mediated Cytokine Scavenging" published in Advanced Healthcare Materials (2023, 12, 2300695). S. Boesveld and Y. Kittel contributed equally and designed the experiments. Y. Kittel performed the microgel synthesis via microfluidics, the functionalization of the microgels, and the characterization of mechanical as well as diffusion properties of the microgels including optimization of the parameters and analysis. S. Boesveld performed the characterization of functionalized microgels, scavenging experiments, and cell experiments including the assays and analysis. D. Rommel partially designed the microgel synthesis. Y. Luo helped with the cell culture experiments. A. Jans and M. Bartneck helped with characterization of the microgels and the cell culture experiment. A. Jans also developed the microfluidic system. C. Preisinger helped with the characterization of immobilized microgels. B. Oezcifci performed FRET experiments under the supervision of A. J. Boersma. S. P. Centeno performed FLIM measurements and did the analysis. T. Haraszti wrote the FRAP analysis in python and helped to optimize the parameters. S. Boesveld and Y. Kittel wrote the manuscript. C. Trautwein, L. De Laporte, A. J. C. Kuehne, and P. Strnad developed the idea, supervised the project, and corrected the article. All authors approved the manuscript for publication.

3. A manuscript in preparation is partially incorporated in **Chapter 4**. Y. Kittel and S. Boesveld contributed equally to the work. Y. Kittel and S. Boesveld contributed intellectual contributions to the project and designed the experiments. Y. Kittel performed the microgel synthesis via microfluidics including the optimization of the system as well as the characterization of the chemical and mechanical properties of the microgels. S. Boesveld investigated the biological properties of the used cell lines. Y. Kittel and S. Boesveld analyzed the adhesion of functional microgels on human intestinal cell lines. K. Selzner optimized the parameters for microgel synthesis and helped with the microgel characterization as well as analysis. M.

Mork developed the high-throughput microfluidic chip. C. Bastard analyzed the cell viability measurements. T. Bosserhoff helped with the microgel purification and characterization. P. Strnad, L. De Laporte and A. J. C. Kuehne developed the project idea and supervised the project.

4. **Chapter 5** was adapted with permission from the publication "Varying the stiffness and diffusivity of rod-shaped microgels independently through their molecular building blocks" published in Angewandte Chemie International Edition (2023, 62, e202309779). Y. Kittel performed the synthesis of hydrogels as well as microgels, the characterization of the materials, and cell experiments including staining, imaging and analysis. Y. Kittel and L. P. B. Guerzoni partially designed the experiments under the supervision of L. De Laporte. C. Itzin partially supported the microgel synthesis, the characterization, and cell experiments including staining and imaging. L. P. B. Guerzoni, D. Rommel, and M. Mork developed the rod-shaped microgel production via continuous plug-flow on-chip microfluidics. Y. Kittel, D. Rommel, M. Mork, and C. Bastard optimized the cell culture experiments for the system. A. Omidinia-Anarkoli and B. Häßel performed the cyro-SEM experiments. S. P. Centeno characterized the porosity of the microgels via STED microscopy. T. Haraszti wrote the FRAP as well as pore size analysis in python and optimized the parameters. K. Kyoohyun performed the Brillouin microscopy and refractive index measurements under the supervision of J. Guck. I wrote the manuscript. L. De Laporte and A. J. C. Kuehne corrected the article. All authors finalized the manuscript and approved for publication.

Eidesstattliche Erklärung

Hiermit erkläre ich, Yonca Kittel (geb. Kayku), an Eides statt, dass ich die vorliegende Dissertation selbstständig verfasst und keine anderen als die angegebenen Quellen und Hilfsmittel verwendet habe.

Yonca Kittel (geb. Kayku), 21.02.2024 Aachen

Table of Contents

1 Motivation and Overview of the Thesis

1.1 Introduction

1.2 Inflammatory bowel diseases

Inflammatory bowel diseases (IBD) affect 2.5 – 3 million patients in Europe alone with increasing incidence.[1] IBD summarizes two diseases: Crohn's disease and ulcerative colitis.[2,3] Crohn's disease is a chronic inflammatory disease of the gastrointestinal tract (GI).[2] It mostly appears in young patients presenting symptoms such as abdominal pain, chronic diarrhoea, weight loss, and fatigue. All segments of the GI can be affected, while the most common are the terminal ileum and colon. The inflammation is typically segmental, asymmetrical, and transmural and leads to bowel damage and disability. Ulcerative colitis, on the other hand, describes a chronic inflammatory disease affecting the colon.[3] Similar to Crohn's disease, it appears in young patients, but here they show mucosal inflammation starting in the rectum that can extend continuously to proximal segments of the colon. The major symptom is bloody diarrhoea. Both diseases show higher risks of developing colorectal cancer.[4,5]

IBD is believed to result from the interplay between different factors, such as genetic susceptibility, environmental factors, and intestinal microflora, resulting in an abnormal mucosal immune response and compromised epithelial barrier function.[6] While in the healthy state, intestinal barrier function is maintained by the mucus layer, patients with IBD exhibit dysbiosis and approximately a third have an increased abundance of mucosa-associated adherent-invasive *Escherichia coli* (*E. coli*) (see Figure 1.1). Thereby, *E. coli* cross the mucosal barrier, adhere to intestinal epithelial cells, and replicate within macrophages, resulting in the secretion of high amounts of pro-inflammatory cytokine tumour necrosis factor α (TNFα).[2]

The treatment of IBD involves an induction and maintenance regimen. The major treatment options as induction regimen for IBD include immunosuppression, while the intestinal damage often requires surgical treatment.[2] For moderate to severe disease, therapeutic

agents, such as anti-TNFα drugs (infliximab, adalimumab, golimumab, and certolizumab pegol), are effective at inducing and maintaining remission.[2,3] In this thesis, I will focus on three key aspects to treat IBD: anti-TNFα therapy to reduce inflammation, specific targeting of inflamed intestinal tissue, and protection and regeneration of damaged epithelial intestinal barrier to achieve intestinal mucosal healing.
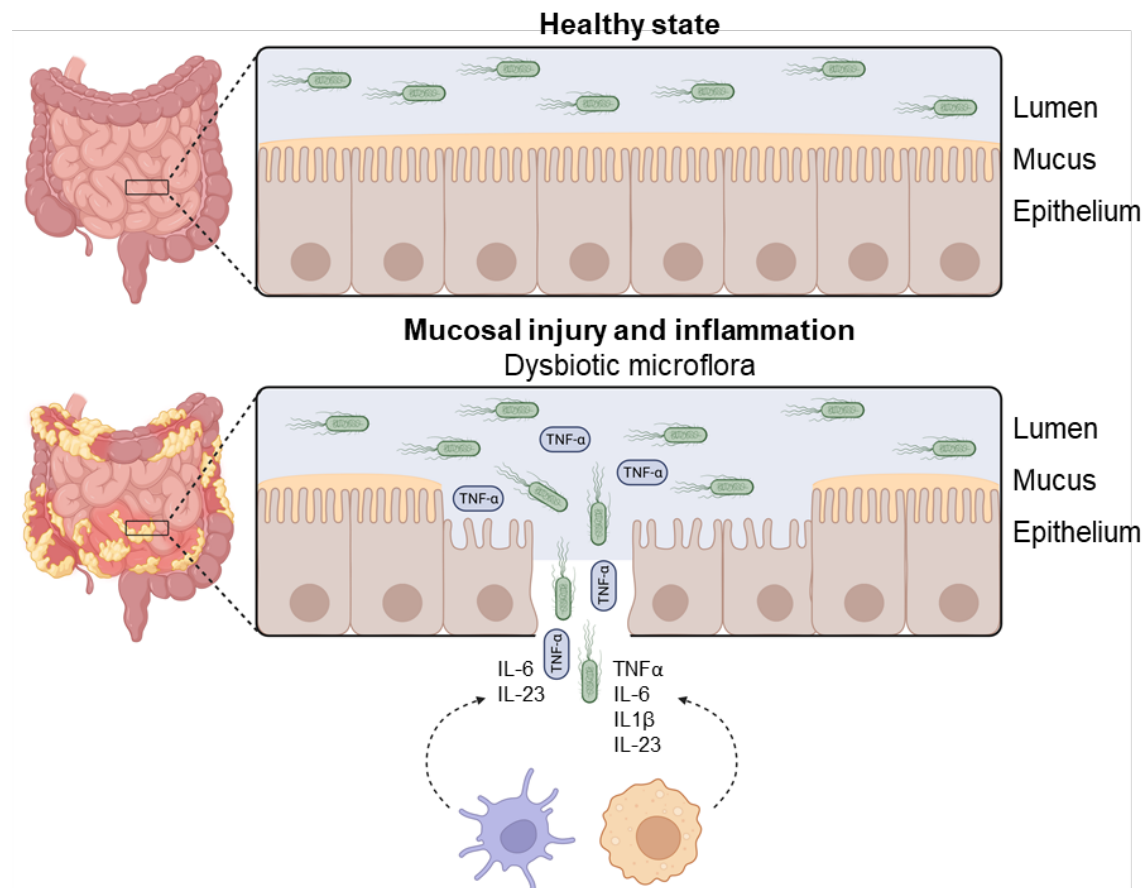
Figure 1.1: Schematic representation of the intestine in the healthy state and for IBD. During the healthy state, the intestinal barrier function is maintained by the mucus layer and epithelial cells.[2,3] Moreover, the intestinal epithelium regulates and separates luminal microflora from the mucosal immune system. During IBD, the mucosal barrier is damaged and the luminal microflora triggers a proinflammatory immune response. Additionally, innate lymphoid cells (ILCs) contribute to the secretion of pro-inflammatory cytokine leading to inflammation. Moreover, mucosal injury and damage is associated with dysbiosis, which is perhaps related to the inflammatory cascade. Created with BioRender.com.

1.2.1   Relevance of TNFα antibody treatment of IBD

TNFα antibodies have been widely used for the treatment of IBD over the last three decades. In 1992, the first patient with severe Crohn's disease was treated with TNFα monoclonal antibodies at the Academic Medical Centre in Amsterdam, which was followed by a series of 10 patients three years later.[7,8] Infliximab [Remicade® (Janssen Biotech, Malvern, PA, USA)] and adalimumab [Humira® (Abbvie, North Chicago, IL, USA)], both based on TNFα monoclonal antibodies, were approved by the Food and Drug

Administration (FDA) in 1998 and 2002, respectively.[9,10] Both drugs have long been established as an effective treatment for patients with IBD.[11] Many clinical studies demonstrate long-term safety, efficacy, as well as increased clinical remission rates for infliximab- and adalimumab-treated patients with moderately to severely active IBD.[9,12–19] For example, in patients with moderately to severely active ulcerative colitis, remission and mucosal healing rates were maintained with adalimumab therapy up to 4 years.[20] Moreover, in a clinical trial between 2007 and 2011, 327 patients with Crohn's disease were treated with either infliximab or adalimumab. 89% of the patients achieved clinical response and clinical remission for 63 and 61 weeks for infliximab and adalimumab, respectively.[11] However, infliximab requires concomitant immunomodulator to achieve optimal maintenance of response in comparison to adalimumab monotherapy. Therefore, the decision to use infliximab or adalimumab depends on prior patient's history of adherence to previous treatment.[11]

Even though the clinical application of TNFα antibodies is well-established for IBD, their systemic administration leads to significant adverse events, such as immunosuppression and, therefore, a higher risk of infections including common bacterial infections of respiratory, urinary, or GI tract, uncommon bacterial infections, such as listeria sepsis and meningitis, as well as systemic inflammatory responses, viral and fungal infections, malignancies, hepatitis B and C, and tuberculosis.[21–25] Furthermore, non-infectious complications, such as patients developing haematological, dermatological, cardiac, and neurological effects, as well as autoimmune-like disorders, have been reported.[21]

TNFα antibodies are typically delivered via intravenous injection (Remicade®) or subcutaneous route (Humira®) in clinics. The advantage of these systemic routes is that large amounts of antibody can be delivered in a short time to enable rapid systemic bioavailability.[26] However, when antibodies are injected systemically, their distribution from the site of injection via the blood flow to the diseased organ is limited. Furthermore, they encounter harsh environmental conditions, which lead to their deactivation and, therefore, require higher concentration to retain efficacy.[26–28]

1.2.1.1 Local administration of TNFα antibody

In comparison to systemic delivery, the non-systemic local administration of antibodies is more effective for confined diseases.[29] Local injection of antibodies allows to use 1/10th to 1/100th of the required systemic dose and, therefore, reduces both adverse events and costs.[27] However, due to the rapid clearance of the antibodies by the body, local delivery is also limited and better drug delivery systems (DDS) are required.[30]

To increase the therapeutic efficacy and minimize the dose and thus systemic adverse events, the immobilization of antibodies on carriers, such as liposomes or nanoparticles (NPs), has been developed as a promising DDS.[30–32] Moreover, the immobilization of antibodies opens up the opportunity to establish a local targeted treatment option for various inflammatory diseases including IBD. For example, it has been published that adalimumab decorated NPs enhance antibody stability and therapeutic outcome in epithelial colitis targeting.[31] Thereby, TNFα antibody adalimumab is covalently crosslinked to poly-lactide-co-glycolide (PLGA)-based NPs with a particle diameter of around 120 nm. The binding of adalimumab to NPs improved the stability of adalimumab against proteolytic degradation *in vitro* and reduced systemic exposure, leading to enhanced therapeutic safety. Furthermore, the intra-colonic administration of adalimumab decorated NPs reduced the severity of clinical symptoms in a murine colitis model more efficiently than delivering adalimumab in solution.

In another example for targeted treatment of IBD, infliximab was loaded on PLGA-polyethylene glycol (PLGA-PEG) NPs with varying particle sizes of 130 – 600 nm via electrostatic interaction. Cell interaction of the NPs was examined in healthy and inflamed *in vitro* models of the intestinal epithelial barrier.[33] Infliximab immobilized NPs enhanced the recovery and healing of the inflamed intestinal barrier compared to free infliximab, while larger NPs with a size of around 600 nm showed the highest accumulation at the barrier, resulting in accelerated recovery of barrier integrity and reduced inflammatory cytokine secretion and cytotoxicity in comparison to treatment with infliximab alone.

However, due to their nanoscale sizes, NP-based system often suffer from accelerated blood clearance and undesired cellular uptake.[34,35] Moreover, the surface area of NPs is limited and the conjugation of antibodies to a surface can sterically restrict access to the binding motif, resulting in low binding capacity.[31,36,37]

1.2.2 Repair of damaged epithelial intestinal barrier

Besides the strategy of using TNFα drugs to reduce the inflamed area in the intestine during IBD, another key treatment approach is to target and regenerate the epithelial barrier function and achieve mucosal healing.

The intestinal mucus layer is a viscoelastic hydrophilic hydrogel-like material that contains a high amount of water (90-95%), lipids, fats, electrolytes, mucins, and additional proteins, such as immunoglobins, growth factors, and antimicrobial peptides.[38,39] The intestinal mucus represents the luminal surface of the intestinal epithelium and acts as a barrier between the external environment and the epithelium.[38,40] Thus, it is a physical and biochemical barrier that actively selects nutrient and drug intake, regulates the microbiome, and keeps the epithelium protected from the attack of pathogens, while dysfunction of the intestinal mucus barrier leads to several diseases.[39,40] In IBD, bowel damage in terms of stricture, fistula, or abscess is present in a fifth of patients at diagnosis, while the annual incidence of admissions to hospital is around 20%, and within 10 years of diagnosis half of the patients will require surgery.[2] However, extensive small bowel disease or multiple surgeries, or both, can result in intestinal failure and short bowel syndrome and – unfortunately, surgery in IBD is not curative as surgical recurrence is reported in 30% of the patients.[2]

Various researchers have suggested different approaches for local targeted treatment of the inflamed intestinal epithelium via regulation of intestine immunity and microflora for mucosal healing in IBD.[41,42] In one approach, as an alternative to engineered microbial therapies to promote mucosal healing by secreting soluble therapeutic proteins[43], researchers genetically engineered the bacteria *E. coli* Nissle 1917 (EcN) to assemble and create fibrous matrices consisting of curli nanofibers, known to promote intestinal barrier function and epithelial restitution.[41] They observed enhanced protective effects of engineered EcN against dextran sodium sulfate (DSS)-induced colitis in mice, associated with mucosal healing and immunomodulation.

As the mucus layer exhibits hydrogel properties, researchers have focused on using natural or synthetic hydrogel systems to either mimic the mucus layer as a physical shield or as a local DDS. For example, bioadhesive hydrogel formed by the crosslinking of sulfhydryl chondroitin sulfate and polydopamine (CS-PDA) was designed for repairing mucosal barrier and scavenging inflammatory mediators.[44] While the presence of PDA ensures the

mucosa-adhesive behaviour, CS in the hydrogel network has proven to promote wound healing and tissue repairing. Furthermore, sodium ferulic (SF), a potent reactive oxygen species (ROS) inhibitor, was incorporated into the CS-PDA hydrogel to scavenge ROS in inflamed colon. After rectal injection of the hydrogel in DSS-induced colitis mice, the hydrogel adhered to the damaged mucosal layer via the interaction between PDA residues and mucins. Moreover, sustained SF release enabled the scavenging of ROS in inflammatory areas. Alternatively, other researchers have focused on inflammation-targeting, mucoadhesive hydrogels as local DDS.[45–47] Hydrogel-based DDS enable protection of therapeutically active molecules from degradation, enhance the efficacy of the drugs, minimize adverse events, and enable controlled release of the drug via biochemical mechanisms.[48] For example, self-healing, injectable, and antibacterial protein hydrogel crosslinked by silver ion-mediated metal-ligand coordination and electronic interaction with sulfhydryl functionalized protein bovine serum albumin (BSA) and heparin, respectively, was developed for balancing inflammation and microthrombosis in the pathogenesis of IBD via continuous release of heparin.[49] The rectal injection of the hydrogel in DSS-induced colitis mice showed higher adhesion at the inflammatory sites compared to normal mucosa due to electrostatic interaction of positively charged inflammatory lesions (due to various cationic exudates) and negatively charged protein hydrogel.

1.3   Microgels as carrier system in therapeutics

Microgels are water-swollen, soft polymer networks with dimensions of the order of 10 nm to a few hundreds of micrometres. They exhibit open-meshes and can, therefore, be functionalized on their inside, resulting in an increased loading capacity of the bioactive molecule in comparison to other solid carriers such as NPs.[50] Furthermore, microgels are stealth against immune recognition to prevent physiological clearance. Depending on their size, microgels can be used for systemic or local injection, and could cross membranes and biological barriers.[51] On the other hand, they can be used for targeted, local therapy at a designated area in the body, without being taken up by the blood circulation system or by cells.[52] The versatile synthesis and functionalization possibilities of microgels enables the conjugation of bioactive molecules during microgel synthesis or via post-modification.[53] Moreover, microgels can be varied in their crosslinking density, which alters their network

porosity and morphology, directly impacting their softness, deformability, degree of swelling, stability, and potential degradation rate, and thus their biomedical application. Further insights to the microgel fabrication and characterization methods, as well as the requirements of the microgels' properties for clinical applications are provided in Chapter 2.

To use microgels in biomedical applications, the choice of polymer plays a key role. More specifically, the chosen polymer needs to fulfil several criteria to enable biocompatibility and biodegradability, while polymeric microgel-based DDS require mechanical stability and softness, a high loading capacity, suitable (bio)chemical functionality, and controlled cell interaction. Polyethylene glycol (PEG) is a non-toxic, highly water-soluble, biocompatible, and medical approved polymer, that is widely used for hydrogel synthesis in biomedical application.[53–55] Depending on the choice of degradable crosslinkers, the degradation rate of PEG-based microgels can be adjusted from minutes to years.[56–58] Furthermore, PEG polymers are available in versatile architectures, such as linear and multi-arm, as well as molar masses.[59] They can be chemically functionalized with reactive end groups for polymerization and crosslinking – or can be biologically modified to introduce cell-microgel interaction or affinity to drugs or biological molecules.[53] Based on the PEG structure, molecular weight, concentration, and reactivity, the internal structure achieved by crosslinking PEG molecules, can be altered, affecting the mechanical and diffusion properties, but also the amount of free functional groups and the degradation rate.

Depending on the desired microgel properties such as size, shape, and mechanical stability, as well as microgel production rate, different fabrication techniques are available.[60] Microgel production techniques, such as mini- and microemulsion, dispersion and precipitation polymerization, emulsion polymerization are limited by small microgel sizes, usually submicron, while in-mold polymerization produces microgel between 0.5 µm and 100 µm but at a lower production rate as a batch process.[61–64] Microfluidics and stop-flow lithography, on the other hand, are continuous high-throughput systems for the production of monodisperse microgels larger than 10 µm. Moreover, stop-flow lithography can be used for the production of microgels with more complex shapes.[64] In microfluidics, precursor droplets can be generated via an active or passive method. While active droplet generation requires electrodes, centrifugation, or laser techniques, passive methods use the microchannel geometry to continuously generate droplets.[65] In general, passive droplet formation is achieved via the emulsification of two immiscible liquids, usually a continuous

oil phase and a dispersed aqueous polymer solution. There are three common droplet generation geometries: T-junction, co-flow, flow-focusing (see Figure 1.2).[65,66] A T-junction is formed by the intersection of the continuous and dispersed phase that are perpendicularly arranged. Commonly, the dispersed phase is injected into the main channel (continuous phase) and breaks up into droplets. The resulting size of the droplets is dependent on the generation method, including squeezing, dripping, or jetting, which in turn depends on different parameters, such as flow rates, Capillary, Weber, and Reynolds number of the two phases.[66] Co-flow describes two concentric capillaries with the inner capillary containing the dispersed phase and outer capillary carrying the continuous phase.[65] Droplets are formed when the dispersed phase enters the main, continuous phase, and viscous stresses created by the continuous phase stretch the interface until it breaks. Thirdly, in the flow-focusing method, the dispersed phase is perpendicularly squeezed by the continuous phase. In comparison to the T-junction method, the main advantage of the flow-focusing droplet generation method lies on the symmetrical geometry where the continuous phase flows from two sides resulting in increased stability and control over droplet formation.[65] Therefore, I used the flow-focusing microfluidic technique throughout this Thesis.
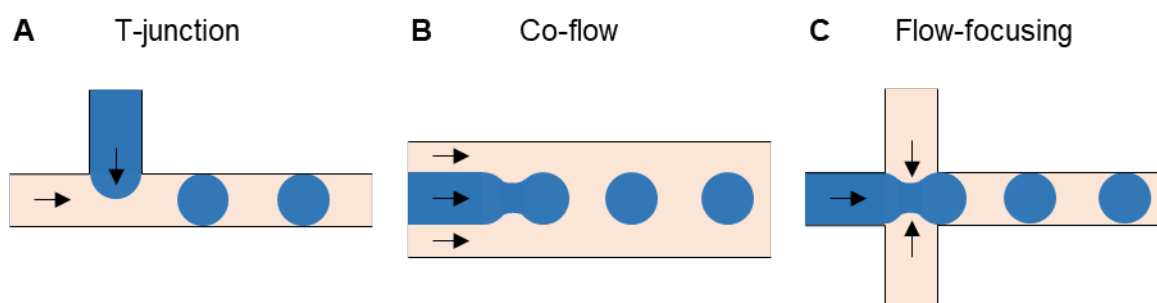
Figure 1.2: Three common droplet generation methods A) T-junction, B) co-flow, and C) flow-focusing in microfluidics. Black arrows indicate flow directions of immiscible liquids continuous oil phase (orange) and dispersed aqueous solution (blue).

Depending on the crosslinking mechanism of the microgels, either chain-growth (e.g., free radical polymerization) or step-growth (e.g., Michael-type addition) polymerization, a different network architecture and internal structure is formed (see Figure 1.3A).[67] Step-growth polymerization results in a more homogeneous polymer network structure and controlled degradation rates, and is, therefore, often used for the incorporation of cells inside microgels for tissue engineering applications.[68,69] Free radical (chain-growth) polymerization results in more heterogeneous polymer network structures, but enables faster polymerization, thus, the production of microgels in high-throughput systems (see

Figure 1.3B).[70] Crosslinking of precursor droplets containing a photoinitiator via free radical polymerization using UV irradiation enables the production of spherical microgels, while on-chip gelation enables crosslinking of spherical or elongated droplets inside of the channels during flow to yield spherical or anisometric rod-shaped microgels, respectively.
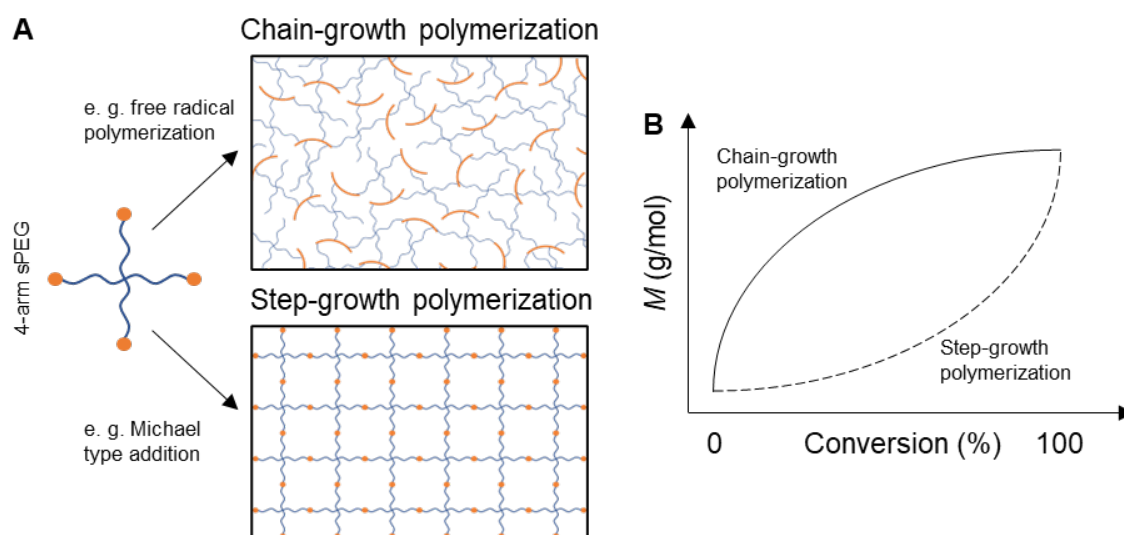
Figure 1.3: Possible crosslinking mechanisms using 4-arm sPEG building block. A) Obtained polymer network structures via step-growth and chain-growth polymerization. B) Polymer growth kinetic profiles for chain-growth and step-growth polymerization.

1.4 Concept of the thesis: Microgels as platforms for treatment of IBD

In our research group, a platform for treatment of cholera toxin (CT)-mediated intestinal infections using functional PEG-based microgels has been developed.[71] CT binds to GM1a ganglioside receptors, presented at the surface of intestinal epithelial cells. Microgels were post-functionalized with GM1a via glycidyl-amine coupling chemistry to create CT-scavengers, which enable binding of toxins allowing their clearance from the intestinal tract. To prevent cellular uptake of the microgels by intestinal epithelial cells, microgels with sizes of 20 µm were produced in droplet-based microfluidics. The microgels exhibit a widely meshed network structure, allowing for the diffusion of the CT deep into the microgels. It was shown that GM1a-functionalized microgels efficiently bind CT in direct binding competition to colorectal cells.

Based on the toxin-scavenging microgel platform for the treatment of toxin-mediated microbial intestinal infections, the focus of my work is to develop multifunctional sPEG-based microgels for local, inflammation-targeted treatment of non-microbial IBD (see

Figure 1.4). In the following, different challenges of IBD and our contribution as a treatment option are presented.
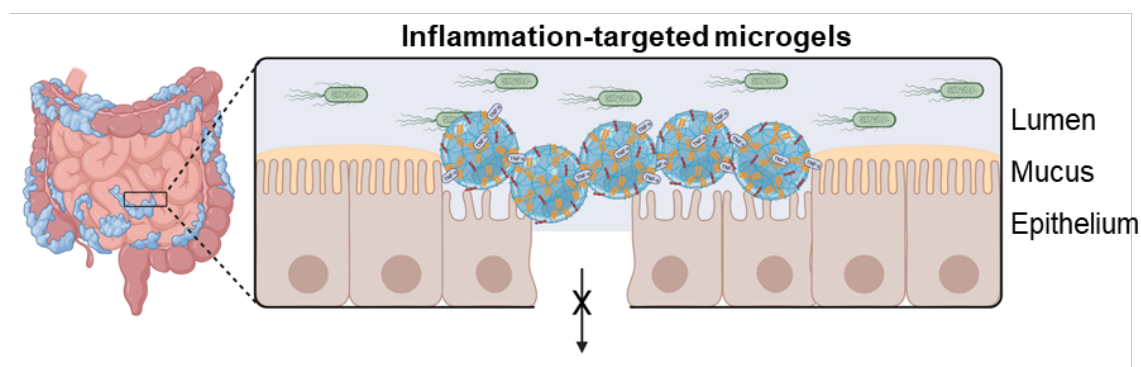
Figure 1.4: Schematic representation of the overall concept of IBD treatment using inflammation-targeted microgels. Microgels address active IBD. Created with BioRender.com.

IBD involves different challenges that need to be treated. As described above, IBD is believed to result from the interplay between different factors that include damaged epithelial barrier and high levels of pro-inflammatory cytokine TNFα. Researchers have focused on the immobilization of TNFα antibodies for local treatment of IBD – and, on using hydrogels to mimic the mucus layer. However, the combination of these therapeutic approaches for local treatment of IBD has not been investigated. Therefore, the main motivation of my work is to develop multifunctional microgels as inflammation-targeting materials for local treatment of IBD inflammatory sites. The microgels address three specific challenges during IBD: scavenging of pro-inflammatory cytokine TNFα, active targeting and binding to inflamed intestinal tissue, and protecting and regenerating the epithelial surface to shield the mucosal tissue from harmful bacteria (see Figure 1.5). Chapter 3 focuses on the post-functionalization of TNFα antibodies into glycidyl-group co-polymerized sPEG-based microgels with highly accessible internal volume to specifically scavenge the pro-inflammatory cytokine TNFα. In Chapter 4, I develop hyaluronic acid (HA)-functionalized PEG-based microgels that specifically target and bind CD44 overexpressing inflamed intestinal tissue to form a dense layer on the epithelial surface to mimic the degraded mucus and shield the mucosal tissue from harmful bacteria. While Chapter 3 and Chapter 4 mainly focus on diffusion and mechanical properties of functional microgels, respectively, Chapter 5 gives a more general overview about microgel properties that affect cell attachment and spreading by systematically investigating the internal structure, stiffness and bioactivity of microgels to be able to better design and employ microgels for biomedical application.

Scavenging of TNFα	Active targeting and binding	Protection and regeneration
Microgels with highly accessible internal volume are post-functionalized with TNFα antibodies to efficiently scavenge pro-inflammatory cytokine TNFα	Microgels are co-polymerized with hyaluronic acid to specifically target and bind CD44 receptor presented at the IBD inflammatory sites	Hyaluronic acid-functionalized soft, deformable microgels will form a dense microgel layer on the epithelial surface to mimic the degraded mucus and shield the mucosal tissue from harmful bacteria

Figure 1.5: Microgels address three key challenges during active IBD as combined therapeutics. 1. Inflammation-mediating cytokine TNFα will be scavenged using TNFα-antibody post-functionalized microgels with highly accessible internal volume. 2. Active and specific targeting of hyaluronic acid (HA)-co-polymerized microgels to CD44 receptor expressing inflamed intestinal cells at the IBD inflammatory sites. 3. Microgels will form a dense layer on the damaged epithelial surface to mimic the damaged mucus layer providing a barrier towards harmful TNFα and bacteria. Created with BioRender.com.

1.4.1 Local administration of TNFα antibody-functionalized microgels for TNFα scavenging

As described above, the non-systemic local administration of immobilized antibodies is more effective for confined diseases to increase their therapeutic efficacy and minimize systemic adverse events compared to systemic administration. The immobilization of TNFα antibodies adalimumab and infliximab on NPs have shown superior antibody stability and therapeutic outcome compared to corresponding free antibody.[31] In fact, certolizumab pegol [Cimzia® (UCB, Brussels, Belgium)] is a TNFα-specific PEGylated monoclonal antibody and was approved by the FDA in 2008 and the European Medicines Agency (EMA) in 2009 for the treatment of Crohn's disease.[72–74] However, the use of NPs involves low binding capacity, as well as clearance from the body due to their solid particle properties and small sizes.

In contrast to NPs, microgels exhibit an open-meshed polymer network and, therefore, enable the diffusion of guest molecules when applied as carriers in DDS or to bind toxins, proteins, or bacteria.[75,76] Thereby, the microgels' internal structure can be altered by the architecture, molar mass, and weight percentage of the chosen polymer and highly influences their binding capacity. Depending on the crosslinking mechanism and the

resulting mesh size of the polymer network, the molecules can diffuse more or less deep into the microgels. Finer meshes with nanoporosity enable the uptake of more molecular cargo, but, on the other hand, limit their size. A more heterogeneous polymer network results in the formation of larger pores that can enhance the diffusion of larger molecules deep into microgels. Besides a crosslinking gradient that affects the diffusion of cargo deep into the microgels, the functionalization of the inner surface of the microgels can limit their capacity, while the presence of polymer dangling chains inside the meshes can impair diffusion. On the other hand, the presence of specific functional groups presented throughout the microgel can increase the interaction with the respective cargo and, thus also increase the loading capacity.

When microgels are applied as drug delivery or scavenging systems, the characterization of their diffusion properties is crucial. Fluorescent markers are often used in research to analyze the dynamic processes inside the microgels.[77] The diffusivity of differently sized fluorescently labelled solutes can be imaged to analyze the pore size of microgels (see Figure 1.6A). Fluorescence correlation spectroscopy (FCS) and fluorescence recovery after photobleaching (FRAP) are well-established methods for the analysis of diffusion, as well as the structural properties of microgels.[78,79]

In FCS, the fluorescence intensity fluctuations of single molecules diffusing through the illuminated volume is analyzed. FCS is highly sensitive, provides fast temporal and high spatial resolution and can measure sample concentrations in the nanomolar range. Furthermore, it can give information about the heterogeneity of the polymer network.[79] In a FRAP experiment, pre-bleach images of the fluorescent sample are monitored at low fluorescence intensity are taken to establish a baseline fluorescence intensity. Subsequently, a high-intensity light exposure is used to photobleach the fluorophores at the region of interest (ROI). The laser intensity is attenuated and the recovery of fluorescence intensity due to the diffusion of unbleached fluorophores in the bleach spot is analyzed via image analysis (see Figure 1.6B). In comparison to FCS method, in FRAP, a relatively high concentration of the diffusive fluorophores is needed and the diffusion coefficient is estimated as an average value for the micrometre sized area (ROI). These properties resemblance more the experimental conditions encountered in a scavenging system, where a high concentration of toxins needs to be tackled, and, therefore, FRAP was chosen for the experimental approach to evaluate the diffusion properties of a fluorescent molecule in the polymer network system.

As fluorescent molecules, small fluorescently labelled polymer chains such as FITC (fluorescein isothiocyanate)-dextrans or small fluorescent dyes are often used.[77] Moreover, based on the calculated diffusion coefficients and size of the fluorescent markers, the average mesh size ξ of the polymer network can be estimated.[80]
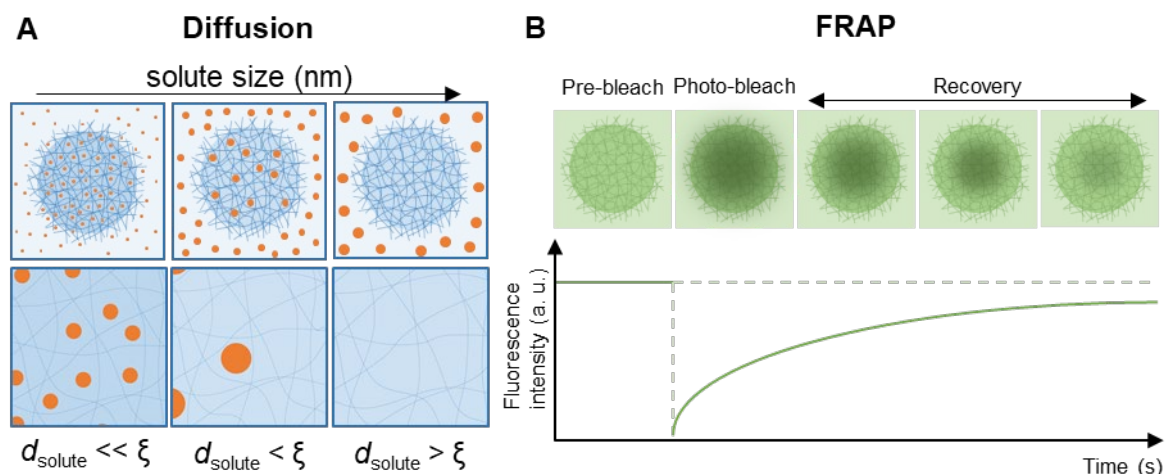
Figure 1.6: Schematic representation of diffusion studies. A) Diffusion of differently sized fluorescently labelled solute (e. g. FITC-dextran) in microgel polymer network to characterize the pore size for calculation of mesh size ξ.[80] B) Fluorescence recovery after photobleaching (FRAP) method shows pre-bleach image, photo-bleach image, and fluorescence recovery images with corresponding fluorescence intensity of the bleaching area as shown in the graph.

In Chapter 3, I use TNFα antibody (adalimumab)-functionalized sPEG-based microgels for the scavenging of pro-inflammatory cytokine TNFα in the presence of human colorectal adenocarcinoma cells. Therefore, I produced microgels with a diameter of around 25 µm using the flow-focusing droplet-based microfluidic technique (see Figure 1.7A). Here, the diffusion of the antibody to bind to the internal surface of the microgels, as well as the diffusion of the antigen inside the microgels after antibody binding, are important. To achieve high diffusion of TNFα antibody, as well as TNFα cytokine after antibody immobilization to the microgel polymer network, I investigated the diffusion of TNFα antibody- and TNFα-mimicking fluorescently labelled dextrans (FITC-dextrans) with similar hydrodynamic radii in microgels prepared with different polymer architectures (4-arm and 8-arm sPEG-Ac) and molar mass (10 kDa, 20 kDa, and 40 kDa) using a total polymer mass concentration of 10 wt%. The diffusion of TNFα antibody-mimicking dextran (hydrodynamic radius ~ 6.0 nm) was homogeneous in all microgel conditions characterized via confocal laser scanning microscopy (CLSM) (see Figure 1.7B). Similarly, the diffusion coefficient of TNFα-mimicking dextran (hydrodynamic radius ~ 3.3 nm) was non-significant for the different microgel conditions analyzed via FRAP technique.
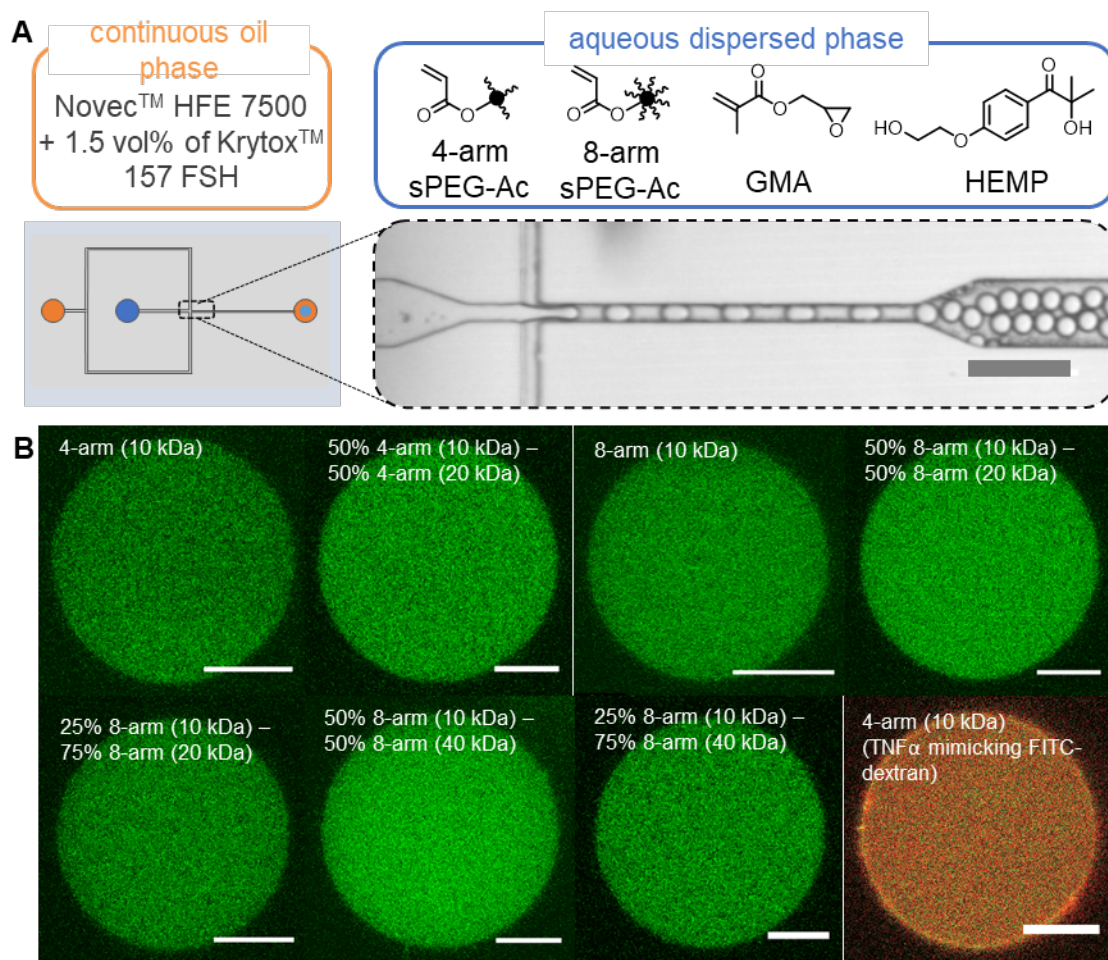
Figure 1.7: A) Schematic representation of microgel synthesis using flow-focusing droplet-based microfluidics. B) Synthesized microgels with different ratio of 4-arm and 8-arm sPEG-Ac and molecular weight (10 kDa, 20 kDa, and 40 kDa) show homogeneous fluorescence of TNFα antibody-mimicking FITC dextran (green). Moreover, microgels (4-arm sPEG-Ac (10 kDa)) that were covalently post-functionalized with TNFα antibody-mimicking fluorescein amine dextran (green) were incubated with TNFα-mimicking FITC dextran (red) and show homogeneous uptake of the TNFα-mimicking FITC dextran (bottom right). Scale bars represent 10 μm.

In general, microgels can be immobilized with bioactive molecules via physical adsorption to take up and deliver drugs of different polarity and charge, via receptor/ligand interaction, or via direct chemical covalent binding.[81] Physical entrapment of cargo or pathogens is often achieved using stimuli-responsive microgels that swell and release the cargo via a certain trigger, such as pH or temperature change, or the induction of light or a magnetic field.[82] For scavenging of the cytokine TNFα, the TNFα antibody is covalently bound to the microgels. Covalent conjugation of antibodies to microgel polymer network can be achieved during microgel synthesis or via an additional post-functionalization step. However, the conjugation of antibodies during microgel synthesis directly affects the microgels' internal structure, and thus the mechanical as well as diffusion properties. To decouple antibody immobilization and microgel crosslinking, I chose post-functionalization. In addition, the purification of microgels often requires washing steps

with organic solvents that can strongly affect protein stability and folding.[83] The covalent immobilization of antibodies in microgels via post-functionalization has been reported via linker-mediated two-step immobilization. Thereby, protein A and protein G are typical antibody-binding proteins, which have been established as linkers due to their ability to selectively adsorb the fragment crystallizable (Fc) region of various types of antibodies, which enables orientation with high biological functionality.[84] However, the antibody-protein A/G conjugate may reversibly dissociate under specific conditions. The easiest antibody-microgel coupling is the one-step antibody covalent immobilization via amino groups (N-terminus and Lys residues) that are distributed over the entire antibody surface (see Figure 1.8). Thereby, N-terminus have lower pK_a (about 7.5) compared to nucleophilic ε-amine of Lys residues (about 10) and, therefore, demonstrate higher reactivity with reactive aldehyde, tosyl, and glycidyl groups under neutral or slightly alkaline pH. However, it is important to note here, that this method results in random orientation of the antibodies and may lead to loss of their biological functionality.
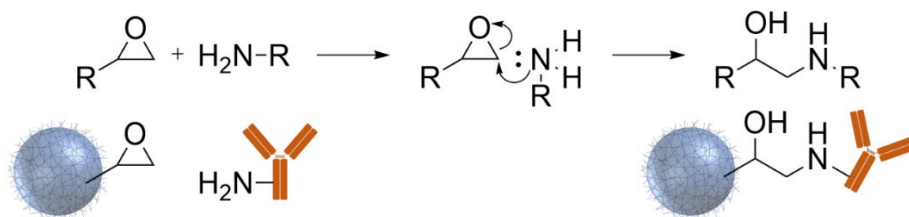
Figure 1.8: Mechanism of amine-glycidyl coupling of GMA co-polymerized 4-arm sPEG-Ac-based microgels with glycidyl-functionality and amine-functional TNFα antibody.

For the immobilization of antibodies in microgels, I co-polymerized the sPEG-Ac-based microgels with glycidyl methacrylate (GMA) to introduce glycidyl groups that enable the addition with amine groups presented in the antibody. In Chapter 3, I characterized the immobilization efficacy of TNFα antibody in microgels. A higher TNFα antibody concentration was observed for the 10 eq. GMA functionalized microgels, when microgels with 4 eq. and 10 eq. GMA are incubated with TNFα antibody and measured via a CBQCA protein quantification kit. Using the 10 eq. GMA functionalized microgels, it was possible to scavenge 88% of the added TNFα ([TNFα] = 2.5 µg mL^{-1}) in a volume of 500 µL. Importantly, all the tested TNFα concentrations were far above disease-relevant levels as, for example, the TNFα concentration in the intestinal tissue during an acute DSS-induced colitis in mice has been reported to be in the pg mL^{-1} range.

Besides the diffusion of TNFα antibody and its immobilization efficacy inside the microgels, the specific antibody-antigen binding inside the microgels – and the activity of

the TNFα antibodies after binding to the microgels are major key points to analyze when immobilizing antibodies on carriers. Förster resonance energy transfer (FRET) is a well-established method to study bi-molecular interactions within cells, but also microgels.[85–87] Thereby, the dipole-dipole mediated non-radiative energy transfer from a donor to an acceptor can only take place when both fluorophores have a distance lower than around 10 nm. For two proteins that are labelled with a donor and acceptor tag, respectively, this distance is only achieved when both interact with each other, resulting in FRET. The FRET process can be visualized by using a donor and acceptor fluorophore and measuring for instance the emission intensity of donor and acceptor. However, the quantification of FRET efficiency by fluorescence intensity-based measurements is tedious and complex since it requires a careful spectral calibration of the instrument and additional measurements of reference FRET constructs.[85] On the other hand, the fluorescence lifetime imaging (FLIM)-FRET approach is much more robust since the FRET efficiency can be estimated solely by the change in the donor lifetime and the binding fraction by the amplitudes characterizing the bi-exponential fluorescence decay.[86] Additionally, fluorescence lifetime measurements are more straightforward than fluorescence intensity measurements because the lifetime is a molecular inherent parameter and it does not depend on concentration. For the reasons mentioned, FLIM-FRET measurements were used to prove the TNFα-antibody interaction.

In this work, I produced Alexa Fluor 546 (AF546)-labelled TNFα antibody (acceptor)-functionalized microgels and incubated them with Alexa Fluor 488 (AF488)-labelled TNFα (donor) representing a FRET pair. In a first step, the fluorescence intensity images of the microgels were recorded in CLSM with 488 nm excitation both in the AF488 donor channel and in the AF546 acceptor channel, the latter confirming the FRET process. In a second step, in order to estimate the FRET efficiency and binding ratio, FLIM-FRET measurements were realized by recording the FLIM image in the donor channel. For this, the fluorescence decay of the previously described system and additionally of the free AF488-labelled TNFα were recorded and analyzed, being characterized by an amplitude averaged lifetime of 2.9 ns and 4.1 ns, respectively. The shortening of the lifetime of the donor from 4.1 ns to 2.9 ns in the antibody functionalized microgels is a clear evidence of the FRET process, and therefore, of the TNFα-antibody interaction. In summary, the combination of the intensity-based FRET and FLIM-FRET experiment confirmed the

existence of the FRET process, and therefore, of the successful TNFα-antibody interaction in the microgels.

Lastly, TNFα antibody-functionalized microgels were exposed to TNFα in the presence of human colorectal adenocarcinoma (HT29) cells (see Figure 1.9). The levels of COX II and the release of pro-inflammatory cytokine IL8 were used as indicators for TNFα toxicity. In comparison to exposure of the cells with TNFα alone, the co-incubation with antibody-functionalized microgels significantly reduced COX II levels, as well as the amount of IL8 in the cell culture supernatant. Importantly, the microgels also scavenged all detectable TNFα produced by human macrophages upon stimulation with lipopolysaccharide (LPS) in the cell culture supernatant, demonstrating their ability to efficiently scavenge the produced TNFα in real-time.
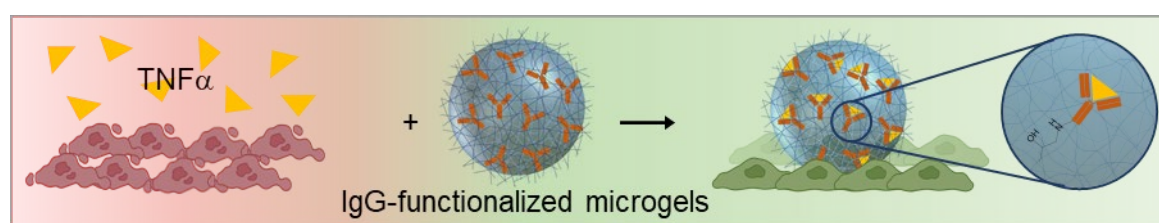
Figure 1.9: Schematic representation of scavenging of TNFα in the presence of human colorectal adenocarcinoma cells using TNFα antibody-functionalized microgels.

1.4.2   Inflammation-targeting adhesive microgels for protecting epithelial surface

As described above, the key strategies to treat IBD are based on TNFα-targeting drugs to reduce the inflamed area in the intestine – and on specifically targeting the inflamed tissue, as well as protecting the degraded mucus and shielding the tissue from harmful bacteria to achieve mucosal healing as described in the following.

1.4.2.1   Targeting of inflamed tissue

Various strategies have been suggested for specific targeting of inflamed tissue during IBD. Generally, the epithelial cells of the inflamed colon can be targeted based on the local pH, levels of specific enzymes or ROS, and via ligand-receptor interaction, electrostatic interaction, and permeability.[88] During the pathogenesis of IBD, many specific antigens and receptors, such as CD44, CD98, and mannose receptor, folate receptor, and transferrin

receptor, are overexpressed by inflamed colonic epithelial cells and activated macrophages, while many ligand-receptor systems have been widely designed and applied for colon-targeted IBD therapy.[42,89]

CD44 is a single-chain transmembrane glycoprotein and highly overexpressed on the intestinal epithelial cells in colitis tissues, making it an effective target in IBD therapy.[89,90] It specifically binds to hyaluronic acid (HA), a biocompatible, biodegradable natural anionic polysaccharide and a major component of the extracellular matrix (ECM) and, thus, essential for cell growth, organ structural stability, and tissue organization.[91] Depending on its molecular weight, HA exhibits different properties. HA with a molecular weight in the range of 10-500 kDa exhibits good viscoelasticity, mucoadhesion, and anti-angiogenic activity, while below 4 kDa, it promotes angiogenesis, inducing the expression of inflammatory mediators and inhibiting tumor growth.[88] Furthermore, higher molecular weight HA shows a greater affinity to CD44 receptors due to the multivalent binding interactions.[92]

Specifically, colon-targeted HA-based NP systems are developed as oral DDS in IBD as they can be designed to release drugs specifically in the GI tract and protect encapsulated agents against harsh biological environments, such as low pH and enzyme degradation.[42,89,93,94] For example, HA-bilirubin core-shell NPs were produced and orally administered to healthy and DSS-colitis mice.[42] The NPs show localized accumulation in CD44 overexpressing DSS-damaged colonic epithelium due to HA-CD44 interaction in comparison to healthy colon of mice. Moreover, bilirubin shows ROS scavenging capacity. Both effects result in protection of colonic epithelial cells against apoptosis by targeting inflamed colon and directly modulating the intestinal barrier and gut microbiota, while exerting a potent anti-inflammatory response against colitis in a murine model. However, these NPs accumulate in the damaged epithelium and pro-inflammatory macrophages and do not shield the epithelial surface from harmful bacteria, limiting this approach.

1.4.2.2 Protecting of damaged mucus

Besides the idea of targeting inflamed colon tissue during IBD via HA-CD44 interaction, the motivation of my research is to combine this approach with the idea of forming a protecting shield from harmful bacteria on the damaged mucus. Therefore, I developed HA-

co-polymerized sPEG-based microgels for specific targeting of inflamed intestinal epithelial cells and to form a dense microgel layer on the epithelial surface to replace the degraded mucus and shield the tissue from pathogens as described in Chapter 4.

Depending on the type, cells mechanically interact with their environment by applying force to their underlying or surrounding matrix, feel the matrix deformation, transduce these signals, and adapt their response accordingly, as described by *mechanobiology*.[95] Therefore, for the interaction with cells, stiffness of the hydrogel matrix is one of the most important and commonly investigated property that can directly affect fundamental cellular processes including spreading, growth, proliferation, migration, differentiation, and organoid formation.[96] This seems reasonable considering the fact that tissue elastic moduli can vary in the body from the softest brain and fat tissue in the range of hundreds of pascals to stiff bone tissue in the range of tens of gigapascals. It has been published that different cell types, including epithelial cells and fibroblasts, behave differently when cultured on stiff or soft surfaces in 2.5D. While on top of soft, lightly crosslinked elastic hydrogels ($E \sim 1$ kPa), cells show diffuse and dynamic adhesion with more round morphologies and more often fail to assemble robust actin stress fibres, on stiffer hydrogels ($E \sim 30$ to 100 kPa) cells adopt spread morphologies and are able to develop large, stable focal adhesions with defined actin stress fibres.[97] However, in 3D cell culture, the trend is reverse with decreased cell spreading in stiffer matrices due to the lack of sufficient space in highly crosslinked gels. For example, in the Anisogel system developed by our research group, aligned rod-shaped microgels are crosslinked in a very soft surrounding bulk hydrogel that exhibits a Young's modulus lower than 1 kPa.[98] It is important to state that in 3D, the internal structure will affect the stiffness, mesh size, and degradation rate, all influencing the support and space the cells need to spread and grow.

In addition, living tissues and ECMs are viscoelastic, which means that they exhibit an instantaneous elastic response (characteristic of purely elastic solids), followed by a time-dependent mechanical response and energy dissipation or loss (characteristic of viscous liquids).[96] To better mimic the natural ECM, hydrogels can be engineered to exhibit viscoelasticity. While an ideal covalent polymer network leads to the formation of mainly elastic hydrogels, non-ideally crosslinked entangled polymer networks with non-crosslinked loose ends or polymer networks crosslinked via supramolecular or dynamic covalent bonds lead to energy dissipation and the formation of viscoelastic hydrogels. Thereby, by varying the concentration of monomer and crosslinker, or by incorporating

non-crosslinked, entangled polymer into crosslinked hydrogels, one can prepare hydrogels with the same stiffness but different viscoelastic properties for different biomedical applications.[96]

Atomic force microscopy (AFM) is a well-established technique that is widely used for the characterization of the mechanical properties of dry and often hard materials in air.[95] However, AFM has also recently been used for the measurement of soft biological samples with a Young's modulus between 0.1 and 10 kPa, such as living cells, but also soft hydrated materials, such as hydrogels.[99] The mechanical properties measured by AFM include force, pressure, tension, adhesion, friction, elasticity, viscosity, and energy dissipation.[100] Furthermore, the topography can be mapped with a spatial resolution ranging from sub-nanometres to millimetres.[100] For the measurement of stiff materials, sharp probes are mostly used as they allow high local pressure to cause a significant indentation and nanometric lateral resolution. However, for soft samples that are measured in liquid, spherical colloidal probes represent a better solution due to reduced local pressure and a less sharp curvature to prevent the sample from damage, as well as the capability of microscopically averaged mechanical characterization.[99] Moreover, the AFM-micro-rheology method has been described for the measurement of viscoelastic properties of hydrogels over a wide range of continuous frequencies of a simple stress-relaxation nanoindentation.[101]

The incorporation of HA into the sPEG-based microgels does not only allow for the interaction with CD44 receptors that are overexpressed on intestinal epithelial cells in colitis tissue, it can also tune the stiffness and viscoelastic properties of the microgels. Depending on its concentration and molecular weight in aqueous solution, HA can form non-covalent, supramolecular hydrogen bonds, the latter introducing more viscous properties to the microgels.[102] This can lead to the formation of soft, deformable materials with shear-thinning behaviour if no covalent bonds are present. The shear-thinning behaviour of HA results from the breakdown of the intermolecular hydrogen bonds and hydrophobic interactions under increasing shear rates.[103] In my case, HA is modified with acrylate groups to form covalent bonds with 4-arm sPEG-Ac, rendering the microgels more elastic.

In Chapter 4, I investigate the adhesion of HA-Ac-co-polymerized 4-arm sPEG-Ac-based microgels on human intestinal adenocarcinoma cell lines HT29 that express CD44 receptors. In comparison to the microfluidic microgel production as described in Chapter 3,

a high-throughput microfluidic system with 100 parallelized droplet generating channels was used to increase the microgel production rate. I characterized the cell-microgel interaction using microgels with varied stiffness, as well as viscoelastic properties, by tuning the total polymer mass concentration (5 wt% and 10 wt%), as well as different concentrations (0%, 3%, 5%, and 10%), molecular weights (50 kDa and 250 kDa), and DoS (1% and 5%) of reactive acrylate groups of HA for covalent polymerization with the PEG matrix. In comparison to NP systems where the NPs are taken up by the cells and cross the intestinal barrier[89], I produced larger microgels with a diameter of around 25 μm to be able to form a protective shield on the epithelial surface.

In general, HA-functionalized microgels made from higher total polymer mass concentration (10 wt%) resulted in higher stiffness of around $30 - 60$ kPa compared to microgels made from 5 wt% ($0.4 - 1.3$ kPa). The viscoelasticity of the microgels prepared with different HA-Ac concentration, molecular weight (50 kDa and 250 kDa), and DoS (1% and 5%) of reactive acrylate groups was non-significant. Due to the limited solubility of HA-Ac in aqueous solution, the maximal HA-Ac content was higher for microgels made from total polymer mass concentration of 5 wt% (4.5 wt% sPEG-Ac and 0.5 wt% HA-Ac (10%)) compared to microgels made from total polymer mass concentration of 10 wt% (9.5 wt% sPEG-Ac and 0.5 wt% HA-Ac (5%)). Even though microgels made from higher total polymer concentration (10 wt%) exhibit lower HA-Ac concentration and presumably less cell adhesion points, they overall show better cell attachment, when incubated with HT29 cell line. Moreover, microgels co-polymerized with HA-Ac with higher molecular weight of 250 kDa and lower DoS of acrylate groups of 1% showed superior cell attachment compared to microgels with HA-Ac of a molecular weight of 50 kDa and higher DoS of acrylate groups of 1% at similar stiffness (around 30 kPa). This is probably because higher molecular weight HA-Ac exhibits larger coils that can interact with the CD44 receptor on the cell surface. The use of lower DoS of reactive acrylate groups leads to less covalent bonds and probably enables more flexibility of the HA-Ac chains. However, the change of DoS entails the change of the stiffness of the microgels, which does not allow for the investigation of those two parameters on cell-microgel adhesion to be analyzed independently.

1.4.3 Importance of understanding the internal structure of microgels

In Chapters 3 and 4, I demonstrated the potential of functional microgels for the treatment of IBD by scavenging pro-inflammatory cytokine TNFα to stop the inflammation and by targeting and adhering to damaged intestinal tissue to protect the epithelial surface from the attack of pathogens. Moreover, I demonstrated the importance of diffusion properties, as well as the stiffness and viscoelasticity of the microgels when interacting with living materials. However, these are not the only factors that affect the interaction between cells with their surroundings.
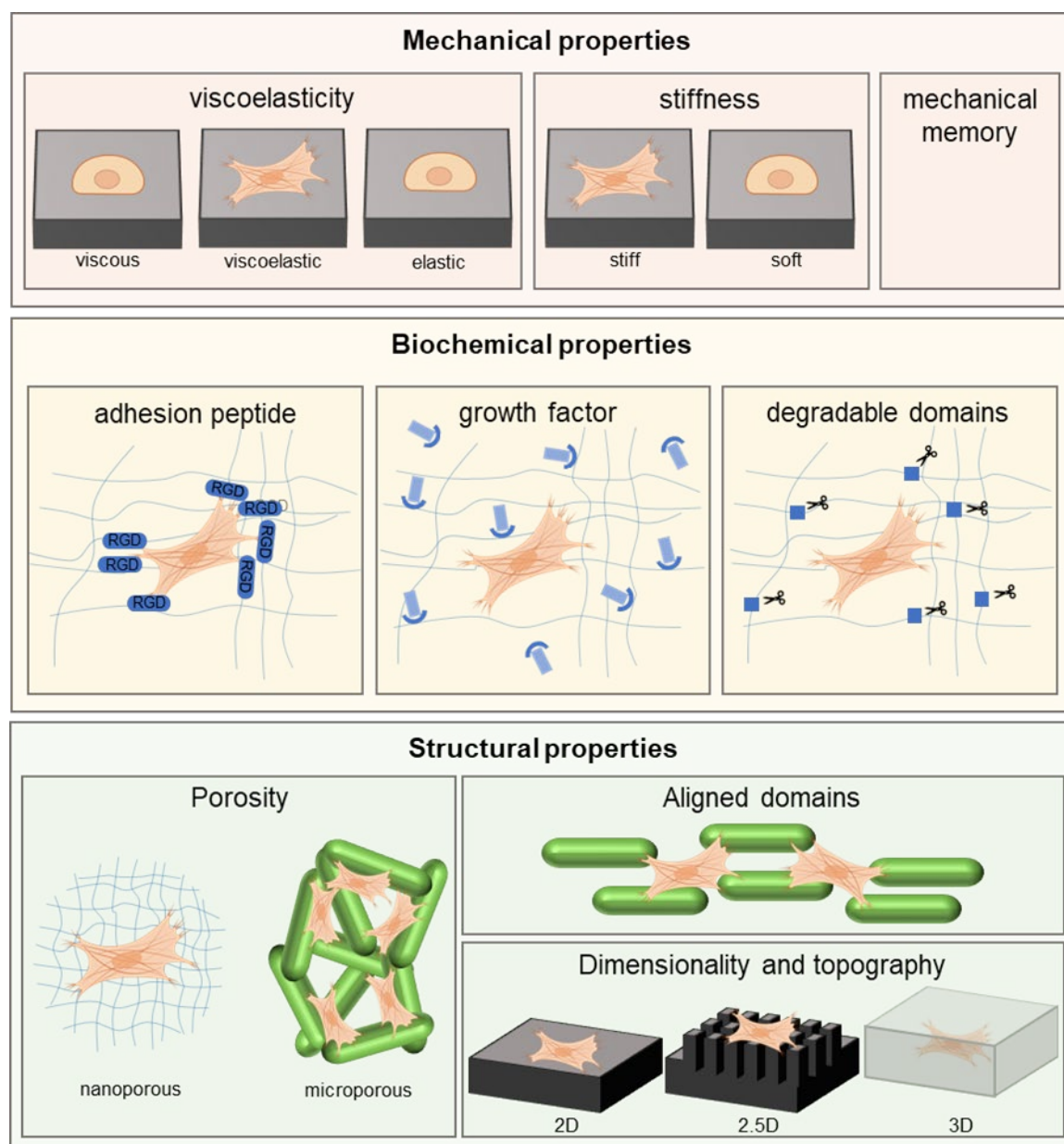
Figure 1.10: Key factors that affect cell behaviour. Mechanical, biochemical, and structural properties of hydrogels need to be investigated separately to understand cell response.

In fact, biochemical, as well as structural properties of the ECM, also directly affect cellular processes, including spreading, migration, proliferation, and differentiation.[104] Therefore, the understanding of how the different categories *mechanical*, *biochemical*, and *structural* properties of microgels affect the interaction with cells is crucial to be able to better design and employ microgels for biomedical applications, such as in my case for the therapeutic application in the GI, but also for scaffold formation to grow cells in 3D and for engineering tissues (see Figure 1.10). However, the internal structure of micron-scale microgels, produced by microfluidics, is not yet fully investigated in literature. Therefore, one of the key motivations of Chapter 5 in my thesis is to systematically investigate how the polymer composition influences the internal structure of soft microgels and how this morphology and the addition of bioactive molecules affects their function and interaction with cells.

The internal structure of microgels unites the hierarchical contributions of molecular crosslink density and their morphological organization into a swollen microgel with different ratios of macropores ($> 50\,\mu m$) that are formed during demixing upon polymerization, mesopores ($2 - 50\,nm$) that are formed due to crosslink density fluctuations, and micropores ($< 2\,nm$) that reflect the free volume inside the polymer coils themselves (see Figure 1.11). Importantly, these different hierarchical structures of the internal structure of microgels play a role when characterizing the stiffness and diffusion properties. Thus, the internal structure affects the swelling and shrinking capacity of a microgel in response to external triggers, such as pH, light, and temperature, the diffusion of molecules through the network, and the mechanical and chemical interaction with their environment.

i) macropores   ii) mesopores   iii) micropores
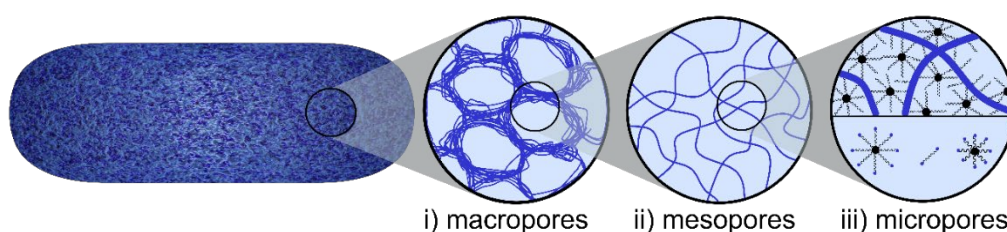
Figure 1.11: Schematic representation of different hierarchical structures of the internal structure of rod-shaped microgels.

To investigate the internal structure, I characterized the mechanical as well as diffusion properties of bulk hydrogels and rod-shaped microgels produced via microfluidics, both crosslinked via free radical polymerization. While most biomedical applications use spherical microgels, anisometric rod-shaped microgels have attracted growing interest in regenerative medicine.[105,106] Rod-shaped microgels entail large open voids when they are

jammed due to their higher aspect ratio. Therefore, they introduce macroscopic porosity, which is beneficial for cell seeding, proliferation, cell-cell interaction, and the exchange of nutrients making them interesting as building blocks for the synthesis of 3D macroporous constructs in tissue engineering.[107] Furthermore, rod-shaped microgels entail anisometry and, therefore, directionality, which allows for structural guidance (see Figure 1.10). The Anisogel system developed by our research group demonstrates a dual anisotropic and injectable hybrid hydrogel consisting of magneto-responsive, rod-shaped, soft microgels and a surrounding hydrogel matrix, which crosslinks *in situ* to fix the oriented microgels.[108] This system is beneficial to promote cell alignment and, for example, oriented nerve growth for the recovery after spinal cord injury.
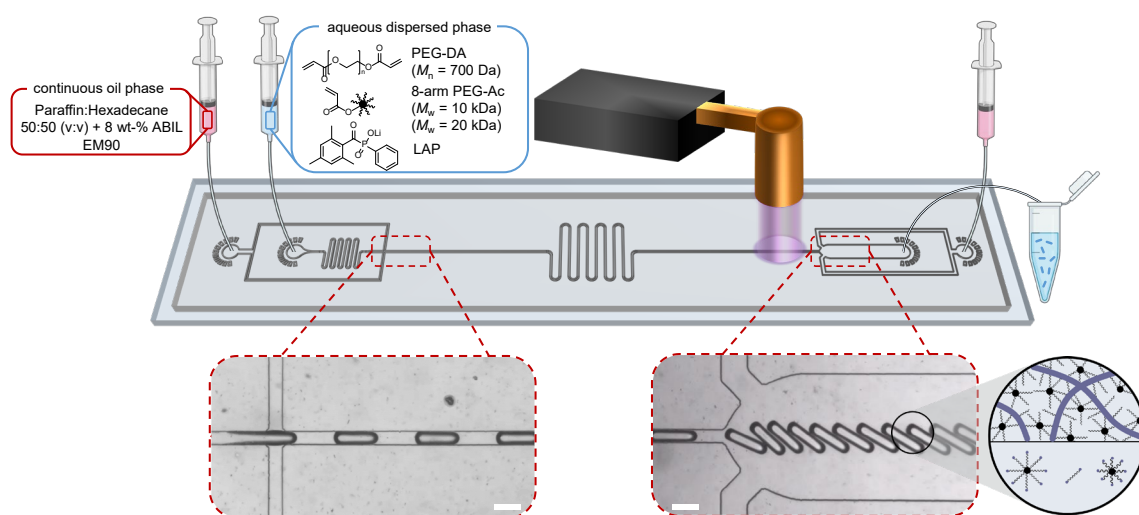
Figure 1.12: Schematic representation of microfluidic continuous plug-flow on-chip production of rod-shaped microgels. Red syringes indicate the continuous oil phase and the blue syringe contains the aqueous dispersed phase.

I systematically produced bulk hydrogels as well as rod-shaped microgels via plug-flow on-chip microfluidics by varying the concentration, molar mass, and ratio of 8-arm sPEG-Ac with molar masses of 10 kDa and 20 kDa in combination with a linear lower molar mass PEG-DA (700 Da) (see Figure 1.12). Here, instead of the 4-arm sPEG-Ac used for the microgel synthesis for the application for the treatment of IBD in Chapters 3 and 4, 8-arm sPEG-Ac was chosen to enhance the crosslinking rate on chip, which is required to maintain the anisometric microgel shape.[109] In addition, a higher amount of non-crosslinked dangling polymer chains is expected for the 8-arm due to higher steric hindrance of the polymer arms during polymerization compared to the 4-arm sPEG-Ac. These non-reacted free acrylate groups at the polymer ends in the microgel polymer network can be used for post-functionalization with cell adhesive peptides GRGDS-PC to support cell attachment. First, a total polymer mass concentration of 5 wt% and 10 wt% was chosen to investigate

the influence of stiffness on cell attachment. However, to use less synthetic material, the focus was set on the 5 wt% total polymer mass concentration. To further soften the polymer network, linear lower molar mass PEG-DA (700 Da) was added. Microgels, as well as bulk hydrogels, were analyzed in terms of their diffusivity, morphology, chemical functionality, and mechanical properties. Moreover, I investigated cell attachment and spreading on GRGDS-PC post-functionalized microgels. In order to keep the system as simple as possible and to be able to characterize only the influence of polymer architecture, concentration, molar mass, and ratio of different molecules on the microgels' internal structure, no chemical or biological functional groups were used during the microgel synthesis on chip, only via post-functionalization.

First, to characterize the mechanical properties using rheology, I produced bulk hydrogels by crosslinking pre-polymer solutions consisting of different ratios of 8-arm sPEG-Ac (M_W = 10 kDa or 20 kDa) and PEG-DA (M_n = 700 Da) via free radical polymerization using photoinitiator lithium-phenyl-2,4,6-trimethylbenzoylphosphinat (LAP) activated with UV light. Surprisingly, the 20 kDa sPEG-Ac system resulted in a stiffer polymer network compared to the 10 kDa system at similar polymer concentrations without PEG-DA. This can be explained by higher crosslinking density of the 20 kDa sPEG-Ac polymer due to less steric hindrance of the polymer.

To characterize the conformation of star-shaped polymers, intrinsic viscosity or light scattering or small angle neutron scattering (SANS) measurements are often performed.[110–112] However, the diameter of the star-shaped polymers can show different scaling behaviour in different regimes depending on the number of arms, chain length, and polymer concentration of the solution, but also on the solvent and temperature. In the case of brushes that are grafted on planar substrate, Alexander and de Gennes have first introduced a theoretical study about the linear dependence of the brush height on the degree of polymerization.[113,114] A generalized theory for brushes that are grafted on curved surface was presented by Daoud and Cotton (DC), who extended the scaling arguments of Alexander and de Gennes to neutral star-shaped polymers in good solvents.[115] The DC model describes that all polymer chains are bound to a central point and the free ends are a uniform distance away from the surface. However, in contrast to a solution of a linear polymer that exhibits a homogeneous density profile, the polymer chains of a single uniform star-shaped architecture includes a strongly inhomogeneous density profile as a star made of f number of branches with different molecular weight (N statistical units of

length *l*) have to join at the centre (see Figure 1.13A and B).[116] The DC model describes locally a single chain behaviour with the correlation length $\xi(r)$, represented as a spherical *blob*.[115] All the blobs at a given distance from the central point have the same size ($\xi(r)$), while with the distance from the centre the blob size increases. Importantly, this means within a blob the swelling parameter is constant, but that the swelling decreases with decreasing distance of the blob to the centre. Thereby, DC described three different regimes for the degree of swelling: the swollen region for monomer-centre distances $r > r_1$, the unswollen region $r_2 < r < r_1$, and the core region for $r < r_2$. Each of these regions exhibit different scaling laws for the correlation length $\xi(r)$, the number of monomers per blob $n(r)$, and the local monomer density within a blob $\rho(r) = n(r)/\xi^3(r)$.[116] This means, the polymer density at the core region is very high, while with increasing distance from the centre the density decreases.

At low molecular weight or at low number of arms (low grafting density), the radius of gyration of the polymer chains R_g does not exceed the interchain spacing and individual chains do not interact with neighbouring chains and, thus, form a mushroom-like conformation (see Figure 1.13C).[117] For longer polymer chains with dominating swollen chain regions, the unswollen and core parts can be ignored.[116] For these stars, the spatial extension, thus the end-to-end distance of the star is larger than that of an isolated chain with the same molecular weight of 2 arms due to the stretching of the chains caused by the confinement of the neighbouring chains in the star architecture.[116] This effect can also be seen with increasing number of arms, for example from 4-arm to 8-arm star-shaped polymer, resulting in a more brush-like conformation.[117] Moreover, with increasing molecular weight, for example from 10 kDa to 20 kDa in 8-arm star-shaped polymer, the radius increases, but not in a linear manner. In the core region, the blob size coincides with the monomer size.[116] In the unswollen region, the blob size is smaller, reaching the ideal chain limit. However, for the swollen region, the blob size exceeds the distance over which the behaviour of the polymer chain is ideal, which means that the chain is self-avoiding as described by the excluded volume parameter by Flory and de Gennes.[116,118,119] In general, it is important to note here that the described effects are highly dependent on the solvent, polymer concentration in solution, and the temperature.
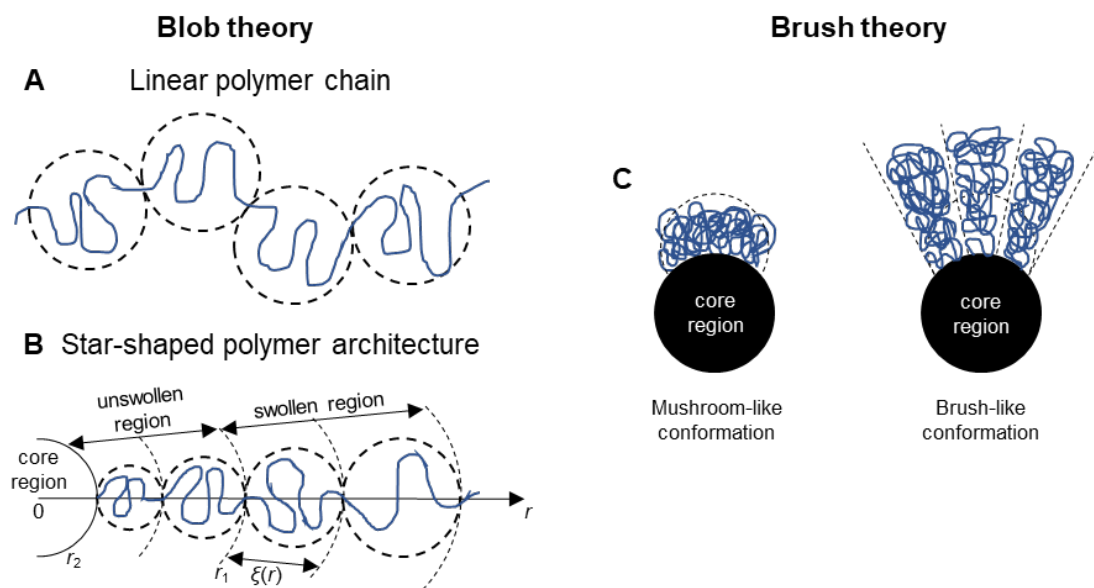
Figure 1.13: Blob picture of A) linear polymer chain and B) of a star-shaped polymer architecture described by Daoud and Cotton (DC).[115] C) Schematic representation of conformational change of polymer brushes attached to a spherical interface.[117]

In summary, these theories led us to hypothesize a higher rigidity, thus bigger end-to-end distance, of the polymer chains in stars with higher molecular weight, when comparing 20 kDa and 10 kDa in 8-arm star-shaped polymer. This would lead to better crosslinking of the 20 kDa polymer as the chain ends can reach each other better – and exhibit less steric hindrance from neighbouring chains. Furthermore, coming back to the higher stiffness of 8-arm star-shaped polymer with a molecular weight of 20 kDa compared to 10 kDa measured via nanoindentation, it is important to consider that nanoindentation is not simply measuring the stiffness of individual stars but how they squeeze upon each other.

To verify the described theories, I measured the intrinsic viscosities of both polymer solutions and found that 20 kDa sPEG-Ac (45.6 mg mL^{-1}) exhibits a lower coil density compared to 10 kDa (194.5 mg mL^{-1}), which allows for better accessibility of the reactive groups for polymerization. Moreover, I produced bulk hydrogels from the same pre-polymer solutions and measured their diffusion properties via confocal microscopy by incubating FITC-dextrans with different sizes and performing FRAP measurements. Hydrogels made from 10 kDa polymer show the slowest dextran diffusion, which indicates that less open space is available. This is in agreement with the fact that 10 kDa sPEG-Ac seems to lead to more steric hindrance due to its higher coil density and, therefore, blocks accessibility of reactive acrylate groups, resulting in only partially crosslinked polymer chains, hindering diffusion within the free volume (micropores) between the polymer chains. Furthermore, as expected, the addition of linear lower molar mass PEG-DA to

sPEG-Ac lead to softer hydrogels as the amount of sPEG-Ac, thus the amount of network stabilizing cores, was decreased. Also, with increasing ratio of PEG-DA in the 20 kDa polymer system, slower diffusion is observed, due to the fact that dangling, partially crosslinked PEG-DA molecules fill up the void space. I confirmed these results by quantifying the non-crosslinked reactive acrylate groups inside the polymer network after photopolymerization via Raman spectroscopy.

In a next step, I characterized the internal structure of anisometric, rod-shaped microgels prepared with the same pre-polymer solutions via plug-flow microfluidics using continuous on-chip gelation of droplets. Correlating with the trends for bulk hydrogels, microgels made from higher molar mass 20 kDa show a higher stiffness and diffusion coefficient, characterized via nanoindentation and FITC measurements, respectively. Moreover, more crude structures were measured for the microgels made from 20 kDa compared to 10 kDa via cryo-SEM, which is in agreement with the diffusion studies that indicated an overall larger mesh size for the 20 kDa microgels. The latter statement was confirmed by comparing the mesoporosity of the 20 kDa and 10 kDa microgels in STED microscopy followed by image analysis.

Lastly, microgels with different internal structures were used for cell attachment using L929 mouse fibroblasts. As described above, cell attachment is highly dependent on the stiffness and viscoelasticity of the microgels; however, the presence of cell binding ECM protein domains is crucial for efficient cell binding. Thus, cell attachment is more dependent on the interplay of the mechanical and biochemical properties of the microgels, influenced by the combination of the type and concentration of cell binding domains present on the outside of the microgels.

In particular, the ECM is a key regulator of cell communication and regulation and contains water, proteins, including collagens, fibronectin, elastin, and laminins, as well as proteoglycans, signalling cues, minerals, and ions.[104] Cell adhesion receptors, integrins and cadherins, are fundamental for cell-ECM and cell-cell communication, respectively. Due to its heterodimer structure containing an α and a β subunit, an integrin receptor can specifically bind to a certain ligand. One of the most studied binding ligands is the RGD (Arg-Gly-Asp) peptide sequence that is presented in many ECM proteins, such as fibronectin, and, therefore, binds to multiple integrin subunits. However, there are

28

numerous peptide sequences that can directly affect multiple biological effects, such as cell adhesion, differentiation, and immunomodulation.[104] Depending on the desired application, synthetic polymers, such as PEG, can be functionalized with RGD motifs to control cell adhesion and spreading[120] or, for example, with laminin-derived peptides including IKVAV to induce cell aggregation and cluster formation during vasculogenesis and neurogenesis.[104] Importantly, besides the type of the ligand, its concentration, availability, and local distribution affects the biological effect.[121,122]

In Chapter 5, I proved the statement that cell adhesion and spreading are not only dependent on the stiffness of the microgels, but also on the presence of cell binding peptides. I investigated microgels made from different pre-polymer solutions containing 8-arm sPEG-Ac with different molar mass of 10 kDa and 20 kDa, different amounts of PEG-DA, different total mass concentration, and different UV light power leading to different stiffness at constant viscoelasticity in cell culture. To support cell attachment to the microgels, I introduced cell binding peptides via base (B)-catalysed post-functionalization of the microgels with GRGDS-PC using thiol-Michael addition of cysteine presented in the peptide with the non-reacted acrylate groups on the surface of the microgels (see Figure 1.14).
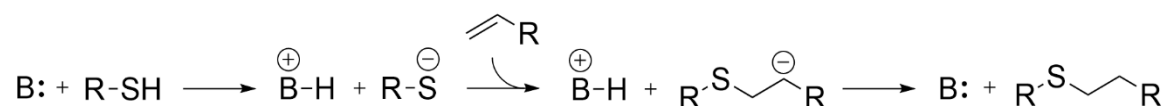
Figure 1.14: Mechanism of base (B)-catalysed post-functionalization of microgels with GRGDS-PC via thiol-Michael addition of cysteine presented in the peptide with the non-reacted acrylate groups on the surface of the microgels.

Microgels made from 5 wt% 8-arm sPEG-Ac (M_W = 20 kDa) and 10 wt% 8-arm sPEG-Ac (M_W = 10 kDa; UV light power = 30 mW) exhibit comparable stiffness of 51.5 ± 8.0 kPa and 46.6 ± 14.8 kPa, respectively, in nanoindentation measurements. However, cell spreading is more efficient for 10 wt% 8-arm sPEG-Ac (M_W = 10 kDa; UV light power = 30 mW) (see Figure 1.15). This might be due to higher RGD concentration on the microgel surface on 10 wt% 8-arm sPEG-Ac (M_W = 10 kDa; UV light power = 30 mW) microgels (8.1% RGD) compared to 5 wt% 8-arm sPEG-Ac (M_W = 20 kDa) microgels (2.1% RGD) analyzed via XPS. When comparing cell interaction on microgels made from 10 wt% 8-arm sPEG-Ac (M_W = 10 kDa) using different UV light power of 30 mW (E_{eff} = 46.6 ± 14.8 kPa) and 300 mW (E_{eff} = 91.8 ± 9.3 kPa) that exhibit a RGD concentration of 8.1% and 6.3% RGD, respectively, a better cell spreading is observed for microgels irradiated with lower UV light power. A reason for this observation could be the

presence of the RGD on the outside of the microgels, as a higher crosslinking and thus less free acrylates is expected for microgels that were irradiated with higher UV light power. Additionally, the stiffness of the microgels may play a role.
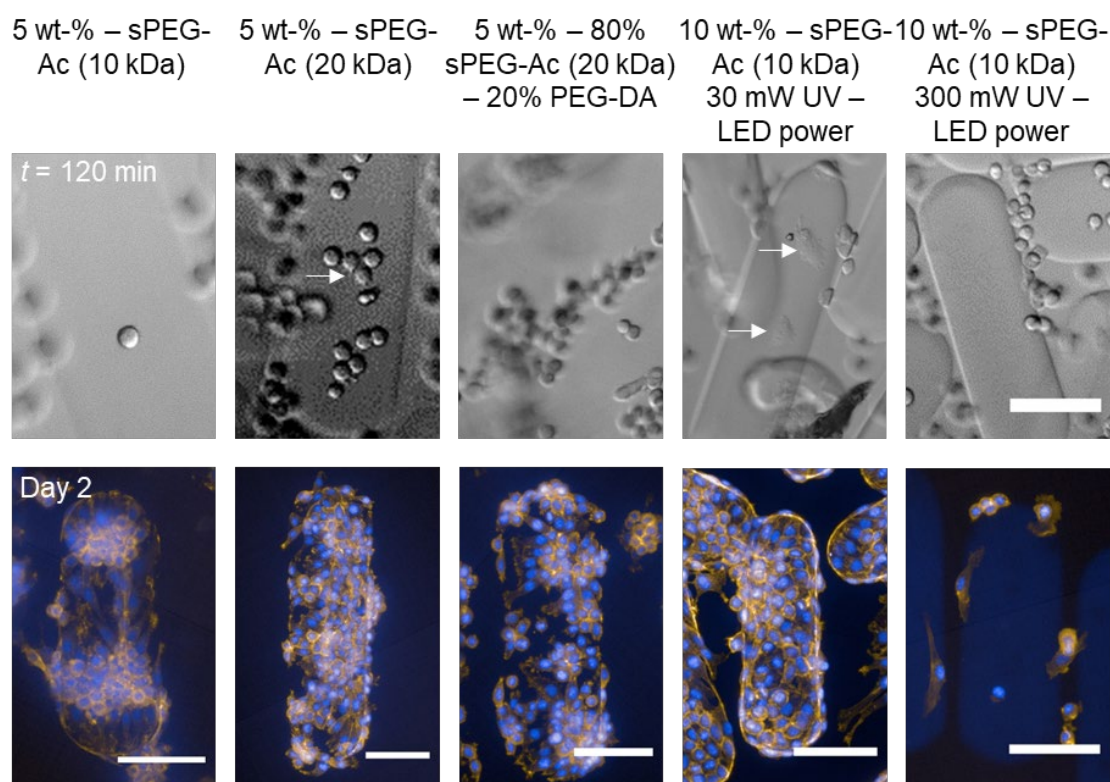
Figure 1.15: Cell culture of L929 fibroblasts on most representative single GRGDS-PC post-functionalized rod-shaped microgels. a) Images of live imaging and b) fluorescent confocal images show cell attachment and spreading on microgels with 5 wt% 8-arm sPEG-Ac (10 kDa), 5 wt% 8-arm sPEG-Ac (20 kDa), 5 wt% 80% 8-arm sPEG-Ac (20 kDa) – 20% PEG-DA, 10 wt% 8-arm sPEG-Ac (10 kDa) 30 mW UV-LED power, and 10 wt% 8-arm sPEG-Ac (10 kDa) 300 mW UV-LED power.

1.5 Summary

The overall goal of my thesis is to develop inflammation-targeting multifunctional star-shaped poly(ethylene glycol) (sPEG)-based microgels as novel combinatorial therapy for local treatment of non-microbial inflammatory bowel diseases (IBD). In **Chapter 1**, I describe the motivation of my work on how three different key challenges of IBD treatment are addressed by altering the microgel properties as desired. **Chapter 2** discusses the state of the art of microgel requirements for clinical applications by giving an overview of key attributes, such as biocompatibility, biodegradability, mechanical stability and softness, loading capacity, chemical functionality, and cell interaction. Moreover, different microgel fabrication, as well characterization, techniques are discussed in detail. In **Chapter 3**, I

make use of the existing systemic TNFα antibody therapy in clinics for IBD treatment – however, I incorporate TNFα antibodies (adalimumab) in sPEG-based microgels for non-systemic but local specific scavenging of the inflammation-mediating cytokine TNFα to inhibit the inflammation in the intestine. Spherical microgels are synthesized via droplet-based microfluidics with a diameter of around 25 μm. I have systematically investigated the diffusion of TNFα antibody, as well as TNFα itself, inside the microgels made from different sPEG-Ac building blocks and GMA as co-polymer. In particular, the high loading of TNFα antibody inside the microgels and sequential TNFα binding capacity of the microgels, due to their high accessibility of internal surface, is shown in the presence of human colorectal adenocarcinoma cells HT29. Furthermore, the microgels scavenge TNFα produced by human macrophages to mimic the *in vivo* situation of IBD. In fact, the microgels scavenge TNFα at concentrations that are far beyond disease relevant levels. **Chapter 4** addresses another major challenge in IBD therapy: the repair of damaged epithelial intestinal barrier. For this purpose, I have produced hyaluronic acid (HA)-functionalized microgels that specifically target and bind CD44 receptor-expressing inflamed intestinal epithelial cells. Therefore, I have investigated the stiffness and viscoelastic properties of the microgels to mimic the mucosal ECM. By active targeting and binding to inflamed intestinal cells, the microgels form a layer on the epithelial surface to replace the degraded mucus and shield the tissue from harmful bacteria. Finally, **Chapter 5** gives a deeper insight of the importance of mechanical, biochemical, and structural properties of microgels, when they are applied in cell culture to be able to better design and employ microgels as building blocks for engineered tissues. For this purpose, I have systematically investigated how the concentration, molecular weight, and architecture of the molecular building blocks influence the internal structure of rod-shaped microgels, and thus their mechanical and diffusion properties. Furthermore, I have characterized how the internal structure, as well as the functionalization of the microgels with cell-adhesive peptide RGD, affect the interaction with cells. In conclusion, this thesis provides a comprehensive overview of the interplay of mechanical, biochemical, and structural properties of microgels when applied for biomedical application, in particular for the treatment of IBD.

2 State of the Art

2.1 Introduction

Hydrogels are three dimensional hydrophilic macromolecular networks containing large amounts of water.[123–125] Bulk hydrogels are often employed for clinical applications; for example as lubricating coatings on catheters and medical devices, as therapeutic delivery depots, and as scaffolds for tissue engineering.[126,127] However, the macroscopic character of hydrogels limits the range of application to those listed above. Conversely, many modern therapeutic strategies require microscopic gel entities to take effect. Such microscopic gels – so called microgels – facilitate targeted systemic or on-site delivery, enables local imaging or allows for utilization of self-assembly and aggregation phenomena at a designated area in the body. Much like their macroscopic relatives, microgels are composed of water-soluble macromolecules that are crosslinked; however, they are much smaller than hydrogels with dimensions of the order of 10 nm to 100 µm. As such, microgels are sufficiently small to allow for injection, and depending on their size, circulation in the body. Microgels are adequately soft to conform to surfaces and cross membranes and biological barriers, and can be chemically modified to attach to biointerfaces, interact with biomolecules, or locally assemble into macroporous constructs.[62,128] Materials on the micro- or nanoscale exhibit fundamentally different properties and functions compared to macroscopic bulk materials, even when they are prepared from the same material. Therefore, microgels represent interesting materials for advanced clinical applications.[129,130] Depending on their application, microgels require different biochemical, mechanical, and structural properties, which can be engineered by altering the biochemical composition, crosslink density, and fabrication method. In addition, dynamic processes can be programmed into the microgels and triggered by *internal* stimuli (induced by the native environment) or by *external* stimuli (light, magnetic field, ultrasound, etc.).

Similar to hydrogels, microgels can be varied in their crosslink density, which alters the network porosity and morphology directly impacting on the softness, degree of swelling, stability, and potential degradation rate of the microgels.

Because of the importance of molecular structure and morphology to the properties of the microgel, the community combines these effects under the term *internal structure*.[60,131] The term internal structure unites the hierarchical contributions of molecular crosslink

density and their morphological organization into a swollen microgel with different ratios of micro-, meso- and macroporosity. While for solid state materials, there is a uniform IUPAC definition for micro- (<2 nm), meso- (2 – 50 nm) and macroporosity (>50 nm), there is no general definition for polymer networks.[132] In the literature one finds a suggestion for swollen soft materials, such as microgels, where the pore or mesh size for microporosity is defined as 10 – 100 nm and for macroporosity as 0.1 – 1 µm.[132] The porosity of the microgel polymer network can be adjusted. To avoid diffusion of specific molecules, such as outward diffusion of imaging units or inward diffusion of nucleases and proteases into microgels, a microporous polymer structure is needed,[133,134] while for cell infiltration and spreading, macroporosity in the polymer network is required, with pores even larger than 1 µm, obtained via network degradation or phase separation.[135,136] Alternatively, supramolecular interactions and dynamic covalent bonds can be employed that cells are able to break to remodel the hydrogel without the need for degradation or larger pores, yet these materials are mainly still bulk hydrogels.[137–139]

When microgel networks and their degradation products are non-toxic and exhibit a desirable biological response for a specific application, they are biocompatible. Their high water content and open-meshed structure offer many interesting functionalities, such as enabling diffusion of guest molecules, deformation to shapes deviating extremely from their relaxed state, and mimicking of the ECM.[124,140]

Depending on the type of molecular building blocks and their degree of crosslinking, microgels can have different properties and responsivity. The building blocks can be of natural origin, like sugars and proteins, or be synthetic, produced from artificial monomers, pre-polymers, and/or engineered peptides, proteins, and glycans. Many microgels consist of a hybrid composition of fused synthetic and natural functionalities to make use of the emergent synergistic effects.[141,142]

Here, we will first discuss the requirements for microgels to be applied in the body of a patient. Then we will give a detailed overview of the different existing technologies to produce microgels, followed by a discussion on how to characterize the microgels.

We provide an overview on how microgels can be employed as local drug or cell delivery vehicles, as scavengers to remove molecules from the body, or as probes that enable

diagnostic visualization. Moreover, we discuss how microgels can act as scaffolds that provide structure to support tissue healing and regeneration.[143]

Finally, an overview will be given of those applications that have already made it into pre-clinical and clinical trials. Along this train of thought, we will highlight existing challenges and chances for future applications. Existing reviews about microgels focus on their mechanical and physicochemical properties.[144–146] There are also reviews about the potential applications of microgels[147–156] also in the biomedical field.[157–167] However, the community is lacking an instructive review that covers the requirements for microgels to be employed in the human body, while at the same time discussing which approaches have already translated into preclinical studies as well as clinical applications. The review at hand fills this gap, making it an important guideline for chemists, material scientists and researchers in the biomedical field.

2.2 Requirements for clinical application

To enable clinical application like drug delivery systems, imaging probes, or building blocks for tissue regeneration scaffolds, microgels need to meet several criteria (see Figure 2.1).
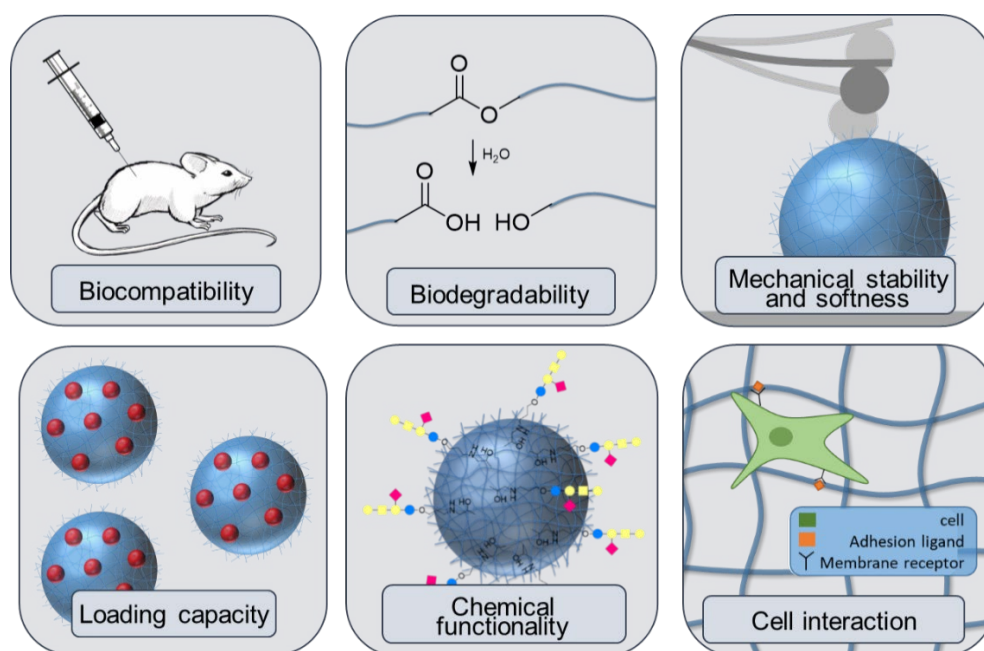
Figure 2.1: Overview of microgel requirements for clinical applications.

Biocompatibility: Biocompatibility describes the ability of a material to perform with an appropriate host response in a specific application.[168] A more simplistic definition is that a material does not create any adverse tissue reactions, so any toxic effects to the body. In general, it is described in literature that non-charged microgels that are hydrophilic and swollen show high biocompatibility.[169] However, depending on the application of the microgels *in vivo*, the biocompatibility of the used polymer and thus the immune response of the body that is generated by the foreign material can change with the nature of the tissue, such as dermis, muscle, or adipose tissue.[170] For example, it is known that the brain does not form fibrotic scars. Poly(ethylene glycol) (PEG)-based materials are known to be biocompatible for *in vivo* applications; but, they have also demonstrated to trigger fibrosis.[171] Therefore, polymer materials are functionalized with biocompatible molecules, such as proteins, to enhance biointegration.

Biodegradability: For most applications, the degradation products of the microgels need to be cleared from the body after the microgels have fulfilled their function. The degradation of a microgel network can occur *via* oxidative/reductive, hydrolytic, or enzymatic cleavage or *via* thermal- or photo-degradation, induced for example by laser irradiation.[56,172–175] The resulting degradation products should be smaller than 4 nm to be excreted renally (through the kidneys) and induce minimal cytotoxic effects and immune response, such as inflammation.[176] The way of molecular breakdown, as well as the degradation rate of the microgel network, are both highly dependent on the chemical and internal structure of the microgel. The crosslink density and swelling capacity of the microgel influence the thermodynamic bond stability as well as the degradation kinetics by affecting diffusion of the degradation trigger (for example hydrolytic enzymes) or uptake of water, acid, or base required for hydrolysis.[56]

Therefore, microgel degradation can be programmed on a molecular level, by using appropriate hydrophilic monomers and polymers that are precisely suited for the desired biomedical application.[170] The degradation time of PEG-based microgels can range from minutes to years depending on the choice of degradable connectors or crosslinkers. Therefore, the speed of degradation can be adjusted to the desired short- or long-term biomedical application.[56,177,178] For rapid degradation, a Michael-type addition between acrylate and thiol can be used, while free radical polymerization of PEG diacrylate (PEGDA) is employed to enable slow degradation through ester hydrolysis at the sterically protected acrylate end-groups.[177,178] *In vivo* degradation experiments where PEGDA has

been compared to PEG diacrylamide (PEGDAA) showed significant degradation of PEGDA samples after 12 weeks, while no measureable degradation could be detected for samples made of PEGDAA.[177] Instead of hydrolytically cleavable moieties, enzyme-sensitive domains can be incorporated between crosslinks to induce degradation upon exposure to the respective enzyme.[179] Importantly, the size of the degradation products is determined by the design of the chosen molecular architecture of the microgel. Star-shaped molecules with the same molecular weight as linear molecules will produce degradation products of smaller hydrodynamic radii, which are cleared faster from the body.[180,181]

Mechanical stability and softness: For many *in vivo* applications, microgels need to exhibit sufficient mechanical stability or softness to fulfil the respective task in the body.[170] The mechanical properties of the microgels, namely, softness or stiffness and in a related sense also their swelling behaviour, can be adjusted by the backbone and crosslink density of the gel.[170] In addition, the type of crosslinking, being either covalent, dynamic covalent, or non-covalent, determines the viscoelastic behaviour of the microgel.[182–185] For example, for the treatment of wound-triggered hemostasis, ultrasoft, highly deformable platelet-like microgels are investigated.[186] It is shown in dissipative particle dynamics simulations, that ultralow crosslinked polyNIPAM microgels (~10 kPa) lead to an increase in clot concentration that reduces the bleeding time.[186,187] By contrast, in locations, such as the heart or the gastrointestinal tracts, higher shear forces are present leading to the requirement of stiffer microgels in the range of kPa up to MPa.[170,188,189]

Loading capacity: One major advantage of microgels is their reversible swelling behavior, which makes them highly suitable for incorporation, storage, and delivery of cells, bio-macromolecules, therapeutic proteins, as well as drug molecules.[190] For delivery, microgels can be swollen and loaded outside of the body. Collapse of the loaded microgel leads to encapsulation of the cargo. In the body, the microgel can be reswollen upon issuing a trigger release of the cargo. Triggers can be pH, redox, light, temperature and other chemical or physical leads.[82]

The encapsulation efficiency is determined by several factors:

- The internal structure influences the capacity of the microgel. Depending on the mesh size of the network the loaded molecules can diffuse more or less deep into the microgel. Finer meshes with higher nanoporosity can take up more molecular

cargo than a microporous microgel, which in turn might be more suitable for encapsulation of cell cargo.[191–193]

- Functional groups presented throughout the microgel can increase the interaction with the respective cargo and hence increase the loading capacity. Due to the open network structure of the microgel, functionalization on "the inside" of the microgel allows for loading capacities surpassing those of solid and mesoporous particles.[147,165]

- Moreover, the heterogeneity of the microgel influences the loading capacity of the microgel. Heterogeneity can often occur as a gradient in structure or functionalization. Heterogeneity is evoked by changing reaction rates or phase separation of the building blocks upon polymerization. While a functionalization gradient limits the capacity towards the inside or (more often) towards the periphery of the microgel, a crosslinking gradient affects diffusion of cargo molecules deep into the microgel. On the other hand, a heterogeneous polymeric network leading to larger pores can enhance diffusion.[145]

Chemical functionality: To direct microgels to their site of action, microgels can be functionalized with targeting units. To enable specific binding to biological interfaces the targeting units need to be attached only in the periphery of the microgel. Specific recognition motifs are often small peptides, glycans or DNA fragments, which bind to surface motifs presented by specific cells or at defined pathological sites in the body. This targeting enhances the selectivity of drug administration and thus the therapeutic efficacy.[190] Here, a remaining challenge is to keep the functional domains available for binding and avoid formation of a protein corona on the microgels when the get in touch with bodily fluids for example in the blood stream.[194] Moreover, microgels can be functionalized to interact with soluble molecules, for example with the glycosphingolipid receptor GM1a to effectively bind cholera toxin for the treatment of bacteria induced diarrhea.[71] It was shown that the microgels could scavenge cholera toxin in direct binding competition to colorectal cell, which demonstrate their great potential as a non-antibiotic treatment for toxin-mediated infectious disorders.

Cell interaction: As an alternative to molecular drug delivery, therapeutic microgels can also be designed to interact with cells for regenerative purposes or immune modulation. Microgels can present antigenic proteins, nucleotides, drugs, and ECM components to interact with intracellular or surficial receptors on host cells.[195] Functional microgels can

modulate the immune system in two ways:[170,196] First, immune cell activation can be down-regulated in hyperactive immune conditions, for example in autoimmune and inflammatory diseases. Secondly, immune cell activation is enhanced to reverse hypoactive immune responses for example in cancer or in chronic infections.[196] In the case of tissue engineering, aligned rod-shaped microgels inside of a gel matrix have been modified with Gly-Arg-Gly-Asp-Ser (GRGDS)-peptides, leading to enhanced fibroblast alignment due to strong interactions between the cells and the biofunctionalized microgels.[120]

Moreover, cells can be loaded inside microgels before injection into the body. Cellular therapy plays an important role in modern medicine for the treatment of cancer and cardiac diseases but remain very expensive, while most cells lose their effectiveness shortly after injection.[197,198] When unprotected cells are injected into the body, they are exposed to high shear and oxidation stresses, which deteriorate their fate and limit therapeutic efficiency. 80 % of the cells undergo cell death or migrate away from the intended site of action.[68,199] Therefore, it is necessary to protect the cells by encapsulation into microgels.[200] The advantage of microgel encapsulation is the softness of the gel and its open degradable mesh structure, which supports all necessary functions of the cell and enables facile exchange of nutrients and metabolites. Microgels can bind to a targeted site and retain the cell locally.

Designing of cytocompatible microgels opens new possibilities for tissue engineering and applications in regenerative medicine.[201] They can function as building blocks and assemble into 3D regenerative constructs with or without cell encapsulation. The micron scaled interstices between the individual assembled microgels facilitate cell infiltration and growth.[202] The cytocompatibility of a microgel is given by its specific molecular interactions at the cell-microgel interface.[140] Successful microgel scaffolds are ECM-mimetics promoting cell adhesion, proliferation, migration, or differentiation of cells by attachment of the respective biomolecular cues to the microgels.[140,203] Arginine-glycine-aspartate (RGD) peptides are coupled to microgels to promote cell adhesion *via* integrin binding.[157,170] Recently, microgels have been implemented in bioinks to create 3D multifunctional scaffolds with properties that are typically found in native tissue.[204] Cell-laden microgels can be mixed with an injectable hydrogel precursors formulated as a bioink, enabling printing of *ex vivo* tissue models.[157,204] These multiscale 3D *microgel-in-hydrogel* biomaterials can be used to recreate the meso-environmental interplay of co-cultured cells, for example, with one microenvironment supporting tumor spheroid

formation of cancer cells and one microenvironment supporting capillary network formation of vascular endothelial cells.[205]

2.3   Microgel fabrication

In general, chemically crosslinked (macroscopic) hydrogels are prepared in two different ways: Either, *via* a step-growth polymerization or chain-growth polymerization. The same is true for the preparation of microgels, where often step-growth *via* Michael addition is employed or a free radical chain-growth polymerization is used. The two different growth mechanisms entail disparate internal structures and morphologies.[206] In step-growth polymerization, hydrophilic poly-functional molecules link together to form a well-controlled homogeneous or more heterogeneous network above or below the critical concentration, respectively; while in free-radical polymerization, reactive monomers link-up to form a molecular chain with statistically distributed crosslinking points, resulting in a gel of heterogeneous structure and crosslink density and often gradients.

Different fabrication techniques are available to prepare microgels depending on their size, shape, production rate, and mechanical stability and softness.[60] Submicrometer microgels are typically produced by free radical synthesis following dispersion-, precipitation-, and emulsion-polymerization, or polymerization in inverse mini- and microemulsion.[63] Larger microgels are produced via soft lithography, microfluidics, and SFL. In the following, we discuss the advantages and disadvantages of the different microgel fabrication techniques, while we give an overview of their respective key attributes in Figure 2.2.

Mini- and microemulsion: For the production of microgels with diameters between 50 – 500 nm, polymerization in inverse miniemulsion can be employed.[63] Here, a water-in-oil (w/o) emulsion is formed with aqueous droplets containing water-soluble monomers dispersed in a non-polar continuous phase.[207] The thermodynamic stability of an inverse miniemulsion is conveyed by the presence of a surfactant, which needs to be removed in a purification step after microgels have been obtained.[208]

Using an inverse microemulsion as a template for the polymerization of microgels allows for even smaller diameters between 10 – 100 nm; however, this requires surfactant levels above the critical micelle concentration (CMC).[208] Both methods deliver spherical microgels, as determined by the shape of the stabilized droplets.
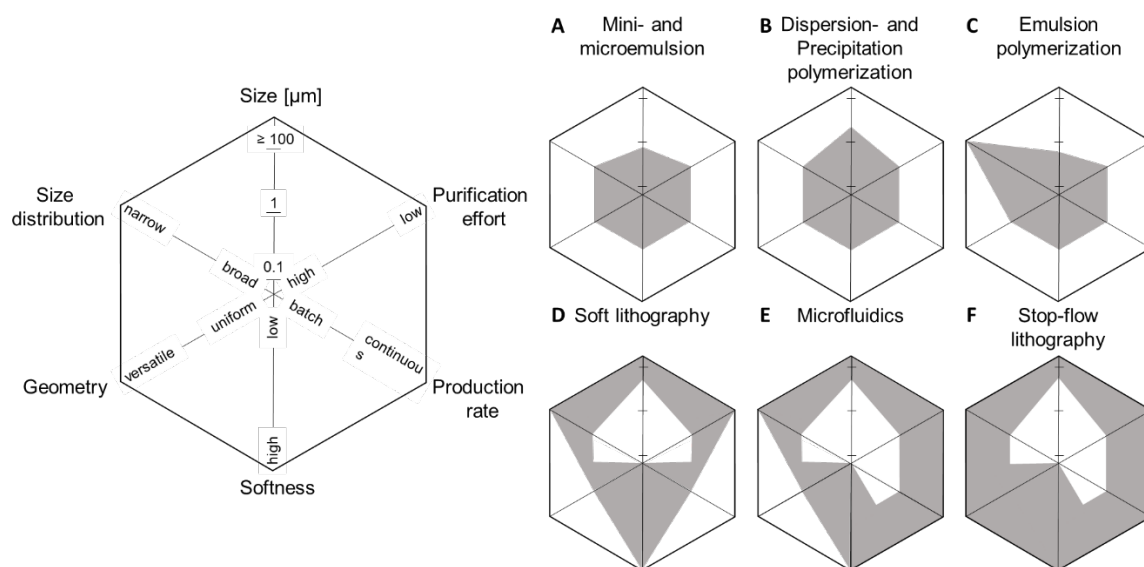
Figure 2.2: Key attributes of different microgel fabrication techniques.

Dispersion- and precipitation polymerization can be used for the production of microgels with diameters in the submicrometer to micrometer regime between $0.1 - 15\,\mu m$. process.[62,145,209] In both dispersion- and precipitation polymerization, the starting materials are dissolved in a solvent, in which initiation of the polymerization takes place. Collapsed microgel particles form upon phase inversion when the dissolved polymers reach a critical molecular weight. Dispersion polymerization is conducted in the presence of a stabilizing agent yielding monodisperse microgels, whereas in precipitation polymerization there is no additional agent leading to less uniform size distributions with microgel sizes between $0.1 - 8\,\mu m$.[210,211] Again, the shape of the resulting microgels is limited to spheres as this represents the lowest surface energy upon phase inversion from a homogeneous solution.

Emulsion polymerization: Precisely monodisperse microgels can be produced using emulsion polymerization.[212] Emulsion polymerization is usually conducted by using hydrophobic monomers that are polymerized inside of micelles in the presence of a polar solvent. The monomers are prepared to switch from hydrophobic during polymerization to hydrophilic to obtain microgels by swelling in water post polymerization.[61] During synthesis, hydrophobic monomer diffuses steadily through the polar solvent and into the micelles to maintain growth of the particles by a radical polymerization.[61] To obtain microgels, the particles containing hydrophobic polymers are transferred into the hydrophilic state by deprotecting monomers or by charging them up by means of pH

activation. Using this technique, extremely narrowly dispersed microgels in the range of hundreds of nanometer have been obtained.

Microgels with dimensions across the entire micrometer range can be fabricated by photolithography, in-mold polymerization, microfluidics, or stop flow lithography.

Photolithographic techniques can be used to produce microgels with complex 2D geometries.[213] In photolithography, a light-sensitive photoresist (monomers or prepolymers; pure or in solution) is spin coated onto a substrate (often a glass or silicon wafer). Patterns are generated by exposing the photoresist with UV light through an appropriate photomask. The exposed areas crosslink, the unexposed photoresist is removed by a "developer" solvent resulting in the desired patterns.[213]

Exposure to water leads to swelling of the produced crosslinked polymer networks and their detachment from the wafer. This method allows the production of monodisperse microgels with tailored sizes and geometries in the µm to mm range. However, some of the required manufacturing steps, such as UV-exposure, baking at high temperatures, and development with solvents, are incompatible with biological compounds and cells as they lead to biomolecular denaturation and cell death.[213] Therefore, folded biomolecules and cells have to be added post-fabrication and purification. Moreover, classical photolithography as borrowed from the microfabrication community gives only little control over the specific surface chemistry.[213]

Soft lithography provides an alternative to photolithography, which avails pattern-transfer by molding using elastomeric biocompatible materials.[213] PRINT (Particle Replication In Nonwetting Templates) is an advanced soft lithographic micromolding technique to produce monodisperse (sub)micrometer-sized microgels with control over particle size, geometry, composition, and functionality (see Figure 2.3A-E).[213] A mold produced from elastomeric perfluoropolyether (PFPE) or polydimethylsiloxane (PDMS) with defined cavities is filled with a polymer precursor solution. Crosslinking can take place via free-radical or step-growth polymerization and is initiated by temperature or light, leading to the formation of microgels that take the shape of the mold cavities.[63] This method additionally allows for the production of multi-compartment microgels with different functionalities in the core and on the surface through consecutively polymerizing different layers of subsequently adding polymer precursor solutions.[214] However, the evaporation of the solvent due to the small volumes of polymer precursor solution in mold

polymerization can also lead to incompletely casted microgels for solutions with low polymer concentrations. To overcome this challenge, non-volatile and non-reactive polymer fillers can be employed, which is washed out and replaced by water in by subsequent purification.[131,215] Altogether, photolithography, soft lithography, and PRINT are time consuming batch processes that are best suited for laboratory scale production rates.

Microfluidics: For continuous high-throughput production of monodisperse microgels larger than 10 μm, microfluidic techniques can be used.[63,216] Microfluidic devices are usually fabricated by soft lithography using PDMS, which is bonded to a glass substrate. Droplets are formed at the junction of two channels containing immiscible liquids, usually a continuous, surfactant containing oil phase and an aqueous polymer precursor solution. The polymer precursor droplets can be crosslinked to spherical microgels by chemical reactions, oftentimes initiated by UV light (e.g., photo-Diels-alder, radical polymerization, thiol-ene click) or ions (e.g., for alginate gels), or by 2 component mixing (for example Michael-type addition) (see Figure 2.3F-I).[63,68,217] Supramolecularly crosslinked microgels have been prepared on-chip *via* hydrogen bonding and hydrophobic interactions. These microgels degrade at increased pH. By varying the geometry of the microfluidic device, the flow rates and viscosities of the liquids, and the reaction times, microgels with different geometries and morphologies can be formed.[63,216] On-chip gelation allows crosslinking of the droplets inside of the channels during flow, where the microgels take the shape of the droplet, which may be confined and elongated in the channel. On-chip gelation can therefore yield anisometric microgel rods or disks (see Figure 2.3J).[68] Multifunctional anisometric Janus microgels with more complex structures can be generated by combining multiple aqueous and oil phases at different flow velocities. The use of multiple channels enables the formation of water-in-oil-in-water (w/o/w) double emulsion to generate hollow microgels, which can be used to encapsulate biomolecules on chip for drug delivery.[218,219] The possibility to use mild reaction conditions in microfluidics renders this technique ideal for incorporation of sensitive bioactive molecules, as well as cells into the microgels.[68,69,220,221] However, the microfluidic technique shows limitation as the geometry and size of the microgels are dictated by the dimensions and cross-section of the microfluidic channels.[60] To overcome this constraint, a technique to produce rod-shaped microgels with significantly smaller diameter than the channel diameter has been developed by operating a microfluidic chip in the jetting regime

rather than the dripping regime. The jet containing the microgel precursors is exposed to a pulsed high intensity light source, ideally a laser.[60] The jet polymerizes only in the exposed segments leading to narrow rods of high aspect ratio and tunable lengths depending on the on-time of the laser and the jet velocity.

Stop-flow lithography (SFL) is a microfluidics-based method combined with photolithography for continuous high-throughput production of soft, anisometric, and multifunctional microgels with more complex geometries, morphologies, and chemical patterns (see Figure 2.3K-O).[64,222] A photo-crosslinkable precursor solution is guided through a microfluidic channel, while patterned UV light irradiates the solution through a mask, by using micro-LED- or micro-mirror displays or direct laser writing techniques. The flow is stopped while the channel segment is exposed to light to form microgels. The produced microgels are moved away from the exposure site by switching the flow on. Synchronizing flow-stopping and starting, light exposure, and channel flushing can lead to acceptable production rates of arbitrarily shaped 2D microgels.[222]
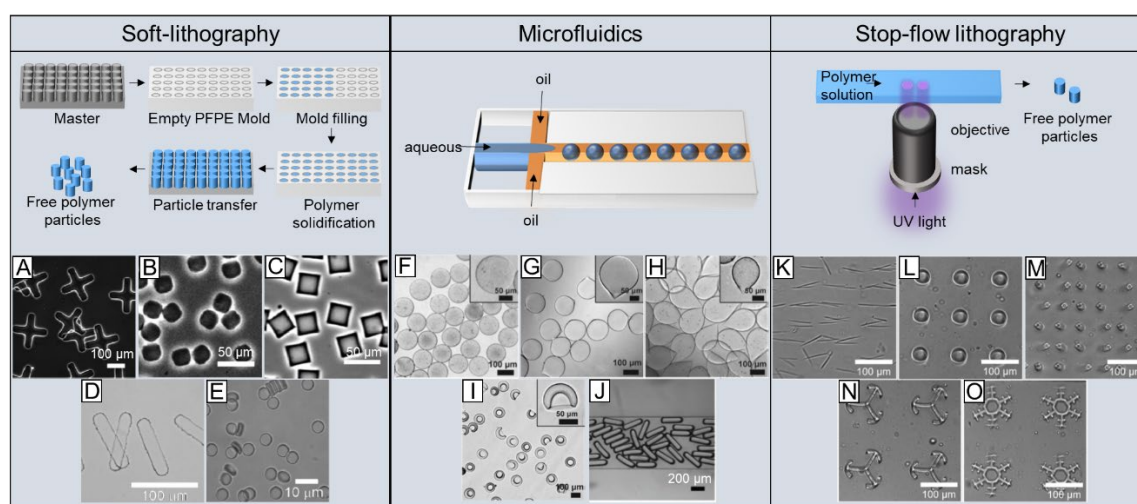
Figure 2.3: Microgel fabrication techniques: *left*: Schematic of a soft-lithography process such as PRINT. A) - E): Different microgel shapes accessible via PRINT: crosses, truncated cylinders, cubes, rods and discs. Reproduced with permission.[223] Copyright 2006, Biomaterials. *middle*: Droplet-based microfluidic device. F) - I) Cured microgels as spheres, droplet and bowl shapes produced by on-chip polymerization. Reproduced with permission.[224] Copyright 2012, Biomicrofluidics. J) Microgel rods produced by on-chip curing under plug-flow conditions. Reproduced with permission.[68] Copyright 2019, Small. *right*: Stop-flow lithography inside microfluidic channels. K) - O): high aspect ratio microgel rods, spheres, cubes and cuboids, rotor and snowflake shapes. Reproduced with permission.[64] Copyright 2020, Lab Chip.

In the future, the advances in 3D stereolithography will be also transferred to hydrogel and microgel research enabling 3-dimensionally patterned microgels, higher production rates, while at the same time preventing clogging.[225] These microgels will provides new possibilities in biomedical engineering and responsive microgels.[64,226]
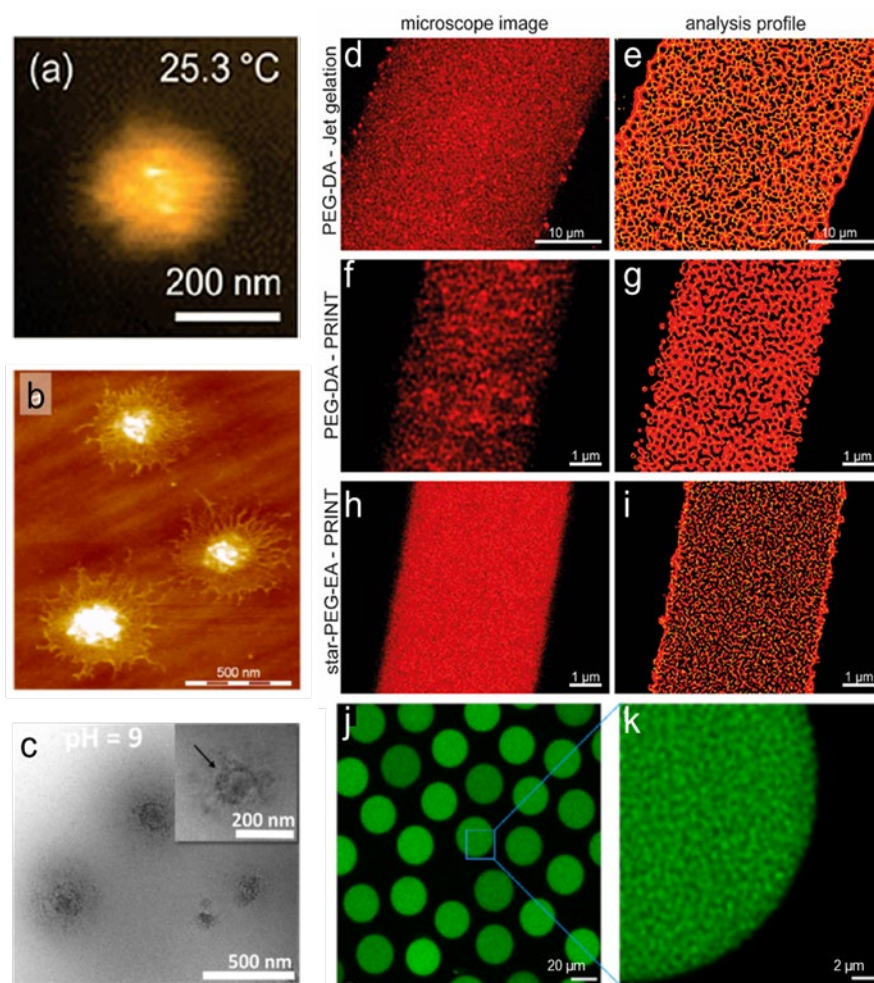
Figure 2.4: Internal structure influenced by different processing techniques and different analytical techniques. A) Precipitation synthesis of a NIPAM microgel in the swollen state analyzed by in situ AFM. The height profile displays a more dense network in the center of the microgel. Reproduced with permission.[227] Copyright 2019, Angew. Chem. Int. Ed. B) Ultrasoft microgels analyzed by AFM clearly showing a denser core with a thin and surface-spreading shell. The fringes and indiscrete perimeter hint at a fuzzy periphery and Individual dangling chains. Reproduced with permission.[228] Copyright 2016, Langmuir. C) Microgels prepared by emulsion polymerization followed by deptrotection and swelling. The cryoTEM images display more contrast in the center and fading contrast towards the outside of the microgel, representing a material density gradient towards the outside also reflecting that there are more crosslinks towards the center of the microgel. Reproduced with permission.[212] Copyright 2015, Soft Matter. D) Microgel rod polymerized by exposure to a strong laser while in the jetting regime inside of a microfluidic device. The deconvolved confocal microscopy images of the fluorescently labeled microgel network display a homogeneous pore size distribution and the image analysis. E) displays that the structure exhibits a skin on the outside, so will be less accessible from uptake. F, G) Deconvolved confocal micrograph on di-functional PEG chain that has been gelled in a PRINT mold. The image shows an open network structure with larger pores and voids as compared to the rod in (D/E). H/J) Same experiment as in (F/G) only with a star-shaped precursor molecules producing also a homogeneous pore-size distribution; however, with much smaller pores than in (F/G). (D/E/F/G/H/I): Reproduced with permission.[60] Copyright 2019, Adv. Mater. J) Spherical microgels of a star-shaped PEG precursor produced by droplet microfluidics. K) Deconvolved confocal microscopy image of the internal microgel structure showing a homogeneous distribution of pores in the same range as the star-shaped PEG microgel produced by PRINT (H/I). (J/K): Reproduced with permission.[71] Copyright 2019, ACS Appl. Mater. Interfaces.

Importantly, the type of microgel fabrication technique also has an impact on the internal structure of the microgel. While dispersion-, precipitation- and emulsion polymerization yield microgels that often have a more densely crosslinked core and a loosely crosslinked periphery, which is fuzzy with many dangling chains (see Figure 2.4A-C), heterophase and confined approaches as in miniemulsions, jet-polymerization, PRINT and droplet

44

microfluidics lead to a more homogeneous distribution of crosslinks (see Figure 2.4D-K). Furthermore, the use of inert fillers, lithographic patterning, and shearing of the precursor solution during crosslinking or network formation have an impact on the internal structure (see Figure 2.4D-I).

2.4 Microgel characterization

While microgel sizes range between 10 nm to 100 μm, the individual chain segments in the microgels are "dissolved", which is why microgels have properties connected to the molecular nature of the material, as well as the colloidal nature connected to their size and shape. Microgels can be envisioned as giant solubilized crosslinked macromolecules, which lack a defined surface. This means that any functional group that has been introduced might not only be exposed on the outside (as they would be in hard particles) but also on the inside of the microgel – significantly increasing the surface area for presenting these domains and, therefore, the binding capacity for the targeted molecules or binding motifs.

Depending on the network porosity and crosslink density, these functionalities are more or less well accessible for molecules or entities to bind to. These unique properties set microgels apart from hard colloidal and granular particles as well as macroscopic bulk hydrogels.[62,229–231]

The different structural properties of the microgels require suitable characterization methods for their analysis (see Table 2.1) – naturally these are coming from the realms of molecular and colloidal materials but also from cellular characterization as there are many similarities between soft microgels and cells.[232–235]

Microgel size, size distribution, and microgel aggregates can be easily and rapidly analyzed using dynamic light scattering (DLS) or static light scattering (SLS) methods.[236–238] This is most suitable for spherical microgels with diameters in a range of 1 nm – 5 μm. These techniques are non-invasive and non-destructive. Microgels are irradiated by a coherent light source, such as a laser, while the scattering angle as well as the intensity of the scattered light are measured.[239] DLS measures the time-dependent fluctuations in the scattering intensity, while SLS records the time-averaged intensity of scattered light. DLS is typically measured at a fixed angle, while SLS is measured over a set of different angles.

Table 2.1: List of advantages and disadvantages of microgel characterization methods.

Characterization method	Size regime	Obtained measure	Advantages	Disadvantages
DLS/SLS[236–238]	10 nm to 5 µm	Hydrodynamic radius, Size distribution, aggregates	Bulk analysis, Polydispersity, In swollen/dispersed state	Refractive index contrast low in swollen state can be insufficient, No probing of individual microgels possible
TEM/HRTEM[240–242]	HRTEM: 1 Å	Morphology, Homogeneity, Chain dynamics	Information about morphology with very high resolution	2D image, Imaging under vacuum → freeze-drying needed → might change structure, Conductive layer is needed → might conceal morphology
Brillouin microscopy/ Refractive index tomography[233,235,243]	500 nm	Internal homogeneity, Mechanical properties	Local structure elucidation inside microgel	Individual measurement
Real-time deformability cytometry[232,233]	~15 µm	Mechanical properties	High-throughput method	Size limitation of microgels to max. ~15 µm
Fluorescence microscopy[60,71]	Nanometer scale	Internal structure	Wide variety of applications using different fluorescent dyes/bioactive molecules	Fluorescent markers needed → might alter structure
FRAP/FCS[78,244,245]	Nanometer scale	Diffusion properties	For a wide variety of microgel sizes and shapes	Suitable models needed for evaluation
NMR[246–249]	Molecular scale	Chemical composition	Quantification of chemical groups, Diffusivity of guest molecules	Sensitivity → Broad signals
AFM[250–252]	Nanometer to sub-nanometer scale	Mechanical properties, Interaction forces	3D surface profile	Individual measurement

DLS gives better information about the size (radius, diameter) of a narrowly dispersed set of microgels, SLS gives better information about the distribution of sizes. During DLS measurement, the charge of microgels can be determined by measuring their electrophoretic mobility in the presence of an electric field.[238]

With these methods, also the size and change of stimuli-responsive microgels upon switching of the pH and temperature can be measured.[147] For the analysis of non-spherical microgels, multi-polarization DLS can be employed. Multi-polarization DLS is a modern approach, which is based on time-resolved measurements of the scattered light intensity at different angles between the incident and scattered light polarizations.[253] However, light scattering techniques should not be employed for microgels larger than 5 µm. For those microgels, optical microscopy can be used for size determination.[236]

Morphology, homogeneity, and chain dynamics: Microgels are often used as drug delivery vehicles with incorporated bioactive molecules, such as proteins and pharmaceuticals. Therefore, it is important to analyze the internal structure with regards to pore size, homogeneity. Furthermore, diffusion of guest molecules and cells through the polymer network is of interest.[254] Scanning electron microscopy (SEM) and transmission electron microscopy (TEM) can be performed for detailed analysis of the morphology and microstructure of the microgels.[240,241] Using high resolution SEM (HRSEM) analysis, "outer" feature sizes down to the nanometer scale can be imaged.[241] TEM additionally gives information about the "inner" morphology of microgel with a resolution of up to 1 Å in high resolution transmission electron microscopy (HRTEM).[242] However, for SEM and TEM measurements the samples are imaged under vacuum, complicating imaging of the microgels in their native water-swollen state.[241] To address this issue, microgel samples are freeze-dried in an attempt to maintain the native structure in the absence of water. Water inside of the microgel is sublimated upon application of a strong vacuum, leading to the formation of a porous dehydrated polymer network. However, sublimation can also change the microgel structure, so the imaged structure might not always represent the original microgel state.[255] Additionally, for the characterization of microgels composed of dielectric polymer networks, a conductive layer is applied by sputtering a thin metal film (often Au or Pt/Pd) on top of the specimen, which might further conceal the real microgel morphology.

As an alternative, *cryo*-electron microscopy can be used for imaging microgel samples, for which freeze-drying is not suitable. In cryo-TEM the microgel structure can be imaged in

its swollen form with almost atomic resolution.[256,257] The aqueous microgel sample is quickly frozen to liquid ethane temperatures, avoiding crystallization of water and leading to a vitrified state resembling the microgel structure in its native form. The vitrified sample can be microtomed and transferred to the TEM on a cooled sample holder.[241] No conductive coating is required due to the intrinsic electrical conductivity of the vitrified water.[241] During imaging, the frozen water can also be sublimated to reveal the naked microgel polymer slice.[256]

The advance of optical microscopy methods also allows imaging of microgels with down to almost molecular resolution. For example, the internal homogeneity of a microgel network and its mechanical properties can be characterized by confocal Brillouin microscopy combined with refractive index tomography.[233] Brillouin microscopy can be performed without any dye- or fluorescent label at high spatial resolution of around 500 nm. The method is therefore of interest for biological samples as well as for studying microgels.[235,243] Brillouin microscopy is based on inelastic scattering of incident photons on collective fluctuations of the molecules (acoustic phonons).[235] The measured Brillouin shift gives information about the longitudinal modulus, refractive index, and the absolute density of the sample.[233] On somewhat larger scales, optical imaging tomography (ODT) can be performed to gain information about the macroscopic homogeneity of the microgel network. Here, radial refractive index profiles are computed from representative phase images, allowing mapping of the internal structure.[233]

Confocal and super-resolution microscopy can be employed to gain 3D insight into the internal structure of microgels with resolution on the nanometer scale (see Figure 2.4D-K). However, for these techniques, the microgel network needs to be equipped with fluorescent markers, which might alter the structure of the microgels compared to a marker-free microgel of the same building blocks.[60,71]

Fluorescent markers also allow investigation of dynamic processes inside of the microgels. Fluorescence correlation spectroscopy (FCS) and fluorescence recovery after photobleaching (FRAP) are well-established methods to study structural and dynamical parameters of a microgel, accepting a wide variety of microgel sizes and shapes.[78,244] Small fluorescently labelled polymer chains (such as FITC-dextrans) or small molecular fluorescent dyes, are used for diffusion experiments inside the microgel samples. FCS measures the temporal fluctuation of fluorescence intensity. In FRAP, a spot in the fluorescent sample is rapidly bleached and the recovery of fluorescence intensity in this

spot is determined as bleached fluorophores diffuse out of the exposed spot and unbleached fluorophores diffuse in. Both techniques deliver diffusion coefficients for the respective microgel sample using suitable models.[78] Diffusion coefficients that are changing over time, suggests a more heterogeneous internal structure. FCS technique provides more accurate diffusion coefficients with better temporal resolution.[244],[245]

Also, nuclear magnetic resonance (NMR) delivers information about diffusivity of guest molecules or the microgel network itself. Transverse relaxation in ^{1}H-NMR measurement deliver proton mobilities, enabling differentiation between specific areas in the microgels of for example the core and the periphery.[246–249] Furthermore, the phase transition of microgels between the swollen and the collapsed state can be followed precisely. Furthermore, the dynamics of solvent, and thus their diffusion coefficient, inside swollen microgels can be determined by diffusion ordered spectroscopy NMR (DOSY-NMR) and nuclear Overhauser enhancement spectroscopy (NOESY-NMR).[248,249]

Mechanical properties: To obtain a first idea of the mechanical properties of a microgel, one can turn to rheological analysis of macroscopic bulk gels of the same polymer composition. Rheology on macroscopic gels is quick, sensitive, and requires relative small amounts of sample.[258] The rheological techniques, such as small amplitude oscillatory shear (SAOS) and linear viscoelasticity (LVE), allow for the determination of the storage and loss moduli, shear thinning properties, visco-elasticity, mechanical strength, etc.[258] This information can be used to estimate the mesh size and thus crosslinking density *via* the rubber elasticity or equilibrium swelling theory.[259] However, mechanical properties of small microgels may vary significantly from the macroscopic analysis, depending on the fabrication techniques that yield different and more or less homogeneous networks (see Figure 2.4).

To investigate the mechanical properties of individual microgels, colloidal probe nanoindentation and atomic force microscopy (AFM) have to be employed.[250,251] In colloidal probe AFM, a tip is modified with a micron-sized colloidal particle, with a diameter of up to 15 µm, which is used to deform and indent the microgel.[252],[260] Bending of the cantilever during contact with the microgel is detected using a laser diode and a split photodetector, which gives information about tip-microgel displacement and the associated interaction force, thus allowing the calculation of Young's moduli for individual microgels.[252,261],[262],[263] Additionally, AFM can be used to measure the interaction forces between microgels with appropriate functionalities (biological recognition motifs or

charges) with surface bound bioactive molecules, such as peptides and proteins as well as cells.[264,265]

Nanoindentation can be combined with fluorescence microscopy to analyze the correlation between mechanical properties and microgel functionalization or combine nanoindentation with Förster resonance energy transfer (FRET) measurements in a confocal microscope. These methods contribute to understand fundamental properties of functional microgels in biomedicine, such as molecular diffusion through the network and cellular interactions or uptake, depending on the microgel dimensions.

Colloidal probe nanoindentation is the most commonly used technique for analysis of mechanical properties of microgel but it is limited to measuring the elastic response at the particle surface and mainly has low throughput. Real-time deformability cytometry (RT-DC) was recently established as a high-throughput technique developed to analyze cell mechanical properties by measuring deformation under shear stress at laminar capillary flow conditions.[266] Besides the measurements of cells, cell-sized soft microgels can be analyzed with this technique as they can flow through a narrow microfluidic channel with a velocity of about $10\,\mathrm{cm\,s^{-1}}$. The deformation of microgels as a response to the hydrodynamic strain induced by the flow in the channel allows to determine the elastic behaviour and Young's moduli of the microgels at high throughput.[232,233]

2.5 Clinical applications

Clinical application of microgels has first been suggested towards the end of the 1990ies. Since then microgels have evolved into a powerful class of materials for a variety of biomedical and therapeutic applications. In Figure 2.5, a timeline to represent the most important developments in terms of microgel production methods with potential for clinical application is shown. Of course, this timeline cannot be complete and is limited to what we see as the most influential works of the time.

50

1998	Self-assembled hydrogel nanoparticle of cholesterol-bearing pullulan as a carrier of protein drugs: complexation and stabilization of insulin[451]
1999 - 2000	First Introduction of the term "Nanogel" to define swollen chemically crosslinked bifunctional networks of a polyion and a non-ionic polymer
2001	Hybrid poly(*N*-isopropylacrylamide)-based (polyNIPAM) microgels for sustainable thermosensitive drug release[452]
2004	PEG- and PEI-based microgels for oligonucleotide delivery across the blood-brain barrier[453]
2005	Direct fabrication and harvesting of monodisperse, shape-specific nanoparticles via PRINT that can contain therapeutic cargo for nanomedicine[454]
2005	New strategy for producing monodisperse solid microparticles with control over size, shape, and composition using microfluidics: production of polymer spheres, rods, disks, and ellipsoids[455]
2005	Controlled synthesis of monodisperse, non-spherical, plug- and disk-shaped microparticles using microfluidics[456]
2005	Novel microgel-quantum dot-hybrid nanoparticle for live cell imaging[457]
2006	Phase I clinical trial: HER2-specific T-cell immune responses in patients vaccinated with truncated HER2 protein complexed with microgels of cholesteryl pullulan[458]
2015	Phase IV clinical trial: Tretinoin microgel versus conventional bulk gel in patients with acne vulgaris: A randomized, active controlled, multicentre, parallel group[459]
2015	First report of microporous annealed particle (MAP) scaffold demonstrating enhanced cell infiltration *in vivo* for tissue engineering[202]
2017	First report of Anisogels using magneto-responsive, anisometric microgels to achieve aligned structures and oriented cell growth in surrounding hydrogel[460]
2019	First report of Microgel Scavengers sopping up toxins[71]

Figure 2.5: Timeline with important milestones.

In the following, therapeutic microgels are discussed in further detail and their potential for translation into the clinic is shown. Here, the focus is on applications as drug delivery or

toxin capturing vehicles, microgels as contrast agents carrying imaging probes, and microgels as building blocks for tissue regeneration scaffolds (see Figure 2.6).[267–269]
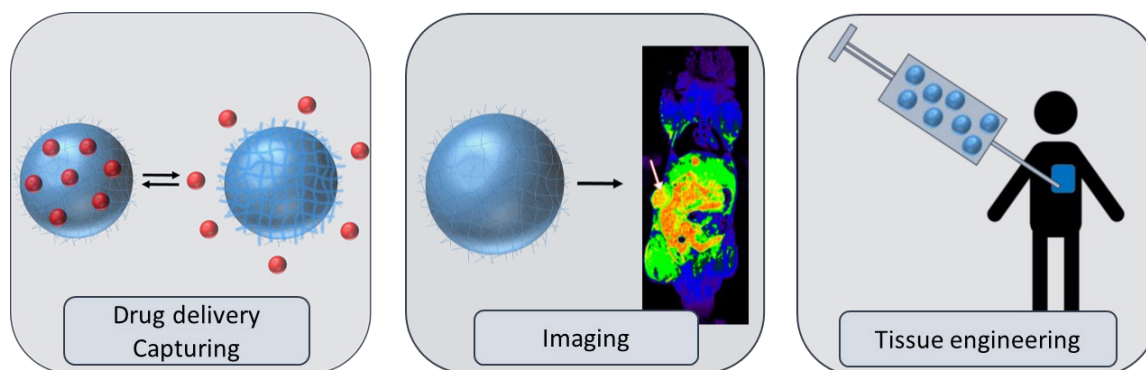
Figure 2.6: Drug delivery, imaging, and tissue engineering applications of microgels in biomedicine. Reproduced with permission.[270] Copyright 2018, ACS Macro Lett.

2.6 Therapeutic Microgels for Delivery and Capturing

Therapeutic microgel formulations can be administrated *via* different routes, such as oral, pulmonary, nasal, parenteral, intra-ocular, rectal, vaginal, or transdermal.[190,271,272] Depending on their chemical and physical properties, microgels can take up and deliver drugs of different polarity and charge.[190,271]

Different strategies for successful incorporation of drugs and active compounds into microgels have been pursued:

Covalent conjugation of bioactive molecules to microgels can be achieved during microgel synthesis or by post-functionalization.[161,230,272] While this mechanism provides high stability to the enclosed drug,[161] usually the drug has to be cleaved off and released from the polymer network to become active. For example, microgels were formed either in inverse microemulsion or dilute aqueous solution by copolymerization of acrylamide-based polymers with acrylic group modified enzymes as biological agents that can be released after hydrolysis.[273] In another approach, a carboxylate containing drug was bound to hydroxyl groups of polysaccharide-based microgels *via* ester linkages. In the presence of esterase enzymes, the drug can be released.[161]

Non-covalent conjugation: Drugs can also be incorporated into microgels through non-covalent interactions, such as Coulomb attraction, hydrogen bonding, or hydrophobic interactions.[161] For drug loading of microgels using non-covalent conjugation to the cargo

molecule, the microgel is swollen in a solution of the cargo and incubated to allow sufficient time for the guest molecules to diffuse into the microgel and interact with the respective supramolecular units. This often leads to relative low encapsulation efficiencies. If the interaction strength is sufficient, the microgels can be removed from the incubation solution (for example by centrifugation). Alternatively, the microgel can be collapsed (using a suitable trigger) – in this case, the cargo can only be released upon swelling of the microgel at the desired location.

The efficiency of drug entrapment and retention in the microgel network is determined mainly by the interaction strength, while diffusion out of the microgel depends on the size of the guest/drug molecule and the internal structure of the microgel.[230] Diffusion out of the microgel is important for *covalently* as well as for *non-covalently* bound cargo.

In therapeutic microgels, the drug-release is often characterized by a burst release and fast decay of the entrapped drug-molecules. This burst leads to high initial drug concentrations, which can be pharmacologically inefficient and dangerous due to concentration dependent toxicity of the drug or cargo molecule. Even a controlled burst release, with acceptable concentrations is often not desired as it requires frequent dosing. Especially drugs of low molar mass exhibit burst release profiles, due to their small size, high osmotic pressure inside of the microgel and fast diffusion through the microgel network.[274] Furthermore, the microgel size, porosity, and geometry, as well as microgel interactions with the environment can influence or prematurely trigger the burst release.[274]

Therefore, pharmaceutical research has focused on ways to avoid such burst releases. A successful pathway to avoid burst release in microgels is by employing a shell around the microgel to reduce the osmotic pressure gradient and facilitate a slower diffusion profile.[274,275] For example, a microgel with a crosslinked shell of ethylene glycol dimethacrylate (EGDMA) reduces the burst release to less than 10% of the initial loading capacity.[276] However, such modifications involve additional and often costly steps, which can sometimes result in reduced drug loading capacities.[274]

One successful example of a non-covalent drug immobilization strategy is through controlled self-assembly of polyelectrolytes.[161] Amphiphilic polymers spontaneously form microgels in aqueous media *via* self-aggregation mediated by intra- and intermolecular association. In the presence of hydrophobic molecules or aggregates, the self-aggregation leads to enclosure of the hydrophobic entities, reducing their interfacial

energy while forming stable and robust microgel structures.[161,272] These participating molecules orient in such a way that the hydrophilic regions are exposed to the aqueous, polar environment and the hydrophobic segments are buried in the core of the microgels. In this case, it is possible to incorporate hydrophobic drugs, such as the anticancer drug doxorubicin (DOX) inside the microgels.

2.6.1 Stimuli-responsive microgels

Bioactive molecules can be retained in the microgels by interacting with specific ligands incorporated into the network. The binding strength of these interactions will affect the diffusion kinetics through the microgel. In addition to diffusive release, available in many swollen polymer-based delivery systems, a triggered release of an active compound or drug from the microgel can occur upon issuing different stimuli that are either biological, chemical, and/or physical in nature (see Figure 2.7).
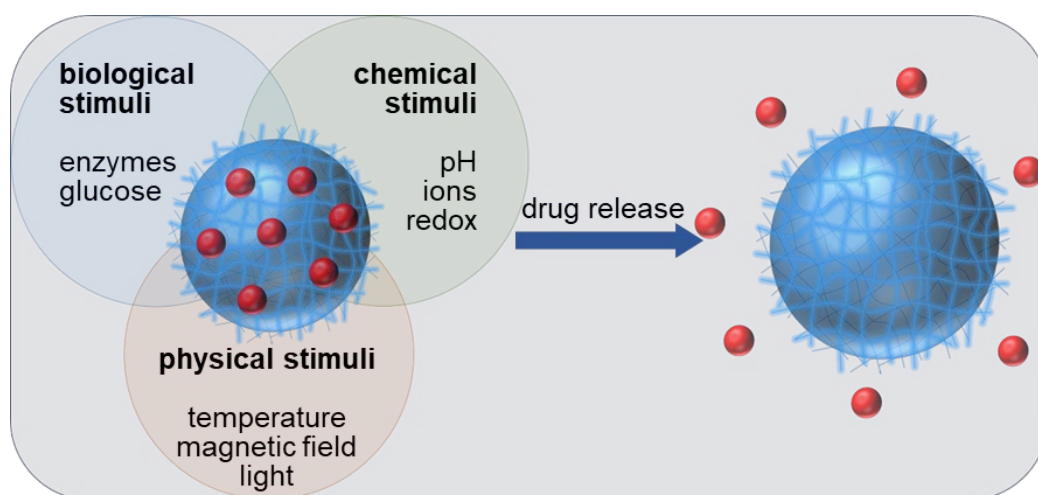
Figure 2.7: Drug release mechanisms of stimuli-responsive microgels.

Importantly, for stimuli-responsive microgels, swelling in an aqueous medium is essential as otherwise the drug molecule cannot be released from the microgel without degradation.[230] Drug release from microgels is always two-step process.

- First, the drug detaches from the network.
- Second, the drug diffuses out of the microgels.

During the second step, other attractive interactions between the network and the drug may take place slowing down the diffusion rate. Both steps can be induced and/or enhanced by

specific triggers.[190,230,277] In the following, we will discuss different examples of such drug-releasing stimuli-responsive microgels.

Chemical stimuli: Inside the body, different chemical signals can hamper the interactions between drug and microgel network. Biological fluids carry enzymes, proteins, and peptides as well as sugars and salts that may influence the swelling behavior, network stability, and degradation process. For example, pH-responsive microgels contain functional groups, such as carboxylic acid and amines or other acid/base type groups.[190,277] These groups gain charge upon protonation or deprotonation depending on the pH. This pH dependency entails also a change in the osmotic pressure, which can induce swelling and undesired release of an electrostatically bound drug.[190] As a result, for biomedical applications we need to design the microgel carrier with the biological environment of application in mind – for example, stomach, intestine, or in tumors.[190,278] Only then can we achieve controlled drug release at a specific physiological or pathological site.[279,280]

For example, pH-responsive microgels have been used to protect insulin from acidic degradation in the stomach, while release is enabled in the intestine, rendering microgel-protected insulin suitable for oral delivery.[281] Acrylic acid-based microgels retain a hydrophobic, collapsed state in the stomach due to protonation of carboxyl groups. After gastric passage, the increase of pH leads to swelling of microgels due to carboxyl ionization and hydrogen bond breakage.[281,282] In another approach, pH-responsive microgels were used to regulate the delivery and release of antitumor drugs for cancer treatment as tumor tissue exhibits a lower pH compared to normal tissue.[281] Here, methacrylated succinyl-chitosan (MASCS) copolymerized with diacrylamide containing ortho esters (OEAM) employed as acid-labile crosslinkers have been polymerized to form pH-responsive microgels.[283] Due to the ortho ester linkages, these microgels degrade at low pH and release DOX selectively in the tumor.[283] Alternatively, drug release can occur through displacement with counterions. For example, microgels based on poly(acrylic acid) (PAA)-polymer with negatively charged carboxyl groups have been used for encapsulation of proteins featuring positively charged amine groups. Protein release occurs *via* displacement of the proteins by adding positively charged ions, for example, calcium ions.[161]

Redox can also be used as a chemical trigger for release, which is of interest for clinical applications as pathological sites may produce of oxidative or reductive environments.

Reduction-responsive microgels make use of the large difference in reductive potential between extra- and intracellular compartments to enable selective intracellular delivery of bioactive molecules, such as anti-cancer drugs, peptides, proteins, siRNA and DNA.[277,284] The reductive potential between extra- and intracellular matrices is due to different concentrations of glutathione, ranging from 2 - 20 µM in body fluids, such as blood and extracellular matrices, to 0.5 - 3 mM in brain tumors[285], while its concentration inside cells is 2 - 10 mM[277]. For example, glutathione-degradable drug-loaded microgels can suppress hepatoma effectively and securely in a mouse model.[286]

In addition to pH and redox, enzyme-responsive microgels have great potential as drug delivery systems as enzymes like lipases, proteases, and glycosidases can recognize specific domains and induce highly selective bond scission.[277],[287,288] For example, glucose-responsive microgels can be employed as a self-regulating drug delivery system for diabetes treatment.[277,278] A glycol chitosan (GC)/sodium alginate (SA)-poly(L-glutmate-*co*-*N*-3-L-glutamylphenylboronic acid) (PGGA) graft polymer microgel has been synthesized by an isotropic gelation and electrostatic interaction between GC and PGGA to form responsive microgels. The assembled microgels swell upon exposure to glucose, which is bound by incorporated boronic acid group on PGGA.[179] Swelling enables release of insulin. This approach resulted in controlled release of therapeutic doses of insulin at diabetic glucose levels over the course of 12 h.[179,278,289]

Physical stimuli: If specific chemical triggers cannot be used to release active molecular cargo or degrade the microgel, physical triggers, such as body temperature, or external triggers, like light, and magnetic fields can be used to locally induce drug release.[290,291] Many polymers and microgels exhibit a cloud point (p_c) due to a lower- (LCST) or upper critical solution temperature (UCST).[190,278] Therefore temperature can be employed to switch the microgels between a swollen and a collapsed state.[190,292],[293,294] LCST and UCST can be tuned by changing the hydrophilic or hydrophobic character of the microgel network.[290] Examples of polymers used to form microgels with an LCST are poly(diethylacrylamide), poly(*N*-isopropylacrylamide) (polyNIPAM), and poly(*N*-vinylcaprolactam) (pVCL).[290,294] When several of these polymers are employed together, microgels with multiple LCSTs – for example dual-temperature-responsive microgels – can be obtained.[295] To obtain microgels with a UCST, polymers need to be chosen that interact by hydrogen bonding as well as electrostatic interactions. Additionally, a certain

degree of hydrophobicity should be present in the polymer to evoke favourable polymer-polymer interactions below the transition temperature.[293] Many UCST-type microgels are based on urea derivatives, such as poly(allyl urea) and poly(2-ureidoethyl methacrylate).[296,297] However, also other mixed polymer systems and composites can be utilized as UCST microgels.

Core-shell microgels consisting of polyNIPAM and zwitterionic sulfobetaine (SPB)-have been synthesized to exhibit combined UCST and LCST behaviour.[298] For increasing temperatures from 4 °C to 25 °C, swelling of the poly-SPB shell with UCST was observed. Upon further increasing the temperature up to 50 °C, the polyNIPAM core of the microgel collapses due to its LCST.[298] It was shown that the respective critical temperatures could easily be tuned by changing the ratio and molecular weight of the constituent polymers.[298] This core-shell microgel approach is particularly interesting for the delivery of therapeutic proteins due to the potency of poly-SPB to suppress protein aggregation.[299] Furthermore, this concept has been employed for biosensing and for the development of temperature-responsive scaffolds.[298]

To enable tunable elastic properties, core-shell microgels with a temperature-responsive polyNIPAM core and a nonresponsive poly(acrylamide) shell have been produced via droplet-based microfluidics.[300] The networks of the core and shells are covalently connected so that a collapse of the core at elevated temperatures lead also to stiffening of the shell.

For all thermos-responsive microgels, the presence of salts can greatly affect the LCST and UCST behaviour of polymers and thus needs to be considered when designing microgels for medical applications.[298,301]

Light-responsive microgels are of interest for drug delivery, as an external light source can easily be focussed on a specific area yielding site specific release. In principle, a variety of different wavelengths could be used and the exposure dose will impact the on-demand release kinetics of the drug.[290] However, for clinical applications, such light-triggered release is limited to wavelengths that can penetrate deep into tissue. Therefore, either wavelengths of the tissue transparency windows in the near-infrared spectrum need to be employed. Alternatively, one has to turn to very high doses to penetrate deep into the tissue; however, there remains a risk of tissue damage when operating outside of the transparency window.

Light-responsive microgels can either be obtained using photoactive organic moieties, such as reversible photoacids, photoswitches, photolabile linkers, or as hybrid systems with inorganic plasmonic nanoparticles.[290] Photoactive groups in the polymer can change the size and shape of the microgel by irradiation.[278] For example, a spiropyrane reversible photoacid turns into its charged merocyanine form upon exposure.[302] Azobenzenes inside of a microgel can change their conformation from *trans*-to-*cis* by UV irradiation, which leads to polarity changes inside of the microgel, triggering a change of the internal structure and potentially drug release.[278]

In the case of incorporated plasmonic nanoparticles, light is absorbed leading to local photothermal heating, which can swell or collapse UCST or LCST microgels, respectively. Beneficially, gold nanoparticles exhibit their plasmon absorption in the range of the tissue transparency window, rendering this type of IR light triggered UCST release suitable for clinical applications.[277,290]

Another way, to remotely induce microgel heating is by using magnetic field-responsive microgels, which are produced by incorporating magnetic nanoparticles, such as Fe_2O_3 and Fe_3O_4 nanoparticles into the microgel network.[277,278] Magnetic nanoparticles generate heat after exposure to an external alternating magnetic field (AMF), which leads to controlled drug release from temperature-responsive UCST microgels.[303,304] Additionally, the generated heat can also be used for localized hyperthermia treatment for cancer producing a therapeutic microgel for combined therapy.[277,278]

Several therapies combine different responsivities to achieve multi-functional and multi-responsive microgels.[277,278] For example, triple responsive photo-, pH- and redox-responsive poly(acrylic acid-*co*-spiropyran methacrylate)-based microgels, crosslinked by disulphide-containing *N,N*-bis(acryloyl)cystamine, have been loaded with DOX *via* non-covalent interactions.[305] Drug release is achieved through breaking of the electrostatic interactions between amino groups of DOX and acrylic acid groups of the microgels due to a local pH change in the tumor. Upon UV-light irradiation, the hydrophobic spiropyran in the microgels isomerized to the hydrophilic merocyanine leading to swelling of the microgels yielding faster release of DOX. Upon the addition of reducing agents, the polymeric network of the microgels degrades in smaller molecules due to oxidative bond scission of the disulphide crosslinkers and the degradation products can now be cleared more easily.[305]

2.6.2 Scavenging – uptake of radicals and pathogens as a strategy for therapeutic microgels

As a novel biomedical approach, microgels can be used as scavengers of molecules that are involved in diseases, such as bacterial infections or inflammatory disorders. Nitric oxide (NO), produced by nitric oxide synthase plays a key role in the human body, showing antibacterial, antitumor, vasodilation, and wound healing effects.[306] However, the overproduction of NO by physiological disorders can induce severe inflammatory diseases, such as rheumatoid arthritis (RA).[306] NO-scavenging microgels can provide a solution and are produced by solution polymerization of acrylamide with a NO-cleavable crosslinker (NOCCL) the treatment of RA.[306] When NO is exposed to NO-scavenging microgels, NOCCL is readily cleaved, consuming at the same time the NO molecule. The therapeutic efficacy in RA treatment has been tested in a mouse model in comparison to a commercial drug – Dexa – that is used in the clinic to suppress NO. Only NO-scavenging microgels could demonstrate long-lasting therapeutic effect until day 35, whereas free Dexa resulted in red and swollen paws after 14 days.[306] Dexa is a small molecule, which may be excreted more rapidly from the body compared to the higher molecular weight microgels, which could further explain the increased therapeutic effect of the microgels versus the free drug. However, possible toxic and side effects resulting from microgel application and their degradation products need to be investigated in further research before they can be transferred into a phase I clinical trial.

Reactive oxygen species (ROS), such as hydrogen peroxide (H_2O_2), hydroxyl radicals ($OH^.$), and superoxide anions ($O_2^{.-}$), are important signalling molecules in the human body, and necessary to maintain metabolism and cellular functions: such as cell proliferation, differentiation, signal transduction, pathogen defence, and regulation of inflammation.[307] An abnormal overproduction of ROS causes severe inflammatory diseases. Several antioxidants have been developed in the biomedical field to resolve high levels of ROS. However, high doses of natural antioxidants might also cause harmful effects on health, such as kidney stones, increased need for oxygen, excess uris acid excretion, and erosion of dental enamel.[308] To overcome this challenge, instead of using antioxidants, phenylboronic acid-tannic acid (TA) microgels as effective ROS scavenger are synthesized *via* self-assembly by simple mixing through to the formation of phenylboronic ester bonds between polymeric phenylboronate and TA. Phenylboronic ester reacts with H_2O_2, while TA is a well-known antioxidant and specifically a free radical scavenger, consuming ROS

radicals. TA-based microgels showed superior ROS scavenging capacity compared to natural antioxidants. Furthermore, the comparison of pure antioxidants to those incorporated in microgels show a significant reduction of inflammation using the microgels due to inherence of TA in the microgel polymer network.[307]

In another approach, PEG-based microgels, can be used as toxin scavengers. Toxin-mediated intestinal infections, such as cholera, shigellosis but also infection with *Clostridium difficile* (*C. diff.*) or pathogenic *Escherichia coli* (*E. coli*) strains result in secretory diarrhoea and intestinal inflammation representing a major health threat in both the industrialized world as well as in developing countries.[71,309] So far, antibiotic treatment is applied to treat these infections. However, antibiotics do not eliminate the accumulated toxins, so a risk of relapse remains. To overcome this challenge for cholera, PEG-based microgels were functionalized with a glycosphingolipid receptor GM1a as scavengers for cholera toxin (CT).[71] It could be shown that CT effectively binds to GM1a-functionalized microgels. GM1a-modified glycol-dendrimers and nanoparticles have been published as CT binding materials in previous reports.[310,311] However, these materials have small sizes and sterically restricted orientations of surface-grafted recognition motifs. Microgels have a larger size, preventing their cellular uptake by intestinal epithelial cells and contain a high degree of internal functionalization due to their meshed polymer network.[71] When HT-29 cells were exposed to CT and GM1a-functionalized microgels, CT had a higher affinity to the microgels compared to the surface receptors on epithelial cells and the HT-29 cells could be protected from the toxin.[71] Further research is needed to investigate the scavenging properties of microgels *in vivo*. However, functionalized microgels as scavengers have great potential to be an alternative to antibiotic treatment for several toxin-induced intestinal diseases.

Microgels have not only been used as scavengers for toxin but also to bind proteins and bacteria. For example, carbohydrate-functionalized temperature-responsive polyNIPAM microgels were produced for temperature-triggered capture of pathogens.[312] Microgels with a size range of 400 - 500 nm were synthesized *via* copolymerization of NIPAM with α-D-mannopyranoside (Man)- and β-D-galactopyranoside (Gal)-functionalized methacrylamide monomers at varying degrees of Man density and non-binding Gal moieties. Man-functionalized microgels bind specifically to the concanavalin A (ConA) carbohydrate receptor, as well as to *E. coli* as a Man-binding model pathogen in a temperature-dependent manner. Microgels with Man densities of 0.2 to 0.4% showed no

clustering with ConA or *E. coli* below the LCST but showed mechanically stable clusters above the LCST of 37 °C of polyNIPAM. Improved binding above LCST was explained by reduced steric repulsion, smoothening of the microgel surface, and, therefore, enhanced accessibility of the Man groups. Microgels exhibit a strong increase in ligand density above the LCST since their volume decreases by an order of magnitude and hydrophilic binding motifs are phase separated and concentrated at the surface of the collapsed microgel.

2.7   Microgels for Imaging and Diagnostics

Imaging is an essential modality in the clinic to retrieve information about morphology, structure, and metabolism of pathogenic tissue for the identification and assessment of diseases.[133] The most commonly used imaging systems in hospitals and practices are computed tomography (CT), positron emission tomography (PET), magnetic resonance imaging (MRI), and optical or ultrasound (US) based imaging techniques.[133] Here, we will focus on these non-invasive imaging modalities in combination with microgels.

In many imaging techniques, the detected signal is generated by using contrast agents.[133] Most contrast agents that are clinically applied are based either on small molecules or on inorganic nanoparticles - but both are so small that they are rapidly cleared from the body, providing only a short temporal windows for imaging. Also, many agents are not specifically targeted towards pathological tissue, which often leads to reduced sensitivity and insufficient contrast.[133] Incorporation of contrast agents into microgels can help to overcome these challenges.[133,313] Microgels act as a cloak for the imaging probes to confer biocompatibility or solubility in biological liquids. Moreover, when the imaging probes are bound to the soluble microgel network, they are protected from aggregation and can unfold their full contrast potential. The controllable size and high colloidal stability of the microgels guarantee good circulation times together with high encapsulation capacity for a range of different contrast agents – especially for those lacking sufficient solubility in water. Likewise, the facile microgel modification with molecular contrast agents, as well as their functionalization with biomedical recognition motifs for targeting, are powerful tools to produce composite microgel systems for imaging application.[133] In contrast to drug-delivery systems, the cargo does not have to be released for contrast agents. Here, the focus lies on long circulation times, targeting, and the degradation or clearance of the carriers.

The development of hybrid microgels with combined stimuli-responsivity for controlled and targeted drug delivery and modification with contrast agents or incorporation of metallic imaging units allows for precise localization and treatment at the specific pathological site.[133] Such *Theranostic microgels* combine therapeutic and diagnostic approaches and represent interesting candidates for advances treatment capabilities, where the pathological site and its extent is visualized, while drug delivery on-site can be monitored at the same time.[314] Such theranostic microgel systems for targeted cancer diagnosis and therapy have gained increasing attention in recent years.[315]

2.8 Microgels as scaffolds for tissue regeneration

For tissue regeneration, three-dimensional constructs are often required, while for soft and sensitive tissues, a minimal invasive approach should be taken to avoid further damage[126,127] In contrast to established hard implantable scaffolds, injectable liquid materials do not require a surgical excision to make space for the scaffold but instead they adjust to irregular shapes and cavities. To produce such a liquid scaffold precursor, one needs precise control over the polymerization and crosslinking reactions. These reactions need to take place under physiological conditions to fill the respective void completely and form the adapted construct while achieving an intimate contact to the surrounding tissue.[316,317] Several injectable hydrogel systems have been developed for the treatment of cartilage, intervertebral discs, bone, adipose tissue, spinal cord, brain, heart and muscle injuries.[317] However, such injectable molecular precursors crosslink into isotropic nanoporous hydrogels, limiting endogenous cell infiltration and do not provide directional guidance for the cells. This guidance is crucial for the reconstruction of many structured tissues. Some approaches to achieve hydrogels with larger micron-scale pores after injection have been presented but still lack defined porosity or they leach non-polymerized monomers or porogen material with unforeseeable adverse side effects that might only become apparent at later stages.[318–321] Moreover, injectable hydrogel materials for tissue regeneration must precisely match the rate of degradation to enable tissue development; too rapid degradation lead to insufficient scaffolding, while a rate that is too slow will prevent proper tissue development and will promote fibrosis.[202] The degradation rates can be adjusted using hydrolytically and enzymatically degradable moietie and crosslinkers. However, every tissue site has unique physical and chemical requirements for functional

tissue regeneration, demanding a material strategy that is versatile and applicable for a variety of challenging cellular environments. To overcome the need for material degradation prior to tissue ingrowth, a new class of injectable biomaterials has been developed. This class is termed microporous annealed particle (MAP) scaffolds[202] and microgels have proven powerful building blocks to intercrosslink and form MAP scaffolds.[322–330] Microgel based MAP scaffolds can have different interstitial pore sizes by changing the microgel diameter.[331,332] These micron- scale interstitial pores facilitate cell infiltration, as the cells do not need to degrade the material to create an open path. The internal network structure of the microgel building blocks mediates softness and can present biomolecular cues, such as growth factors. The concept of MAP scaffolds combines injectability and microporosity for efficient cellular network formation, bulk tissue integration, and regeneration *in vivo*.[202,324,326,327,329,333] It was shown that the MAP scaffold properties, such as microgel size, void space, stiffness of microgels, cell adhesion ligand concentration and presentation, as well as modular block size of the scaffold can modulate cell spreading, proliferation, and non-viral gene transfer to cells cultured with scaffold.[325,330,334] These findings reveal that the properties of MAP scaffolds can be altered on demand for biomedical applications. There are currently several promising publications of MAP scaffolds used in tissue regeneration applications.[202,324,326,329,333,335,336] For example, an injectable and adaptable microporous hydrogel was formed by the assembly of two oppositely charged microgels.[329] Thereby, gelatin-methacryloyl (GelMA) microgels containing negatively charged carboxy groups and chitosan oligomer methacrylate (ChitoMA) microgels containing positively charged amino groups interacted with each other. MAP hydrogels with suitable micropores provide mechanical support for rapid cell migration and transport of bioresponsive cues to direct cell adhesion and growth. The incorporation of growth factors into the building blocks, combined with the cell-penetrative connected pores constructed by the MAP scaffold inside a nerve conduit, effectively showed Schwann cell (SC) migration and induced dramatic bridging effects of peripheral nerve defects by accelerated axon outgrowth.[329] In another approach, MAP scaffolds were used for wound repair by immunomodulation.[336,337] PEG-based microgels were produced via inverse suspension polymerization and loaded with human mesenchymal stem cells (hMSCs) before MAP scaffolds were formed.[337]. It is known that hMSCs have the unique ability to shift macrophage polarization from an activated pro-inflammatory M1 phenotype to a deactivated anti-inflammatory M2 phenotype. In this study, hMSC-laden MAP scaffolds were cultured in the presence of prepolarized M1

macrophages and found to limit activation to the M1 phenotype, even in the presence of pro-inflammatory cytokines such as TNFα.

In contrast to spherical microgels that form densely packed colloidal glasses, rod-shaped microgels with higher aspect ratios can be jammed, resulting in larger pores and the possibility to convey directionality.[60] These 3D constructs permit cell interaction with the microgels, while providing sufficient space for ingrowth of more cells and potential formation of blood vessels to support tissue maturation.

To obtain directional hydrogel structures with defined guiding elements after injection, magneto-responsive anisometric microgels were mixed inside a hydrogel precursor solution, forming a so called Anisogel.[108] The Anisogel microgels are based on PEG and prepared by in-mold PRINT polymerization. Once injected, a magnetic field is applied to align the rod-shaped microgels, providing directionality inside the final Anisogel with a common director, along the magnetic field. For this alignment, the field can be as low as a few mT (millitesla) – and the orientation is fixed by the surrounding crosslinking hydrogel precursor, which enables removal of the magnetic field.[338] When mixed with cells or neurons, the cells align and grow parallel to the aligned rods. As the fibronectin produced by the oriented fibroblasts is also oriented, this provides a positive feedback cycle as the natural oriented ECM can replace the degrading Anisogel and thus maintain the previously induced directionality.[120] This technology fills a gap between existing implantable anisotropic scaffolds and injectable isotropic materials.

A comparative study with variable microgel dimensions, aspect ratios, and distances revealed that microgels with a length of 50 µm and a width of 2.5 µm significantly enhanced neurite growth without jeopardizing cell alignment. By contrast, 5 µm wide microgels likely inhibit some axonal growth due to the larger cross-sections. Importantly, when the width was reduced to half, the distance between microgels had to be reduced from 34 to 24 µm to maintain unidirectional neurite extension; in fact it reduced the volume fraction of microgels from 1 vol% to 0.45 vol%, producing an very infiltratable Anisogel scaffold for cells.[339],[340,341]

Besides functioning as building blocks of injectable regenerative scaffolds, microgels can function also as individual containers to transplant cells or produce cell laden scaffolds *in vivo*.[68][341] Cell transplantation promises advanced therapy for stroke, spinal cord injury, and organ vascularization and regeneration.[342–344] However, in current systems only a

small fraction of the cells are functional and remain at the target site, resulting in high cost and low efficiency. Here, the microgels can offer a solution by providing mechanical, physical, and biochemical stimuli to the cells, while they enhance the local retention at the site of injection in the body, and protect the cells from immune attacks. By coating the cells with different ECM proteins *via* layer-by-layer deposition, their viability inside the microgels can be further enhanced. Microgel encapsulated with a co-culture of human fibroblasts and cardiomyocytes derived from pluripotent stem cells demonstrated a native like heartbeat.[345]

In conclusion, injectable, interlinkable, and alignable microgel composites can pave the way for minimal invasive microgel therapies with or without therapeutic cells to regenerate sensitive and complex tissues, such as heart tissue after myocardial infarction or nerve tissue after spinal cord lesions. The use of microgels to form hierarchical and structured regenerative materials was recently part of a comprehensive review paper.[346]

These microgels cannot only function as scaffold but also support cellular therapies, which will play a more important role in the treatment of cancer, cardiac diseases, and tissue regeneration in the future. However, cell-laden microgels have only been tested in preclinical trials, using mice, rabbit, and pig models. In contrast to microgels, bulk hydrogel systems for tissue engineering and regenerative medicine applications are already undergoing clinical trials[347] as the use of microgels in this field is a more recent development. However, considering the named benefits of microgels, they have great potential to be applied in clinical studies in the nearby future.

3 Antibody-functionalized microgels scavenge TNFα cytokine

Yonca Kittel, Sarah Boesveld, Yizhao Luo, Alexander Jans, Burak Oezcifci, Matthias Bartneck, Christian Preisinger, Dirk Rommel, Tamás Haraszti, Silvia P. Centeno, Arnold J. Boersma, Laura De Laporte, Christian Trautwein, Alexander J. C. Kuehne, Pavel Strnad

3.1 Introduction

Since their introduction more than three decades ago, therapeutic antibodies have become the predominant treatment modality for various diseases, such as rheumatoid arthritis, psoriasis, Crohn´s disease or ulcerative colitis. Consequently, many of the best-selling drugs today are monoclonal antibodies.[348] Several of these antibody drugs are designed to scavenge cytokines, such as TNFα, IL-1ß, IL-6 or IL-12/23, as key inflammatory mediators and are used for treatment of different immune-mediated disorders. Among them, TNFα antibodies represent the most widely used class of antibody drugs.[348] However, its systemic administration leads to significant immunosuppression and increases the risk of serious infections and malignancies, as well as systemic inflammatory responses.[349,350] Moreover, *in vivo*, the antibodies encounter harsh environmental conditions, which lead to their deactivation and therefore requires higher concentrations of the administered antibodies to retain efficacy. To increase the therapeutic efficiency, minimize the dose and systemic side-effects, the immobilization of antibodies on carriers, such as liposomes or nanoparticles, represents a promising approach.[30,351,352] IL-6 antibodies have been immobilized on the surface of polymeric nanoparticles to selectively capture the pro-inflammatory cytokine IL-6 in inflammatory diseases, such as arthritis.[30] Moreover, the co-immobilization of two types of monoclonal antibodies against effector and tumor cells on nanoparticles has shown therapeutic superiority, in comparison to free antibody and mono-functionalized nanoparticles *in vitro* and *in vivo* in cancer immunotherapy.[352] However, such antibody-nanoparticle conjugates often suffer from accelerated blood clearance[353] and conjugating an antibody to a surface might sterically restrict access to the binding motif, resulting in low binding capacity and strength.[37]

To overcome these challenges, we propose to use water-swollen, soft microgel as carriers, which exhibit high internal binding capacity as well as stealth against immune recognition to evade physiological clearance.[354] As opposed to typical nanoparticle approaches, microgels exhibit an open meshed polymer network and can therefore also be functionalized on their inside, greatly increasing the capacity of these carrier systems.[355] To date, microgels have only been employed for presenting antibodies to isolate tumor cells from the environment via cancer immunotherapy, or to scavenge NO (nitric oxide) and ROS (reactive oxygen species).[356–359] Extending these microgel functions to scavenging of cytokines would greatly enhance the spectrum of treatments for inflammatory diseases by increasing the binding performance and reducing side effects. The size and stiffness of microgels can be tuned so that they can be applied systemically or locally, while precisely controlling their ability to cross and interact with barriers[360], such as cell membranes[51], the intestine and mucus[361,362], blood vessels[363], skin[364], and the blood-brain barrier[365]. Whereas anti-inflammatory antibodies against TNFα that are released in the intestine can still pass the intestinal barrier and enter the blood circulation[366,367], engineered microgels with micron-scale diameters could prevent this transition.[362] Such micron-sized microgels are biocompatible, deformable, stable against changes in pH, and cellular uptake is prevented. The route of administration will depend on the type of disease. For example, in the case of inflammatory bowel disease, a chronic intestinal disorder, an oral administration would be advantageous. This would enable a local therapy with subsequent excretion of the microgels. We have previously presented a microgel scavenging system that can take up and multivalently bind cholera toxin, leading to higher affinity as compared to surface receptors of HT29 intestinal cells.[71]

Here, we develop immunoglobulin G (IgG) antibody functionalized polyethylene glycol (PEG)-based microgels as scavengers for the pro-inflammatory cytokine TNFα (schematically shown in Figure 3.1C). The microgels are produced by microfluidics and have diameters of about 25 μm. The IgG antibodies are conjugated to reactive glycidyl groups in the PEG-based microgels using mild glycidyl-amine coupling. Our microgel system shows high binding capability of the cytokine TNFα in a biologically relevant range.

3.2 Results and Discussion

3.2.1 Microgel synthesis and characterization

To prevent cellular uptake and crossing of the intestinal barrier, uniform microgels with a defined diameter in the range of the size of a cell (diameter ~ 25 μm) are synthesized via a previously described flow-focusing microfluidic technique[71,309] (see Figure 3.1A and B). Monodisperse droplets are formed in the microfluidic chip using the dispersed phase consisting of an aqueous solution of star-PEG acrylate (sPEG-Ac) polymers with glycidyl methacrylate (GMA; 10 mol per mol sPEG-Ac) and Irgacure 2959 as the photo-initiator and the continuous oil phase.
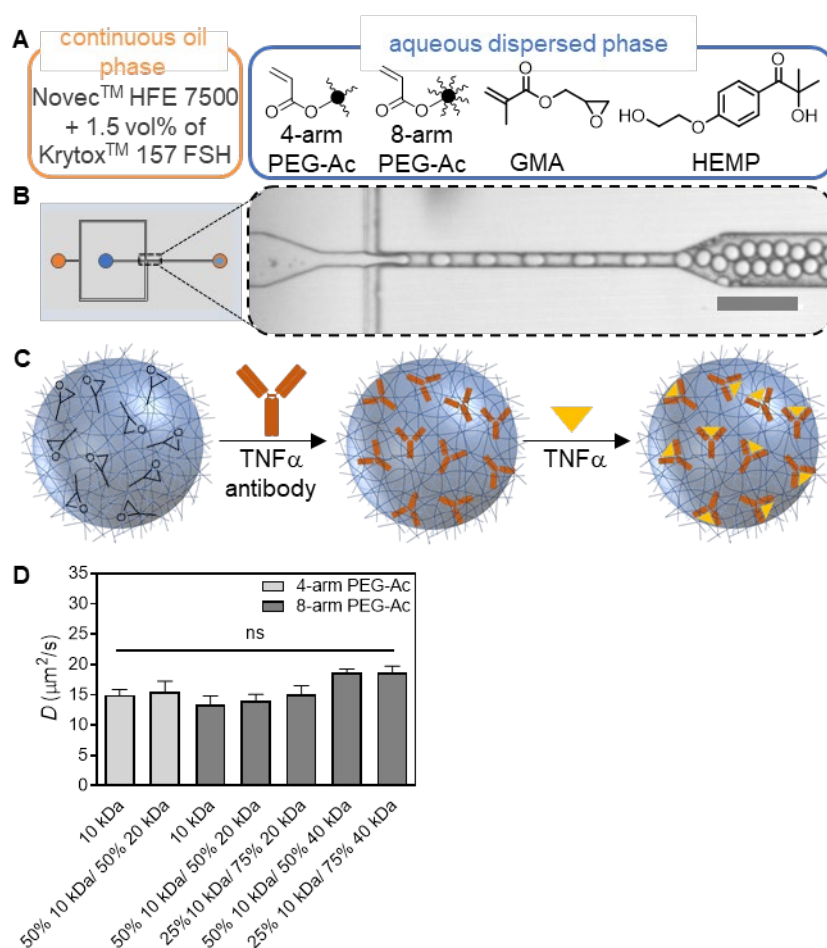
Figure 3.1: A) Composition of continuous and aqueous dispersed phases used in microfluidics. Continuous phase consists of Novec HFE 7500 (a fluorinated ether) with 1.5 vol% of Krytox H as a stabilizing agent, while glycidyl methacrylate (GMA) and 2-Hydroxy-4′-(2-hydroxyethoxy)-2-methylpropiophenone (HEMP, also known as Irgacure 2959) is added to the aqueous phase. B) Microfluidic set-up for the production of spherical microgels with different star polyethylene glycol acrylate (sPEG-Ac) polymers at a total concentration of 10 wt%. C) Schematic representation of TNFα scavenging microgels: glycidyl-co-polymerized PEG microgels are post-functionalization with TNFα antibodies to scavenge TNFα. D) Diffusion coefficients D of fluorescein isothiocyanate (FITC) dextran (20 kDa) in microgels with different polymer compositions and 10 eq. GMA was determined via FRAP technique. Data are shown as mean ± standard deviation, $n = 5$ microgels. Statistical significance is performed using two-way ANOVA with Tukey′s test for multiple comparisons: ns = non-significant = $P > 0.05$.

The collected droplets are irradiated with UV light at a wavelength of $\lambda = 365$ nm (200 mW, $t = 180$ s), inducing free radical polymerization and crosslinking to form the microgels. The microgels are then separated from the continuous phase, purified, and sterilized as explained in detail in the Materials and Methods section.

3.2.2 Diffusion studies with antigen- and antibody mimicking dextrans

Before testing therapeutic IgG antibodies and targeted antigens, we employ dextran, labelled with fluorescein isothiocyanate (FITC), with a molecular weight of 20 kDa and a hydrodynamic radius (R_h) of approx. 3.3 nm to mimic TNFα ($R_h = 3.2 \pm 0.04$ nm)[368], and a second set of fluorescently labelled dextran with molecular weight of 70 kDa (R_h approx. 6.0 nm) to mimic the IgG antibody ($R_h = 5.6 \pm 0.24$ nm)[368]. The latter has an amine functionality that is able to bind to the glycidyl-groups introduced via the GMA co-monomer and functions as a proof-of-concept molecule to examine the accessibility, reactivity, and ability of our microgels to take up and bind macromolecules. In a first step, diffusion of the FITC dextran ($M_n = 20$ kDa) is analyzed inside microgels prepared from various PEG compositions and 10 equivalents (eq.) of GMA per sPEG-Ac to investigate the impact of the crosslink density of the polymer network on the diffusion coefficient D. Therefore, we synthesize microgels with four- or eight-armed sPEG-Ac and different molecular weights of 10 kDa, 20 kDa, or 40 kDa at varying ratios and determine the diffusion coefficient using fluorescence recovery after photobleaching (FRAP) method (see Figure 3.1A and D). For all microgels, the diffusion coefficient is around $D = 15$ μm^2/s and thus not affected by the different microgel networks. Sequentially, we monitor diffusion of the larger fluorescein amine dextran ($M_n = 70$ kDa) into the same microgels after 96 h incubation time at a theoretical molar ratio dextran:GMA of 1 by confocal laser-scanning microscopy (CLSM) (see Figure 3.2). Similar as for the small 20 kDa FITC dextran, no differences in diffusion are observed for the different microgels. Based on the diffusion coefficients and the Ogston expression[369], the average mesh size is estimated to be between ca. 6.1 – 8.8 nm for all microgel conditions, which is larger than the hydrodynamic diameter of the antibody mimicking dextran ($M_n = 70$ kDa, ~ 6 nm) (see Table 3.1 and Figure 3.3). We used this obstruction model (as described in the method section), which is based on the premise that solute movement through the microgel network is impeded by the polymer chains.[369]
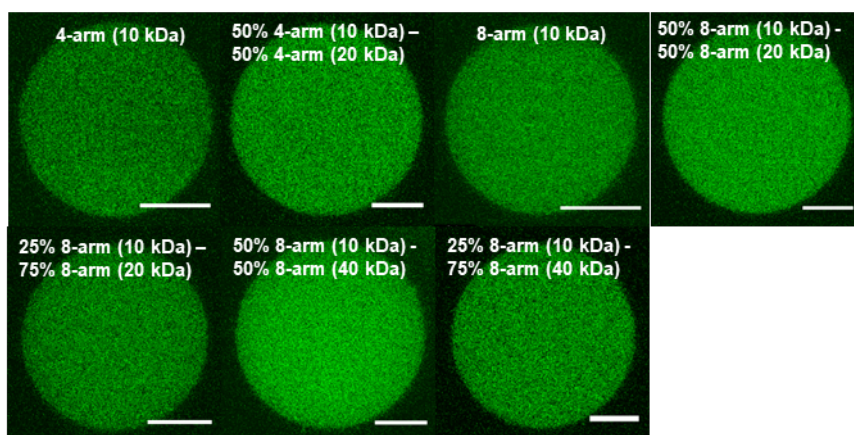
Figure 3.2: Confocal laser-scanning microscopy (CLSM) images of the diffusion of fluorescein amine dextran (70 kDa) after 96 h incubation time into microgels (10 eq. GMA) with different compositions. Scale bars represent 10 μm.

Table 3.1: Diffusion experiments with microgels prepared from different polymer compositions. The average mesh sizes of the microgel polymer networks are calculated based on the diffusion coefficients of FITC-dextran (20 kDa) and the Ogston expression.[369] The diffusion inside the microgels of 70 kDa and 150 kDa FITC-dextran is shown via CLSM measurements.

| Microgel	**Mesh size (nm)** based on diffusion coefficient of FITC-dextran (20 kDa) and Ogston expression[369]	**Diffusion** inside microgel of 70 kDa fluorescein amine dextran (~6 nm)	**Diffusion** inside microgel of150 kDa FITC-dextran (~8.5 nm)
10 wt% 4-arm PEG-Ac (10 kDa)	7.0	+++	-
10 wt% 50% 4-arm PEG-Ac (10 kDa) - 50% 4-arm PEG-Ac (20 kDa)	7.0	+++	-
10 wt% 8-arm PEG-Ac (10 kDa)	6.1	+++	++
10 wt% 50% 8-arm PEG-Ac (10 kDa) - 50% 8-arm PEG-Ac (20 kDa)	6.3	+++	+
10 wt% 25% 8-arm PEG-Ac (10 kDa) - 75% 8-arm PEG-Ac (20 kDa)	7.2	+++	++
10 wt% 50% 8-arm PEG-Ac (10 kDa) - 50% 8-arm PEG-Ac (40 kDa)	8.7	+++	+
10 wt% 25% 8-arm PEG-Ac (10 kDa) - 75% 8-arm PEG-Ac (40 kDa)	8.8	+++	+
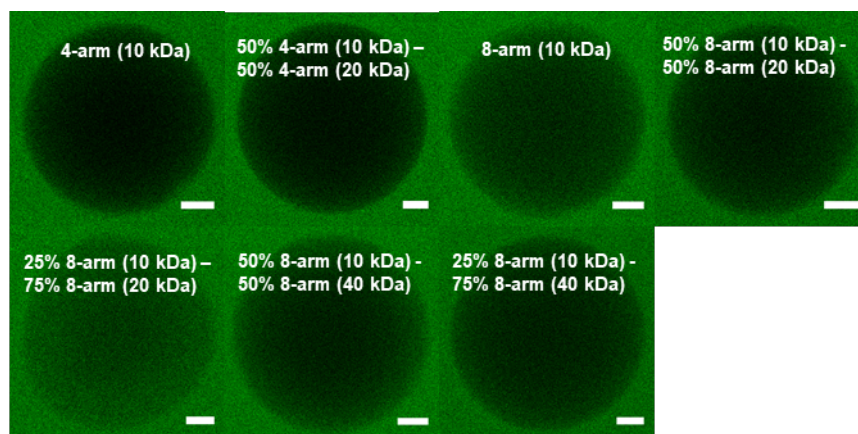
Figure 3.3: Confocal laser-scanning microscopy (CLSM) images of the diffusion of FITC-dextran (150 kDa) after 96 h incubation time into microgels (10 eq. GMA) with different compositions. Scale bars represent 5 µm.
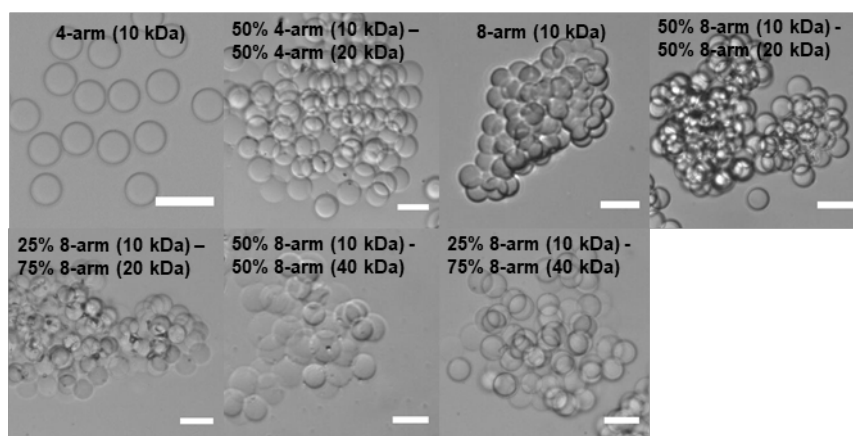
Figure 3.4: Brightfield images of collected and purified microgels (10 eq. GMA) with different compositions show aggregation in PBS. Scale bars represent 50 µm.

Importantly, the microgels produced with 4-arm sPEG-Ac (10 kDa) are the most stable and do not aggregate compared to the other microgel conditions (see Figure 3.4). Therefore, this composition is selected for the continuation of this study. Microgel aggregation can occur due to increasing hydrophobicity by increasing the number of acrylate groups by changing the number of arms and molecular weight of the used sPEG-Ac. With increasing hydrophobicity, the microgels behave more like solid particles, so elevated attraction forces may be induced.[131]

To further assess the immobilization efficiency of our functional microgels via amine/glycidyl addition, we incubate microgels made with 4-arm sPEG-Ac (10 kDa) and
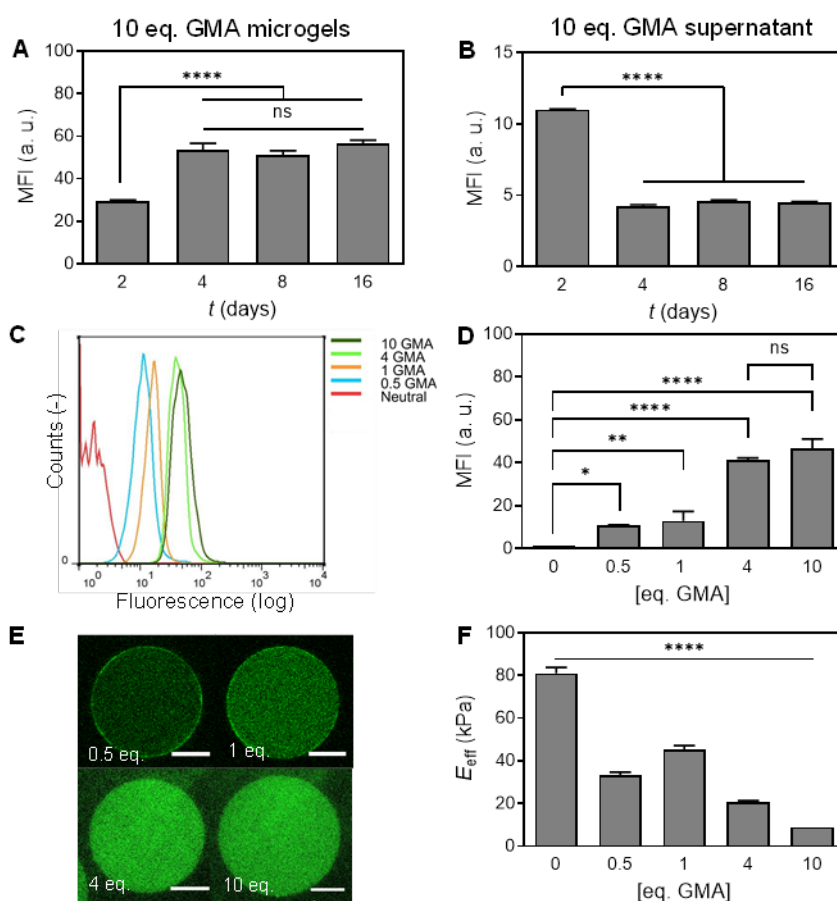
10 eq. of GMA per sPEG-Ac with fluorescein amine dextran (M_n = 70 kDa) for 2, 4, 8, and 16 days and measure the level of their fluorescence via flow cytometry. After 4 days of incubation, saturation is reached as verified by investigating the fluorescence of the supernatant, (see Figure 3.5A). The fluorescence in the supernatant does not decrease significantly after 4 days of incubation, meaning that the microgels have reached their uptake limit (see Figure 3.5B).

3.2.3   Optimization of GMA concentration inside the microgels

To investigate the required amount of GMA inside the microgels to link a maximum number of antigen binding sites inside the microgel, we vary the GMA concentration during synthesis. Therefore, we synthesize microgels with 0.5, 1, 4, or 10 eq. GMA per sPEG-Ac and incubate them over the course of 4 days with a stoichiometric concentration of fluorescently labelled amine dextran (dextran:GMA of 1). The fluorescence intensity is analyzed using flow cytometry analysis and CLSM (see Figure 3.5C-E). While a significant augmentation of dextran binding is observed for an increase from 1 to 4 eq. of GMA, no further differences are observed in the fluorescence signal between microgels made with 4 and 10 eq. GMA (see Figure 3.5C-E). Microgels without copolymerized GMA show only negligible fluorescence, indicating minimal unspecific binding to the fluorescein amine dextrans. Importantly, the incorporation of more or less GMA will affect the network morphology, as it separates the sites for crosslinking and increases the mesh size – at least before any binding motifs are attached to the glycidyl units. This is confirmed by the increased stiffness for the lower GMA concentrations of 0.5 and 1 eq. (see Figure 3.5F), suggesting a smaller mesh size. To analyze this, FRAP experiments on the microgels with different GMA concentrations is performed with FITC dextran (M_n = 20 kDa), mimicking the size of the antigen. Only in the case of 4 and 10 eq. GMA microgels (10 wt% 4-arm PEG-Ac (10 kDa)), we were able to measure a diffusion coefficient of 7.4 μm^2/s and 18.3 μm^2/s, respectively. In the case of 0.5 and 1 eq., FITC dextran (M_n = 20 kDa) did not diffuse into the microgels as the mesh size becomes too small (not shown). Furthermore, to study the effect of increasing mesh size with increasing GMA, we determine the Young's modulus via nanoindentation on isolated microgels immobilized on a surface. As expected, microgels with higher GMA concentration are softer than those with no or low concentrations of GMA (see Figure 3.5F). Notably, such a decrease in stiffness has

previously also been reported for introducing amine methacrylate as a co-monomer in microfluidically produced sPEG-Ac microgels.[107] Microgel stiffness and deformability are important when interacting with biological interfaces. PEG-based rod-shaped microgels with an effective Young's modulus of around 20 kPa, and modified with RGD, supported cell attachment, spreading, and growth when incubated with human fibroblasts and HUVECs.[107] Moreover, sPEG-based spherical microgels were assembled to microporous tissue scaffolds, while scaffolds with a storage modulus of 13.5 kPa showed best cell proliferation when incubated with human fibroblasts.[370] These stiffnesses are comparable to our microgels made from 10 wt% 4 arm sPEG-Ac (10 kDa) and a GMA amount of 10 eq. and 4 eq.

Figure 3.5: Time dependent binding of fluorescein amine dextran to GMA functionalized microgels (10 wt% 4 arm sPEG-Ac (10 kDa). A) Flow cytometry-based mean fluorescence intensity (MFI) of microgels (10 eq. GMA) incubated with fluorescein amine dextran (70 kDa) for 2, 4, 8. and 16 days, B) Measurements of fluorescence in corresponding supernatant via plate reader, C) Flow cytometry plots of microgels containing increasing amounts of GMA ranging from 0.5 eq. to 10 eq. that are incubated with fluorescein amine dextran for 4 days, D) Corresponding plot of the mean fluorescence intensity (MFI) shown in (C), $n \geq 3$, E) Confocal images of microgels containing different amounts of GMA (0.5 eq., 1 eq., 4 eq., and 10 eq.) that are incubated with fluorescein amine dextran (70 kDa) for 4 days. Scale bars represent 10 µm. F) Effective Young's modulus (E_{eff}) of microgels containing different eq. of GMA determined via nanoindentation; $n \geq 10$ microgels. Data is presented as mean ± standard deviation. Statistical significance is performed using two-way ANOVA with Tukey's test for multiple comparison: ns = non-significant = $P > 0.05$, *$P < 0.05$, **$P < 0.01$, ****$P < 0.0001$.

After demonstrating homogeneous uptake and binding of the dextran as an IgG antibody-mimicking molecule, we investigate whether a second molecule could still diffuse through the polymer network after the first functionalization. In the real system, TNFα would need to diffuse through the network and bind to the IgG antibody. To mimic TNFα, we incubate the 70 kDa dextran-coupled microgels (10 eq. GMA, 4-arm sPEG-Ac (10 kDa)) with a second dextran (M_n = 20 kDa) labelled with red fluorescent Rhodamine B, at a concentration of dextran:GMA of 1 over a course of 96 h. Analysis via CLSM shows homogeneously green (before) and red-fluorescing microgels (after incubation), indicating that a small molecule like TNFα will be able to diffuse and bind into the microgel network after coupling the IgG (see Figure 3.6).
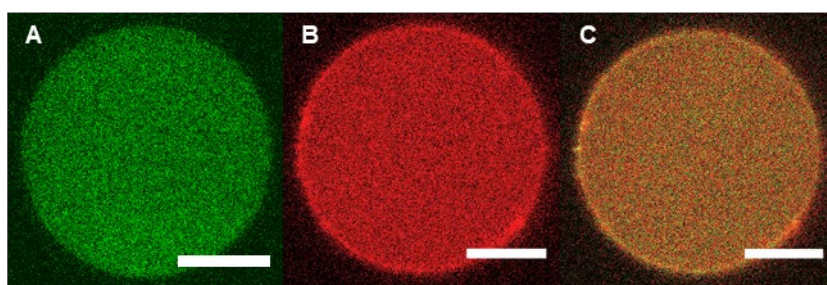
Figure 3.6: Diffusion studies in microgels (10 wt% - 4-arm PEG-Ac (10 kDa) with 10 eq. GMA. A) Diffusion of Fluorescein amine dextran (70 kDa) into microgels. B) Diffusion of Rhodamine B dextran (20 kDa) into microgels; C) overlay of A and B. Scale bars represent 10 µm.

3.2.4 Antibody binding inside the microgels

Based on our binding efficiency experiments, we consider microgels with 4 or 10 eq. GMA as most suitable to function as antigen scavengers as they showed significantly higher fluorescence intensity compared to lower eq. GMA. Therefore, microgels (10 wt% 4-arm sPEG-Ac (10 kDa)) with 4 and 10 eq. are incubated with IgG antibody for 4 days to quantify uptake and binding to the microgel network via amine-glycidyl addition. After purification of the microgels, we analyze the bound protein content with a CBQCA protein quantification kit. It becomes clear that for both types of microgels, the level of bound IgG antibody increases with higher amounts of incubated antibody. Interestingly, microgels with 10 eq. GMA bind significantly more IgG antibody compared to microgels with 4 eq. GMA, although this difference is not observed in the binding study with fluorescently labelled amine dextran of 70 kDa (see Figure 3.5C-E and 3.7), which could be related to fluorescence quenching. For the quantitative protein assay, different molar ratios of

IgG:GMA, ranging from 0.01 to 1, are tested. In the case of IgG:GMA = 0.1 for 4 eq. GMA in the microgels, a concentration of bound IgG [IgG] = 191.62 ± 4.1 μg of IgG/10^5 microgels (μGs) is observed, while for 10 eq. GMA in the microgels, [IgG] = 330 ± 6.6 μg/10^5 μGs. When we increase the IgG concentration during incubation, we see that the amount of bound antibody increases proportionally up to the theoretical stoichiometric ratio of IgG:GMA = 1, demonstrating that IgG can easily reach and react with the glycidyl-groups. However, it is also clear that most IgG remains in the supernatant and does not bind to the microgels. This is expected as ~100,000 microgels (total volume of ~ 400 μL) are incubated in a volume of 1,200 μL containing the IgG. Based on these results, microgels made with 10 eq. GMA are selected for the continuation of the study. In order to decouple microgel stiffness with the antibody conjugation, quenching of free glycidyl groups to simulate less antigen binding sites in the 10 eq. GMA microgels will be performed in future experiments.
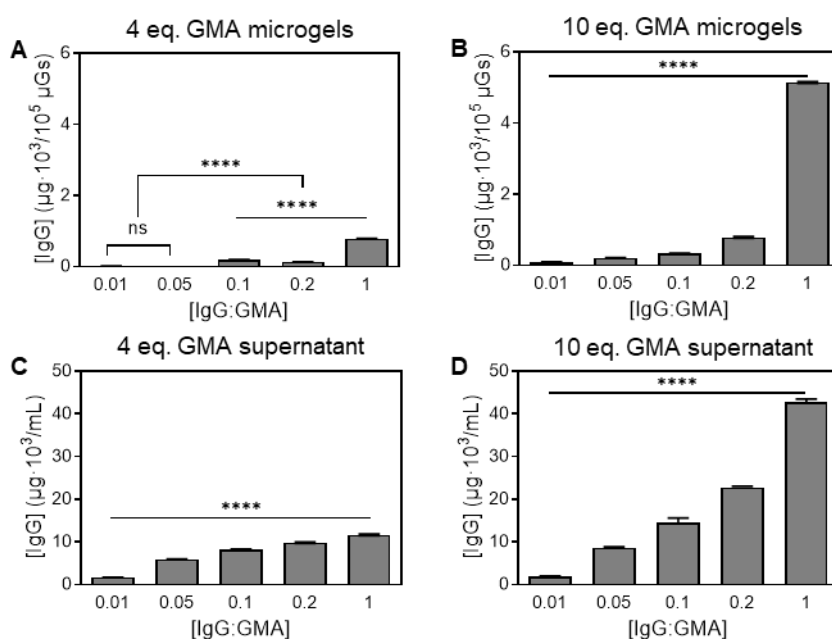
Figure 3.7: Functionalization of microgels (10 wt% 4 arm sPEG-Ac (10 kDa, 4 and 10 eq. GMA)) with IgG antibody against human TNFα. The concentration of antibody in microgels prepared with 4 A and 10 B eq. of GMA, as well as in the corresponding supernatants C and D, is measured via CBQCA protein quantification kit. Data is presented as mean ± standard deviation, $n = 3$. Statistical significance is performed using two-way ANOVA with Tukey´s test for multiple comparison: ns = non-significant = $P > 0.05$, ****$P < 0.0001$.

3.2.5   Specific antibody-antigen binding inside the microgels

First, in order to ensure that the antibody is still active after binding to the microgels, we investigate different methods to bind the antibody to the GMA equipped microgels without

losing its activity. The microgels are functionalized with the antibody directly, with Protein A and in a second step with the antibody, or with a Protein A-antibody complex (see Figure 3.8). From these results, it is clear that direct coupling of the antibody to GMA in the microgels is the most efficient.
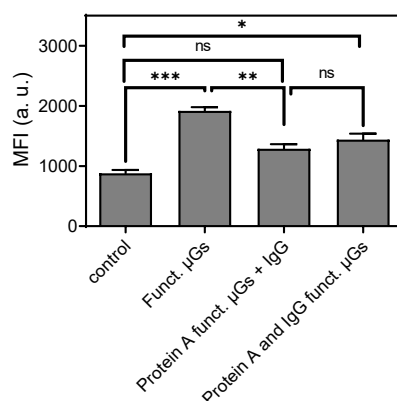
Figure 3.8: Flow cytometry analysis of microgels. Binding of 0.01 μM biotinylated TNFα to non-functionalized microgels, TNFα antibody functionalized microgels (direct coupling), microgels that were first functionalized with Protein A and subsequently coupled to TNFα antibody (protein A funct. μGs + IgG), as well as microgels that were coupled to a Protein A – TNFα antibody complex (protein A and IgG funct. μGs). Bound biotinylated TNFα was detected via APC-labelled streptavidin by the flow cytometer. Statistical significance is performed using two-way ANOVA with Tukey's test for multiple comparison: ns = non-significant = $P > 0.05$, $*P < 0.05$, $**P < 0.01$, $***P < 0.001$.

To investigate whether TNFα can diffuse and bind to the antibody functionalized microgels, we incubate either ~100,000 non-functionalized or functionalized microgels with two different TNFα concentrations, 0.5 μg/mL ($2.9 \cdot 10^{-8}$ mol/mL) (see Figure 3.9A) and 2.5 μg/mL ($1.5 \cdot 10^{-7}$ mol/mL) (see Figure 3.9B), in a volume of 500 μL and analyze the supernatant via ELISA. Even though non-functionalized microgels behave like sponges and absorb approximately half of the applied TNFα when using a concentration of 0.5 μg/mL, functionalized microgels with IgG:GMA = 0.01 scavenge significantly more TNFα compared to non-functionalized microgels (see Figure 3.9A). Increasing the IgG:GMA ratio further increases the scavenging potential, showing complete uptake at a ratio of 0.05 for an applied concentration of 0.5 μg/mL TNFα (see Figure 3.9A). This experiment shows that at low [TNFα] = 0.5 μg/mL, microgels with IgG:GMA = 0.05 scavenge virtually all TNFα and are as efficient as for the case of stoichiometric functionalization. To further test the limits of the microgels to scavenge TNFα, the same microgels are incubated with a 5-fold higher concentration of [TNFα] = 2.5 μg/mL (see Figure 3.9B). Here, it requires microgels with a stoichiometric IgG:GMA ratio of 1 to be able to scavenge 88% of the applied TNFα. Moreover, for microgels with a theoretical

IgG:GMA ratio of 0.1, around 50% of the applied TNFα is scavenged, when incubated with [TNFα] = 2.5 µg/mL.

Importantly, both tested TNFα concentrations are far beyond the disease-relevant levels. For example, the TNFα concentration in the intestinal tissue during an acute dextran sodium sulfate (DSS) induced colitis in mice has been reported to be in the pg/mL range.[371,372] For this reason, the following experiments are performed using microgels with IgG:GMA = 0.1, as this ratio is adequate to incorporate sufficient antibodies with respect to physiological levels of TNFα and will allow for ample binding to scavenge the antigen in cytokine mediated diseases. At this ratio, we can nearly completely remove TNFα up to concentrations of 0.5 µg/mL, which is still far above the physiological concentration (see Figure 3.9C).

Unfortunately, we are not able to calculate or estimate a dissociation constant for the antibody in the microgels as we already went up to a level of TNFα, which exceeds the physiological concentration range by far and still we do not reach saturation of the microgels, which would be required to estimate or determine an uptake efficiency.
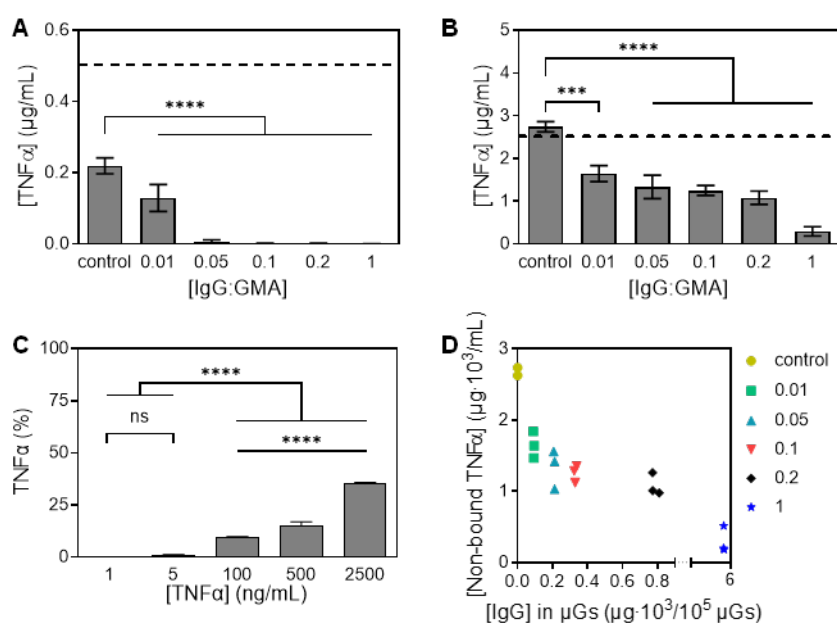
Figure 3.9: TNFα binding to microgels (10 wt% 4 arm sPEG-Ac (10 kDa, 10 eq. GMA)) ([microgels] = 200,000 microgels/mL = 100 µg/mL). A) 0.5 µg/mL TNFα is incubated with microgels containing different glycidyl-antibody ratios [IgG:GMA]. Non-bound TNFα is measured in the supernatant via TNFα ELISA. B) 2.5 µg/mL TNFα is incubated with microgels containing different glycidyl-antibody ratios [IgG:GMA]. Non-bound TNFα is measured in the supernatant via TNFα ELISA. C) Antibody-functionalized microgels (IgG:GMA = 0.1) are incubated with increasing concentrations of TNFα. Non-bound TNFα is measured in the supernatant via TNFα ELISA and shown as percentage. D) shows the correlation between the amount of incorporated antibody and scavenged TNFα for a fixed concentration of 2.5 µg/mL TNFα. Data is presented as mean ± standard deviation, $n = 3$. Statistical significance is performed using two-way ANOVA with Tukey´s test for multiple comparison: ns = non-significant = $P > 0.05$, ***$P < 0.001$, ****$P < 0.0001$.

To further quantify how efficiently TNFα diffuses into and binds to the antibody functionalized microgels (10 eq. GMA, 0.1 IgG:GMA), we label the antibody (IgG) inside of the microgels with Alexa Fluor 546 (AF546) and the TNFα antigen with Alexa Fluor 488 (AF488). These two dyes can engage in Förster resonance energy transfer (FRET) and therefore represent a FRET pair, with the antibody functioning as the FRET acceptor and TNFα as the donor. First, we incubate microgels without the FRET donor with the fluorescently labelled antibody and we observe fluorescence emission (represented in purple) inside the microgels after washing and excitation at 561 nm (see Figure 3.10A and B). This corroborates that the functionalization with the fluorescently labelled antibody is successful. Secondly, we image the fluorescently labelled TNFα inside of the microgels in absence of the FRET acceptor IgG resulting in a homogeneous fluorescence emission after excitation at 488 nm (represented in yellow) (see Figure 3.10C). After this, the fluorescently labelled TNFα FRET donor is incubated at 138 µg/mL with ~50,000 microgels carrying the FRET acceptor functionalized antibodies. When we excite only with the 488 nm laser line, we observe fluorescence of AF488 in the donor channel (yellow) and in addition the fluorescence of AF546 in the acceptor channel (purple), which indicates that the Förster energy transfer is efficient, and we can therefore infer that the TNFα is binding specifically to the TNFα antibodies (see Figure 3.10D).

However, to confirm FRET[373] as the origin for the acceptor emission, we performed additionally Fluorescence Lifetime Imaging (FLIM)[374] measurements of 10 different microgels. In the FLIM experiments, we excite also with the 488 nm laser line but collect only the fluorescence of the donor. In addition to the number of photons, we can resolve the kinetics of the fluorescence emission. By looking at the lifetime of the fluorescence decay, we can detect the FRET process, since in such a case the lifetime of the donor is shortened, due to the additional FRET deactivation channel. Indeed, we observe a shift of the lifetime of the donor labelled TNFα (see fluorescence lifetime image in Figure 3.10F and schematically shown in Figure 3.10I) from, approximately, 4.02 ± 0.02 ns in solution (see Figure 3.10M) to a value of 3.01 ± 0.09 ns (see Figure 3.10M), (intensity averaged lifetime), confirming the FRET interaction (see fluorescence lifetime image in Figure 3.10H and schematically shown in Figure 3.10K). However, we also observe some quenching of the donor lifetime to a value of approximately 3.61 ± 0.09 ns (intensity averaged lifetime) (see Figure 3.10M) when donor labelled TNFα is freely diffusing in the

microgels without the antibody-acceptor moiety (see Figures 3.10G and schematically shown in Figure 3.10J).
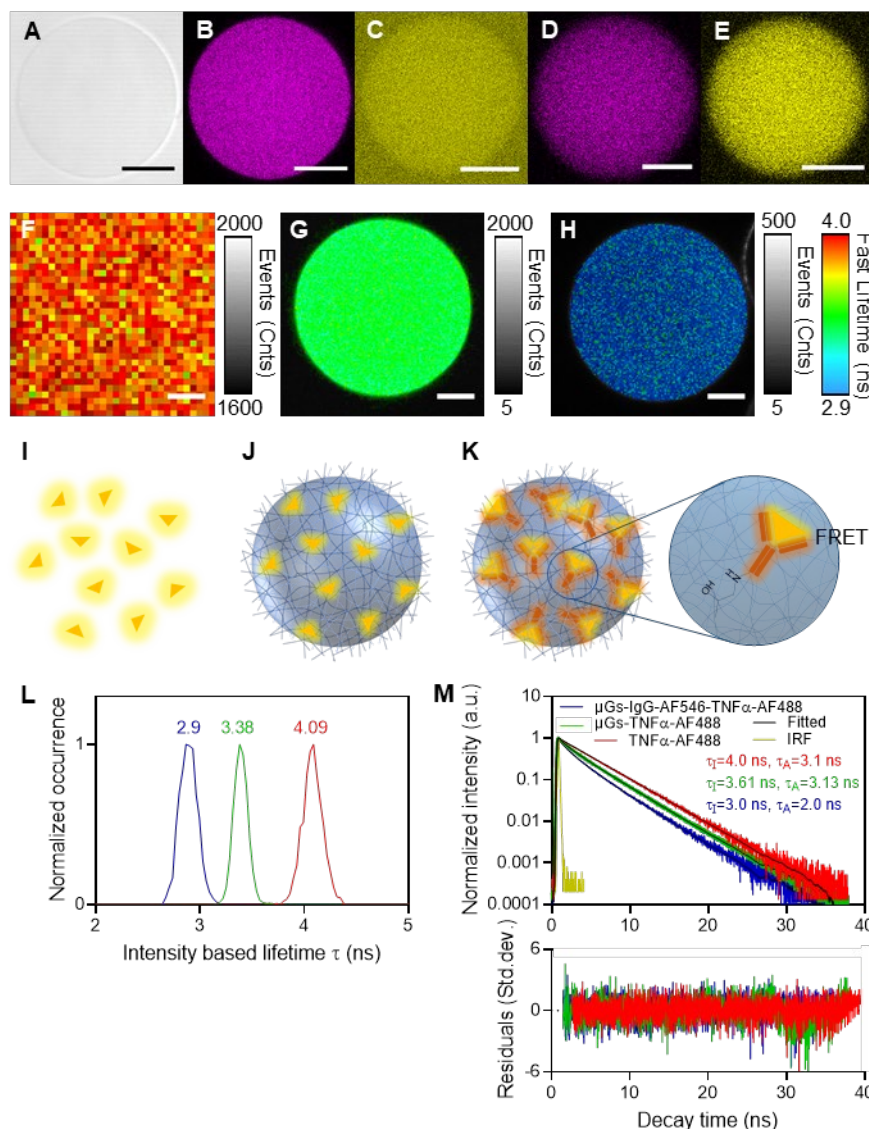
Figure 3.10: Specific TNFα binding to TNFα antibody-functionalized microgels ([microgels] = 50,000 microgels/mL). Confocal images of microgels (10 wt% 4 arm sPEG-Ac (10 kDa, 10 eq. GMA)) to show FRET signal. A) Brightfield image, B) TNFα antibody (acceptor, Alexa Fluor 546) functionalized microgels are excited ($\lambda = 561$ nm) and detected ($\lambda = 571\text{-}700$ nm) at acceptor wavelength, C) TNFα (donor, Alexa Fluor 488) incubated with non-functionalized microgels are excited ($\lambda = 488$ nm) and detected ($\lambda = 498\text{-}540$ nm) at donor wavelength, and D) FRET signal: TNFα antibody (acceptor) functionalized microgels incubated with TNFα (donor) are excited at donor excitation wavelength ($\lambda = 488$ nm) and detected ($\lambda = 571\text{-}700$ nm) at acceptor wavelength. E) TNFα antibody (acceptor) functionalized microgels incubated with TNFα (donor) are excited at donor excitation wavelength ($\lambda = 488$ nm) and detected ($\lambda = 498\text{-}540$ nm) at donor wavelength. Fluorescence lifetime images (FLIM) of F) only donor in solution, G) non-functionalized microgels incubated with donor and H) TNFα antibody (acceptor) functionalized microgels incubated with donor (FRET sample). All scale bars represent 10 μm. I) Schematic of only donor in solution, K) Schematic of non-functionalized microgels incubated with donor and L) Schematic of TNFα antibody (acceptor) functionalized microgels incubated with donor (FRET sample). M) Lifetime histograms from the FLIM images F (red curve), G (green curve), and H (blue curve). N) The fluorescence decays and respective exponential fittings corresponding to the FLIM images F-H.

Unfortunately, this quenching, which is observed as a multiexponential decay (Tables 3.2 and 3.3), prevents us from being able to quantify the cytokine/antibody binding with

fidelity. The origin of the non-FRET quenching was not further investigated in this work but is likely caused by interaction with the microgel network. Further studies are needed to determine whether the binding of the antibody to the microgels reduces its efficiency, potentially by surface plasmon resonance.

Table 3.2: Exemplary exponential fitting parameters for TNFα-AF488 diffusing in a microgel without TNFα-antibodies (non-FRET reference sample).

τ_i (ns)	A_I (kctns)	I_I (kctns)	τ_A (ns)	τ_I (ns)	χ^2	A_{rel}
4.0±0.02	156	38103	3.13 ± 0.05	3.61 ± 0.09	1.07	0.63
2.10±0.02	63	8289	-	-	-	0.25
0.58±0.02	28	1017	-	-	-	0.11

Table 3.3: Exemplary exponential fitting parameters for TNFα-AF488 diffusing in a microgel with TNFα-antibodies (non-FRET reference sample).

τ_i (ns)	A_I (kctns)	I_I (kctns)	τ_A (ns)	τ_I (ns)	χ^2	A_{rel}
3.90±0.02	2.67	649	2.59 ± 0.05	3.64 ± 0.09	0.96	0.60
1.44±0.02	0.66	60	-	-	-	0.15
0.13±0.02	1.10	8.90	-	-	-	0.25

3.2.6   Microgels protect HT29 cells from TNFα induced inflammation

Our optimized microgels for TNFα scavenging are now tested in their ability to protect HT29 colorectal adenocarcinoma cells from cytokine toxicity. We perform a competition experiment, where HT29 cells are exposed to TNFα and microgels (antibody functionalized and non-functionalized) at the same time. The levels of COX II and the release of IL8 or LDH into the cell culture medium are used as indicators for the TNFα toxicity.[375,376] Exposing the cells to TNFα at a concentration of 5 ng/mL is sufficient to induce the biosynthesis of COX II, as well as the release of IL8 and LDH into the supernatant (see Figure 3.11A-D). The presence of a robust inflammation upon stimulation with TNFα is confirmed by increased mRNA expression of the pro-inflammatory cytokines TNFα and IL8 (see Figure 3.11E and F).
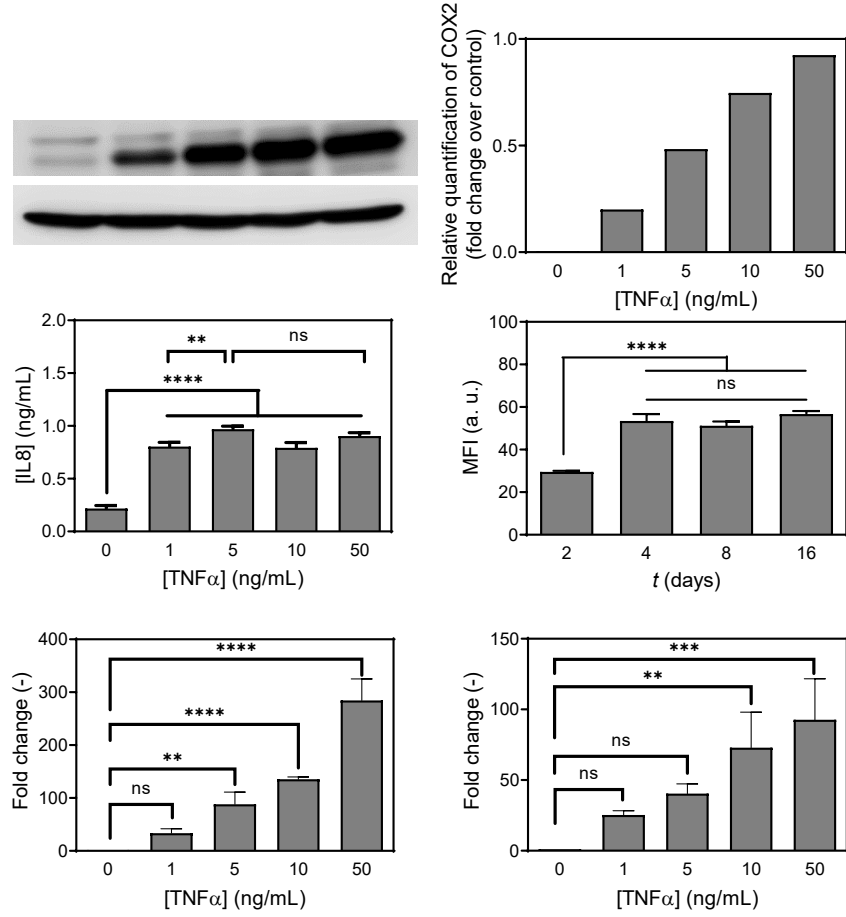
Figure 3.11: Inflammatory reaction of HT29 cells upon exposure to different concentrations of TNFα ranging from 0 (control) to 50 ng/mL for 24 h. A) shows cyclooxygenase II (COX II) western blot from protein lysates of harvested cells and the corresponding quantification B. The release of the pro-inflammatory cytokine interleukin (IL) 8 as well as the release of lactate dehydrogenase (LDH) are shown in C) and D). Real-time polymerase chain reaction (RT-PCR) determines the relative mRNA levels of the pro-inflammatory cytokines E) TNFα and F) IL8. Beta actin was used as an internal control. Data is presented as mean ± standard deviation, $n = 3$. Statistical significance is performed using two-way ANOVA with Tukey´s test for multiple comparison: ns = non-significant = $P > 0.05$, $*P < 0.05$, $**P < 0.01$, $***P < 0.001$, $****P < 0.0001$.

To test the scavenging function of the microgels, HT29 cells are simultaneously exposed to 5 ng/mL TNFα and either 100 µg/mL of antibody-functionalized or non-functionalized microgels, which are about ~200,000 microgels/mL. Compared to treatment with TNFα alone, the co-incubation with antibody-functionalized microgels significantly reduced COX II levels, as well as the amount of the pro-inflammatory cytokine IL8 in the cell culture supernatant (see Figure 3.12A and B). These results suggest that TNFα has a higher affinity to antibody-functionalized microgels than the corresponding receptors present on the cell surface. Importantly, non-functionalized microgels do not show this reduction in inflammatory markers. Exposure of the cells to either antibody-functionalized or non-functionalized microgels without TNFα does not induce any inflammatory or toxic effects, indicating that the microgels themselves are biocompatible (not shown).
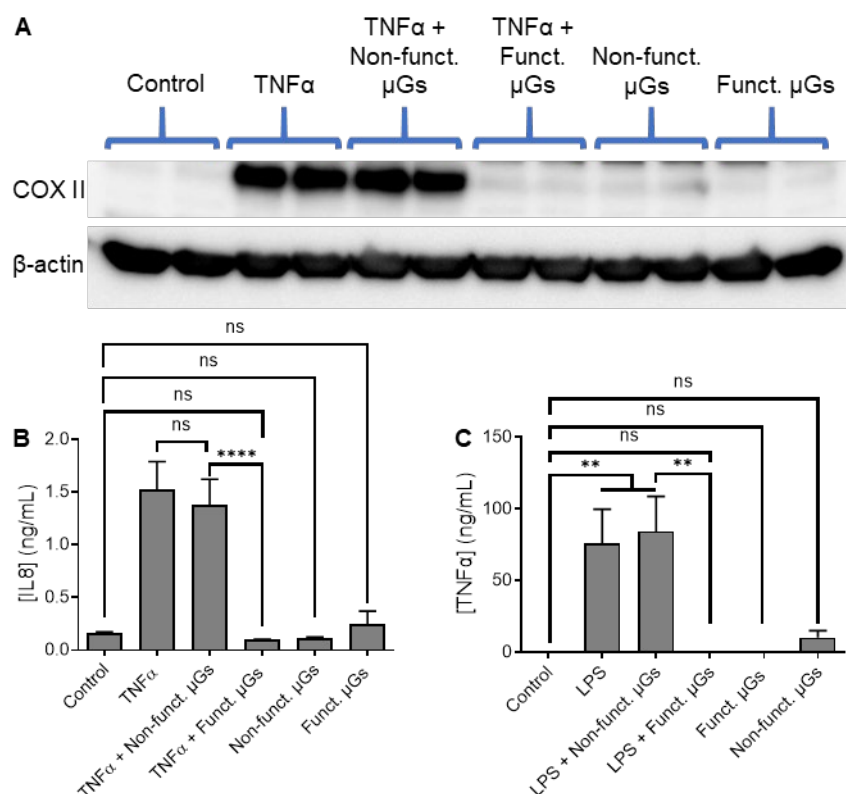
Figure 3.12: Microgels efficiently scavenge TNFα in two different cellular models. A) and B) TNFα antibody-functionalized microgels protect HT29 cells from TNFα induced cyclooxygenase II (COX II) production, as well as interleukin 8 (IL8) release into the cell culture supernatant. Cells are exposed with 5 ng/mL TNFα alone, with TNFα together with 100 µg/mL of antibody-functionalized or non-functionalized microgels or with microgels only for 24 h. A shows a COX II western blot of protein lysates of harvested cells. ß-actin is used as a loading control. B) IL8 concentration in the cell culture supernatant is measured after an incubation for 24 h. Data is presented as mean ± standard deviation, $n = 3$. Statistical significance is performed using two-way ANOVA with Tukey´s test for multiple comparison: ns = non-significant = $P > 0.05$, ****$P < 0.0001$. C) TNFα antibody-functionalized microgels scavenge TNFα produced by human macrophages upon stimulation with lipopolysaccharide (LPS) ($n = 5$ donors). Macrophages are stimulated with 100 ng/mL LPS, LPS and either antibody-functionalized or non-functionalized microgels, or microgels only for 24 h. As negative control, the cells are treated with normal cell culture medium. The graph shows the levels of TNFα in the cell culture supernatant of the different groups. Data is presented as mean ± standard deviation, $n = 5$. Statistical significance is performed using two-way ANOVA with Tukey´s test for multiple comparison: ns = non-significant = $P > 0.05$, **$P < 0.01$.

3.2.7 Microgels scavenge TNFα produced by human macrophages

To achieve a supraphysiological cytokine burst, human macrophages are stimulated with lipopolysaccharide (LPS) to induce the production of TNFα instead of administering TNFα to the media.[377,378] This stimulation leads to the release of approximately 60 ng/mL of TNFα into the cell culture supernatant. Co-incubation of activated macrophages with non-functionalized microgels produces the same level of TNFα release (see Figure 3.12C). By contrast, co-incubation with TNFα antibody-functionalized microgels depletes TNFα virtually completely in the cell culture supernatant demonstrating their ability to scavenge

the produced TNFα in real time. Notably, co-incubation of human macrophages (no LPS activation) with non-functionalized or antibody-coupled microgels alone triggers no or only minimal TNFα production (see Figure 3.12C). These results suggest that microgels themselves neither activate the macrophages nor induce an inflammation, which demonstrates their biocompatibility.

3.3   Conclusion

In summary, we show that microgels are able to bind large amounts of antibodies, which are able to efficiently scavenge pro-inflammatory antigens, in this case TNFα. We optimized the microgels' chemical composition to incorporate large amounts of antibody but also determined the minimal required antibody concentration inside the microgels to scavenge sufficient cytokines. Our microgels constitute an attractive approach to locally bind antigens as a treatment of cytokine mediated inflammatory diseases. Our concept for local scavenging can be transferred and potentially be applied to various diseases, such as inflammatory bowel disease or rheumatoid arthritis, which are conventionally treated by systemic injection of therapeutic antibodies. In the next step, we plan to establish an inflammatory bowel disease animal model to test the efficacy of the antibody functionalized microgels *in vivo*.

3.4   Materials and Methods

3.4.1   Preparation of PDMS-based Microfluidic Devices

Microfluidic chips are used for the production of microfluidic devices via soft lithography. Sylgard 184 silicone elastomer (PDMS) and curing agent are mixed in a ratio of 10:1 in a plastic cup for 5 min. The mixture is placed in a desiccator under vacuum (10^{-3} mbar) to remove entrapped air. It is subsequently casted into the form and the air is evacuated again in the desiccator. The PDMS is cured in the oven for 12 h at 60 °C. The cured PDMS is cut out and holes for inlets and outlets in the channels are punched (biopsy puncher, inner diameter 0.75 mm). The PDMS form is washed three times with iso-propanol and water. A glass slide (76 x 52 x 1 mm, Marienfeld, Germany) is rinsed three times with acetone, iso-

propanol, and water. For bonding, the PDMS replica and glass slide are activated in an oxygen plasma oven (PVA TePla 100E, Germany, Wettenberg) at an oxygen flow of 30 mL/min for 40 s at 100 W. The PDMS replica is bonded to the glass slide with the structured side and baked in the oven for 3 h at 60 °C for complete adhesion.

A hydrophobic surface coating inside of the microfluidic device channels is achieved by silanization with Tridecafluoro-1,1,2,2-tetrahydrooctyl-trichlorosilane. To enable that, the microfluidic device is positioned in a desiccator together with the silane and evacuated overnight. NovecTM HFE 7500 with 1.5 vol% of KrytoxTM 157 FSH surfactant is used to remove remaining residues of the silane from the microfluidic device.

3.4.2   Microgel Synthesis

A mixture of NovecTM HFE 7500 and 1.5 vol% of KrytoxTM 157 FSH surfactant is served as continuous oil phase for microgel synthesis. The dispersed aqueous phase is prepared by dissolving PEG acrylate (10 wt%) in water (HPLC gradient grade). GMA is added at a desired concentration and stirred until a homogenous solution is obtained. The radical photoinitiator 2-hydroxy-4'-(2-hydroxyethoxy)-2-methylpropiophenone (HEMP/Irgacure® 2959) (0.6 wt%) is subsequently added to the solution. The vial is wrapped with aluminum foil to protect it against light-initiated polymerization.

For microfluidic synthesis of droplet-based microgels, the continuous oil and dispersed aqueous phases are each placed in a pressure vessel. The solutions are connected to the microfluidic device via PE tubing (0.38 mm ID/1.09 mm OD). The continuous oil phase consists of Novec HFE 7500 (a fluorinated ether) with 1.5 vol% of Krytox H as a stabilizing agent and the dispersed aqueous solution is prepared by mixing an aqueous solution of star-PEG acrylate (sPEG-Ac) polymers with glycidyl methacrylate (GMA; 10 mol per mol sPEG-Ac) and Irgacure 2959 as the photo-initiator. The applied pressures for droplet generation for the continuous oil phase and the dispersed aqueous solutions are 220 mbar and 260 mbar, respectively. The produced monodisperse droplets are left out of the microfluidic device via a PE tubing in the outlet channel. The tubing is irradiated with UV light (λ_{max} = 365 nm, 200 mW, t = 180 s) to polymerize the droplets via free radical polymerization. The microgels are collected in an Eppendorf vial filled with continuous oil phase to prevent them from drying out. The microgels are stored at 4 °C until purification.

Prior to purification, the continuous oil phase and aqueous phase containing microgels formed a two-phase system. First, the oil phase is removed using a syringe with a needle. The microgels are dispersed in a mixture of n-hexane and 1 wt% Span® 80. After sedimentation of the microgels, the solution is removed with a syringe and a needle. The microgels are dispersed again in the solution and this step is repeated five times. Subsequently, this process is repeated with the solvents n-hexane, iso-propanol, and water. The microgels are finally dispersed in water and stored at 4 °C.

3.4.3 Synthesis of TNFα-antibody-functionalized microgels

The microgels are dispersed in 1xPBS (pH 7.4) in an Eppendorf vial. After their sedimentation, PBS is removed with a syringe and a needle. This washing step is repeated five times. Microgels with a corresponding amount of glycidyl groups are dispersed in PBS and TNFα antibody (Amgevita Adalimumab, Amgen®, Germany) is added in a ratio of 1:1 to the glycidyl groups. The solution is stirred using a rotating stirrer for 72 h at room temperature to facilitate diffusion and binding of TNFα antibody to the microgels via amine-glycidyl coupling. After sedimentation of the microgels, the microgels are washed five times with fresh PBS as described above. Afterwards, remaining glycidyl groups are quenched by reaction with 2-aminoethanol for 2 h at room temperature using a rotating stirrer. The microgels are washed five times with fresh PBS and stored at 4 °C until further use.

3.4.4 Flow cytometry based binding studies

50,000 GMA-coupled microgels (10 eq. GMA) are incubated with fluorescein amine dextran (70 kDa) with a concentration of 1:1 related to the glycidyl groups for different periods of time, ranging from 1 day to 16 days at room temperature. In a second experiment, the amount of GMA is varied, ranging from 0.5 eq. to 10 eq., and the microgels are incubated with fluorescein amine dextran (1:1 related to the glycidyl groups) for 4 days. Subsequently, microgels are washed with PBS three times and re-suspended in 150 μL fresh PBS. Flow cytometry analysis is performed at a medium flow rate using the blue

$\lambda = 488$ nm laser. 10,000 events are recorded for every sample. Measurements are carried out in triplicates and evaluated by use of the FlowJo software (Treestar, OR, USA).

3.4.5 Diffusion studies and specific TNFα - antibody binding

Diffusion of fluorescently labelled FITC-dextran (20 kDa) inside the microgels are measured via Fluorescence Recovery After Photobleaching (FRAP) technique using Confocal Laser Scanning Microscopy (CLSM) on a Leica TCS SP8 microscope (Leica Microsystems, Germany). The microgels are incubated in PBS with FITC-dextran (1 mg/mL) via stirring for 48 h at room temperature. FRAP is performed using a 63x dry objective and an excitation wavelength of $\lambda = 488$ nm of an Argon-ion laser operating at 80% output power, while the emission is detected at a wavelength of $\lambda = 500 - 550$ nm. A circular region of interest (ROI) with a diameter of 10 μm is placed into the middle of the microgel. A series of images (512 x 512 pixels) is taken with an interval of 1.292 s using a highly attenuated laser beam (1.3% transmission). After recording 30 pre-bleach images, the ROI is bleached at maximum laser intensity (100% transmission) for 1.292 s and another 150 post-bleach images are taken.

The FRAP analysis was based on solving the diffusion equation in the Fourier domain and using that the inverse relative intensity (1-I_{rel}) follows the same differential equation, as the concentration.[379] Transforming the image stack to its spatial Fourier transform, we can collect information from the pixels closest to the center (zero spatial frequency component).

$$I_{rel} = \frac{(I - I_b)}{(I_0 - I_b)} \frac{I_{ref,0}}{I_{ref}}$$

$$c(q_x, q_y, t) = c_0(q_x, q_y)e^{-4\pi(q_x^2 + q_y^2)D\,t}$$

An algorithm was written for the analysis in python [https://www.python.org, https://scipy.org] fitting the individual spatial frequency components and the selected components together. This way we could detect if any spatial anisotropy occurred in the data set. This method allows us to obtain the diffusion coefficient independent of the bleaching profile as long as the spatial variation of the original concentration is low in comparison to that of the bleached area.

To determine the diffusion of antibody mimicking dextran, the microgels are incubated in PBS with fluorescein amine dextran (70 kDa) with a concentration of 1:1 related to the glycidyl groups via stirring for 24 h to 96 h at room temperature. Microgels are washed five times with PBS and imaged using CLSM as described above using a 63x dry objective. An excitation wavelength of $\lambda = 488$ nm of an Argon-ion laser operating at 25% output power and an emission wavelength of $\lambda = 500 - 550$ nm are employed.

Confocal Fluorescence microscopy and Fluorescence lifetime imaging microscopy (FLIM) is performed using Confocal Laser Scanning Microscopy (CLSM) on a Leica TCS SP8 microscope (Leica Microsystems, Germany). Alexa488 labelled TNFα (custom synthesis TNFα protein conjugated with AlexaFluor 488, Thermo Fisher Scientific, USA) is used as donor and Alexa546 labelled TNFα antibody (Amgevita - Adalimumab (Amgen®, Germany)), Thermo Fisher Scientific, USA) as acceptor. An excitation wavelength of $\lambda = 488$ nm as well as a $\lambda = 488$ nm notch filter are used in front of the detector. The detection band is restricted from 500 nm to 540 nm with a multiband spectrophotometer. A Single Molecule Detection Hybrid Detector (SMD HyD) in combination with PicoHarp 300 Time-Correlated Single Photon Counting (TCSPC) module has been used to acquire the FLIM decay curves. The decay curves are fitted with a n-Exponential Reconvolution fitting model of SymPhoTime 64 (PicoQuant, Germany) software where the experimental IRF of the instrument was fitted. The IRF was measured in the same excitation-emission conditions of the FRET samples with a solution of fluorescein quenched with KI. For the intensity-based Fluorescence images an HCX PL Fluotar 5x/0.15 dry objective was used and for the FLIM images a HC PL APO 63x/1.30 glycerol objective was used to record 512x512 pixels images with a pixel size of 60 nm (64x64 with a pixel size of 500 nm for the donor solution). All measurements were realized at a room temperature of 22.5 °C.

3.4.6 Mechanical properties of microgels

The mechanical properties of the microgels with different amounts of GMA are quantified with the high-throughput mechanical screening Nanoindenter Pavone (Optics11Life, Amsterdam, The Netherlands). For each type, a minimum number of 10 microgels are measured. The indentation measurements are performed using a cantilever-based probe with a spherical tip radius of 9.5 µm and a cantilever stiffness of 0.31 N/m. The indentation speed is set to 1 µm/s and the indentation depth to 1 µm. The effective Young's modulus

E (kPa) is determined by fitting the load-indentation curves using the Hertzian model.[380] All measurements are performed in PBS at a room temperature.

3.4.7 Quantification of TNFα antibody in the microgels

Glycidyl equipped microgels are incubated with different concentrations of TNFα antibody for 96 h at room temperature. Subsequently, microgels are washed three times with fresh 1xPBS to remove the excess of non-bound antibody. To quantify the amount of TNFα antibody bound to the microgels a CBQCA Protein quantification kit (ThermoFisher Scientific) is used according to the manufacturer's instructions. Briefly, a fixed number of microgels is diluted in a final volume of 135 µL reaction buffer, 5 µL potassium cyanide are added and the reaction is started by the addition of 10 µL ATTO-TAG CBQCA reagent with a working concentration of 2 nM. Both, bovine serum albumin (BSA) and TNFα antibody are used to prepare standard curves as suggested by the manufacturer. Read out is performed by a BioTek Cytation 3 plate reader (BioTek Instruments GmbH, Bad Friederichshall, Germany) by measuring the fluorescence emission at $\lambda = 550$ nm with excitation at $\lambda = 465$ nm.

3.4.8 TNFα binding experiments

Microgels (100 µg = 200,000 microgels/mL) are incubated with different concentrations of recombinant human TNFα (R&D Systems) for 1 h at 37 °C. Subsequently, samples are centrifuged for 10 min at 3000 rpm and the concentration of TNFα in supernatant is measured by an ELISA kit according to the manufacturer's instructions (R&D Systems).

3.4.9 Cell experiments (HT29)

The human colorectal adenocarcinoma HT29 cells (ATCC HTB38) are cultured in T75 cell culture flasks (Greiner Bio-One GmbH, Frickenhausen, Germany) in RPMI-1640 cell culture medium containing 1% (v/v) penicillin-streptomycin and 10% (v/v) fetal bovine serum. The cells are kept at 37 °C, 5% CO_2 and 95% O_2 in a humidified incubator (Heracell 150i CO_2 incubator, Thermo fischer scientific). Cells are seeded in 6 well plates at a density

of 500,000 cells per well and allowed to grow to approx. 80% confluency overnight. Next day, cells are stimulated with TNFα alone, TNFα and microgels, or microgels alone for 24 h at 37 °C. Supernatant is collected and kept at -80 °C until use. Cells are washed with cold PBS to remove the media and harvested in 500 µL cold PBS using a cell scraper. After centrifugation the supernatant is removed, and the cell pellet is kept at -80 °C.

3.4.10 Protein isolation and western blot (COX II)

Proteins are isolated with 1% NP40 lysis buffer containing protease inhibitor, phosphatase inhibitor, and DTT and the protein concentration is quantified applying a Bradford protein assay (BioRad) according to the manufacturer's instructions. The absorbance is measured using a plate reader (BioTek Instruments GmbH) at a wavelength of $\lambda = 450$ nm. Extracted proteins are separated using SDS-PAGE, transferred to Polyvinylidene difluoride (PVDF) membranes, and incubated with a specific antibody against cyclooxygenase-II (COX II) (Santa Cruz Biotechnology) or an antibody against β-Actin (Sigma) as control. Following washing, a horseradish peroxidase (HRP)-conjugated secondary antibody (Life Technologies) is used, and the desired protein is visualized by use of enhanced chemiluminescence reagent (GE Healthcare).

3.4.11 IL8 ELISA

The IL8 ELISA (R&D systems, Minneapolis, Germany) is used according to the manufacturer's instructions with slight modifications. 96 well plates are coated with 50 µL of the provided capture antibody, diluted in PBS overnight at 4 °C. Next day, the plates are washed with washing buffer consisting of PBS with 0.05% Tween 20, followed by blocking with 5% BSA in PBS for 1 h at room temperature to avoid unspecific binding. Subsequently, 50 µL of sample or standards, diluted in PBS containing 1% BSA (v/w), are pipetted into the wells and incubated at 4 °C overnight. Next day, samples are removed, the plate is washed and 50 µL of biotin conjugated detection antibody, diluted in PBS with 1% BSA (v/w), is pipetted into each well and incubated for 1 h at room temperature. Plates are washed, and each well is exposed to 50 µL streptavidin HRP for 40 min at room temperature. After washing, 100 µL TMB substrate solution is added per well to induce

color change. After 10 min, the reaction is stopped by adding 50 μL 2N H_2SO_4. Read out is performed by a BioTek Cytation 3 plate reader (BioTek Instruments GmbH, Bad Friederichshall, Germany) at $\lambda = 450$ nm absorbance.

3.4.12 Macrophage isolation and scavenging experiments

Monocytes are isolated from buffy coats provided by the transfusion medicine department of University hospital RWTH Aachen. The blood is diluted with PBS in a 1:1 ratio and a Ficoll-based density gradient centrifugation is performed for 1 h at room temperature without the use of the brake as described earlier.[381] Serum of the corresponding donors is heat-inactivated for 1 h at 57 °C.

To isolate monocytes for macrophage culture, the isolated Peripheral Blood Mononuclear Cells (PBMCs) are placed on 2 cm petri dishes at a density of 2 million cells per mL at a total volume of 2 mL per well. The incubation took place in RPMI cell culture medium containing 5% (v/v) human autologous serum for up to maximal 40 min and is carried at 37 °C in a humidified incubator (5% CO_2). During the incubation, monocytes adhered to the petri dish, while leucocytes remained in the supernatant and are removed by subsequent washing with pre-warmed cell culture media. Monocytes are differentiated to macrophages by culturing them 6 days in RPMI cell culture medium containing 5% (v/v) human autologous serum.

Macrophages are stimulated with cell culture medium alone (negative control), LPS alone, LPS and 100 μg/mL microgels, or only microgels for 24 h in a humidified incubator at 37 °C. Supernatant is collected and frozen at -80 °C until use. TNFα is measured with a TNFα ELISA kit (R&D systems) as described above. To harvest cells, they are washed by cold PBS and detached by use of a cell scraper.

3.4.13 Statistical analysis

Statistical analysis is performed with Origin 2018, graph pad prism 8 and ImageJ. Statistical significance is performed using two-way ANOVA with Tukey´s test for multiple comparison. Asterisks are used to highlighted following two-tailed P values: ns = non-significant = $P > 0.05$, *$P < 0.05$, **$P < 0.01$, ***$P < 0.001$, ****$P < 0.0001$.

4 Hyaluronic acid-functional microgels bind to CD44 receptor-expressing human colorectal adenocarcinoma cells

Yonca Kittel, Sarah Boesveld, Katrin Selzner, Matthias Mork, Céline Bastard, Theresa Bosserhoff, Pavel Strnad, Laura De Laporte, Alexander J. C. Kuehne

4.1 Introduction

Healthy cells are typically surrounded by a glycocalyx.[382,383] In the intestinal epithelia it is an approximately 0.3 µm thick complex layer found at the apical surface of the cells, which does not only generate a physical and biochemical barrier between external environment and the epithelium, but also creates space for adsorption and final step digestion.[382–384] The glycocalyx, which is composed of different mucins, is covered by a layer of loose mucus, mainly mucin II that serves as a nutrition source for the commensal microbiota.[382] Mucins show viscoelastic, hydrogel-like characteristics and play an important role in maintaining the gut homeostasis.[39] Glycocalyx and mucus layer actively select nutrient and drug intake, regulate the microbiome, and keep the epithelium protected from the attack of pathogens.[385] During an acute intestinal inflammation as it occurs during inflammatory bowel disease (IBD), intestinal dysbiosis and epithelial dysregulation lead to epithelial barrier dysfunction resulting in decreased transepithelial resistance and increased permeability of the mucosa.[2,3] IBD affects approximately 2.5 million patients in Europe, with rising incidence.[2,3] The disease is incurable and predisposes to colorectal cancer. Therefore, the restoration of intestinal barrier functions by mucosal healing via targeted therapy has recently attracted the attention of the researchers.[386–388]

CD44 is a single-chain transmembrane glycoprotein that is highly overexpressed by intestinal cells during colitis, making it an effective target in IBD therapy.[389] Importantly, hyaluronic acid (HA), a biocompatible, biodegradable natural anionic polysaccharide and a major component of the extracellular matrix (ECM), specifically binds to CD44 receptor.[91] Colon-targeted HA-based carrier systems such as nanoparticles, cubosomes, and nanogels have been designed to release drugs specifically in the inflamed area of the intestine and protect encapsulated agents against the harsh environmental conditions of the gastrointestinal tract, such as low pH and enzyme degradation.[89,390,391] However, due to

the small sizes of these carrier systems, they are often taken up by cells, such as activated macrophages. Moreover, nanoparticles are solid particles that can release drugs but are not suitable to shield the cells and thereby reduce the exposure to proinflammatory antigens and bacteria.[89] Given that a diminished mucus layer and epithelial damage are the hallmark of active IBD,[2] the aim of our project is to develop microgels that will specifically bind to inflamed intestinal cells and protect intestinal areas with a compromised mucus barrier.

Here, we develop 4-arm poly(ethylene glycol) (PEG)-HA copolymerized microgels for active CD44-receptor targeted binding to human colorectal adenocarcinoma cells to form a protective layer for intestinal cells as they occur in inflammatory bowel disease (IBD). Microgels with diameters of ≈ 30 μm are produced via free radical polymerization (FRP) using acrylate functional polymers in multi-channel high-throughput microfluidics. Our microgels show good adhesion on CD44-expressing human colorectal adenocarcinoma cells HT29.

4.2   Results and Discussion

4.2.1   Bulk hydrogels

Before investigating the adhesion of PEG-HA microgels to human colorectal adenocarcinoma cells, the mechanical properties of bulk hydrogels are characterized via rheology (see Figure 4.1). Pre-polymer solutions are prepared from 4-arm PEG acrylate (sPEG-Ac) (10 kDa) and HA-acrylate (HA-Ac) with a total polymer mass concentration of 10 wt% or 5 wt%. Due to the limited solubility of HA-Ac in water, its concentration is chosen up to the highest possible, which is 0%, 1%, 3%, 5% and 0%, 5%, and 10% for a total polymer mass concentration of 10 wt% and 5 wt%, respectively. Two different molecular weights of HA-Ac of 50 kDa and 250 kDa are chosen as these are known to exhibit good biocompatibility, viscoelasticity, and mucoadhesion.[88] HA can form non-covalent, supramolecular hydrogen bonds between the polysaccharide chains, introducing more viscous properties to the microgels.[102] However, to covalently crosslink the HA-Ac with the 4-arm PEG-Ac polymer during microgel synthesis, but still enable the formation of supramolecular hydrogen bonds, HA-Ac with a low degree of substitution (DoS) of acrylate groups of 1% and 5% is used.

Bulk hydrogels are crosslinked via FRP using 25 mol% of the photoinitiator lithium phenyl-2,4,6-trimethylbenzoylphosphinate (LAP) with respect to the reactive acrylate groups in solution, activated with a UV dose of 3 mW cm^{-2}. The suitable LAP concentration for this system has been determined in microfluidic experiments as shown in Figure 4.2. In general, a higher storage modulus G' is observed for hydrogels exhibiting higher mass concentration of 10 wt% compared to 5 wt% (see Figure 4.1). For both concentrations, G' decreases with increasing HA-Ac concentration. However, this effect is more dominant for microgels made from HA-Ac with a DoS of acrylate groups of 1%. For microgels produced from HA-Ac with a DoS of acrylate groups of 5%, no significant difference of G' can be observed for HA-Ac with a molecular weight of 250 kDa. This is probably, due to higher number of covalent crosslinks compared to polymer network produced from DoS of 1%. Furthermore, higher molecular weight of HA-Ac (250 kDa) probably leads to more entanglement and less diffusion compared to lower molecular weight HA-Ac (50 kDa) leading to stiffer bulk hydrogels. For the 10 wt% pre-polymer solution, G' is not significantly different between 1% and 0% HA-Ac. Therefore, pre-polymer solution with 1% HA-Ac is not used for further experiments.
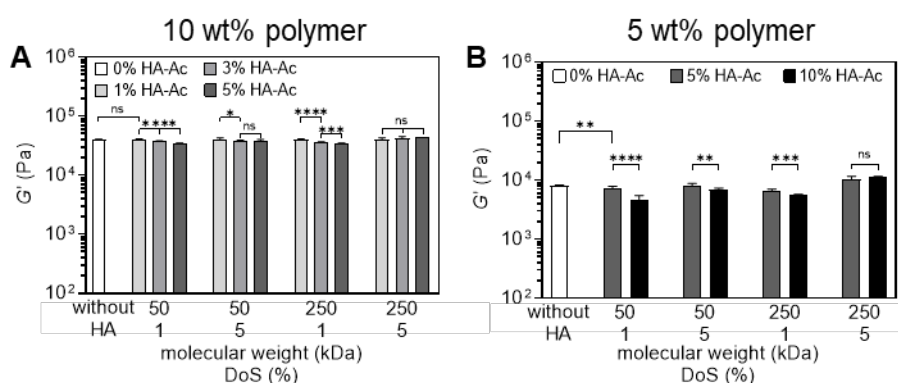
Figure 4.1: Characterization of pre-polymer solution via rheology. Bulk mechanical properties of hydrogels prepared from aqueous pre-polymer solutions with total polymer mass concentration of A) 10 wt% and B) 5 wt% containing 4-arm PEG-Ac (10 kDa), HA-Ac with different molecular weight (50 kDa and 250 kDa), a DoS of acrylate groups (1% and 5%), and the HA-Ac concentration in the pre-polymer solution with 25 mol% LAP is measured via rheology at room temperature. Data are presented as mean ± standard deviation, $n = 3$. Statistical significance is performed using one-way ANOVA with Tukey´s test: ns = non-significant = $P > 0.05$, *$P < 0.05$, **$P < 0.01$, ***$P < 0.001$, ****$P < 0.0001$.

4.2.2   Microgel synthesis and characterization

After characterization of the bulk mechanical properties of pre-polymer solutions, we use the analyzed solutions to produce spherical uniform microgels using flow-focusing microfluidic technique. The microgels exhibit a diameter of approximately 30 µm to

prevent cellular uptake. In comparison to the microfluidic system described in Chapter 3, a multichannel microfluidic chip with 100 channels is used to produce microgels with much higher production rates. Monodisperse droplets are formed using a dispersed phase consisting of aqueous solution of 4-arm PEG-Ac (10 kDa), HA-Ac, and photoinitiator LAP and the continuous phase consisting of NovecTM HFE 7500 with 1.5 vol% of KrytoxTM 157 FSH surfactant (see Scheme 4.1). The collected droplets are crosslinked via FRP using UV light at a wavelength of $\lambda = 365$ nm and a dose of 274 mW cm^{-2} to form stable microgels. The microgels are purified as described in Section *Materials and Methods* section.
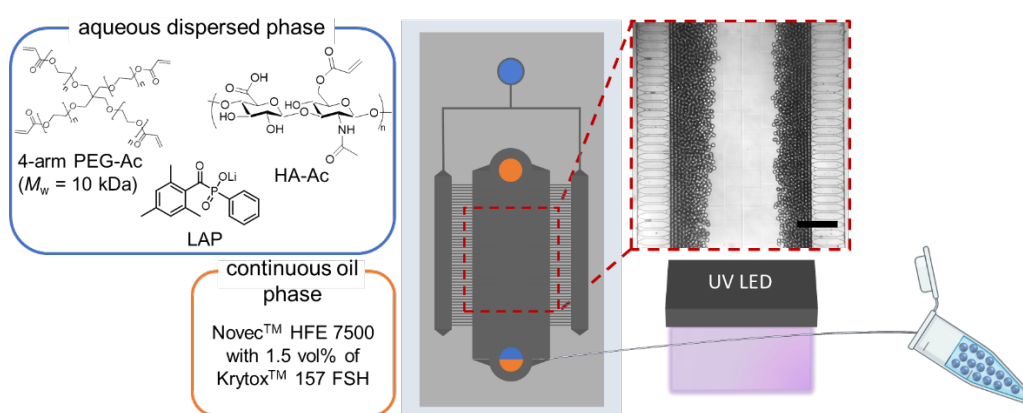
Scheme 4.1: Schematic representation of multi-channel microfluidic set-up. Dispersed aqueous phase consists of Novec HFE 7500 (a fluorinated ether) with 1.5 vol% of Krytox 157 FSH as a stabilizing agent. Continuous oil phase consists of 4-arm PEG-Ac (10 kDa), HA-Ac with different concentration, molecular weight (50 kDa and 250 kDa) and DoS of acrylate groups (1% and 5%), and LAP as photoinitiator. Droplets are UV irradiated to form stable PEG-HA microgels. Scale bar represents 100 μm.

4.2.2.1 Suitable LAP concentration

To achieve sufficient rapid gelation of the microgels, the suitable LAP concentration for this is determined. Therefore, sPEG-Ac microgels with a total polymer mass concentration of 10 wt% and without the use of HA-Ac are produced using LAP concentrations between 1 mol% and 100 mol% related to the reactive acrylate groups of sPEG-Ac in microfluidics under constant experimental parameters. Furthermore, the pre-polymer solutions are either used as prepared or purged with nitrogen (N$_2$) to investigate the influence of oxygen on the polymerization reaction. The mechanical properties of the synthesized microgels are characterized via nanoindentation (see Figure 4.2). Microgels prepared from pre-polymer solutions that are used as prepared (not purged with N$_2$) show similar effective Young's

modulus (E_{eff}) for LAP concentrations between 25 mol% and 100 mol%. Lower LAP concentrations did not lead to stable microgels. However, when the pre-polymer solution is purged with N_2 for synthesis, lower LAP concentration up to 3 mol% lead to the formation of stable microgels. This is probably due to the presence of oxygen in the unpurged pre-polymer solutions that can react as a radical and inhibit the radical polymerization. Furthermore, the microgels exhibit increasing E_{eff} with increasing LAP concentration from 3 mol% to 12.5 mol%. This is expected as lower LAP concentration results in lower number of reactive radicals to start the polymerization. Therefore, longer polymer chains need to be formed to build a stable network. Due to the use of star-shaped polymer, there are probably more dangling polymer chains, as there are not enough radicals to start a new reactive chain for propagation at lower LAP concentration leading to softer network. For LAP concentration higher than 25 mol% for both conditions, purged and not purged with N_2, there is a higher number of radicals that can start the polymerization reaction with a higher number of reactive chain ends of the star-shaped polymer and form a higher branched, stable network. Further increase of the LAP concentration up to 100 mol% does not affect the E_{eff}, which can be explained by a higher number of termination reactions. In general, comparing the E_{eff} of microgels prepared from pre-polymer solutions that were purged and not-purged with N_2 at the same LAP concentration, microgels prepared from pre-polymer solutions that were purged with N_2 exhibit higher E_{eff}. This is expected as oxygen radicals can stop the chain propagation by termination of the polymerization reaction resulting in shorter, more dangling chains and thus less stable polymer network.
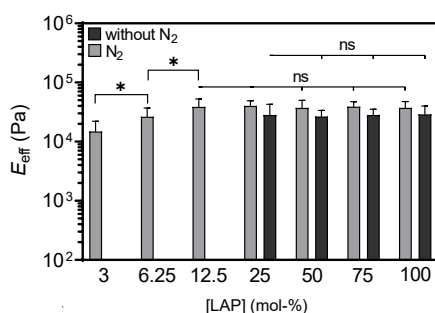
Figure 4.2: Suitable LAP concentration for microgel synthesis. Effective Young's modulus E_{eff} of microgels (4-arm PEG-Ac (10 kDa)) without HA-Ac containing different LAP concentrations between 1 mol% and 100 mol% per acrylate group in polymer solution is measured via nanoindentation. Pre-polymer solutions are either used as prepared (without N_2) or purged with N_2 for microfluidic synthesis. Data are presented as mean ± standard deviation, $n \geq 10$ microgels. Statistical significance is performed using one-way ANOVA with Tukey's test: ns = non-significant = $P > 0.05$, *$P < 0.05$.

In the following, to use a LAP concentration that is as low as possible, but also guarantee sufficient crosslinking, 25 mol% LAP is chosen for further experiments, while pre-polymer solutions are purged with N_2.
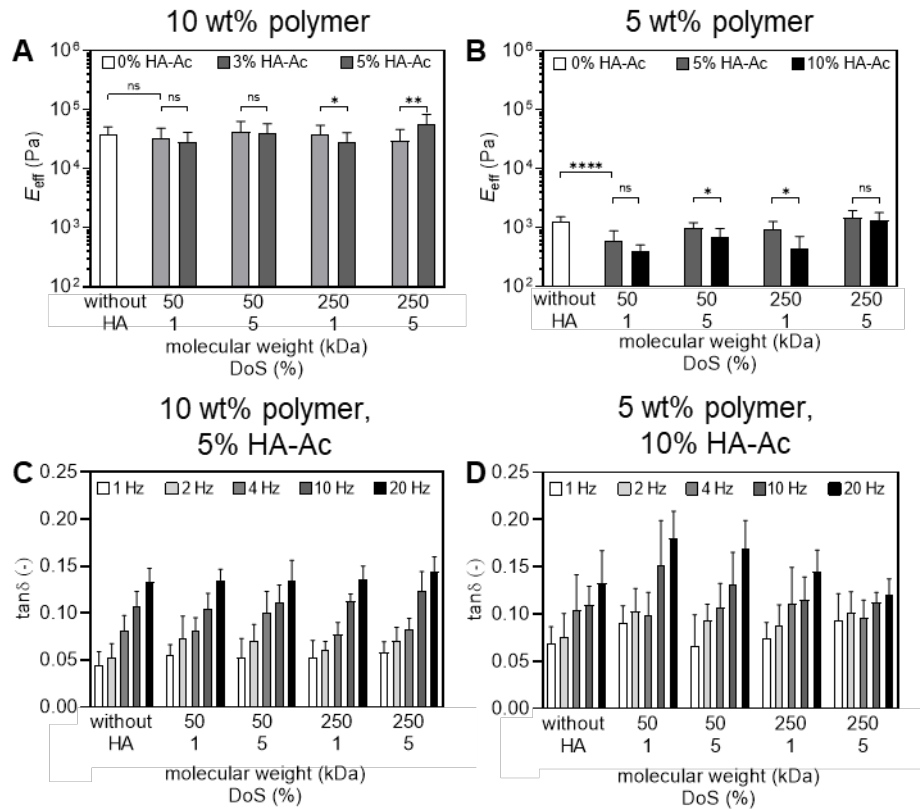
4.2.2.2 Characterization of PEG-HA microgels

To investigate the influence of incorporated HA in the microgels on the microgel-cell adhesion, we vary the molecular weight (50 kDa and 250 kDa), the DoS of acrylate groups (1% and 5%), and the HA-Ac concentration in the pre-polymer solution containing total polymer mass concentrations of 10 wt% and 5 wt%.

For the characterization of microgel-cell adhesion, the stiffness of the microgels is one of the most important properties to investigate as it can directly affect fundamental cellular processes.[96] Therefore, we characterize the influence of the different properties of HA-Ac on the mechanical properties of the microgels via nanoindentation (see Figure 4.3A and B). In general, similar trends are observed for the stiffness of the microgels as for the bulk hydrogels prepared from the same pre-polymer solutions. However, the influence of the HA-Ac on the mechanical properties of the material is less dominant for microgels compared to bulk hydrogels. PEG-HA microgels made from higher total polymer mass concentration (10 wt%) exhibit higher E_{eff} of around $30 - 60$ kPa compared to microgels made from 5 wt% ($0.4 - 1.3$ kPa). For microgels made from 5 wt% total polymer mass concentration, E_{eff} decreases with increasing HA-Ac concentration for HA-Ac (50 kDa, DoS = 5%) and HA-Ac (250 kDa, DoS = 1%). For microgels made from 10 wt%, a decrease of E_{eff} can only be observed when produced with HA-Ac (250 kDa, DoS = 1%). In fact, the difference of E_{eff} of microgels without HA-Ac and with HA-Ac is higher for microgels made from 5 wt% total polymer mass concentration. This is because these have higher HA-Ac ratio (4.5 wt% sPEG-Ac and 0.5 wt% HA-Ac (10%)) compared to microgels made from 10 wt% (9.5 wt% sPEG-Ac and 0.5 wt% HA-Ac (5%)) due to the limited solubility of HA-Ac in aqueous solution. The reason why a decrease of E_{eff} can only be seen for microgels made with HA-Ac (250 kDa, DoS = 1%) for 10 wt% is probably due to less covalent crosslinks with the PEG polymer network. Even though HA (50 kDa, DoS = 1%) has the same amount of reactive acrylate groups, shorter chain length probably leads to less entanglement, better diffusion, and enables more covalent crosslinks. Surprisingly, microgels made from 10 wt% total polymer mass concentration and HA-Ac

(250 kDa, DoS = 5%) show an increase of E_{eff} with increasing HA-Ac concentration from 3% to 5%. This is probably because HA-Ac with a DoS of acrylate groups of 5% forms more covalent crosslinks in the polymer network compared to HA-Ac with a DoS of acrylate groups of 1%. Furthermore, the higher molecular weight of HA-Ac of 250 kDa compared to 50 kDa probably leads to more entanglement and less diffusion of the HA chains leading to higher stiffness of the microgels.

Figure 4.3: Characterization of the mechanical properties of PEG-HA microgels via nanoindentation. Effective Young's modulus E_{eff} of PEG-HA microgels (4-arm PEG-Ac (10 kDa) and HA-Ac with different concentration, molecular weight (50 kDa and 250 kDa, and DoS of acrylate groups of 1% and 5%) containing different HA-Ac:sPEG-Ac ratio produced from total polymer mass concentration of A) 10 wt% and B) 5 wt% measured in Milli Q. Dynamic mechanical analysis (DMA) of microgels made from C) 10 wt% total polymer mass concentration and 5% HA-Ac and D) 5 wt% total polymer mass concentration and 10% HA-Ac at different oscillation frequencies from 1 Hz to 20 Hz. Tan δ describes the ratio between loss G'' and storage G' modulus, while tan δ = 0.05 – 0.20 indicates that the elastic part of the microgels is dominant. Data are presented as mean ± standard deviation, $n \geq 10$ microgels. Statistical significance is performed using one-way ANOVA with Tukey's test: ns = non-significant = $P > 0.05$, *$P < 0.05$, **$P < 0.01$, ****$P < 0.0001$.

ECMs, such as the intestinal mucus are viscoelastic.[39] In particular, the viscoelasticity of the microgels has an influence on microgel-cell interaction.[96] To characterize the viscoelastic properties, we measure G' and the loss modulus G'' of the microgels containing the highest possible concentration, different DoS of acrylate groups, and molecular weight of HA-Ac for total polymer mass concentrations of 10 wt% and 5 wt% via dynamic mechanical analysis (DMA) at different oscillation frequencies between 1 Hz and 20 Hz (see Figure 4.3C and D). Thereby, G' characterizes the elastic and G'' the

viscous character of the material.[392] The ratio between G'' to G' describes the loss factor tan δ that is used to evaluate the viscoelastic behavior of microgels. As a result, the material behaves more like a viscous liquid if $G'' > G'$ (tan δ > 1) and more like an elastic solid if $G' > G''$ (tan δ < 1).[393]

Even though microgels made from 5 wt% total polymer mass concentration exhibit higher HA-Ac ratio compared to microgels made from 10 wt%, no significant change of tan δ can be observed for both conditions. In general, tan δ is between 0.05 and 0.20 indicating that the elastic behavior is more dominant for all the different microgel conditions, which results from the covalent polymer network structure. In theory, the incorporation of HA-Ac should increase the viscous part of the material. However, when comparing tan δ of microgels made from total polymer mass concentration of 10 wt% without incorporated HA-Ac and polymerized with 5% HA-Ac, no difference can be observed. This is probably due to the low HA-Ac:sPEG-Ac ratio and thus more dominant covalent bonds compared to supramolecular bonds. Furthermore, tan δ slightly increases with increasing oscillation frequency from 1 Hz to 20 Hz. This effect can also be seen for microgels made from pure sPEG-Ac (0% HA-Ac). Slower motion, thus lower oscillation frequency leads to more flexible and mobile behavior of the polymer chains. With increasing oscillation frequency, the elastic portion of the viscoelastic behavior is comparably more dominant as the molecular network is less flexible and stiffer. This can be explained by the relationship between the chain segment movement and the change of the frequency.[392]

Additionally, we measure the E_{eff} as well as the viscoelastic properties of the microgels depending on the solvent, as we later use the microgels in cell media for the microgel-cell adhesion experiments. The incorporation of HA into the microgels introduces supramolecular hydrogen bonds whose formation is dependent from the salt concentration in the solvent and temperature.[394] We characterize the influence of media PBS, RPMI, and DMEM on the mechanical properties of PEG-HA microgels. Microgels made from 5 wt% were not stable in the different media and dissolved over time, probably due to their low stiffness (0.4 – 1.3 kPa in Milli Q). For this reason, microgels made from 5 wt% were not investigated in further characterization. For microgels synthesized from total polymer mass concentrations of 10 wt% without HA-Ac (0% HA-Ac), no significant difference of E_{eff} can be observed for the different media (see Figure 4.4A). Furthermore, the E_{eff} in different media is measured, exemplarily, for microgels made with 5% HA-Ac (250 kDa,

DoS = 1%). A decrease of E_{eff} is determined for microgels measured in both cell media RPMI and DMEM in comparison to the solvents Milli Q and PBS. HA exhibits negative charge on its carboxy group that can form hydrogen bonds with hydrogen present in water molecules. The addition of salt, as it is present in medium, results in the formation of ionic interactions between negatively charged carboxy groups and cations in medium. This leads to reduced formation of hydrogen bonds and, thus, less stable polymer network resulting in lower E_{eff}.
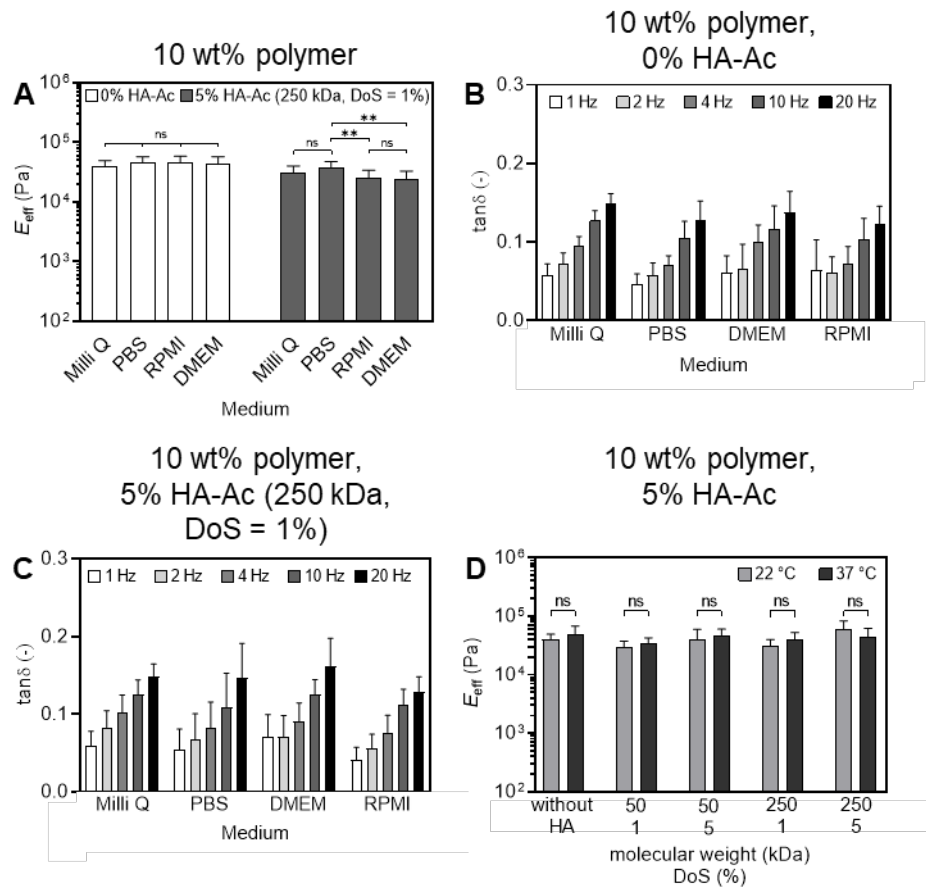
Figure 4.4: Characterization of the mechanical properties of PEG-HA microgels depending on the solvent and temperature. A) Effective Young's modulus E_{eff} of microgels made from 10 wt% total polymer mass concentration with 0% HA-Ac and 5% HA-Ac (250 kDa, DoS = 1%) in dependence of solvent PBS as well as cell media DMEM and PRMI. Dynamic mechanical analysis (DMA) of microgels made from 10 wt% total polymer mass concentration with B) 0% HA-Ac and C) 5% HA-Ac (250 kDa, DoS = 1%) at different oscillation frequencies from 1 Hz to 20 Hz. Tan δ describes the ratio between loss G'' and storage G' modulus, while tan δ = 0.05 – 0.20 indicates that the elastic part of the microgels is dominant. D) Effective Young's modulus E_{eff} of microgels made from 10 wt% total polymer mass concentration and 5% HA-Ac and measured at room temperature and physiological temperature of 37 °C. Data are presented as mean ± standard deviation, $n \geq 10$ microgels. Statistical significance is performed using one-way ANOVA with Tukey's test: ns = non-significant = $P > 0.05$, **$P < 0.01$, ****$P < 0.0001$.

Besides the stiffness, the viscoelastic properties of microgels made from 10 wt% total polymer mass concentration and 0% HA-Ac as well as 5% HA-Ac (250 kDa, DoS = 1%) is exemplarily shown in different media (see Figure 4.4B and C). Again, a slightly increase

of tan δ is observed with increasing oscillation frequency. However, no difference of tan δ can be observed between the two microgels for different media.

Furthermore, the mechanical properties of the PEG-HA microgels made from 10 wt% total polymer mass concentration and 5% HA-Ac is measured at physiological temperature of 37 °C (see Figure 4.4D). No significant difference of E_{eff} is observed for microgels made from 0% HA-Ac and 5% HA-Ac with different molecular weight and DoS of acrylate groups, measured at room temperature and 37 °C. Probably, the HA-Ac concentration is too low to measure an effect of the temperature on the E_{eff} of the microgels.

In a next step, to characterize the distribution of HA inside the microgels, we use fluorescently labelled FITC-HA-Ac (250 kDa, DoS = 1%) during microgel synthesis in microfluidics. The confocal image reveals a homogeneous distribution of the FITC-HA-Ac throughout the microgel network measured via CLSM (see Figure 4.5). Additionally, as a comparison, we use HA (250 kDa) without acrylate functionality introducing non-crosslinked entangled HA chains in the microgel network. The confocal images show a homogeneous distribution of the fluorescently labelled HA (250 kDa, DoS = 0%); however, a lower fluorescence intensity can be seen at the edge of the microgel (see Figure 4.5B). This is probably because the HA is entangled to the PEG polymer network inside of the microgel, but diffuses out at the surface.
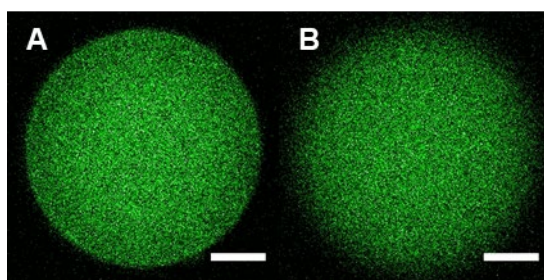
Figure 4.5: Confocal images of PEG-HA microgels (4-arm PEG-Ac (10 kDa)) with A) FITC-labelled 5% HA-Ac (250 kDa, DoS = 1%) and B) 5% HA-Ac (250 kDa, DoS = 0%) produced from total polymer mass concentration of 10 wt%. Scale bars represent 10 μm.

4.2.3 Cell culture

4.2.3.1 HA-functionalized microgels bind to human colorectal adenocarcinoma cells

First, the biocompatibility of PEG-HA microgels on human colorectal adenocarcinoma HT29 and TC7 cell lines is analyzed via MTT cell viability and proliferation assay (see Figure 4.6). As expected, a high viability of both cell lines in the presence of the microgels with different HA-Ac:sPEG-Ac ratios is observed for 24 h and 48 h. We already showed the high biocompatibility of PEG-based microgels functionalized with the cholera toxin binding domain towards HT29 cells.[71] All cells show a good proliferation confirmed by the MTT assay in the presence of the tested PEG-HA microgels, which is crucial for supporting the intestinal cells to recover during an acute inflammation as it occurs during IBD (see Figure 4.6). Here, three microgel conditions used for later cell binding tests are chosen for both assays using microgels prepared from 10 wt% total polymer mass concentration containing 0% HA-Ac, 5% HA-Ac (50 kDa, DoS = 1%), or 5% HA-Ac (250 kDa, DoS = 1%).
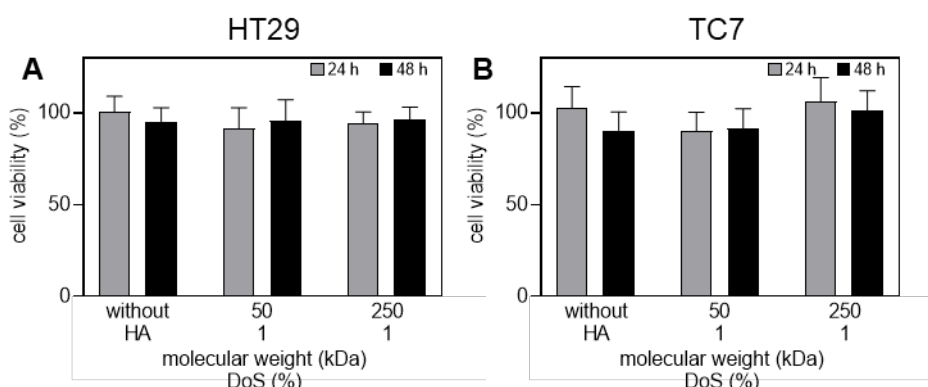
Figure 4.6: Cell viability and proliferation of A) HT29 and B) TC7 human colorectal adenocarcinoma cell lines are determined via MTT Proliferation Kit.

HA functionalized microgels are now tested in their ability to specifically bind CD44 expressing cells. To that end, the CD44 expression of both human intestinal adenocarcinoma cell lines TC7 and HT29 is characterized via flow cytometry analysis and real-time polymerase chain reaction (RT-PCR) analysis in the first step (see Figure 4.7). HT29 cells are often used as model cell lines to study the effectiveness of HA-based carrier systems as they express CD44.[89,390] As expected, HT29 cells show a high expression of CD44 compared to TC7 cells which are used as CD44 negative cells for the following experiments.
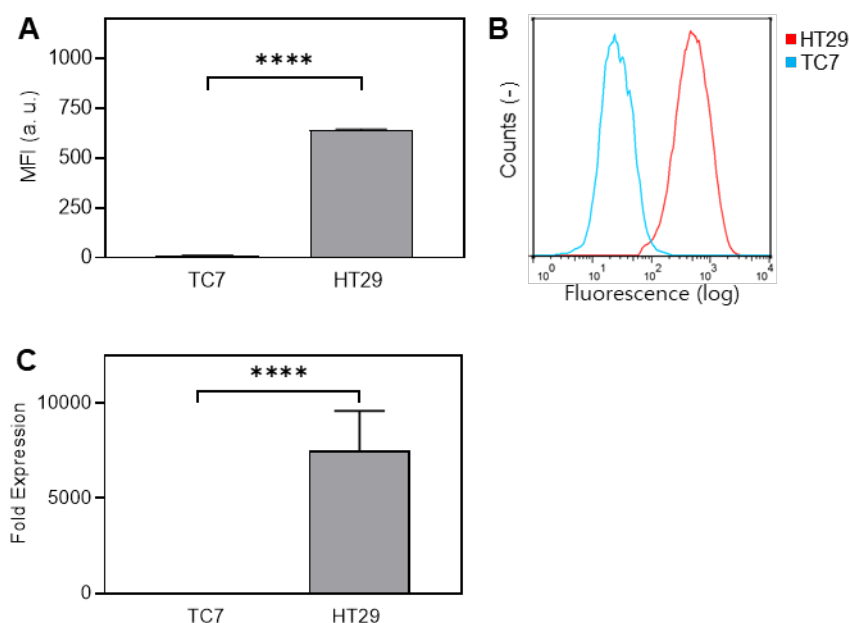
Figure 4.7: CD44-receptor expression of human colorectal adenocarcinoma cell lines TC7 and HT29. Flow cytometry analysis. A) shows the mean fluorescence intensity (MFI) of cells, incubated with a FITC-labelled CD44 antibody and B shows the corresponding flow cytometry shifts in fluorescence. C) Real-time polymerase chain reaction (RT-PCR) to determine mRNA levels of CD44 in TC7 and HT29 cells. β-Actin was used as an internal control. Data are presented as mean ± standard deviation, $n \geq 3$. Statistical significance is performed using one-way ANOVA with Tukey´s test for multiple comparisons: ****$P < 0.0001$.

To characterize the ability of PEG-HA microgels to bind to CD44 expressing cells, microgels containing different HA-Ac concentration, DoS, and molecular weight were incubated for 3 h at 37 °C with both cell lines HT29 and TC7. Subsequently, microgels are washed off and the remaining, adhered microgels are counted. In preliminary experiments, microgels containing 3% HA-Ac with a DoS of 5% and molecular weight of 50 kDa and 250 kDa, respectively, showed very low cell attachment on both cell lines (data not shown). Therefore, cell binding experiments were reproduced with microgels containing 0% HA-Ac as a negative control, as well as 5% HA-Ac with a DoS of 1% and molecular weight of 50 kDa and 250 kDa, respectively (see Figure 4.8). Microgels produced without HA-Ac do not show cell binding for both cell lines HT29 and TC7. Furthermore, microgels produced with 5% HA-Ac (50 kDa, DoS = 1%) almost show no binding for both cell lines. However, the incorporation of higher molecular weight HA-Ac (250 kDa, DoS = 1%) show significantly higher cell binding (45% of the microgels bound) for the CD44 expressing HT29 cells. As expected, no cell attachment can be observed for these microgels for TC7 cells.
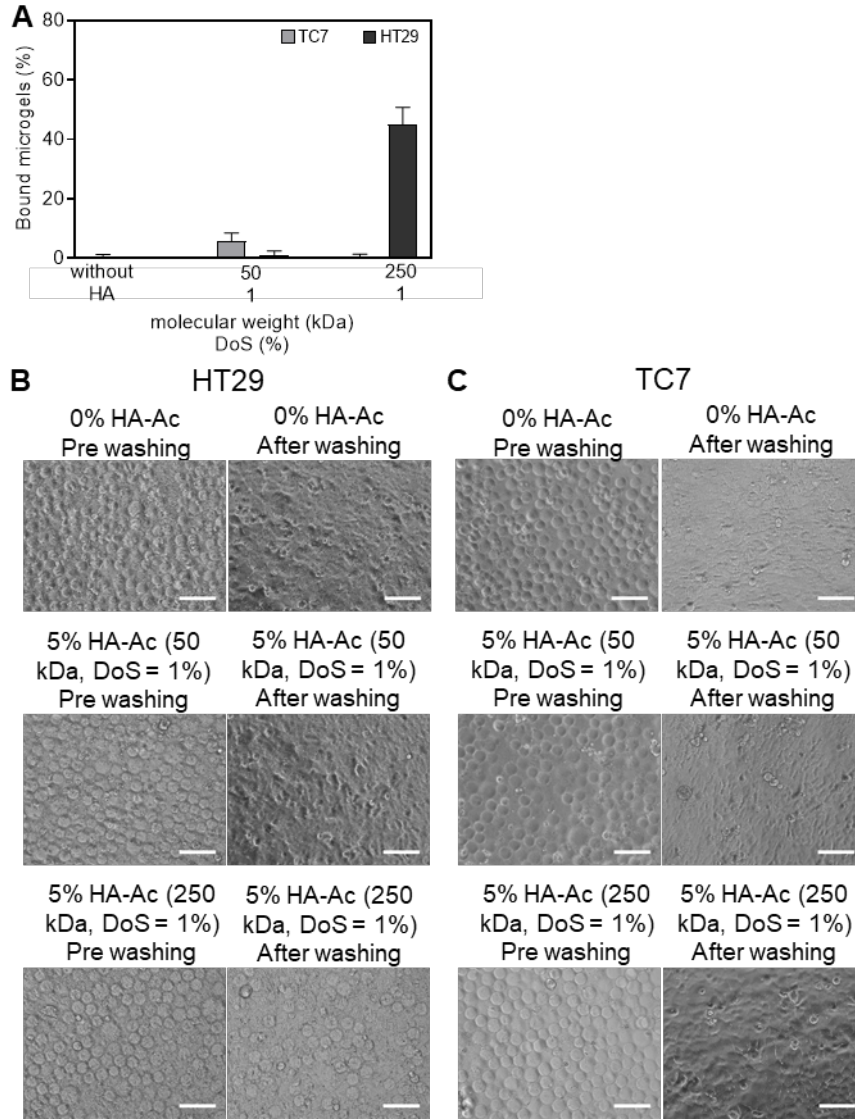
Figure 4.8: Microgel-cell adhesion on human colorectal adenocarcinoma cell lines HT29 and TC7. A) Bound PEG-HA microgels produced from 10 wt% total polymer mass concentration and 5% HA-Ac with DoS of 1% and molecular weight of 50 kDa and 250 kDa on both cell lines. PEG-HA microgels are incubated for 3 h at 37 °C on the cells and washed two times with media. Data are presented as mean ± standard deviation, $n = 3$. Brightfield images of microgels before (pre) washing and bound microgels after 3x washing on B) HT29 and C) TC7 cell lines. Scale bars represent 100 µm.

4.3 Conclusion

In conclusion, we show that our PEG-HA microgels are able to bind to CD44-receptor expressing human intestinal adenocarcinoma cells HT29. We synthesized PEG-HA microgels with a multi-channel high-throughput microfluidic system with higher production rates. We optimized the total polymer mass concentration as well as determined the optimal concentration, DoS of acrylate groups, and molecular weight of the incorporated HA-Ac inside the microgels. Our PEG-HA microgels demonstrate a first

approach for the protection of the damaged mucus barrier during inflammatory bowel diseases. In the next step, we would like to perform the cell-microgel binding in flow to be able to generate a reliably reproducible system. Furthermore, we plan to apply the microgels in the DSS colitis mouse model which represents an established IBD model to show the adhesion of microgels to inflamed intestinal cells *in vivo*. Furthermore, the HA functionality of microgels can be combined with our previously published anti-TNFα functionalized microgels[395] to scavenge the pro-inflammatory cytokine TNFα as a targeted multifunctional approach for local treatment of IBD.

4.4 Materials and Methods

4.4.1 Chemicals, Cells Lines, and Cell Culture Material

The following materials are purchased and used as per the instruction. 4-arm PEG acrylate 10 kDa (Biopharma PEG, ≥95%), Dulbecco's modified Eagle medium (DMEM, PAN-Biotech), ethanol absolute (Sigma Aldrich, >99.8%), hyaluronate acrylate (M_W = 50 kDa, DoS = 1%, Creative PEGWorks, >95%), hyaluronate acrylate (M_W = 50 kDa, DoS = 5%, Creative PEGWorks, >95%), hyaluronate acrylate (M_W = 250 kDa, DoS = 1%, Creative PEGWorks, >95%), hyaluronate acrylate (M_W = 250 kDa, DoS = 5%, Creative PEGWorks, >95%), hyaluronate fluorescein (M_W = 250 kDa, DoS = 0%, Creative PEGWorks, >95%), hyaluronate acrylate fluorescein (M_W = 250 kDa, DoS = 1%, Creative PEGWorks, >95%), Krytox[TM] (Indoment), 3M[TM] Novec[TM] 7500 (3M[TM], > 99%), lithium phenyl-2,4,6-trimethylbenzoylphosphinate (Sigma Aldrich, ≥95%), MTT cell proliferation assay kit (Cayman Chemical), phosphate buffered saline (PBS, *p*H = 7.4 and *c* = 1x, Lonza), RPMI 1640 medium 1x (Thermo Fisher Scientific), SYLGRAD[TM] 184 silicone elastomer kit (Dowsil), TrypLE™ Express (Thermo Fischer).

4.4.2 Preparation of PDMS-based microfluidic devices

PDMS-based microfluidic chips are prepared via soft lithography. Therefore, a microfluidic master for high-throughput microgel production containing 100 parallel channels with a height of 10 µm and width of 5 µm at the cross section is used. SYLGRAD[TM] 184 silicone elastomer (PDMS) and curing agent are mixed and degassed in

104

a ratio of 10:1 in a plastic cup using a conditioning mixer (THINKY ARE – 250, Nivelles, Belgium) for 4 min at 2000 rpm. After pouring the mixture on the microfluidic master, it is placed in the desiccator (10^{-3} mbar) to remove entrapped air. The PDMS is cured for 10 h at 60 °C. The PDMS-chip is demoulded, and holes are punched (biopsy puncher, inner diameter 0.75 mm) for inlets and outlets in the channel. The PDMS chip is rinsed three times with *iso*-propanol and water. Moreover, a glass slide (76 x 52 x 1 mm, Marienfeld, Germany) is washed three times with acetone, *iso*-propanol, and water. To bond the PDMS chip on the structured side of the glass, both are activated in an oxygen plasma oven (PVA TePla 100E, Wettenberg, Germany) at an oxygen flow of 28 mL min^{-1} for 40 s at 100 W. The microfluidic chip is baked in the oven for 10 h at 60 °C. Before using in microfluidics, the channels are surface-coated via rinsing with hydrophobic for 2-5 min. Afterwards, the channels are purged with air.

4.4.3   Preparation of pre-polymer solutions

To prevent undesired photoinitiation, all pre-polymer solutions are prepared in brown glass vials. First, aqueous solutions of hyaluronate acrylate (HA-Ac) derivates are prepared using a vortex mixer (Heathrow Scientific™ Vortexer™, Schwerte, Germany) for mixing the solutions for 30 min and 2 h for HA-Ac with molecular weight of 50 kDa and 250 kDa and DoS of 1% and 5%, respectively.

For the preparation of pre-polymer solutions, 4-arm PEG acrylate (sPEG-Ac) ($M_W = 10$ kDa) is added to the aqueous solution of HA-Ac ($M_W = 50$ kDa, DoS = 1%; 50 kDa, DoS = 5%; 250 kDa, DoS = 1%; or 250 kDa, DoS = 5%) to obtain a total polymer concentration of 10 wt% or 5 wt% using 25 mol% lithium phenyl-2,4,6-trimethylbenzoylphosphinate (LAP) photoinitiator with respect to the reactive acrylate groups (see Table 4.1-4.4). Absolute concentrations of pre-polymer solutions used for the determination of suitable LAP concentration for the production of bulk hydrogels and microgels in microfluidics is shown in Table 4.5.

Table 4.1: Absolute concentrations of polymer solutions (10 wt%) containing 4-arm PEG-Ac (10 kDa), HA-Ac (50 kDa), and 25 mol% LAP that are used for rheology measurements and production of microgels in microfluidics.

4-arm PEG-Ac (%)	HA-Ac (%)	DoS HA-Ac (%)	c(4-arm PEG-Ac) (mol/mL)	c(4-arm PEG-Ac) (mg/mL)	c(HA-Ac) (mol/mL)	c(HA-Ac) (mg/mL)	c(LAP) (mol/mL)	c(LAP) (mg/mL)
95	5	1	$9.5 \cdot 10^{-6}$	95	$1 \cdot 10^{-7}$	5	$9.53 \cdot 10^{-6}$	2.80
97	3	1	$9.7 \cdot 10^{-6}$	97	$6 \cdot 10^{-8}$	3	$9.72 \cdot 10^{-6}$	2.86
99	1	1	$9.9 \cdot 10^{-6}$	99	$2 \cdot 10^{-8}$	1	$9.91 \cdot 10^{-6}$	2.91
95	5	5	$9.5 \cdot 10^{-6}$	95	$1 \cdot 10^{-7}$	5	$9.64 \cdot 10^{-6}$	2.84
97	3	5	$9.7 \cdot 10^{-6}$	97	$6 \cdot 10^{-8}$	3	$9.78 \cdot 10^{-6}$	2.88
99	1	5	$9.9 \cdot 10^{-6}$	99	$2 \cdot 10^{-8}$	1	$9.92 \cdot 10^{-6}$	2.92
100	0	0	$1 \cdot 10^{-5}$	100	-	-	$1 \cdot 10^{-5}$	2.94

Table 4.2: Absolute concentrations of polymer solutions (10 wt%) containing 4-arm PEG-Ac (10 kDa), HA-Ac (250 kDa), and 25 mol% LAP that are used for rheology measurements and production of microgels in microfluidics.

4-arm PEG-Ac (%)	HA-Ac (%)	DoS HA-Ac (%)	c(4-arm PEG-Ac) (mol/mL)	c(4-arm PEG-Ac) (mg/mL)	c(HA-Ac) (mol/mL)	c(HA-Ac) (mg/mL)	c(LAP) (mol/mL)	c(LAP) (mg/mL)
95	5	1	$9.5 \cdot 10^{-6}$	95	$1 \cdot 10^{-7}$	5	$9.53 \cdot 10^{-6}$	2.80
97	3	1	$9.7 \cdot 10^{-6}$	97	$6 \cdot 10^{-8}$	3	$9.72 \cdot 10^{-6}$	2.86
99	1	1	$9.9 \cdot 10^{-6}$	99	$2 \cdot 10^{-8}$	1	$9.91 \cdot 10^{-6}$	2.91
95	5	5	$9.5 \cdot 10^{-6}$	95	$1 \cdot 10^{-7}$	5	$9.64 \cdot 10^{-6}$	2.84
97	3	5	$9.7 \cdot 10^{-6}$	97	$6 \cdot 10^{-8}$	3	$9.78 \cdot 10^{-6}$	2.88
99	1	5	$9.9 \cdot 10^{-6}$	99	$2 \cdot 10^{-8}$	1	$9.92 \cdot 10^{-6}$	2.92

Table 4.3: Absolute concentrations of polymer solutions (5 wt%) containing 4-arm PEG-Ac (10 kDa), HA-Ac (50 kDa), and 25 mol% LAP that are used for rheology measurements and production of microgels in microfluidics.

4-arm PEG-Ac (%)	HA-Ac (%)	DoS HA-Ac (%)	c(4-arm PEG-Ac) (mol/mL)	c(4-arm PEG-Ac) (mg/mL)	c(HA-Ac) (mol/mL)	c(HA-Ac) (mg/mL)	c(LAP) (mol/mL)	c(LAP) (mg/mL)
90	10	1	$4.5 \cdot 10^{-6}$	45	$1 \cdot 10^{-7}$	5	$4.53 \cdot 10^{-6}$	1.33
95	5	1	$4.75 \cdot 10^{-6}$	47.5	$5 \cdot 10^{-8}$	2.5	$4.76 \cdot 10^{-6}$	1.40
90	10	5	$4.5 \cdot 10^{-6}$	45	$1 \cdot 10^{-7}$	5	$4.64 \cdot 10^{-6}$	1.37
95	5	5	$4.75 \cdot 10^{-6}$	47.5	$5 \cdot 10^{-8}$	2.5	$4.28 \cdot 10^{-6}$	1.42
100	0	0	$5 \cdot 10^{-6}$	50	-	-	$5 \cdot 10^{-5}$	1.47

Table 4.4: Absolute concentrations of polymer solutions (5 wt%) containing 4-arm PEG-Ac (10 kDa), HA-Ac (250 kDa), and 25 mol% LAP that are used for rheology measurements and production of microgels in microfluidics.

4-arm PEG-Ac (%)	HA-Ac (%)	DoS HA-Ac (%)	c(4-arm PEG-Ac) (mol/mL)	c(4-arm PEG-Ac) (mg/mL)	c(HA-Ac) (mol/mL)	c(HA-Ac) (mg/mL)	c(LAP) (mol/mL)	c(LAP) (mg/mL)
90	10	1	$4.5 \cdot 10^{-6}$	45	$2 \cdot 10^{-8}$	5	$4.53 \cdot 10^{-6}$	1.33
95	5	1	$4.75 \cdot 10^{-6}$	47.5	$1 \cdot 10^{-8}$	2.5	$4.76 \cdot 10^{-6}$	1.40
90	10	5	$4.5 \cdot 10^{-6}$	45	$2 \cdot 10^{-7}$	5	$4.64 \cdot 10^{-6}$	1.37
95	5	5	$4.75 \cdot 10^{-6}$	47.5	$1 \cdot 10^{-8}$	2.5	$4.28 \cdot 10^{-6}$	1.42

Table 4.5: Absolute concentrations of polymer solutions (10 wt%) containing 4-arm PEG-Ac (10 kDa) with different LAP concentrations that are used for the production of microgels in microfluidics.

LAP per acrylate group in 4-arm PEG-Ac (mol%)	c(4-arm PEG-Ac) (mol/mL)	c(4-arm PEG-Ac) (mg/mL)	c(LAP) (mol/mL)	c(LAP) (mg/mL)
1	$1 \cdot 10^{-5}$	100	$4 \cdot 10^{-7}$	0.12
3	$1 \cdot 10^{-5}$	100	$1.2 \cdot 10^{-6}$	0.35
6.25	$1 \cdot 10^{-5}$	100	$2.5 \cdot 10^{-6}$	0.74
12.5	$1 \cdot 10^{-5}$	100	$5 \cdot 10^{-6}$	1.47
25	$1 \cdot 10^{-5}$	100	$1 \cdot 10^{-5}$	2.94
50	$1 \cdot 10^{-5}$	100	$2 \cdot 10^{-5}$	5.88
75	$1 \cdot 10^{-5}$	100	$3 \cdot 10^{-5}$	8.83
100	$1 \cdot 10^{-5}$	100	$4 \cdot 10^{-5}$	11.77

4.4.4 Rheology measurements

Rheological analysis of pre-polymer solutions is performed on a TA Instrument Discovery HR-3 hybrid rheometer using a 20 mm cone-plate or flat plate geometry. The polymerization of the hydrogels is determined via time-dependent measurements for 100 - 150 s at an UV light intensity of 3.0 mW cm^{-2} and a frequency of 1 Hz and an oscillation strain of 0.1%. Moreover, strain-dependent measurements are performed at strains between 0.1% and 1000% at a frequency of 0.1 Hz. The data is measured using the software TA Instruments Trios. The storage and loss moduli are determined from the viscoelastic region of the time, frequency, and oscillation sweep.

4.4.5 Microgel synthesis

Droplet-based spherical microgels are synthesized using a flow-focusing microfluidic technique. The dispersed phase is prepared as described in section *preparation of pre-polymer solutions*. The vial is wrapped with aluminum foil to prevent undesired light-initiated polymerization. The continuous phase is prepared from a mixture of Novec™ HFE 7500 and 1.5 vol% of Krytox™ 157 FSH surfactant. The flow rates are controlled using

Hamilton® syringes and PHD ULTRA syringe pumps by Harvard Apparatus. Aqueous droplets are formed inside the chip and crosslinked off-chip in a BTPE-50 tubes before being collected in Eppendorf tubes. The polymerization is initiated via irradiation using a UV-LED ($\lambda = 365$ nm) light intensity of 274 mW cm^{-2} (dose = 14.0 J cm^{-2}). Collected microgels are purified by washing five times with a mixture of n-hexane and span80 (1 wt%), n-hexane, iso-propanol, and water, respectively.

4.4.6 Characterization of mechanical properties of microgels

The mechanical properties of PEG-HA microgels is characterized using a Pavone Nanoindenter (Optics11Life, Amsterdam, The Netherlands). A cantilever-based probe with a spherical tip radius of 3 µm and a cantilever stiffness of 0.49 – 0.53 N m^{-1} is used. Indentation experiments are conducted using a piezo speed of 1 µm s^{-1} and a indentation depth of 1 µm. For each sample, a minimum number of 10 microgels are measured. Microgels are measured in different media Milli Q, PBS, RPMI, and DMEM as well as at room temperature and physiological temperature of 37 °C. The effective Young's modulus (E_{eff}) is calculated from the obtained load-indentation curves using the Hertzian contact model and the analysis of the data is performed using the software Dataviewer V2.5 (Optics11Life, Amsterdam, The Netherlands).

Furthermore, the viscoelastic properties of PEG-HA microgels are characterized in different media and temperatures by measuring the storage modulus G' and loss modulus G'' via dynamic mechanical analysis (DMA) using the same device. Oscillatory frequency sweep is measured on a minimum number of 10 microgels for each sample at a frequency of 1 Hz, 2 Hz, 4 Hz, 10 Hz, and 20 Hz, an amplitude of 100 nm and an indentation depth of 1 µm.

4.4.7 Characterization of HA distribution in the microgels

For the preparation of fluorescently labelled PEG-HA microgels, hyaluronate acrylate fluorescein (FITC HA-Ac (250 kDa, DoS = 1%)) is dissolved in aqueous solution using a vortex mixer (Heathrow Scientific™ Vortexer™, Schwerte, Germany) for mixing the solutions for 30 min and 2 h. 4-arm PEG acrylate (M_{w} = 10 kDa) is added to the solution

to obtain a total polymer mass concentration of 10 wt% using 25 mol% LAP with respect to the acrylate groups. Furthermore, same pre-polymer solution is prepared using hyaluronate fluorescein (FITC HA-Ac (250 kDa, DoS = 0%)). The absolute concentrations are equal to pre-polymer solutions that are prepared with non-fluorescent HA-Ac (see Table 4.2).

4.4.8   Cell viability test

Cell viability and proliferation are analyzed using MTT cell proliferation assay by Cayman chemicals. Cells are cultured in 96 tissue culture well plates (28,000 cells/well for HT29, and 25,000 cells/well for TC7 cell line) using 150 µL cell medium for 18 h at 37 °C with 5% CO_2 at humid environment. Microgels are incubated for 24 h and 48 h at 37 °C with 5% CO_2 at humid environment. As a live control, cells are incubated without microgels. Moreover, as a dead control, cells are incubated with ethanol for 10 min. The assay buffer tablet is solved in 100 mL sterile Milli Q water as described in the manufacturer instructions. Subsequently, the MTT reagent is solvent in 5 mL of the buffer solution shortly before usage. Microgels are incubated with the cells for 24 h and 48 h. At the end of the incubation time, 10 µL MTT reagent is added, mixed via an orbital shaker for 5 min and incubated for 3.5 h. According to manufacturer instructions, 100 µL of crystal dissolving solution is added and the samples are incubated for further 21 h before being measured using a Synergy fluorescent plate reader at a wavelength of 570 nm. The negative control is subtracted from all samples and the cell viability is calculated according to equation 1.

$$\text{Cell viability [\%]} = \frac{\text{Absorbance sample [a. u.]}}{\text{Absorbance live control [a. u.]}} \qquad 1$$

4.4.9   CD44 expression of human colorectal adenocarcinoma cells (Flow cytometry)

For the experiments, cells are seeded in 6-well plates at a density of 500,000 cells and allowed to grow to 80-90% confluency overnight. Cells are washed with cold PBS to remove the remaining media and harvested in 2 mL cold PBS by the use of a cell scraper. The supernatant was removed after centrifugation and the cells are stained with a FITC-

labelled CD44 monoclonal antibody (ThermoFisher Scientific) diluted 1:200 in cold PBS for 30 min at 4 °C. Cells are washed, re-suspended in 200 μL cold PBS and analyzed via a flow cytometer (FACS Canto II, BD bioscience, NJ, USA) using the blue laser at 488 nm and medium flow rate. 50,000 events are recorded for every sample. Measurements are carried out in triplicates and analyzed using FlowJo Software (Treestar, OR, USA).

4.4.10 CD44 expression of human colorectal adenocarcinoma cells (RT-PCR)

For the experiments, cells are seeded in 6-well plates at a density of 500,000 cells and allowed to grow to 80-90% confluency overnight. Cells are washed with cold PBS to remove the remaining media and harvested in 2 mL cold PBS by the use of a cell scraper. The supernatant was removed after centrifugation and the cell pellet is frozen at -80 °C. Next day, samples are allowed to thaw on ice and RNA is isolated using RNeasy Mini kit (Qiagen, Hilden, Germany) as recommended by the manufacturer. Subsequently, RNA concentration and purity are measured with a spectrophotometer NanoDrop 2000c (Thermo Scientific, Dreieich, Germany). Following, the isolated messenger RNA (mRNA) is transcribed into complementary DNA (cDNA). To that end, reverse transcription is performed with an Omniscript RT Kit (Qiagen, Hilden, Germany) according to the manufacturer's instructions. 1 μg isolated RNA is mixed with an omniscript master mix, containing 10x buffer RT, random primer (0.3 μg/μL), desoxyribonucleosidtriphosphates (5 mM), and omniscript RT polymerase (4 units/μL) in a final volume of 20 μL. For the transcription the samples are placed into a thermocycler (biometra, Goettingen, Germany) for 1 h at 37 °C. The reaction is terminated by heating the samples to 95 °C for 5 min. Synthesized cDNA is stored at -20 °C until RT-PCR is performed using a 7300 Fast Real time PCR System (Applied biosystems, Dreieichs, Germany). The quantification is tracked using the fluorescent DNA dye SYBR Green (Applied Biosystems, Dreieich, Germany). For this, a mixture containing DEPC treated water, forward and reverse primer (human CD44 primer: F:, R:), and SYBR green is prepared. First, 25 ng cDNA is pipetted into the 96-well PCR plate, followed by the primer-SYBR green mixture to a final volume of 10 μL. β-actin (human β-actin primer: F:, R:) serves as an internal control. Samples are measured in duplicates and evaluated using the ΔΔCt method.

4.4.11 Microgel-cell adhesion experiments

Microgels are sterilized via UV sterilization for 1 h. Human colorectal carcinoma cell lines HT29 and TC7 are cultured in tissue culture flasks in RPMI (HT29) and Dulbecco's modified eagle' medium (DMEM, Gibco) (TC7) supplemented with 10% FBS (Biowest or Gibco), 1% antibiotics micotic (AMB, Gibco) at 37 °C with 5% CO_2 at humid environment.

For microgel-cell adhesion experiments, cells (200,000 cells/well for HT29 and 100,000 cells/well for TC7) are cultured in 48 tissue culture well plates for 24 h at 37 °C with 5% CO_2 at humid environment. Microgels (47,600 microgels/well) are added into the cell medium and cultured for 3 h. Brightfield images of the microgels are taken using a Zeiss Axio Vert.A1 microscope. The medium containing the non-adhered microgels is removed and exchanged three times with fresh medium. Brightfield images of the adhered microgels are taken. The number of microgels before and after washing at the exact same position is determined. The percentage of adhered microgels is calculated. All experiments are performed in triplicates.

4.4.12 Statistical analysis

All data points are shown as mean average with error bars indicating standard deviation ($\pm$SEM) with at least a sample size of 3. Statistical analysis is performed with Origin 2018, graph pad prism 8 and ImageJ. Statistical significance is performed using one-way ANOVA with Tukey´s test for multiple comparison. Asterisks are used to highlighted following two-tailed P values: ns = non-significant = $P > 0.05$, $*P < 0.05$, $**P < 0.01$, $***P < 0.001$, $****P < 0.0001$.

5 Varying the stiffness and diffusivity of rod-shaped microgels independently through their molecular building blocks

Yonca Kittel, Luis P. B. Guerzoni, Carolina Itzin, Dirk Rommel, Matthias Mork, Céline Bastard, Bernhard Häßel, Abdolrahman Omidinia-Anarkoli, Silvia P. Centeno, Tamás Haraszti, Kyoohyun Kim, Jochen Guck, Alexander J. C. Kuehne, Laura De Laporte

5.1 Introduction

Micron-scaled gels represent powerful colloidal building blocks for scaffold materials in tissue engineering and regenerative medicine. Such microgels are crosslinked polymer networks that are swollen with water. These finite, colloidal gels exhibit variable stiffness, degree of swelling, mesh size, and shape, all of which influence their function and response to their environment and depend on the internal structure of the microgels.[51,107] The term *internal structure* has been coined to account for the fact that heterogeneity in gel networks may occur across length scales, spanning several orders of magnitude. The internal structure depends on the architecture, molar mass, and concentration of the molecular building blocks, as well as the mechanism of crosslinking and its rate.[396–399] The internal structure affects the diffusivity (the diffusion of molecules through the network), the swelling and shrinking capacity of a microgel in response to external triggers, such as pH, light, and temperature, and the mechanical and chemical interaction with their surroundings, for example other microgels, proteins, cells, or plants.[355,400]

In bulk hydrogels, the internal structure has been analyzed with regard to its effect on the diffusivity, correlating mesh size and morphology to diffusion properties.[80,401–405] Many studies have focussed on hydrogels made from polyethylene glycol (PEG), representing a biologically inert and biocompatible polymer, which is clinically approved and currently used in patients as solubilizing units in imaging probes and contrast agents, in many drug formulations, and as injectable organ spacers.[406–408] The diffusivity of PEG hydrogels depends on the mechanism that is chosen for crosslinking during hydrogel network formation. More specifically, *chain-growth* polymerization produces a different network architecture and internal structure compared to *step-growth* polymerization.[409] Even

though step-growth polymerization leads to more homogeneous polymer network structures and controlled degradation rates, and is therefore often used for the incorporation of cells inside hydrogels for tissue engineering application, it is limited by lower polymerization and thus hydrogel production rates compared to chain-growth polymerization.[69] Chain-growth polymerization results in more heterogeneous polymer network structures but enables faster polymerization and, therefore, the production of microgels in high-throughput systems.

In another example, the swelling ratio and internal pore structure of hydrogels formed from poly(*N*-isopropylacrylamide) (NIPAm), copolymerized with PEG-diacrylate (PEG-DA) as a crosslinker, can be precisely tuned by changing the molar mass of the PEG-DA and its compositional ratio (NIPAm to PEG-DA).[410] By contrast, systematic studies to alter the internal structure of micron-scaled PEG-based microgels and its effect on stiffness, swelling behaviour, and diffusivity are absent to date.

Microgels with dimensions in the range of several micrometers are typically produced by employing one of the following fabrication techniques: in-mold polymerization, photo-lithography, stop flow lithography, droplet microfluidics, or compartmentalized jet polymerization.[60,64,71,131] In the case of confined microfluidic droplets or in filled cavities, the chosen process of crosslinking and its rate lead to different physical and mechanical properties of the microgels – in turn these vary greatly from bulk hydrogels.[108] For example, in the case of in-mold polymerization, a liquid non-reactive PEG filler has been employed to avoid solvent evaporation during crosslinking.[131] When crosslinking the mixture of pre-polymer in the presence of an inert polymer filler by free radical polymerization, phase separation occurs, which is well described by the Flory-Huggins-theory as the molecular weight increases during polymerization, affecting the Gibbs-free energy. This leads to large mesh sizes and soft microgels. When the microgels are prepared via thermally-induced amine-epoxy addition, phase separation does not occur, likely due to the more homogeneous network formed during step-growth polymerization, counteracting phase separation between the crosslinking and non-crosslinking phases. These microgels demonstrated a more homogenous internal structure with smaller meshed pores.[108]

In contrast to in-mold polymerization and photolithography, microfluidics can be operated continuously with the benefit of high production rates. While most microfluidic syntheses yield spherical microgels, more recent works have focused on preparing soft, rod-shaped

114

microgels.[107][411,412] Rod-shaped microgels feature anisometry and, therefore, directionality, which is important for a variety of applications. Jammed microgel rods produce large open voids, due to their higher aspect ratio.[107] This macroscopic structure is beneficial for cell seeding, proliferation, cell-cell interactions, and the exchange of nutrients, rendering these jammed microgel rods interesting as injectable regenerative scaffolds. In addition, magneto-responsive rod-shaped microgels can be magnetically aligned inducing enhanced directionality and enabling oriented cell growth, a requirement for scaffolds aiming at the growth of nerves or muscle tissue.[338] While the magnetic alignment of the microgel rods is well understood, the effect of their internal structure and mechanical properties on their organization on the colloidal level when assembled and interlinked to form a tissue-engineering scaffold is not yet clarified.

Rod-shaped microgels, produced via droplet microfluidics, exhibit Young's moduli between 1.8 to 10 kPa (measured via nanoindentation using atomic force microscopy (AFM)) for PEG concentrations ranging from 2% to 3% (w/v) when crosslinked via Michael-type addition.[68] This is around 10 to 18-fold higher, compared to the storage modulus of bulk hydrogels prepared with the same polymer composition and reaction mechanism, as determined by rheology. In the case of free-radical photo-polymerization of rod-shaped microgels, the UV dose (intensity and time) on chip will also affect the internal structure.[107] Moreover, the addition of charged co-monomers significantly increases the swellability and reduces the stiffness of rod-shaped PEG microgels.[107]

In this report, we aim to gain understanding of the different parameters that affect the internal structure of rod-shaped micron-scaled microgels produced via microfluidics versus bulk hydrogels, both crosslinked via free-radical polymerization. We perform systematic characterization by varying the concentration, molar mass, and ratio of 8-arm star-shaped PEG-acrylate (sPEG-Ac) and PEG-DA components.[413] Different ratios of 8-arm sPEG-Ac with molar masses of 10 kDa and 20 kDa in combination with a lower molar mass PEG-DA (700 Da) are tested to produce microgels and bulk hydrogels, which we analyze in terms of their diffusivity, morphology, chemical functionality, and mechanical properties. Bulk hydrogels are produced as reference materials, crosslinked using comparable conditions as in microfluidics. We also investigate the interaction of the rod-shaped microgels with cells by modifying the microgels with H-Gly-Arg-Gly-Asp-Ser-Pro-Cys-OH (GRGDS-PC) as a cell adhesive peptide, and we correlate these results with the physical and mechanical properties of the microgels' network. The gained knowledge will

allow us to better design and employ microgels as building blocks for applications, such as scaffold formation to grow cells in 3D and for engineered tissues.

5.2   Results and Discussion

5.2.1   Bulk hydrogels

We start by characterizing the gelation kinetics and the resulting mechanical properties of bulk hydrogels using rheology (see Figure 5.2A and B). The bulk hydrogels are produced by crosslinking pre-polymer solutions with a total amount of 5 wt% PEG, consisting of different ratios of 8-arm PEG-Ac (M_W = 10 kDa or 20 kDa) and PEG-DA (M_n = 700 Da), via free radical polymerization using 50 mol% of the photoinitiator lithium phenyl-2,4,6-trimethylbenzoylphosphinate (LAP) (with respect to the reactive acrylate groups) activated with a UV dose of 10 mW cm^{-2}. The gelation time is determined by extrapolating to where the increasing storage modulus G' reaches the plateau. A suitable LAP concentration has been previously determined in microfluidic experiments as described in Section *materials and methods* and shown in Figure 5.4.

As expected, decreasing the molar mass of 8-arm PEG-Ac from 20 to 10 kDa leads to faster gelation, simply because the number of reactive acrylate groups doubles when the overall PEG-Ac mass-concentration is kept constant (see Figure 5.2A). The successful gelation of a precursor solution only containing 8-arm PEG-Ac confirms that intermolecular links dominate the polymerization reaction.

While the combination of PEG-DA with 10 kDa sPEG-Ac does not significantly influence the gelation time t_{gel}, we observe shortening of t_{gel} when 20 kDa sPEG-Ac is mixed with PEG-DA up to a ratio of 50:50 by weight percent (see Figure 5.2A). Above 50% PEG-DA t_{gel} increases again. Since 20 kDa sPEG-Ac has a larger coil volume of about 73×10^{-20} mL as determined by intrinsic viscosity measurements (see Figure 5.1), and therefore slower molecular diffusion compared to 10 kDa sPEG-Ac (coil volume = 8.5×10^{-20} mL), we believe that the shorter t_{gel} of the 20 kDa sPEG-Ac:PEG-DA system is the result of improved molecular diffusion by the short PEG-DA and the fact that in the presence of sPEG-Ac, fewer reactions are required to form a continuous gel network.

116
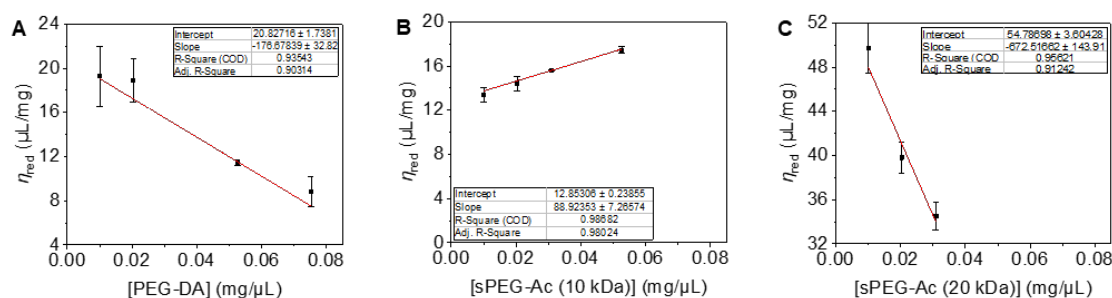
Figure 5.1: Determination of intrinsic viscosities of A) PEG-DA, B) sPEG-Ac (10 kDa), and C) sPEG-Ac (20 kDa). The intrinsic viscosity is determined by graphically plotting the reduced viscosity η_{red} as a function of the polymer concentration. The critical overlap concentration is calculated to be the inverse of the intrinsic viscosity. Data is presented as mean ± s. d., $n = 3$.

With increasing ratio of PEG-DA above 50%, there are less sPEG-Ac crosslinker units in the solution, requiring more coupling steps before a continuous gel is achieved. By contrast, increasing amounts of PEG-DA do not affect the gelation rate of 10 kDa sPEG-Ac significantly, likely because 10 kDa sPEG-Ac has a smaller coil volume (8.5×10^{-20} mL, see Figure 5.1) than the 20 kDa sPEG-Ac (73×10^{-20} mL) and its molecular diffusion is fast enough to rapidly form a stable polymer gel network. In the case of the pure PEG-DA system, very slow gelation kinetics occur compared to the mixed systems, due to the lack of multi-armed reactive precursors. It is important to note here that the effect of molecular diffusion, the number of reactive groups per molecule, and the total number of reactive acrylate groups in solution on the gelation process are difficult to decouple.

More surprisingly, we observe a higher *G'* in the 20 kDa sPEG-Ac systems compared to the 10 kDa sPEG-Ac (see Figure 5.2A). This is counterintuitive and could be explained by the density of the polymeric sPEG crosslinkers. While 20 kDa sPEG-Ac exhibits a bigger coil volume compared to 10 kDa sPEG-Ac, the 20 kDa sPEG-Ac has a significantly lower coil density of 45.6 mg mL^{-1} compared to the 10 kDa sPEG-Ac at 194.5 mg mL^{-1}, as determined by intrinsic viscosity measurements (see Figure 5.1). Consequently, we believe that the 20 kDa sPEG-Ac may achieve greater conversion because of augmented accessibility of the reactive acrylate groups, leading to stiffer hydrogels. Single chain elasticity is inversely proportional to the chain length for an ideal polymer. Shorter chains can more easily interact with each other, which may contribute to a lowered mobility to crosslink with other molecules. For sPEG, the node in the centre of the molecules causes a high chain density, decreasing mobility in the core range. For the 20 kDa chains, however, the eight reactive groups are distributed on a higher effective surface due to the longer chains, while the chains themselves also have a higher flexibility, resulting in more crosslinks and thus a stiffer gel. The intra-polymer free volume increases with the polymer

size for sPEG, resulting in easier diffusion of the small PEG-DA to fill up these pores and reducing diffusion of dextran through the network. Indeed, for both sPEG molecules, the addition of PEG-DA leads to a decrease of hydrogel stiffness down to few kPa (see Figure 5.2B). The softest hydrogels are obtained for 100% PEG-DA after a long t_{gel} of 40 s, yielding a G' of only ~0.14 kPa. The addition of PEG-DA to sPEG-Ac also influences the internal structure of the hydrogel, not only in terms of stiffness but also its diffusivity. Here, different hierarchical structures of the internal structure of hydrogels and microgels play a role when characterizing the stiffness and diffusion properties. Thereby, it is important to differentiate between i) macropores (≥ 50 µm)[414] that are formed during demixing upon polymerization[415–417], ii) mesopores (2 - 50 nm)[414] that are formed due to crosslink density fluctuations and network inhomogeneities[418,419], and iii) micropores (≤ 2 nm)[414] that reflect the free volume inside the polymer coils themselves[420], and are highly dependent on the polymer and solvent[421–423].

To investigate the internal structure, we produce bulk hydrogels as described above using a UV-LED ($\lambda = 365$ nm) with a dose of 467 mJ mm^{-2} and analyze the diffusion of differently sized fluorescein isothiocyanate (FITC)-dextrans through the bulk of the gels over a distance of 100 µm using confocal laser scanning microscopy (CLSM) (in height, z-direction in the coordinate system of the CLSM) (see Figure 5.2D-F). This allows us to probe the hydrogels for diffusion. Using FITC-dextrans with a size of 10 kDa, 20 kDa, or 60 – 76 kDa (stokes radii $\approx$ 2.3 nm, 3.3 nm, or 6.0 nm), we compare hydrogels produced from 100 % sPEG-Ac 20 kDa, mixtures of sPEG-Ac 20 kDa and PEG-Da (700 Da), or 100 % sPEG-Ac 10 kDa. As polymer mixtures made from sPEG-Ac 10 kDa and PEG-DA (700 Da) do not lead to stable microgels, we did not produce them as bulk hydrogels.

The dextran diffusion is significantly reduced for 10 kDa; in fact, the diffusion in sPEG-Ac (10 kDa) is even slower than in pure PEG-DA hydrogels (see Figure 5.2D-F). Better diffusion properties are observed for 20 kDa sPEG-Ac, which indicates that more open space is available for 20 kDa than in 10 kDa sPEG-Ac hydrogels, likely due to the lower coil density. Furthermore, with increasing ratio of PEG-DA:sPEG-Ac (20 kDa) less diffusion takes place through the hydrogel, likely due to the fact that dangling, partially crosslinked PEG-DA molecules fill up the void space (in z-direction, see Figure 5.2D-I).
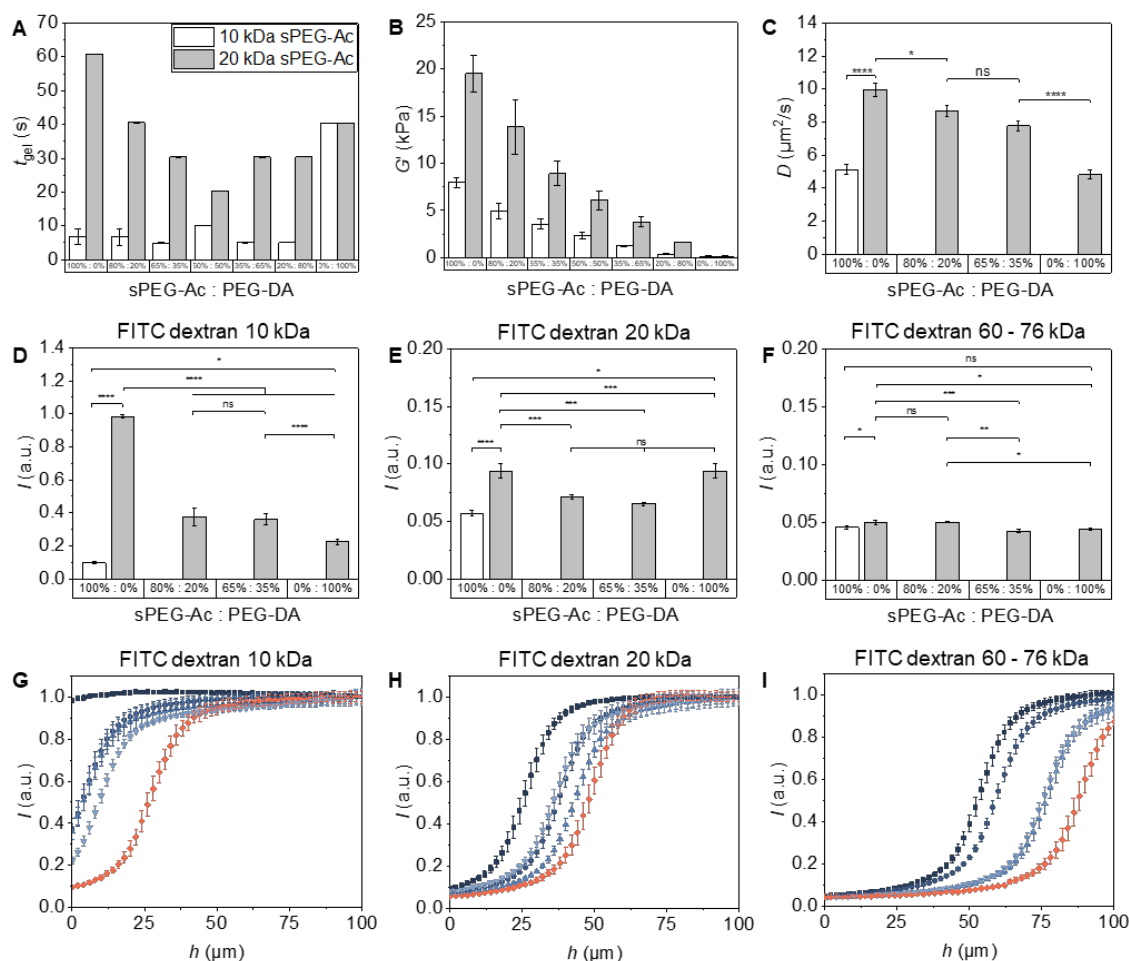
Figure 5.2: Characterization of pre-polymer solution and bulk hydrogels. Rheology measurements of samples with 5 wt-% pre-polymer concentration and 50 mol-% LAP containing mixtures of sPEG-Ac (10 kDa or 20 kDa) and PEG-DA: A) gelation time t_{gel}, and B) storage modulus G'. C) Diffusion coefficients D of FITC in bulk hydrogels are determined via FRAP method. Bulk hydrogels with a height of 100 µm are incubated with FITC-dextrans for 48 h. Normalized intensity I of FITC-dextrans D) 10 kDa, E) 20 kDa, and F) 60-76 kDa at a height of 0 µm (bottom of hydrogels) is measured in hydrogels with 5 wt-% pre-polymer concentration and an irradiation dose of 467 mJ mm^{-2}. The intensity is normalized to the highest fluorescence intensity of FITC. Data is presented as mean ± s. d., $n = 3$ hydrogels. Statistical significance is calculated using one-way ANOVA with Bonferroni correction, ns = non-significant = $P > 0.05$, *$P < 0.05$, ****$P < 0.0001$. Fluorescence intensity I at a hydrogel height between 0 µm and 100 µm of differently sized FITC-dextrans G) 10 kDa, H) 20 kDa, and I) 60-76 kDa in hydrogels (■ 100% sPEG-Ac (20 kDa) – 0% PEG-DA, ● 80% sPEG-Ac (20 kDa) – 20% PEG-DA, ▲ 65% sPEG-Ac (20 kDa) – 35% PEG-DA, ▼ 0% sPEG-Ac (20 kDa) – 100% PEG-DA, and ◆ 100% sPEG-Ac (10 kDa) – 0% PEG-DA) after 48 h with 5 wt-% pre-polymer concentration and an irradiation dose of 467 mJ mm^{-2}. Data is presented as mean ± s. d., $n = 3$ hydrogels.

Moreover, we determine the diffusion coefficient D of FITC in our hydrogels via fluorescence recovery after photobleaching (FRAP) (see Figure 5.2C). In agreement with the results of the just described macroscopic diffusion experiments, D determined by the FRAP experiments is lower for the hydrogels made from 10 kDa sPEG-Ac compared to the gels produced with 20 kDa sPEG-Ac. This confirms our previous hypothesis that the smaller molar mass sPEG-Ac exhibits more interchain interactions, while contributing less to crosslinking. Instead, smaller sPEG-Ac leads to more crowded meshes, and thus reduced diffusion. The higher coil density of the 10 kDa sPEG-Ac polymer seems to lead to steric hindrance and, therefore, blocked accessibility of reactive acrylate groups, resulting in only

119

partially crosslinked polymer chains, hindering diffusion within the free volume (micropores) between the polymer chains. Also, we obtain lower D of FITC with increasing PEG-DA amount in the 20 kDa sPEG-Ac:PEG-DA system, while the lowest D is obtained for 100 % PEG-DA hydrogel (see Figure 5.2C). This suggests that an increased amount of PEG-DA leads to more crowded networks and less void space, due to the increased density of partially crosslinked PEG chains. Interestingly, 100 % sPEG-Ac (10 kDa) and pure PEG-DA hydrogels show comparable D (see Figure 5.2C). This demonstrates that the stiffer sPEG-Ac (10 kDa) and softer PEG-DA hydrogels exhibit similar steric hindrance, while the sPEG-Ac (10 kDa) results in more crosslinks. These results indicate that the addition of PEG-DA indeed leads to the presence of partially crosslinked polymer chains hindering the diffusion of molecules, while resulting in very soft hydrogels. Within this crowded network, the diffusion of the PEG chains will be reduced, so that for most molecules only one of the acrylate groups of PEG-DA becomes incorporated during polymerization. The dangling chain-ends fill up the pores of the hydrogel without increasing the crosslink density or stiffening of the network.

To verify this hypothesis (dangling polymer chains reduce the free volume and thus the diffusivity, while softening the gel due to less crosslinks and more free acrylates), we determine the amount of remaining reactive free acrylate groups inside the polymer network after photopolymerization. Bulk hydrogels are crosslinked with a UV dose of 467 mJ mm^{-2} for 30 sec, which mimics the exposure of the microgels. The free acrylates are quantified via Raman spectroscopy (see Figure 5.3). Thereby, the hydrogels are freeze-dried and the solid powder is measured, which allows for the detection of the acrylate groups throughout the whole polymer network. The individual peaks representing the acrylate groups, as well as C-C bonds of the PEG units enables the qualitative as well as quantitative analysis of the acrylate groups related to C-C PEG units presented in the hydrogel polymer network. As already indicated, we measure a significantly higher ratio of free acrylate groups with respect to C-C PEG units for hydrogels made from sPEG-Ac (10 kDa) (24.2%) compared to sPEG-Ac (20 kDa) (2.3%) (see Table 5.1) based on the calibration of free acrylate groups (see Figure 5.3A-C). More free acrylate groups are also present with increasing PEG-DA amount, entailing the reduced diffusivity. The addition of PEG-DA to sPEG-Ac (20 kDa) increases the amount of free acrylate groups from 2.3% to 35.4% and 35.5% (for 20% and 35% PEG-DA, respectively), which is consistent with the decreasing stiffness of the polymer networks (see Table 5.1). This results are in line with a

previous report where reducing the fraction of PEG-DA and increasing the amount of star-shaped polymer stabilizes the hydrogel network by connecting multiple polymer backbones together, increasing the stiffness.[55]
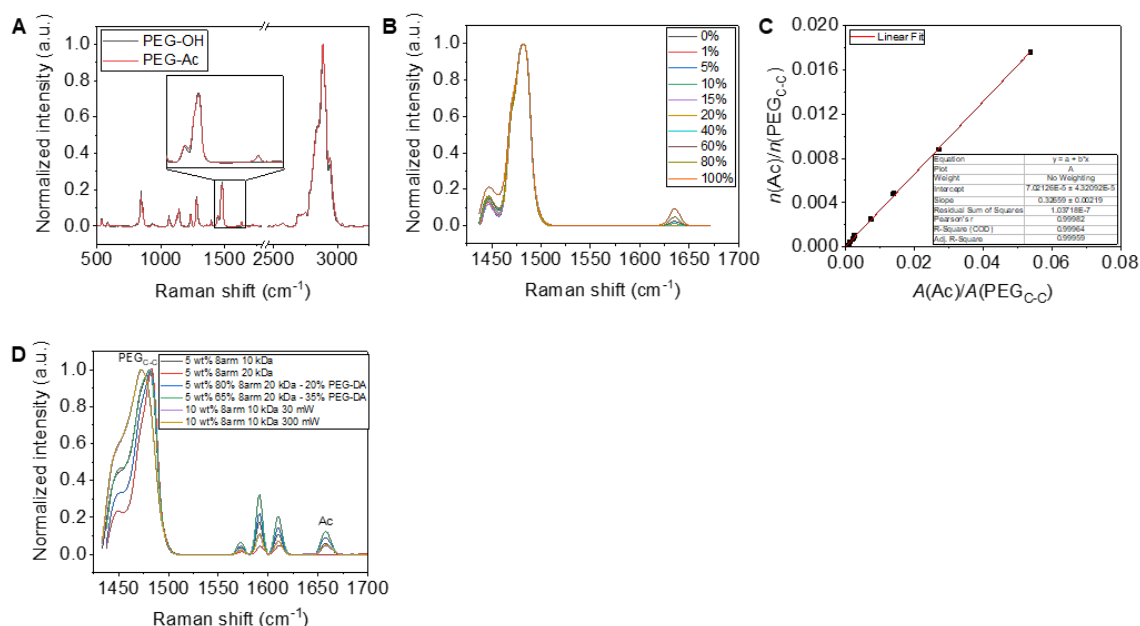

Figure 5.3: Characterization of remaining reactive acrylate groups in bulk hydrogels after polymerization reaction via Raman spectroscopy. A) Raman spectra of linear PEG-OH (20 kDa) and sPEG-Ac (20 kDa). B) Raman spectra of different molar ratios of end groups of linear PEG-OH (20 kDa) and sPEG-Ac (20 kDa). C) Calibration graph based on the relation of peak areas of acrylate to aliphatic C-C groups in PEG units of PEG-OH (20 kDa) and sPEG-Ac (20 kDa). Peak areas of aliphatic C-C groups are determined by integrating the peak at a Raman shift of 1456 cm^{-1} to 1508 cm^{-1}, while the peak area of the acrylate peak is integrated at a Raman shift of 1618 cm^{-1} to 1653 cm^{-1}. D) Raman spectra of bulk hydrogels with 5 wt-% pre-polymer concentration and an irradiation power of 300 mW (100% sPEG-Ac (10 kDa), 100% sPEG-Ac (20 kDa) – 0% PEG-DA, 80% sPEG-Ac (20 kDa) – 20% PEG-DA, 65% sPEG-Ac (20 kDa) – 35% PEG-DA) and 10 wt-% polymer (sPEG-Ac (10 kDa) 30 mW UV LED power and sPEG-Ac (10 kDa) 300 mW UV LED) are used to calculate remaining reactive acrylate groups after photopolymerization based on the linear equation in (c). Peak area of the aliphatic C-C groups and acrylate groups are integrated at a Raman shift of 1454 cm^{-1} to 1508 cm^{-1} and 1648 cm^{-1} to 1670 cm^{-1}, respectively.

Table 5.1: Calculated reactive acrylate groups related to PEG units in bulk hydrogels based on Raman spectroscopy measurements in Figure 5.3.

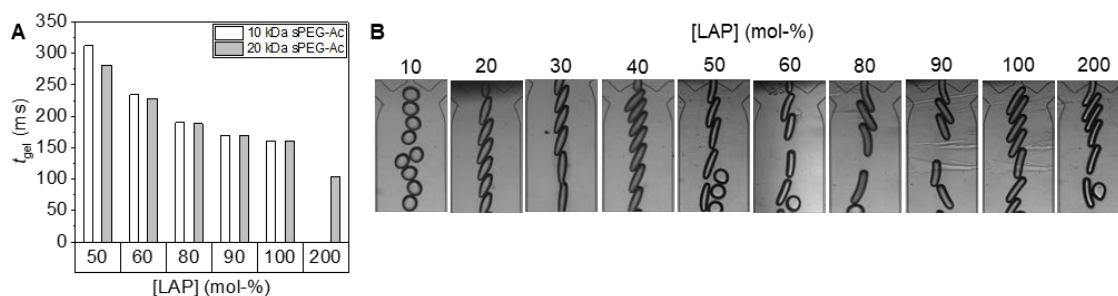| Sample	Reactive acrylate groups [%]
5 wt-% - sPEG-Ac (10 kDa)	24.2
5 wt-% - sPEG-Ac (20 kDa)	2.3
5 wt-% - 80% sPEG-Ac (20 kDa) – 20% PEG-DA	35.4
5 wt-% - 65% sPEG-Ac (20 kDa) – 35% PEG-DA	35.6
10 wt-% - sPEG-Ac (10 kDa) – 30 mW UV-LED power	18.6
10 wt-% - sPEG-Ac (10 kDa) – 300 mW UV-LED power	19.5

5.2.2 Rod-shaped microgels produced via microfluidics

After analysis of the internal structures of the bulk hydrogel systems, we now produce rod-shaped microgels with the same precursor solutions. The microgels are made by continuous on-chip gelation of droplets produced in the plug-flow regime of a microfluidic channel device (see Scheme 5.1).
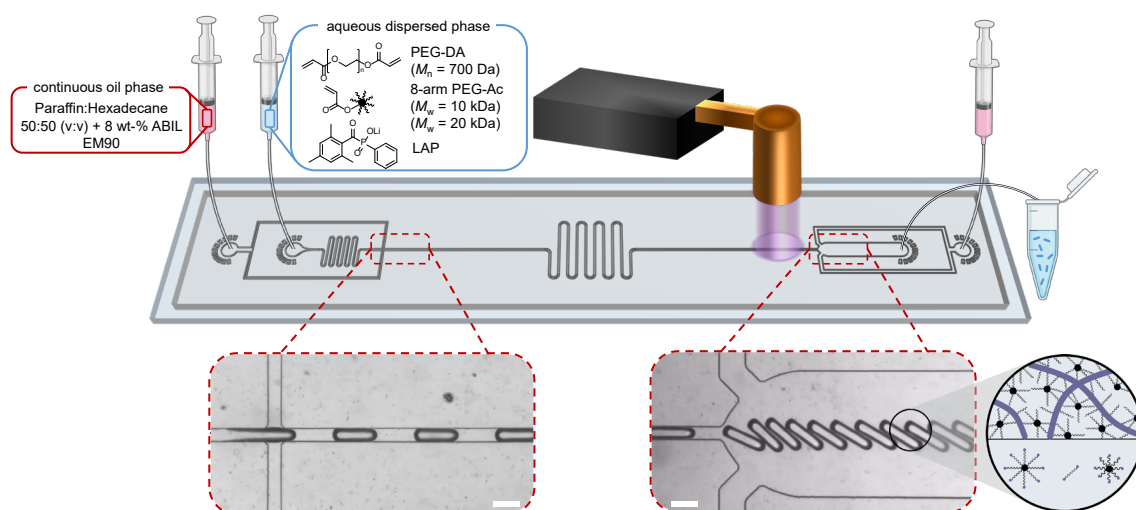
Scheme 5.1: Schematic microfluidic chip design for continuous plug-flow on-chip production of rod-shaped microgels. Red syringes show the inlets for first (for pinching-off the dispersed droplets) and second continuous phase (before outlet for diluting or separating of the polymerized microgel rods). Blue syringe indicates the inlets for the dispersed phase. The purple shading represents the UV irradiation on chip. Dashed inserts represent brightfield images of characteristic section of the microfluidic chip taken during operation. Scale bars represent 100 µm. Created with BioRender.com

The precursor solution is broken up into elongated droplets with a length of approximately 300 µm and subsequently UV crosslinked inside of the microfluidic channels, affording anisometric, rod-shaped microgels that are collected off-chip, as described previously.[107] Sufficient crosslinking on chip is essential to maintain the shape of the rod-shaped microgels after they exit the chip. To induce rapid gelation, the water-soluble LAP radical-photo-initiator (50 mol%) is mixed with the precursor molecules (sPEG-Ac, PEG-DA). The optimal LAP concentration for the synthesis of stable rod-shaped microgels has been previously determined in microfluidic experiments as described in Section *materials and methods* and shown in Figure 5.4. Depending on the molar mass and concentration of sPEG-Ac, the required t_{gel} – during which polymerization and crosslinking occurs to form the microgel rods – varies. To ensure that the microgels are fully crosslinked for all tested precursor solutions, we irradiate continuously at a maximum power of 300 mW leading to a dose of 467 mJ mm^{-2} for each droplet or microgel, as we maintain the flow rates for the dispersed and continuous phases identical at $\dot{V}_{disp} = 35$ µL h^{-1} and $\dot{V}_{cont} = 35$ µL h^{-1}. This leads to a rate of around 220 droplets per minute.

Figure 5.4: Determination of suitable LAP concentration for polymerization reaction via single pulsing experiments in microfluidics using different LAP molar ratio related to reactive acrylate groups in sPEG-Ac (10 kDa and 20 kDa). A) Gelation time t_{gel} of microgels using different LAP concentrations. B) Brightfield images of microgels produced in plug-flow microfluidics by on-chip crosslinking. Suitable LAP concentration of 50 mol-% is defined as the microgels are rod-shaped and do not snap back in spherical shape. Scale bar represents 200 µm.

Using this set-up, we produce microgels with 100 % sPEG-Ac (10 kDa), 100 % sPEG-Ac (20 kDa), 80 % sPEG-Ac (20 kDa) – 20 % PEG-DA, and 65 % sPEG-Ac (20 kDa) – 35 % PEG-DA, while maintaining a constant total precursor concentration of 5 wt%. At this concentration, a combination of PEG-DA and sPEG-Ac (10 kDa) does not lead to stable microgels under the tested conditions. Microgels with higher molar mass sPEG-Ac (20 kDa) show significantly higher stiffness (higher effective Young's modulus E_{eff}) compared to lower molar mass sPEG-Ac (10 kDa) in nanoindentation measurements (see Figure 5.5A). In addition, D of FITC is significantly higher in microgels made from 20 kDa sPEG-Ac compared to the 10 kDa homologue (see Figure 5.5B). These trends correlate with the observations made in bulk hydrogels. Moreover, the E_{eff} of the microgels decreases with increasing amounts of PEG-DA in the sPEG-Ac (20 kDa) system. Interestingly, in contrast to the bulk hydrogels, diffusion of FITC slightly increases with the addition of PEG-DA to sPEG-Ac (20 kDa). This suggests that the internal structure of the microgels is different from the bulk hydrogels. The difference may arise from polymerization in the confined spaces of the droplets in microfluidics and different polymer thickness of the bulk hydrogels.

To better understand the correlation between the mechanical and diffusion properties, we perform Brillouin microscopy and optical diffraction tomography (ODT) measurements (see Figure 5.5C-F). Brillouin microscopy is a powerful technique to provide label-free, non-contact, and spatially resolved measurements of the mechanical properties of biological samples[424–426], but it has also been employed for microgels.[233,427–429] The Brillouin frequency shift is measured, which is related to the longitudinal modulus, refractive index (RI), and the absolute density of the sample.[426] The longitudinal modulus

determines the compressibility of the samples. The ODT measures RI of the samples, which is linearly proportional to the mass density of most biological samples and microgels.[233,430] We observe a higher Brillouin frequency shift and RI for the 20 kDa compared to the 10 kDa microgels. Here, higher RI of the 20 kDa sample indicates that the microgels contain less water, due to less swelling, which is in agreement with the higher crosslinking density based on the higher stiffness of the sPEG-Ac (20 kDa) microgels, measured by nanoindentation.[426] The addition of PEG-DA added to sPEG-Ac (20 kDa) leads to a decrease of Brillouin frequency shift and RI, while no significant difference can be observed between 20 % or 35 % of added PEG-DA. This decrease in the Brillouin frequency shift and RI indicates a lower crosslink density, which is corroborated by the slightly improved diffusion when PEG-DA is added.
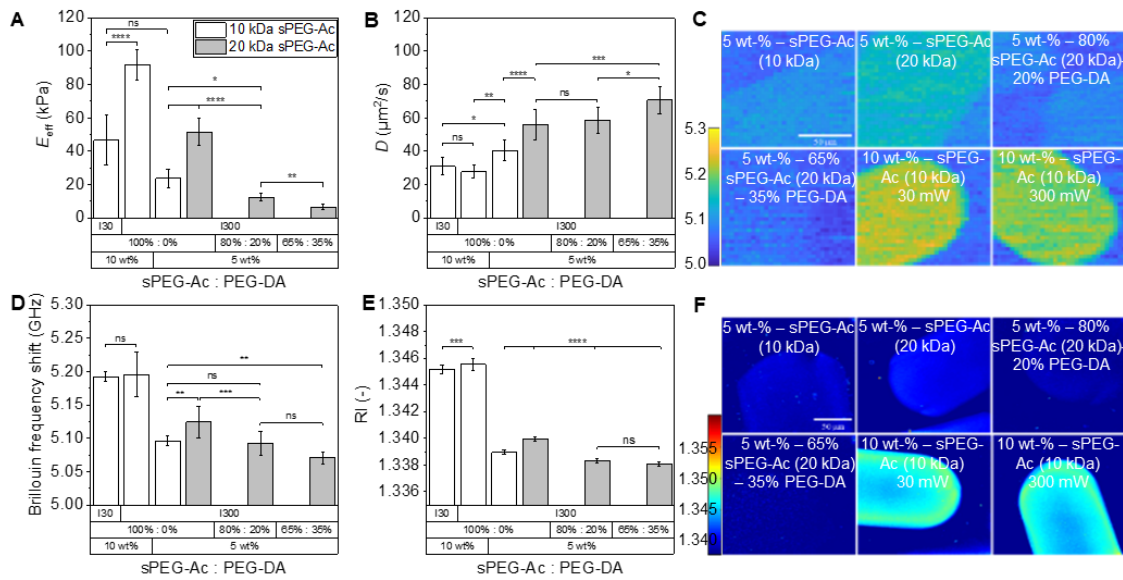
Figure 5.5: Characterization of rod-shaped microgels produced in plug-flow on-chip microfluidics. A) Effective Young's moduli E_{eff} of microgels is determined via nanoindentation measurements. Data is presented as mean ± s. d., n = 15 microgels per type at a minimum of 3 different locations. B) Diffusion coefficient D of FITC in the microgels is determined via FRAP method. C) Brillouin frequency shift maps, D) Brillouin frequency shift measurements, E) Refractive indices (RI) and F) tomographic RI reconstructions of microgels with different polymer compositions. Data is presented as mean ± s. d., n = 5 microgels. Statistical significance is calculated using one-way ANOVA with Bonferroni correction, ns = non-significant = P > 0.05, *P < 0.05, **P < 0.01, ***P < 0.001.

Furthermore, we investigate our microgels using cryo-SEM (scanning electron microscopy). We observe more crude structures for the 20 kDa microgels, while the structure of 10 kDa appears more defined (see Figure 5.6). This is in agreement with the diffusion studies that indicate overall larger mesh sizes for the 20 kDa microgels, while for the 10 kDa partially crosslinked polymer chains may hinder molecule diffusion.
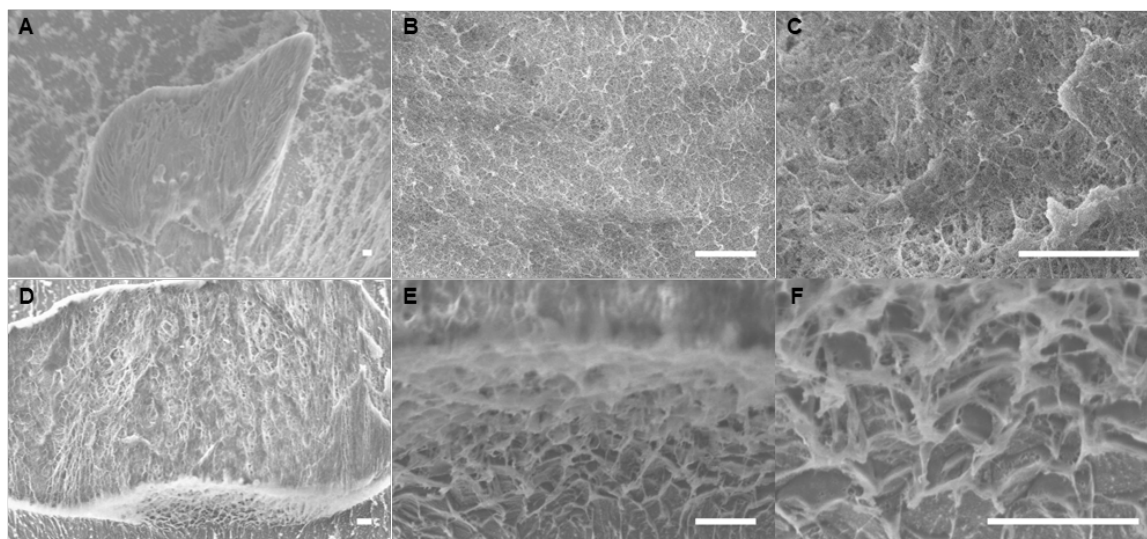
Figure 5.6: Cryo-SEM images of microgels with 5 wt-% - sPEG-Ac A) – C) 10 kDa and D) – F) 20 kDa. Scale bars represent 5 µm.

To corroborate that indeed larger hierarchical pores are formed for the 20 kDa sample, we characterize the macroporosity of the 20 kDa and 10 kDa sPEG-Ac microgels using STED (Stimulated Emission Depletion) microscopy followed by image analysis (see Figure 5.7). In the obtained porosity histogram, we observe larger macroscopic pores with radii up to 200 nm and 76.5% of the pores having a radius below 120 nm for the 20 kDa compared to the 10 kDa microgels, where 92.8% of the pores have a radius lower than 120 nm. This explains the results from the local D measurements by FRAP in microgels in Figure 5.5B, but also the macroscopic diffusion experiments with fluorescent dextrans in the bulk hydrogels (see Figure 5.2D-F). The clear phase separation for the 20 kDa polymer network can occur due to lower solubility of the higher molar mass 20 kDa in solvent compared to the 10 kDa homologue.
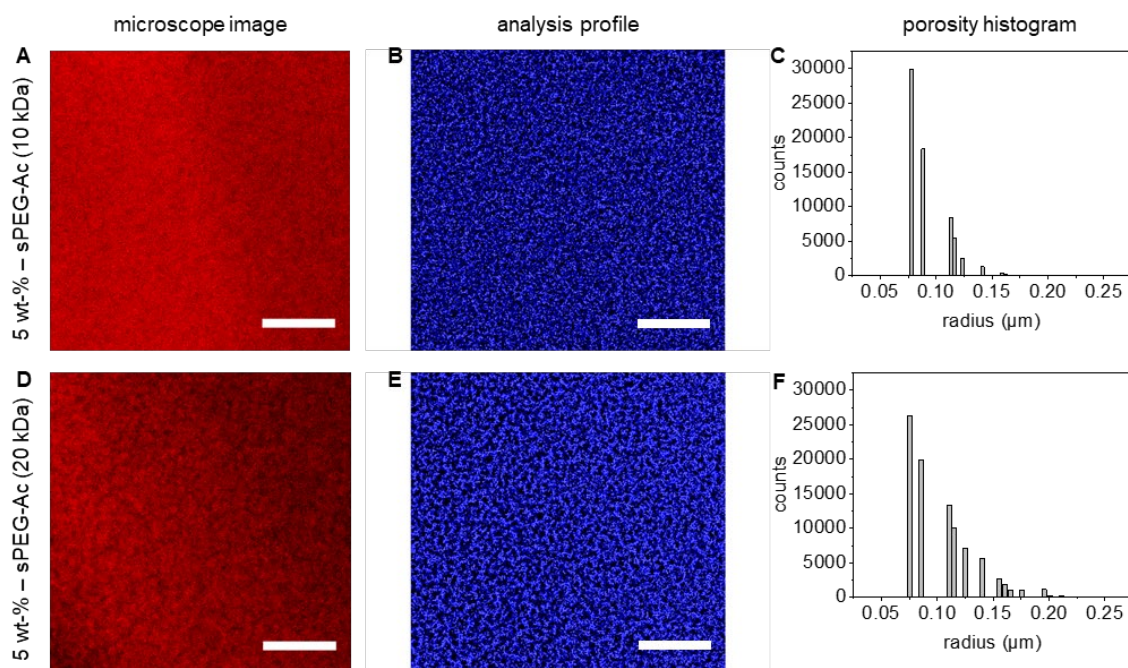
Figure 5.7: Microgel porosity is characterized via STED microscopy and Image analysis. The microscope images A) 5 wt-% – sPEG-Ac (10 kDa) and D) 5 wt-% – sPEG-Ac (20 kDa) are processed to the analysis profiles B) 5 wt-% – sPEG-Ac (10 kDa) and E) 5 wt-% – sPEG-Ac (20 kDa). The resulting porosity histogram shows lower pore sizes for the 5 wt-% – sPEG-Ac (10 kDa) microgels C) compared to the 5 wt-% – sPEG-Ac (20 kDa) microgels F).

To better investigate the effect of a lower UV dose on the mechanical and diffusion properties of the microgels, we crosslink the same droplets of polymer precursor with 10 wt% sPEG-Ac (10 kDa) using a UV-LED of 300 mW (dose = 467 mJ mm^{-2}) or 30 mW (dose = 46.7 mJ mm^{-2}). This concentration is chosen because it allows production of stiffer crosslinked, stable microgels that are irradiated with a very low UV light power of 30 mW. Microgels, irradiated with this lower power (30 mW) show a significantly lower E_{eff}. However, the diffusion properties of both microgels are not significantly different. Again, to better understand the correlation between the mechanical and diffusion properties, we perform Brillouin microscopy and RI measurements (see Figure 5.5C-F). We observe similar Brillouin frequency shifts (see Figure 5.5D) for microgels irradiated with 30 mW or 300 mW, but higher RI for the microgels irradiated at 300 mW (see Figure 5.5E). Interestingly, the microgels irradiated at the higher power of 300 mW exhibit higher RI at the periphery of the microgels. Furthermore, both conditions exhibit a similar amount of reactive acrylate groups measured via Raman spectroscopy (see Table 5.1 and Figure 5.3). The RI and E_{eff} of microgels irradiated with higher power suggest that the crosslinking density is higher at the periphery as the E_{eff} is measured at the surface of the microgels. However, the similar Brillouin frequency shift, diffusion properties, and amount of reactive acrylate groups indicate that the overall polymer network structure is similar for both

conditions. Moreover, 10 wt% microgels made from sPEG-Ac (10 kDa) show a higher Brillouin frequency shift and RI compared to 5 wt% microgels, which is consistent with the increase in stiffness and reduced diffusion. In general, the 5 wt% samples show homogeneous structures in the Brillouin frequency shift maps (see Figure 5.5C) and tomographic RI reconstruction images (see Figure 5.5F). Interestingly, the 10 wt% microgels show slightly higher RI at the periphery of the rod-shaped microgels compared to the core (see Figure 5.5F), which can be explained by stronger crosslinking at the interfaces, typical for photopolymerization reactions.

5.2.3   Cell culture

We have shown how the variation of molecular building blocks influence the internal structure of rod-shaped microgels, which affects the mechanical and diffusion properties of the material, both playing a major role in 3D cell culture. In this report, the biocompatibility and cell-adhesiveness of selected microgels is shown in 2.5D cell culture experiments using L929 mouse fibroblasts.

To introduce cell adhesion peptides to the microgels and render them suitable for cell culture, we post-functionalize our rod-shaped microgels with GRGDS-PC using thiol-Michael addition of cysteine (present in the peptide) with the free acrylate groups of the microgel.

To characterize cell-microgel interactions, the microgels are seeded with L929 mouse fibroblasts. Cell attachment depends on the microgel stiffness and the accessibility of RGD binding domain in GRGDS-PC, and is characterized via live imaging of at least 7 microgels per condition during 120 min after cell seeding at 37 °C, 5% CO_2 in humid environment (see Figure 5.8). We observe several filopodial protrusion of cells on 5 wt% sPEG-Ac (20 kDa) microgels, which indicates initiated cell adhesion. Moreover, fully spread cells can be observed on 10 wt% sPEG-Ac (10 kDa) microgels (dose = 46.7 mJ mm^{-2}, 30 mW UV-LED power irradiation). Both these microgels have a similar elastic modulus around 50 kPa thus the difference in cell spreading is likely due to variable accessibility of RGD (see Figure 5.5A). On elastic hydrogels, cell spreading is usually enhanced on stiffer gels.[431] However, in the case of stiffer 10 wt% sPEG-Ac (10 kDa) (dose = 467 mJ mm^{-2}, E_{eff} ~92 kPa), we observe no stable cell attachment.

To better understand cell attachment on the different microgels, we characterize the amount of GRGDS-PC incorporated into the polymeric network of the microgels via XPS (X-Ray Photoelectron Spectroscopy) analysis (see Table S5, Supporting Information). We measure the nitrogen-to-carbon (N/C) ratio as only the peptide contains nitrogen and thus this ratio indicates how much peptide is coupled to the microgels. The highest N/C ratio of 8.1 % is observed for the microgels with best cell attachment (10 wt% sPEG-Ac (10 kDa) (46.7 mJ mm^{-2}). Moreover, microgels with 5 wt% sPEG-Ac (20 kDa) exhibit 2.1% N/C ratio, which may explain the observed low number of attached but rounded cells. All other microgel types do not show considerable cell attachment after 120 min, in agreement with the XPS results where no GRGDS-PC peptides could be detected on these microgels. Microgels with higher PEG-DA amount (5 wt% – 65 % sPEG-Ac (20 kDa) – 35 % PEG-DA) dissolve in ethanol when sterilized and can therefore not be used for cell culture experiments. It is surprising that cell attachment failed for microgels irradiated with higher power (10 wt% sPEG-Ac (10 kDa) (467 mJ mm^{-2})) as an N/C ratio of 6.3 % is observed (see Table 5.2). This is lower compared to 10 wt% sPEG-Ac (10 kDa, 46.7 mJ mm^{-2}) microgels but higher than 5 wt% sPEG-Ac (20 kDa) microgels (dose = 467 mJ mm^{-2}). A reason for this observation could be the presence of the RGD on the outside of the microgels. In microfluidic technique, we assume more crosslinking at the outside of the microgels and thus less free acrylates to couple the peptide. This effect is probably stronger for the higher dose in the 10 wt% system, and in the case of a higher crosslinking density for 20 kDa sPEG in comparison to the 10 kDa sPEG-Ac due to less steric hindrance of the polymer. The significantly lower percentage of free acrylate groups for the sPEG-Ac (20 kDa) microgels also explains the lower concentration of coupled peptide.

Table 5.2: N/C ratio in microgels post-functionalized with GRGDS-PC analyzed via XPS analysis.

Sample	N/C ratio from XPS analysis [%]
5 wt-% - sPEG-Ac (10 kDa)	-
5 wt-% - sPEG-Ac (20 kDa)	2.1
5 wt-% - 80% sPEG-Ac (20 kDa) – 20% PEG-DA	-
10 wt-% - sPEG-Ac (10 kDa) – 30 mW UV-LED power	8.1
10 wt-% - sPEG-Ac (10 kDa) – 300 mW UV-LED power	6.3
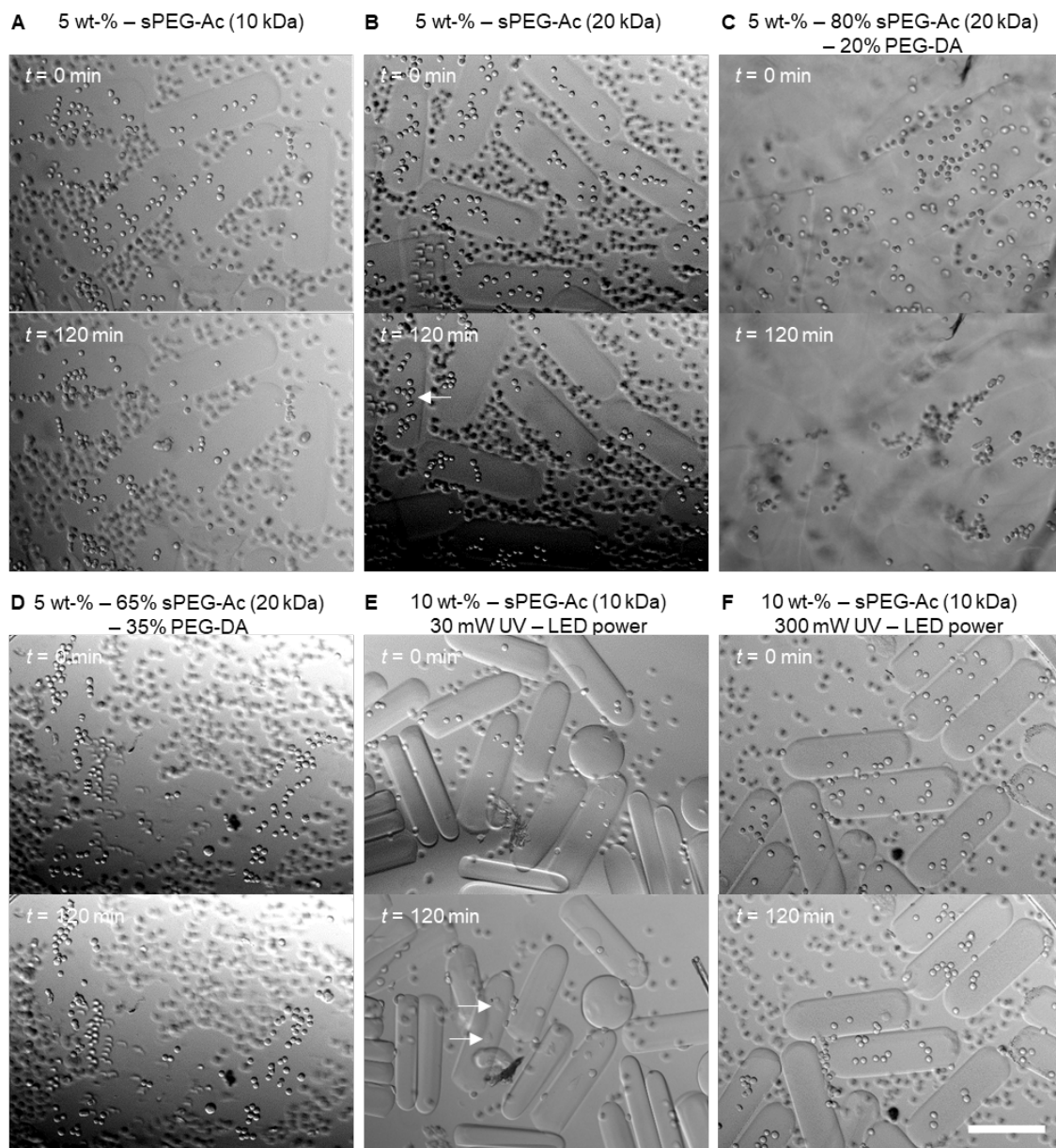
Figure 5.8: L929 fibroblast adhesion on single rod-shaped microgels. Microgels were post-functionalized with GRGDS-PC. Images of live imaging of the microgels A) 5 wt% – 100% sPEG-Ac (10 kDa) – 0% PEG-DA, B) 5 wt% – 100% sPEG-Ac (20 kDa) – 0% PEG-DA, C) 5 wt% – 80% sPEG-Ac (20 kDa) – 20% PEG-DA, D) 5 wt% – 65% sPEG-Ac (20 kDa) – 35% PEG-DA, E) 10 wt% – sPEG-Ac (10 kDa) – 0% PEG-DA, 30 mW UV-LED power, and F) 10 wt% – sPEG-Ac (10 kDa) – 0% PEG-DA, 300 mW UV-LED power are taken via differential interference contract (DIC) microscopy at $t = 0$ min and $t = 120$ min are taken. White arrowheads show filopodial protrusion, which indicates cell-microgel interaction. 5 wt-% – sPEG-Ac (20 kDa) microgels show several filopodial protrusion, while for 10 wt-% – sPEG-Ac (10 kDa) (30 mW UV-LED power) microgels a larger number of filopodial protrusion can be observed. Cell attachment for the other microgel samples show more rounded cells after $t = 120$ min. Scale bar represents 200 μm.

In a next step, we seed L929 fibroblasts on the microgels and culture them for 1 or 2 days (see Figure 5.9), after which the cells are fixed and their nucleus and actin filaments are fluorescently labelled with DAPI and Phalloidin594, respectively, to image cell spreading. This experiment is performed in triplicate and we analyze more than 30 microgels per condition. As indicated by the live imaging, cell protrusion on the 5 wt% sPEG-Ac (20 kDa) microgels started after 120 min, but after 2 days of culture, the cells still look

round and clustered. For the 5 wt% sPEG-Ac (10 kDa) microgels, there is attachment of several round cells after 1 day of culture – with some cells starting to spread, while on day 2, the cells are mostly spread on the microgel surface. For the 5 wt% – 80 % sPEG-Ac (20 kDa) – 20 % PEG-DA microgels, there is only attachment of several round cells after 1 day of culture, while after 2 days cluster formation on the microgels can be observed. This is a typical observation when cells do not interact well with the substrate. Then they produce ECM proteins as a rescue mechanism and interact with each other instead of the substrate. Interestingly, the 10 wt% sPEG-Ac (10 kDa) (30 mW UV-LED power irradiation) microgels strongly support cell proliferation on the microgels surface already after 1 day, while after 2 days of culture, the cells spread over the entire microgel surface (see Figure 5.9).
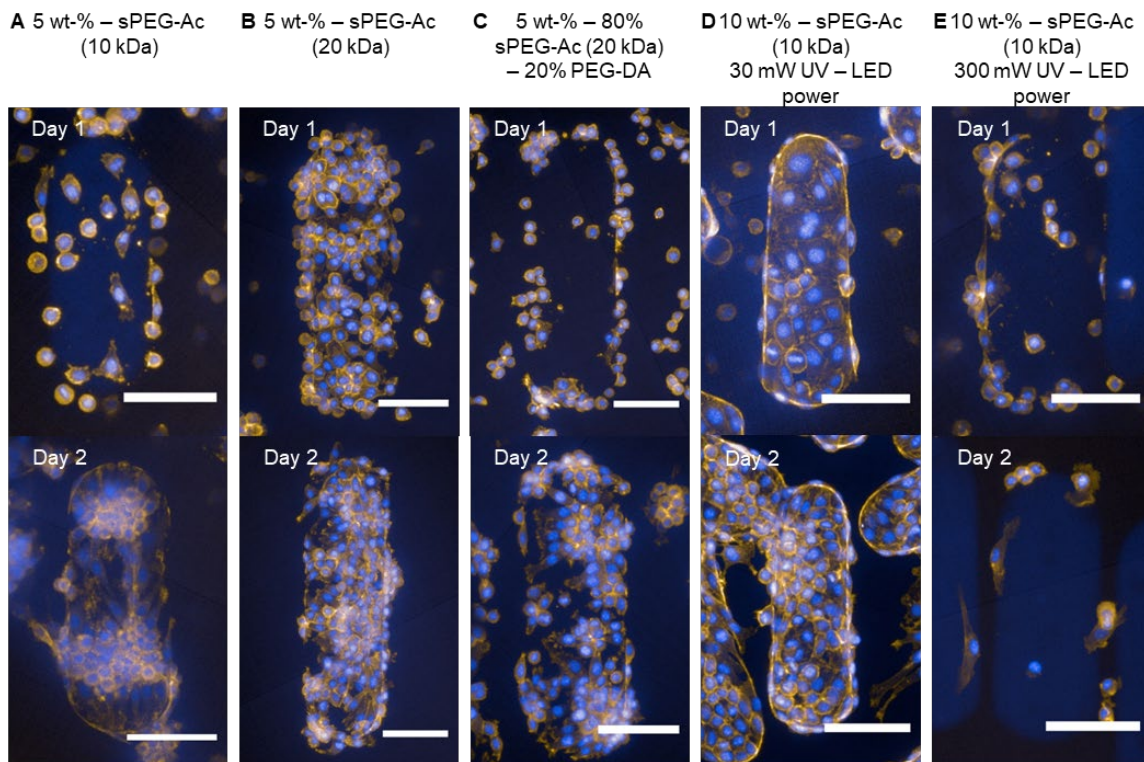
Figure 5.9: L929 cell-microgel interaction. Fluorescent confocal images show cell attachment and spreading on microgels ($n > 30$) A) 5 wt% – 100% sPEG-Ac (10 kDa) – 0% PEG-DA, B) 5 wt% – 100% sPEG-Ac (20 kDa) – 0% PEG-DA, C) 5 wt% – 80% sPEG-Ac (20 kDa) – 20% PEG-DA, D) 10 wt% – sPEG-Ac (10 kDa) – 0% PEG-DA, 30 mW UV-LED power, and E) 10 wt% – sPEG-Ac (10 kDa) – 0% PEG-DA, 300 mW UV-LED power after 1 day and 2 days of culture. Cell nuclei and actin filament are fluorescently labelled with DAPI (blue) and Phalloidin594 (yellow), respectively. Scale bars represent 100 μm.

The microgels exposed to 300 mW UV-LED do not support any cell attachment, even after 2 days, likely due to the highly crosslinked surface, not allowing the peptide GRGDS-PC to bind there. To better understand the mechanobiology on the 10 wt% sPEG-Ac (10 kDa) (30 mW UV-LED power irradiation) microgels, we immunostain the Yes-associated

protein (YAP) as it shows an intracellular localization, which can be correlated to how well cells interact with their substrate. YAP is predominantly in the cell nucleus when cells are grown and spreading nicely on stiff substrates (50 kPa).[432–434] Supporting previously published trends, we observe predominant localization of YAP in the cell nucleus for our 10 wt% sPEG-Ac (10 kDa) (30 mW UV-LED power irradiation) microgels (see Figure 5.10).[432,433]
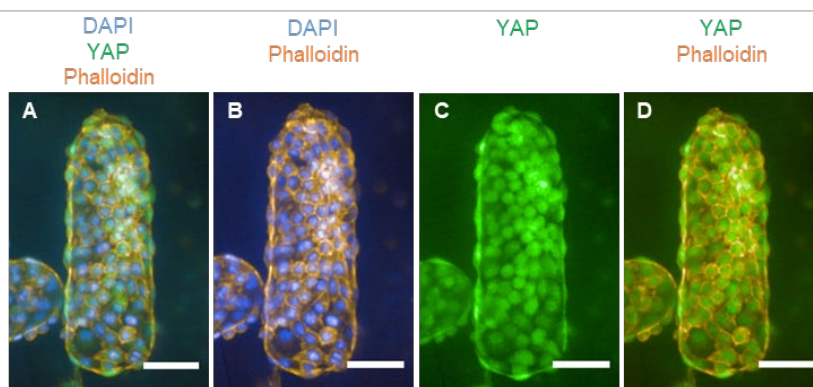
Figure 5.10: Characterization of mechanobiology via immunostaining of Yes-associated protein (YAP). L929 cells attached on the microgels (10 wt-% - sPEG-Ac (10 kDa) 30 mW UV – LED power) are stained with A) DAPI405 (blue), YAP488 (green), and Phalloidin594 (orange), B) DAPI405 (blue) and Phalloidin594 (orange), C) YAP488 (green), and D) YAP488 (green) and Phalloidin594 (orange). Scale bar represents 100 μm.

Besides stiffness, it has already been reported that the viscoelasticity of hydrogels can significantly influence cell-material interaction.[96,435,436] Recent work has revealed that viscoelasticity of a material can regulate fundamental cell behaviour, such as spreading, growth, proliferation, migration, and differentiation, enabling cells to spread also on softer viscoelastic hydrogels.[96] Therefore, we characterize the storage modulus G' and loss modulus G'' of the microgels as shown in Figure 5.11. The viscoelastic behaviour of the microgels is evaluated by the parameter $\tan \delta$ that describes the ratio between G'' to G', while for $\tan \delta < 1$, the elastic and for $\tan \delta > 1$, the viscous part of the material is dominant. We observe similar $\tan \delta$ for all microgels in a range of $\tan \delta = 0.1$-0.2, which means that the microgels are elastic and that mainly the accessibility of the RGD peptide influences cell adhesion, spreading, and proliferation.
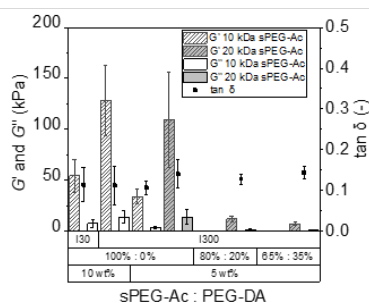
Figure 5.11. Mechanical characterization of rod-shaped microgels for determination of viscoelasticity. Storage modulus *G'* and loss modulus *G''* are determined at a frequency of 1 Hz, an oscillation amplitude of 100 nm and an indentation depth of 1 μm using dynamic mechanical analysis (DMA) mode of the Pavone Nanoindenter (Optics11Life, Amsterdam, Netherlands). Tan δ = 0.1 – 0.2 indicates that elastic behaviour is represented in all microgels. Data is presented as mean ± s. d., *n* > 10 microgels.

5.3   Conclusion

In this study, we obtain better understanding of how the internal structure of soft rod-shaped microgels in comparison to bulk hydrogels can be affected by changing different parameters of the molecular building blocks. This internal structure influences both the stiffness and the diffusion properties of molecules throughout the gels. We also demonstrate that the microgels can support cell spreading and growth and that this mainly depends on how efficiently the cell adhesive peptide GRGDS-PC can be coupled to the free acrylates on the microgel surface.

In conclusion, our findings represent a roadmap to design rod-shaped microgels for tissue engineering or drug delivery applications, to vary their internal structures and obtain the desired stiffness and diffusion properties for nutrients and other bioactive molecules. Furthermore, our microgels can easily be modified with biological or chemical functional groups. They can be used for the synthesis of 3D macroporous constructs that allow for 3D cell culture and tissue growth.

5.4   Materials and Methods

5.4.1   Chemicals, Cells Lines, and Cell Culture Material

The following materials are purchased and used as per the instruction. ABILEM 90 (Evonik Nutrition), 8-arm PEG-acrylate 10 kDa (Biochempeg Scientific Inc., ≥95%), 8-arm PEG-

acrylate 20 kDa (Biochempeg Scientific Inc., ≥95%), 4',6-diamidino-2-phenylindole (Thermo Fisher Scientific), Dulbecco's modified Eagle medium (DMEM, Gibco), ethanol (VWR-chemicals,99.8%), fluorescein isothiocyanate (Thermo Fisher Scientific), fluorescein isothiocyanate dextran average mol wt 10 kDa (Sigma-Aldrich), fluorescein isothiocyanate dextran average mol wt 20 kDa (Sigma-Aldrich), fluorescein isothiocyanate dextran average mol wt 60-76 kDa (Sigma-Aldrich), goat anti-mouse secondary antibody, Alexa Fluor 488 (Invitrogen), GRGDS-PC (H-Gly-Arg-Gly-Asp-Ser-Pro-Cys-OH (trifluoroacetate salt), CPC Scientific), hexane (Sigma-Aldrich, >99%), lithium phenyl-2,4,6-trimethylbenzoylphosphinate (Sigma-Aldrich, ≥95%), methacryloxyethyl thiocarbamoyl rhodamine-B (Polyscience), mouse dermal fibroblasts, Novec 7100 (Sigma-Aldrich), oil red o (Sigma-Aldrich), paraffin (VWR-chemicals), paraformaldehyde (Sigma-Aldirch), phosphate buffered saline (PBS, pH=7.4, $c = 1\times$, Thermo Fisher Scientific), phalloidin-iFluor 594 reagent (abcam), 2-propanol (99.5%), polyethylene glycol diacrylate 700 Da (Sigma-Aldrich), quinoline yellow (Sigma-Aldrich, 95%), SYLGARD 184 silicone elastomer kit (Dowsil), Tridecafluoro-1,1,2,2-tetrahydrooctyl-trichlorosilane (Sigma-Aldrich, 97%), and toluene (VWR-chemicals, 99.5%), yes-associated protein 1 (YAP) (Santa Cruz Biotechnology).

5.4.2   Preparation of PDMS-Based Microfluidic Devices

Microfluidic chips are used for the production of microfluidic devices via soft lithography. Sylgard 184 silicone elastomer (PDMS) (20 g) and curing agent (2 g) were mixed in a ratio of 10:1 in a plastic cup. Colored devices were prepared by adding a mixture of oil red O (60 mg) and quinoline yellow (3.0 mg) dissolved in toluene (2.0 g). The mixture was placed in a desiccator under vacuum (10^{-3} mbar) to remove entrapped air. It was subsequently casted into the form and the air was evacuated again in the desiccator. The PDMS was cured in the oven for 12 h at 60 °C. The cured PDMS is cut out and holes for inlets and outlets in the channels are punched (biopsy puncher, inner diameter 0.75 mm). The PDMS form is washed three times with *iso*-propanol and water. A glass slide (76 x 52 x 1 mm, Marienfeld, Germany) is rinsed three times with acetone, *iso*-propanol and water. For bonding, the PDMS replica and glass slide were activated in an oxygen plasma oven (PVA TePla 100E, Germany, Wettenberg) at an oxygen flow of 30 mL min^{-1} for 40 s at 100 W. The PDMS replica is bonded to the glass slide with the structured side and baked in the

oven for 3 h at 60 °C for complete adhesion. A hydrophobic surface coating inside of the microfluidic device channels is achieved by silanization with Tridecafluoro-1,1,2,2-tetrahydrooctyl-trichlorosilane. To enable that, the microfluidic device is positioned in a desiccator together with the silane and evacuated overnight. NovecTM HFE 7500 with 1.5 vol% of KrytoxTM 157 FSH surfactant was used to remove remaining residues of the silane from the microfluidic device.

5.4.3 Preparation of pre-polymer solutions

Pre-polymer solutions are prepared in brown glass vials to prevent undesired photoinitiation. Mixtures of 8-arm PEG-acrylate (M_W = 10 kDa or 20 kDa) and PEG-diacrylate (700 Da) with a total concentration of 5 wt-% or 10 wt-% are dissolved in Milli-Q water using 50 mol-% lithium phenyl-2,4,6-trimethylbenzoylphosphinate (LAP) photoinitiator with respect to reactive free acrylate groups. The absolute concentrations of the pre-polymer solutions containing different molar mass and ratios of 8-arm PEG-Ac (M_W = 10 kDa or 20 kDa) to PEG-DA (M_n = 700 Da) are shown in Table 5.1-5.3. The pre-polymer solutions are used for rheology measurements as well as microfluidics.

Table 5.3: Absolute concentrations of polymer solutions (5 wt-%) containing 8-arm PEG-Ac (10 kDa) and PEG-DA (700 Da) that are used for rheology measurements and production of hydrogels as well as microgels in microfluidics.

8-arm PEG-Ac [%]	PEG-DA [%]	c(8-arm PEG-Ac) [mol/mL]	c(8-arm PEG-Ac) [g/mL]	c(PEG-DA) [mol/mL]	c(PEG-DA) [g/mL]	c(LAP) [mol/mL]	c(LAP) [g/mL]
100	0	$5.30 \cdot 10^{-9}$	$5.30 \cdot 10^{-5}$	0	0	$2.12 \cdot 10^{-8}$	$6.23 \cdot 10^{-6}$
80	20	$4.21 \cdot 10^{-9}$	$4.21 \cdot 10^{-5}$	$1.50 \cdot 10^{-8}$	$1.05 \cdot 10^{-5}$	$3.18 \cdot 10^{-8}$	$9.37 \cdot 10^{-6}$
65	35	$3.40 \cdot 10^{-9}$	$3.40 \cdot 10^{-5}$	$2.61 \cdot 10^{-8}$	$1.83 \cdot 10^{-5}$	$3.97 \cdot 10^{-8}$	$1.17 \cdot 10^{-6}$
50	50	$2.60 \cdot 10^{-9}$	$2.60 \cdot 10^{-5}$	$3.71 \cdot 10^{-8}$	$2.60 \cdot 10^{-5}$	$4.75 \cdot 10^{-8}$	$1.40 \cdot 10^{-6}$
35	65	$1.81 \cdot 10^{-9}$	$1.81 \cdot 10^{-5}$	$4.80 \cdot 10^{-8}$	$3.36 \cdot 10^{-5}$	$5.53 \cdot 10^{-8}$	$1.63 \cdot 10^{-6}$
20	80	$1.03 \cdot 10^{-9}$	$1.03 \cdot 10^{-5}$	$5.88 \cdot 10^{-8}$	$4.12 \cdot 10^{-5}$	$6.29 \cdot 10^{-8}$	$1.85 \cdot 10^{-6}$
0	100	0	0	$7.30 \cdot 10^{-8}$	$5.11 \cdot 10^{-5}$	$7.30 \cdot 10^{-8}$	$2.15 \cdot 10^{-6}$

Table 5.4: Absolute concentrations of polymer solutions (5 wt-%) containing 8-arm PEG-Ac (20 kDa) and PEG-DA (700 Da) that are used for rheology measurements and production of hydrogels as well as microgels in microfluidics.

8-arm PEG-Ac [%]	PEG-DA [%]	c(8-arm PEG-Ac) [mol/mL]	c(8-arm PEG-Ac) [g/mL]	c(PEG-DA) [mol/mL]	c(PEG-DA) [g/mL]	c(LAP) [mol/mL]	c(LAP) [g/mL]
100	0	$2.64 \cdot 10^{-9}$	$5.28 \cdot 10^{-5}$	0	0	$1.06 \cdot 10^{-8}$	$3.11 \cdot 10^{-6}$
80	20	$2.10 \cdot 10^{-9}$	$4.20 \cdot 10^{-5}$	$1.50 \cdot 10^{-8}$	$1.05 \cdot 10^{-5}$	$2.34 \cdot 10^{-8}$	$6.88 \cdot 10^{-6}$
65	35	$1.70 \cdot 10^{-9}$	$3.39 \cdot 10^{-5}$	$2.61 \cdot 10^{-8}$	$1.83 \cdot 10^{-5}$	$3.29 \cdot 10^{-8}$	$9.67 \cdot 10^{-6}$
50	50	$1.30 \cdot 10^{-9}$	$2.60 \cdot 10^{-5}$	$3.71 \cdot 10^{-8}$	$2.60 \cdot 10^{-5}$	$4.23 \cdot 10^{-8}$	$1.24 \cdot 10^{-5}$
35	65	$9.04 \cdot 10^{-10}$	$1.81 \cdot 10^{-5}$	$4.80 \cdot 10^{-8}$	$3.36 \cdot 10^{-5}$	$5.16 \cdot 10^{-8}$	$1.52 \cdot 10^{-5}$
20	80	$5.14 \cdot 10^{-10}$	$1.03 \cdot 10^{-5}$	$5.88 \cdot 10^{-8}$	$4.12 \cdot 10^{-5}$	$6.08 \cdot 10^{-8}$	$1.79 \cdot 10^{-5}$
0	100	0	0	$7.30 \cdot 10^{-8}$	$5.11 \cdot 10^{-5}$	$7.30 \cdot 10^{-8}$	$2.15 \cdot 10^{-5}$

Table 5.5: Absolute concentrations of polymer solutions (10 wt-%) containing 8-arm PEG-Ac (10 kDa) and PEG-DA (700 Da) that are used for rheology measurements and production of hydrogels as well as microgels in microfluidics.

8-arm PEG-Ac [%]	PEG-DA [%]	c(8-arm PEG-Ac) [mol/mL]	c(8-arm PEG-Ac) [g/mL]	c(PEG-DA) [mol/mL]	c(PEG-DA) [g/mL]	c(LAP) [mol/mL]	c(LAP) [g/mL]
100	0	$1.13 \cdot 10^{-8}$	$1.13 \cdot 10^{-4}$	0	0	$4.50 \cdot 10^{-8}$	$1.32 \cdot 10^{-5}$

5.4.4 Determination of suitable LAP concentration

The required LAP concentration for the synthesis of bulk hydrogels as well as microgels is determined via pulsing experiments using the microfluidic set-up as described. Aqueous pre-polymer solution of sPEG-Ac (10 kDa or 20 kDa) with total concentration of 5 wt-% and different ratios of photoinitiator LAP between 10 mol-% and 200 mol-% related to reactive free acrylate groups are prepared. The gelation time of the microgels is determined as that is needed to produce sufficiently polymerized rod-shaped microgels, which do not change their shape after leaving the microfluidic channel (see Figure 5.4). The gelation time of the microgels needs to be very short, so rods can be created inside the microfluidic channel with high speed. Thus, setting the gelation time, we get a minimum suitable LAP concentration of 50 mol-% that is used for all experiments, since higher initiator concentration might lead to undesired polymerization termination reactions.

5.4.5 Microgel synthesis

Microgel rods are synthesized via on-chip gelation in a flow focusing microfluidic device with a channel diameter of 80 µm operated in plug-flow regime as described previously.[107] The flow rates are controlled using Hamilton® syringes and PHD ULTRA syringe pumps by Harvard Apparatus. The microfluidic devices are colored to prevent undesired light scattering. The dispersed phase is prepared and used as described previously.[107] The continuous phase is formed by a mixture of paraffin oil and hexadecane (v:v 1:1) with 8 % (w/w) of ABIL® EM90 as surfactant. On-chip polymerization of the dispersed phase is initiated via irradiation using a UV-LED ($\lambda = 365$ nm, spot diameter = 4.7 mm) light intensity of 17 mW mm^{-2} (dose = 467 mJ mm^{-2}) with controllable energy transfer (at 300 mW) in the straight part of the chip (Scheme 1) as previously reported.[107] Obtained microgel rods are purified by washing five times with n-hexane, iso-propanol, and water, respectively.

5.4.6 Rheology measurements

Rheological characterization of pre-polymer solution is performed using a TA Instrument Discovery HR-3 hybrid rheometer with a 20 mm parallel-plate geometry. 381 µL of the pre-polymer solution is pipetted in the rheometer at a temperature of 25 °C. To polymerize the hydrogel, a time-dependent measurement at UV light intensity of 10 mW cm^{-2} and a frequency of 1 Hz and an oscillation strain of 1% is conducted. Subsequently, frequency-dependent measurements at a set oscillation strain of 1% was performed. Finally, strain-dependent measurements at a frequency of 1 Hz are performed.

5.4.7 Determination of critical overlap concentration

For the rheological characterization of the intrinsic viscosity of the polymers, the rheometer is used with a cone-plate geometry, which has a diameter of 40 mm and a cone angle of 1.986°. Aqueous pre-polymer solutions containing 8-arm PEG-acrylate (10 kDa), 8-arm PEG-acrylate (20 kDa), and PEG-diacrylate (700 Da) with total concentrations between 1 wt% and 7 wt% are prepared, respectively, while no photoinitiator was added. 581 µL of the solution is pipetted in the rheometer and the viscosity is measured as a function of

increasing shear rate (1 - 1000 Hz). The intrinsic viscosity is determined as the y-intercept by graphically plotting the reduced viscosity as a function of the polymer concentration (see Figure 5.1). The critical overlap concentration is calculated to be 2.5 divided by the intrinsic viscosity.

5.4.8   Characterization of diffusion properties of bulk hydrogels

Bulk hydrogels are formed in 96 well plates from aqueous pre-polymer solutions containing 100% sPEG-AC (10 kDa), 100% sPEG-AC (20 kDa), 80% sPEG-AC (20 kDa) – 20% PEG-DA, and 65% sPEG-AC (20 kDa) – 35% PEG-DA while maintaining a constant total concentration of 5 wt-%. The hydrogels are crosslinked via FRP using 50 mol-% photoinitiator LAP related to reactive free acrylate groups. The polymerization reaction is triggered by UV-irradiation on the pre-polymer solution, while the same UV-LED ($\lambda = 365$ nm) light dose (467 mJ mm^{-2}) as during the microfluidics is used for comparability. 50 µL of aqueous FITC-dextran solutions are pipetted on the bulk hydrogels are incubated for 48 h to guarantee required diffusion time. The diffusion of FITC-dextrans is characterized in triplicates creating z-stacks in hydrogel heights of 100 µm in confocal laser scanning microscopy (CLSM).

5.4.9   Characterization of mechanical properties of microgel rods

The mechanical properties of the microgel rods are determined using a Pavone Nanoindenter (Optics11Life, Amsterdam, The Netherlands) containing a cantilever-based probe with a spherical tip radius of 9 µm and a cantilever stiffness of 0.241 N m^{-1}. For each sample, 15 microgels are measured at a minimum of 3 different locations. The piezo speed is 1 µm s^{-1} and the indentation-depth is 2 µm. All measurements are performed in aqueous solution and at room temperature. The effective Young's modulus E_{eff} (kPa) is calculated from the obtained load-indentation curves using the Hertzian contact model. The analysis of the data is performed using the Software Dataviewer V2.5 (Optics11Life, Amsterdam, The Netherlands).

Moreover, dynamic mechanical analysis (DMA) of the microgels is conducted to determine the storage modulus G' and loss modulus G'' using the same device and cantilever-based

probe. Oscillatory frequency sweep is measured on at least microgels for each sample at a frequency of 1 Hz, an amplitude of 100 nm and an indentation depth of 1 μm.

5.4.10 Characterization of diffusion properties of microgel rods

The diffusion properties of FITC in the polymer network of microgel rods is characterized via Fluorescence Recovery After Photobleaching (FRAP) technique using CLSM on a Leica TCS SP8 microscope (Leica Microsystems, Germany). The microgels are incubated in a PBS solution of FITC (1 mg mL^{-1}) by stirring for 48 h. The bleaching experiments are performed using a 10x dry objective and a 488 nm-line of an Argon-ion laser operating at 80% output power. A region of interest (ROI) is set on the microgel and a time-series of digital images (512x512 pixels) are recorded with an interval of 1.292 s using a highly attenuated laser beam (1.3% transmission). After recording of 30 pre-bleach images, a circularly area with a diameter of ca. 10 μm is bleached at maximum laser intensity (100% transmission) for 1.292 s. Another time-series of 100 post-bleach images with the same settings are recorded. The analysis was based on solving the diffusion equation in the Fourier domain (Tsay et al., 1991 and Migliorini et al., 2017)[437,438] and noticing that the inverse relative intensity 1-I_{rel} follows the same differential equation, as long as the concentration.

$$I_{rel} = \frac{(I - I_b)}{(I_0 - I_b)} \frac{I_{0,ref}}{I_{ref}}$$

Where I_{rel} is the relative intensity, I is the intensity in the image, I_0 is the intensity without bleaching, obtained as the average of the prebleach images. I_b is a constant background offset, the dark count of the detector (may be set to 0). The reference intensity, I_{ref} is the intensity of a non-bleached area normalized to the average of the same area in the prebleach average image, $I_{0,ref}$. This reference compensates for the bleaching caused by the imaging itself.

Transforming the image stack to its spatial Fourier transform, we can collect information from the pixels closest to the center (the zero spatial frequency component). The diffusion equation has a solution in the form:

$$c(q_x, q_y, t) = c_0(q_x, q_y) e^{-4\pi(q_x^2 + q_y^2)D\,t}$$

An algorithm was written for the analysis in python [https://www.python.org, https://scipy.org] fitting the individual spatial frequency components and the selected components together. This way we could detect if any spatial anisotropy occurred in the data set. This method allows us to obtain the diffusion coefficient independent of the bleaching profile as long as the spatial variation of the original concentration is low in comparison to that of the bleached area.

5.4.11 Porosity in STED microscopy and analysis

STED Fluorescence microscopy was performed on microgels labelled with Rhodamine B using CLSM on a Leica TCS SP8 3X microscope (Leica Microsystems, Mannheim, Germany) equipped with an 80 MHz pulsed White Light Laser (Leica Microsystems, Mannheim, Germany) for excitation and a pulsed 775 nm laser (Leica Microsystems, Mannheim, Germany) for the stimulated emission depletion. The excitation wavelength was set to 541 nm and the detection band was restricted from 560 nm to 700 nm with a multiband spectrophotometer in front of a Hybrid Detector (HyD, Leica Microsystems, Mannheim, Germany). All images were recorded at a room temperature of 22.5 °C using a 86x/1.2 NA water immersion objective (Leica HC PL APO CS2 - STED White) in a 1024x1024 pixels format with 20 nm pixel size.

Images were processed using a custom written python script (python 3.10 [https://python.org]) based on the ImageP processing package ([https://github.com/tomio13/ImageP]). Images were sharpened removing off-plane light with a background correction. Background was calculated convolving the images with a somewhat flattened Gaussian kernel with a standard deviation of 10 pixels, but truncated to a window size of 41 pixels (normalized to its sum). Then this background was subtracted and negative intensity values were set to zero.

The resulted image was smoothened convolving it with another Gaussian kernel (standard deviation of 1 pixel, windows size 7 pixels). The result was turned to a binary image cut with a threshold determined using Otsu's method[439]. The so identified pores were subjected to skeletonization based on a distance transform, where local maxima were identified with a minimum step size of 1 (intensity difference between neighbors). Because the distance transform sets the pixels to the square of their Eucledian distance from the

nearest edge pixel, the double of the square root of the maximum pixels provides a local size measure of the pores. These values were collected and used to build histograms of the distances within the image.

5.4.12 Characterization of microgel rods via cryo-SEM

To characterize the structure of microgel rods in a swollen state, a cryo-SEM analysis was used. Samples from microgel suspension (in water) were placed on a sample holder and frozen in liquid ethane for 1 min. The frozen samples were transferred and kept in liquid nitrogen before imaging. To better visualize their internal structures, microgels were sectioned inside the pre-chamber and were imaged at 3 kV and 2.3 µA using the field emission scanning electron microscope SU4800 (Hitachi Ltd. Corporation). Several sublimation steps (5 - 15 min up to −80 °C) were performed to remove the ice crystals and reduce the artifacts during imaging.

5.4.13 Characterization of the density of microgel rods via optical diffraction tomography

The refractive index (RI) distribution of the microgel rods was measured by optical diffraction tomography (ODT). The ODT setup employs Mach-Zehnder interferometry to measure multiple complex optical fields from various incident angles, as previously described elsewhere.[440] A solid-state laser beam (λ = 532 nm, 50 mW, CNI Optoelectronics Technology Co.) was split into two paths using a beamsplitter. One beam was used as a reference beam and the other beam illuminated the sample on the stage of an inverted microscope (Axio Observer 7, Carl Zeiss AG) through a tube lens (f = 175 mm) and a water-dipping objective lens (NA = 1.0, 40×, Carl Zeiss AG). The beam diffracted by the sample was collected by a high numerical aperture objective lens (NA = 1.3, 63×, water immersion, Carl Zeiss AG). To reconstruct a 3D RI tomogram of the sample, the sample was illuminated from 150 different incident angles scanned by a dual-axis galvanomirror (GVS212/M, Thorlabs Inc.) located at the conjugate plane of the sample. The diffracted beam interfered with the reference beam at an image plane, and generated a spatially modulated hologram, which was recorded with a CMOS camera (MQ042MG-CM-TG, ximea GmbH). The field-of-view of the camera covers 173.6 µm × 173.6 µm. The

complex optical fields of light scattered by the samples were retrieved from the recorded holograms by applying a Fourier transform-based field retrieval algorithm.[441] The 3D RI distribution of the samples was reconstructed from the retrieved complex optical fields via the Fourier diffraction theorem, employing the first-order Rytov approximation.[442,443] A more detailed description of tomogram reconstruction can be found elsewhere.[444] The MATLAB script for ODT reconstruction can be found under https://github.com/OpticalDiffractionTomography/ODT_Reconstruction.

5.4.14 Characterization of the mechanical properties of microgel rods via Brillouin microscopy

The acquisition of Brillouin frequency shift maps was performed by Brillouin microscopy. The optical setup for Brillouin microscopy employs a custom-made confocal configuration for acoustic phonon excitation and signal detection and a Brillouin spectrometer consisting of a two-stage virtually imaged phase array (VIPA) etalon, as previously described in detail elsewhere.[445] Briefly, the sample was illuminated by a frequency-modulated diode laser beam (λ = 780.24 nm, DLC TA PRO 780, Toptica). The laser light was coupled into a single-mode fibre and directed into the side port of a commercial inverted microscope stand (Axio Observer 7, Zeiss), where an objective lens (20×, NA = 0.5, EC Plan-Neofluar, Zeiss) illuminated the focused laser beam on the sample mounted on a motorized stage of the microscope stand. The backscattered light from the sample was collected by the same objective lens and coupled into the second single-mode fibre to achieve confocality before being delivered to the Brillouin spectrometer. Within the Brillouin spectrometer, two VIPA etalons (OP-6721-6743-4, Light Machinery) with the free spectral range of 15.2 GHz converted the frequency shift of the light into the angular dispersion in the Brillouin spectrum, which were acquired by a sCMOS camera (Prime BSI, Teledyne) with an exposure time of 0.5 s per measurement point. The two-dimensional Brillouin frequency map of the sample was measured by scanning the x-y motorized stage on the microscope stand, with the translational step size of 0.5 μm. The Brillouin microscope was controlled with custom acquisition software written in C++ (https://github.com/BrillouinMicroscopy/BrillouinAcquisition).

5.4.15 Characterization of reactive acrylate groups via Raman spectroscopy

The remaining reactive acrylate groups of bulk hydrogels after photopolymerization reaction are determined via Raman spectroscopy using a Bruker RFS 100/S spectrometer equipped with a neodymium-doped yttrium aluminum garnet laser with a wavelength of 1064 nm. The bulk hydrogels are freeze-dried and solid samples are measured with an output power of 200 mW and 1000 scans for each sample, while the spectral range is set from 400 to 4000 cm^{-1} with a resolution of 4 cm^{-1}. The baseline correction of the spectra is realized with the software OPUS 4.0. Further analysis of the spectra and normalization are performed with OriginPro 2018. A calibration graph is recorded for different molar ratios of end groups of linear PEG-OH (20 kDa) and sPEG-Ac (20 kDa) dissolved in DCM, while the evaporated homogeneous samples are measured. Thereby, the molar ratio is plotted against the ratio of peak areas of PEG-OH (20 kDa) (Integrated peak area at a Raman shift of 1456 cm^{-1} to 1508 cm^{-1}) and sPEG-Ac (20 kDa) (Integrated peak area at a Raman shift of 1618 cm^{-1} to 1653 cm^{-1}). Bulk hydrogels are produced as described for the characterization of diffusion properties of bulk hydrogels. For the calculation of reactive acrylate groups in the hydrogels, the peak areas of aliphatic C-C and acrylate groups are integrated at a Raman shift of 1454 cm^{-1} to 1508 cm^{-1} and 1648 cm^{-1} to 1670 cm^{-1}, respectively.

5.4.16 Characterization of GRGDS-PC on microgel surface via XPS analysis

Microgels are post-functionalized with GRGDS-PC via thiol-Michael addition of cysteine present in the peptide with the free acrylate groups of the microgels. Therefore, 1500 microgels are incubated with 1 aliquot (10 µL) of GRGDS-PC solution (25 mg/mL) in phosphate buffer (200 µL, pH 8.0) overnight. Microgels are washed 3 times with PBS. A droplet of microgels is pipetted on a glass surface and the surface of the dried sample is measured via XPS (X-Ray Photoelectron Spectroscopy) using an Ultra Axis Spectrometer (Kratos Analytical, Manchester, UK). The samples are excited with monoenergetic Al Kα1,2 radiation (1486.6 eV) with a total output of 144 W (12kV x 12mA). The spectral resolution, i.e. the half-width of the ester carbon 1s line determined on a PET sample, was <0.68 eV for the high-resolution elemental spectra. The information depth is approx. 10 nm

for polymeric materials. A nitrogen-to-carbon (N/C) ratio is determined (see Table S5), which indicates how much peptide is coupled to the microgels.

5.4.17 Cell culture

L929 fibroblasts are cultured in tissue culture flasks in Dulbecco's modified eagle's medium (DMEM, Gibco) supplemented with 10% FBS (Biowest or Gibco), 1% Antibiotics micotic (AMB, Gibco) at 37°C with 5% CO_2 at humid environment.

For cell culture experiments, a thin layer of sterile PDMS (40:1 PDMS:curing agent) is coated on a glass-bottom well plate and crosslinked at 60 °C for 90 min. A droplet of microgel suspension (20 µL) is transferred on the PDMS and microgels are sedimented for 1 h. The well plates are filled up with media. L929 mouse fibroblasts cells (100 µL) with a concentration of 1000 cells $µL^{-1}$ are seeded in the microgel suspension and cultivated for 1 and 2 days.

5.4.18 Cell-microgel interaction via live imaging

Microgels are incubated at room temperature overnight with GRGDS-PC (1 Aliquot (10 µL (25 mg mL^{-1})) per 1500 microgels) in phosphate buffer (pH 7.4, 200 µL). Microgels are 3 times washed with PBS and incubated with ethanol (70%) for 1 h and UV sterilized. Afterwards, microgels are washed 5 times with sterile water. A droplet of microgel suspension (20 µL) is transferred on glass-bottom well plate (Ibidi GmbH). After microgels are sedimented for 1 h, the well plates are filled up with media DMEM with 10% FBS and 1% AMB (DMEM+). L929 mouse fibroblasts cells (100 µL) with a concentration of 1000 cells $µL^{-1}$ are seeded and live images are recorded via differential interference contract (DIC) microscopy on a ZEISS Axio Observer Z1 inverted microscope at 37 °C and 5% CO_2 at humid environment. Images are taken every 1 min at a fixed z-position for 120 min.

5.4.19 Immunostaining and image processing

After 1-2 days of culture, the samples are washed 2 times with PBS and the cells are fixed using 4% paraformaldehyde for 30 min at room temperature, followed by washing with

PBS for 10 min, 0.1% TritonX 100 (v/v) for 10 min and again PBS for 10 min. F-actin filaments of the cells are stained using phalloidin594 (1:1000 Abcam) in 4% BSA in PBS for 1 h, followed by washing with PBS. Cell nuclei are stained using 4',6-diamidino-2-phenylindole (DAPI) (1:100) in PBS for 20 min, followed by washing twice with PBS. Additionally, YAP protein (Santa Cruz Biotechnology) is stained using YAP primary antibody (1:200) in 1% BSA in PBS and 0.1% TritonX 100 (v/v) for 2 h. The samples are washed 3 times with PBS for 10 min. Anti-mouse secondary 488 (Invitrogen, 1:200 in PBS) is incubated for 1 h and afterwards washed again with PBS. The samples are stored at 4°C.The stained cells are imaged using an Opera Phenix Plus High-Content Screening System (PerkinElmer, USA) with a 20x water objective and the 405 nm, 488 nm and 568 nm laser. Z-stacks of around 100 μm thickness are acquired for each sample.

5.4.20 Statistical analysis

All data points are shown as mean average with error bars indicating standard deviation (±SEM) with at least a sample size of 3. Statistical analysis is used to calculate significance using Bonferroni method and performed in OriginPro2018, while the P values for statistical significance are represented with stars (ns = non-significant = $P > 0.05$, *$P < 0.05$, **$P < 0.01$, ***$P < 0.001$, ****$P < 0.0001$).

144

6 Outlook

Microgels, incorporated with TNFα antibodies (adalimumab) for non-systemic specific scavenging of inflammation-mediating cytokine TNFα are described in **Chapter 3** and demonstrate to be promising candidates as a new approach for local treatment of IBD. Due to the high accessibility of their internal surface, the microgels have shown high specific binding capacity of TNFα in the presence of human colorectal adenocarcinoma cells. In particular, the microgels also scavenge TNFα produced by human macrophages to mimic the *in vivo* situation of IBD. Besides for the treatment of IBD, these antibody-functionalized microgels could be applied via intra-articular injection in the treatment of rheumatoid arthritis.

In **Chapter 4**, the specific targeting and binding of HA-functionalized microgels to CD44 receptor-expressing human colorectal adenocarcinoma cells HT29 has been shown by the formation of a microgel layer on the epithelial surface, with the aim to mimic the degraded mucus and shield the tissue from harmful bacteria. In further experiments, to better mimic the *in vivo* situation and guarantee a reliable and reproducible experimental set-up, the microgels can be incubated with CD44 expressing intestinal cell lines in an *in vitro* intestinal model including a representative flow chamber.

To further test the ability of these functional microgels to locally treat IBD, the scavenging of pro-inflammatory cytokine TNFα, as well as targeting and binding to inflamed intestinal cells to mimic the degraded mucus, could be combined in multifunctional microgels. To achieve this, sPEG-based microgels can be co-polymerized in microfluidics with the corresponding optimal GMA and HA-Ac concentrations as determined in the previous studies. Afterwards, the microgels can be post-functionalized with TNFα antibodies under mild aqueous conditions. Besides using *in vitro* intestine models, the functionality of the microgels should be tested *in vivo* using animal models.

To localize the path and accumulation of the microgels in the intestine, the microgels could be functionalized with imaging units. For this purpose, the glycidyl-functional microgels could be functionalized with near-infrared fluorescent dyes, such as commercially available amine-functionalized IRDye 800CW. Alternatively, photoacoustically active conjugated polymer particles with a size range between 200 nm and 500 nm can be incorporated inside the microgels to enable photoacoustic imaging. As a further option, microgels can be

functionalized with commercially available amine-functionalized porphyrins with gadolinium cation (Gd^{3+}) or magnetic nanoparticles to use MRI.

For the evaluation of the biological efficacy of the microgels *in vivo*, they could be applied in an IBD mouse model. As IBD is believed to result from the interplay between different factors, such as microbial dysbiosis, damage of epithelial barrier integrity, and immune cell deregulation, different intestinal injury mouse models have been used to investigate the therapeutic activity of different antibody-based drugs or antibiotics.[446] For example, the rectal infusion of *clostridium difficile* toxin A (TcdA) triggers local colonic inflammation and damage of colonic mucosa in mouse model.[447] Besides various chemical induced colitis models, DSS-induced colitis in mice is widely used as an IBD disease model.[448] As a third option, a chronic intestinal inflammation has been seen in interleukin 10 knockout (IL10-KO) mice.[449] The microgels can be applied either via gavage (DSS and IL10-KO model) or rectal infusion (TcdA model). The biological effect of the microgels can be assessed via histological analysis, as well as RT-PCR-based quantification of inflammatory markers. Different treatment regimen can help to understand whether the microgels can have a healing effect on the induced disease models. To prove the therapeutic efficacy of multifunctional microgels, direct delivery of the therapeutic molecules, as well as non-functionalized microgels, can be applied as controls.

Besides the production of functional microgels to address different challenges of IBD, a deeper insight is given in **Chapter 5** how to alter the mechanical, biochemical, and structural properties of the microgels by changing the precursor molecules and how this affects diffusion of molecules through the microgels and the interaction with cells. For this purpose, the influence of the concentration, molecular weight, and architecture of the molecular building blocks on the internal structure of rod-shaped microgels was systematically investigated. Rod-shaped microgels were chosen due to their growing importance in 3D cell culture and tissue engineering, as their larger aspect ratio provides more opportunities to structure materials. Therefore, the influence of post-functionalization with RGD on cell-microgel interaction was analyzed.

In a next step, the studied rod-shaped microgels could be easily chemically or biologically modified and interlinked to form macroporous scaffolds that allow for 3D cell culture and

tissue growth. Due to their high aspect ratio, rod-shaped microgels entail large open voids when they assemble and interlink to form scaffolds, introducing macroscopic porosity. Furthermore, the polymer network structure of the microgels enables the diffusion of oxygen and nutrients to supply the cells inside the voids of the scaffold, avoiding the formation of a necrotic core when the tissue grows dense.[107]

Depending on the application, rod-shaped microgels with different dimensions can be produced via microfluidics, or via PRINT and compartmentalized jet microfluidics for microgel sizes down to 1 μm. In comparison to isotropic microgels, rod-shaped microgels entail directionality due to their anisometric shape, which allows for structural guidance and, therefore, can induce regeneration of more complex oriented tissues, such as heart, muscle, or spinal cord.[450]

In general, 3D *in vitro* grown hierarchical tissues could be used to better mimic human organs as part of the organ-on-a-chip technology. These devices could be a key technology for disease modelling, drug testing, and toxicity screening.

References

[1]   A. Kumar, N. Yassin, A. Marley, V. Bellato, C. Foppa, G. Pellino, P. Myrelid, M. Millan, B. Gros, N. Avellaneda, et al., *Therap. Adv. Gastroenterol.* **2023**, *16*, 1.

[2]   J. Torres, S. Mehandru, J. F. Colombel, L. Peyrin-Biroulet, *Lancet* **2017**, *389*, 1741.

[3]   R. Ungaro, S. Mehandru, P. B. Allen, L. Peyrin-Biroulet, J. F. Colombel, *Lancet* **2017**, *389*, 1756.

[4]   R. J. Porter, M. J. Arends, A. M. D. Churchhouse, S. Din, *J. Crohn's Colitis* **2021**, *15*, 2131.

[5]   C. H. R. Choi, I. Al Bakir, A. L. Hart, T. A. Graham, *Nat. Rev. Gastroenterol. Hepatol.* **2017**, *14*, 218.

[6]   G. Roda, S. Chien Ng, P. G. Kotze, M. Argollo, R. Panaccione, A. Spinelli, A. Kaser, L. Peyrin-Biroulet, S. Danese, *Nat. Rev. Dis. Prim.* **2020**, *6*, 22.

[7]   B. Derkx, J. Taminiau, S. Radema, A. Stronkhorst, C. Wortel, G. Tytgat, S. van Deventer, *Lancet* **1993**, *342*, 173.

[8]   H. M. van Dullemen, S. J. H. van Deventer, D. W. Hommes, H. A. Bijl, J. Jansen, G. N. J. Tytgat, J. Woody, *Gastroenterology* **1995**, *109*, 129.

[9]   R. Melsheimer, A. Geldhof, I. Apaolaza, T. Schaible, *Biol. Targets Ther.* **2019**, *13*, 139.

[10]   L. M. Genaro, L. E. M. Gomes, A. P. M. de F. Franceschini, H. D. Ceccato, R. N. de Jesus, A. P. Lima, C. K. Nagasako, J. J. Fagundes, M. de L. S. Ayrizono, R. F. Leal, *Am. J. Transl. Res.* **2021**, *13*, 13916.

[11]   J. D. Doecke, F. Hartnell, P. Bampton, S. Bell, G. Mahy, Z. Grover, P. Lewindon, L. V. Jones, K. Sewell, K. Krishnaprasad, et al., *Aliment. Pharmacol. Ther.* **2017**, *45*, 542.

[12]   J. Hyams, W. Crandall, S. Kugathasan, A. Griffiths, A. Olson, J. Johanns, G. Liu, S. Travers, R. Heuschkel, J. Markowitz, et al., *Gastroenterology* **2007**, *132*, 863.

[13]   G. Horneff, M. M. B. Seyger, D. Arikan, J. Kalabic, J. K. Anderson, A. Lazar, D. A. Williams, C. Wang, R. Tarzynski-Potempa, J. S. Hyams, *J. Pediatr.* **2018**, *201*, 166.

[14]   J. F. Colombel, P. J. Rutgeerts, W. J. Sandborn, M. Yang, A. Camez, P. F. Pollack, R. B. Thakkar, A. M. Robinson, N. Chen, P. M. Mulani, et al., *Clin. Gastroenterol. Hepatol.* **2014**, *12*, 414.

[15]   M. A. Kamm, S. B. Hanauer, R. Panaccione, J. F. Colombel, W. J. Sandborn, P. F. Pollack, Q. Zhou, A. M. Robinson, *Aliment. Pharmacol. Ther.* **2011**, *34*, 306.

[16]   S. Schreiber, W. Reinisch, J. F. Colombel, W. J. Sandborn, D. W. Hommes, A. M. Robinson, B. Huang, K. G. Lomax, P. F. Pollack, *J. Crohn's Colitis* **2013**, *7*, 213.

[17] R. Panaccione, J. F. Colombel, W. J. Sandborn, G. D'Haens, Q. Zhou, P. F. Pollack, R. B. Thakkar, A. M. Robinson, *Aliment. Pharmacol. Ther.* **2013**, *38*, 1236.

[18] W. J. Sandborn, J. F. Colombel, G. D'Haens, G. Van Assche, D. Wolf, M. Kron, A. Lazar, A. M. Robinson, M. Yang, J. D. Chao, et al., *Aliment. Pharmacol. Ther.* **2013**, *37*, 204.

[19] J. S. Hyams, A. Griffiths, J. Markowitz, R. N. Baldassano, W. A. Faubion, R. B. Colletti, M. Dubinsky, J. Kierkus, J. Rosh, Y. Wang, et al., *Gastroenterology* **2012**, *143*, 365.

[20] J. F. Colombel, W. J. Sandborn, S. Ghosh, D. C. Wolf, R. Panaccione, B. Feagan, W. Reinisch, A. M. Robinson, A. Lazar, M. Kron, et al., *Am. J. Gastroenterol.* **2014**, *109*, 1771.

[21] U. N. Shivaji, C. L. Sharratt, T. Thomas, S. C. L. Smith, M. Iacucci, G. W. Moran, S. Ghosh, N. Bhala, *Aliment. Pharmacol. Ther.* **2019**, *49*, 664.

[22] J. Li, Z. Zhang, X. Wu, J. Zhou, D. Meng, P. Zhu, *Front. Pharmacol.* **2021**, 12:746396.

[23] T. Bongartz, A. J. Sutton, M. J. Sweeting, I. Buchan, E. L. Matteson, **2014**, *295*.

[24] V. E. R. Asscher, Q. van der Vliet, K. van der Aalst, A. van der Aalst, E. C. Brand, A. E. van der Meulen-de Jong, B. Oldenburg, M. J. Pierik, B. van Tuyl, N. Mahmmod, et al., *Int. J. Colorectal Dis.* **2020**, *35*, 2331.

[25] E. H. Lee, Y. A. Kang, A. Y. Leem, M. S. Park, Y. S. Kim, S. K. Kim, J. Chang, S. Y. Kim, *Sci. Rep.* **2017**, *7*, 6473.

[26] A. Pitiot, N. Heuzé-Vourc'h, T. Sécher, *Antibodies* **2022**, *11*, 56.

[27] R. G. A. Jones, A. Martino, *Crit. Rev. Biotechnol.* **2016**, *36*, 506.

[28] C. C. Baniel, E. G. Sumiec, J. A. Hank, A. M. Bates, A. K. Erbe, A. A. Pieper, A. G. Hoefges, R. B. Patel, A. L. Rakhmilevich, Z. S. Morris, et al., *J. Immunother. Cancer* **2020**, *8*, e001262.

[29] A. D. Lam, I. K. Styles, D. Senyschyn, E. Cao, A. Anshabo, M. Abdallah, R. Mikrani, C. J. Nowell, C. J. H. Porter, O. M. Feeney, et al., *Mol. Pharm.* **2023**, *20*, 2053.

[30] A. C. Lima, C. Cunha, A. Carvalho, H. Ferreira, N. M. Neves, *ACS Appl. Mater. Interfaces* **2018**, *10*, 13839.

[31] M. Ries, B. Moulari, M. A. Shetab Boushehri, M. E. Ali, D. Molnar, A. Béduneau, Y. Pellequer, A. Lamprecht, *Pharmaceutics* **2022**, *14*, 352.

[32] M. R. Abedin, K. Powers, R. Aiardo, D. Barua, S. Barua, *Sci. Rep.* **2021**, *11*, 7347.

[33] L. J. Mohan, J. S. Daly, B. M. Ryan, Z. Ramtoola, *Eur. J. Pharm. Sci.* **2023**, *183*, 106379.

[34] H. J. Im, C. G. England, L. Feng, S. A. Graves, R. Hernandez, R. J. Nickles, Z. Liu,

D. S. Lee, S. Y. Cho, W. Cai, *ACS Appl. Mater. Interfaces* **2016**, *8*, 17955.

[35]   S. Behzadi, V. Serpooshan, W. Tao, M. A. Hamaly, M. Y. Alkawareek, E. C. Dreaden, D. Brown, A. M. Alkilany, O. C. Farokhzad, M. Mahmoudi, *Chem. Soc. Rev.* **2017**, *46*, 4218.

[36]   W. J. Smith, G. Wang, H. Gaikwad, V. P. Vu, E. Groman, D. W. A. Bourne, D. Simberg, *ACS Nano* **2018**, *12*, 12523.

[37]   M. R. Gordon, M. Canakci, L. Li, J. Zhuang, B. Osborne, S. Thayumanavan, *Bioconjug. Chem.* **2015**, *26*, 2198.

[38]   M. Garcia-Diaz, M. del Mar Cendra, R. Alonso-Roman, M. Urdaniz, E. Torrents, E. Martinez, *Pharmaceutics* **2022**, *14*, 1552.

[39]   R. Donahue, J. K. Sahoo, S. Rudolph, Y. Chen, D. L. Kaplan, *Adv. Healthc. Mater.* **2023**, 2300301.

[40]   L. Sardelli, D. P. Pacheco, A. Ziccarelli, M. Tunesi, O. Caspani, A. Fusari, F. B. Vangosa, P. Petrini, **2019**, 15887.

[41]   P. Praveschotinunt, A. M. Duraj-thatte, I. Gelfat, F. Bahl, D. B. Chou, N. S. Joshi, *Nat. Commun.* **2019**, 5580.

[42]   Y. Lee, K. Sugihara, M. G. G. Iii, S. Jon, N. Kamada, J. J. Moon, *Nat. Mater.* **2020**, *19*, 118.

[43]   E. Filidou, G. Kolios, *Pharmaceuticals* **2021**, *14*, 1181.

[44]   D. Li, J. Li, T. Chen, X. Qin, L. Pan, X. Lin, W. Liang, Q. Wang, *ACS Appl. Mater. Interfaces* **2023**, *15*, 38273.

[45]   S. Zhang, J. Ermann, M. D. Succi, A. Zhou, M. J. Hamilton, B. Cao, J. R. Korzenik, J. N. Glickman, P. K. Vemula, L. H. Glimcher, et al., *Sci. Transl. Med.* **2015**, *7*, 300ra128.

[46]   H. Liu, Z. Cai, F. Wang, L. Hong, L. Deng, J. Zhong, Z. Wang, W. Cui, *Adv. Sci.* **2021**, *8*, 2101619.

[47]   J. Xu, M. Tam, S. Samaei, S. Lerouge, J. Barralet, M. M. Stevenson, M. Cerruti, *Acta Biomater.* **2017**, *48*, 247.

[48]   J. Li, D. J. Mooney, *Nat. Rev. Mater.* **2016**, *1*, 16071.

[49]   L. Hong, G. Chen, Z. Cai, H. Liu, C. Zhang, F. Wang, Z. Xiao, J. Zhong, L. Wang, Z. Wang, et al., *Adv. Sci.* **2022**, *9*, 2200281.

[50]   D. J. McClements, *Adv. Colloid Interface Sci.* **2017**, *240*, 31.

[51]   V. K. Switacz, S. K. Wypysek, R. Degen, J. J. Crassous, M. Spehr, W. Richtering, *Biomacromolecules* **2020**, *21*, 4532.

[52]   M. Tian, X. Mu, D. Fan, Z. Liu, Q. Liu, K. Yue, Z. Song, J. Luo, S. Zhang, *Adv. Mater.* **2023**, *35*, 2303436.

[53] J. Zhu, *Biomaterials* **2010**, *31*, 4639.

[54] Z. Wang, Q. Ye, S. Yu, B. Akhavan, *Adv. Healthc. Mater.* **2023**, *12*, 2300105.

[55] C. C. Lin, K. S. Anseth, *Pharm. Res.* **2009**, *26*, 631.

[56] E. Bakaic, N. M. B. Smeets, T. Hoare, *RSC Adv.* **2015**, *5*, 35469.

[57] S. P. Zustiak and J. B. Leach, *Biomacromolecules* **2010**, *11*, 1348.

[58] S. C. Rizzi, M. Ehrbar, S. Halstenberg, G. P. Raeber, H. G. Schmoekel, H. Hagenmüller, R. Müller, F. E. Weber, J. A. Hubbell, J. A. Hubbell, *Biomacromolecules* **2006**, *7*, 3019.

[59] M. Zacchigna, F. Cateni, S. Drioli, G. M. Bonora, *Polymers (Basel).* **2011**, *3*, 1076.

[60] A. J. D. Krüger, O. Bakirman, L. P. B. Guerzoni, A. Jans, D. B. Gehlen, D. Rommel, T. Haraszti, A. J. C. Kuehne, L. De Laporte, *Adv. Mater.* **2019**, *31*, 1903668.

[61] K. Han, R. Tiwari, T. Heuser, A. Walther, *Macromol. Rapid Commun.* **2016**, *37*, 1323.

[62] J. A. Bonham, M. A. Faers, J. S. Van Duijneveldt, *Soft Matter* **2014**, *10*, 9384.

[63] J. K. Oh, R. Drumright, D. J. Siegwart, K. Matyjaszewski, *Prog. Polym. Sci.* **2008**, *33*, 448.

[64] H. J. M. Wolff, J. Linkhorst, T. Göttlich, J. Savinsky, A. J. D. Krüger, L. De Laporte, M. Wessling, *Lab Chip* **2020**, *20*, 285.

[65] T. Glawdel, C. Elbuken, C. L. Ren (**2013**) Droplet Generation in Microfluidics. In: Li, D. (eds) Encyclopedia of Microfluidics and Nanofluidics. Springer, Boston, MA. https://doi.org/10.1007/978-3-642-27758-0_1713-1

[66] T. Trantidou, M. S. Friddin, A. Salehi-Reyhani, O. Ces, Y. Elani, *Lab Chip* **2018**, *18*, 2488.

[67] Z. Zhang, Q. Li, C. Yesildag, C. Bartsch, X. Zhang, W. Liu, A. Loebus, Z. Su, M. C. Lensen, *Polymers (Basel).* **2018**, *10*, 970.

[68] L. P. B. Guerzoni, J. C. Rose, D. B. Gehlen, A. Jans, T. Haraszti, M. Wessling, A. J. C. Kuehne, L. De Laporte, *Small* **2019**, *15*, 1900692.

[69] T. Rossow, J. A. Heyman, A. J. Ehrlicher, A. Langhoff, D. A. Weitz, R. Haag, S. Seiffert, *J. Am. Chem. Soc.* **2012**, *134*, 4983.

[70] T. Femmer, A. Jans, R. Eswein, N. Anwar, M. Moeller, M. Wessling, A. J. C. Kuehne, *ACS Appl. Mater. Interfaces* **2015**, *7*, 12635.

[71] S. Boesveld, A. Jans, D. Rommel, M. Bartneck, M. Möller, L. Elling, C. Trautwein, P. Strnad, A. J. C. Kuehne, *ACS Appl. Mater. Interfaces* **2019**, *11*, 25017.

[72] N. d'Avanzo, C. Celia, A. Barone, M. Carafa, L. Di Marzio, H. A. Santos, M. Fresta, *Adv. Ther.* **2020**, *3*, 1900170.

[73] M. A. Shetab Boushehri, D. Dietrich, A. Lamprecht, *Pharmaceutics* **2020**, *12*, 510.

[74] E. D. Namiot, A. V. Sokolov, V. N. Chubarev, V. V. Tarasov, H. B. Schiöth, *Int. J. Mol. Sci.* **2023**, *24*, 787.

[75] A. Pepe, P. Podesva, G. Simone, *Sci. Rep.* **2017**, *7*, 6014.

[76] F. Schröer, T. J. Paul, D. Wilms, T. H. Saatkamp, N. Jäck, J. Müller, A. K. Strzelczyk, S. Schmidt, *Molecules* **2021**, *26*, 263.

[77] S. Bulut, S. H. Jung, T. Bissing, F. Schmitt, M. Bund, S. Braun, A. Pich, *Small* **2023**, *19*, 13.

[78] D. Wöll, *RSC Adv.* **2014**, *4*, 2447.

[79] N. Hauck, N. Seixas, S. P. Centeno, R. Schlüßler, G. Cojoc, P. Müller, J. Guck, D. Wöll, L. A. Wessjohann, J. Thiele, *Polymers (Basel).* **2018**, *10*, 1055.

[80] E. Axpe, D. Chan, G. S. Offeddu, Y. Chang, D. Merida, H. L. Hernandez, E. A. Appel, *Macromolecules* **2019**, *52*, 6889.

[81] T. R. Hoare, D. S. Kohane, *Polymer (Guildf).* **2008**, *49*, 1993.

[82] D. Klinger, K. Landfester, *Polymer (Guildf).* **2012**, *53*, 5209.

[83] Y. Yu, J. Wang, Q. Shao, J. Shi, W. Zhu, *Sci. Rep.* **2016**, *6*, 19500.

[84] S. Gao, J. M. Guisán, J. Rocha-Martin, *Anal. Chim. Acta* **2022**, *1189*, 338907.

[85] A. Margineanu, J. J. Chan, D. J. Kelly, S. C. Warren, D. Flatters, S. Kumar, M. Katan, C. W. Dunsby, P. M. W. French, *Sci. Rep.* **2016**, *6*, 28186.

[86] E. K. Petutschnig, L. Pierdzig, J. Mittendorf, J. M. Niebisch, V. Lipka, *J. Exp. Bot.* **2023**, 746.

[87] B. Valeur, *Mol. Fluoresc.* **2001**, *8*, 247.

[88] E. Mauri, S. Scialla, *cosmetics* **2023**, *10*, 113.

[89] S. P. Hlaing, J. Cao, J. Lee, J. Kim, A. Saparbayeva, D. Kwak, H. Kim, S. Hwang, H. Yun, H. R. Moon, et al., *Pharmaceutics* **2022**, *14*, 2118.

[90] F. I. Camacho, C. Muñoz, L. Sánchez-Verde, A. I. Sáez, M. Alcántara, R. Rodríguez, *Histopathology* **1999**, *35*, 144.

[91] M. Yu, S. Jambhrunkar, P. Thorn, J. Chen, W. Gu, C. Yu, *Nanoscale* **2013**, *5*, 178.

[92] L. Zhong, Y. Liu, L. Xu, Q. Li, D. Zhao, Z. Li, H. Zhang, H. Zhang, Q. Kan, J. Sun, et al., *Asian J. Pharm. Sci.* **2019**, *14*, 521.

[93] N. G. Kotla, O. Burke, A. Pandit, Y. Rochev, *Nanomaterials* **2019**, *9*, 1246.

[94] J. M. Rios de la Rosa, P. Pingrajai, M. Pelliccia, A. Spadea, E. Lallana, A. Gennari, I. J. Stratford, W. Rocchia, A. Tirella, N. Tirelli, *Adv. Healthc. Mater.* **2019**, *8*, 1901182.

[95] M. D. A. Norman, S. A. Ferreira, G. M. Jowett, L. Bozec, E. Gentleman, *Nat. Protoc.* **2021**, *16*, 2418.

[96]   O. Chaudhuri, J. Cooper-White, P. A. Janmey, D. J. Mooney, V. B. Shenoy, *Nature* **2020**, *584*, 535.

[97]   D. E. Discher, P. Janmey, Y. L. Wang, *Science (80-).* **2005**, *310*, 1139.

[98]   S. Babu, I. Chen, S. Vedaraman, J. Gerardo-Nava, C. Licht, Y. Kittel, T. Haraszti, J. Di Russo, L. De Laporte, *Adv. Funct. Mater.* **2022**, *32*, 2202468.

[99]   M. Galluzzi, C. S. Biswas, Y. Wu, Q. Wang, B. Du, F. J. Stadler, *NPG Asia Mater.* **2016**, *8*, e327.

[100] M. Krieg, G. Fläschner, D. Alsteens, B. M. Gaub, W. H. Roos, G. J. L. Wuite, H. E. Gaub, C. Gerber, Y. F. Dufrêne, D. J. Müller, *Nat. Rev. Phys.* **2019**, *1*, 41.

[101] Y. H. Chim, L. M. Mason, N. Rath, M. F. Olson, M. Tassieri, H. Yin, *Sci. Rep.* **2018**, *8*, 14462.

[102] E. Larrañeta, M. Henry, N. J. Irwin, J. Trotter, A. A. Perminova, R. F. Donnelly, *Carbohydr. Polym.* **2018**, *181*, 1194.

[103] A. Fallacara, E. Baldini, S. Manfredini, S. Vertuani, *Polymers (Basel).* **2018**, *10*, 701.

[104] C. Ligorio, A. Mata, *Nat. Rev. Bioeng.* **2023**, *1*, 518.

[105] K. Sano, Y. Ishida, T. Aida, *Angew. Chemie - Int. Ed.* **2018**, *57*, 2532.

[106] T. H. Qazi, J. Wu, V. G. Muir, S. Weintraub, S. E. Gullbrand, D. Lee, D. Issadore, J. A. Burdick, *Adv. Mater.* **2022**, *34*, 2109194.

[107] D. Rommel, M. Mork, S. Vedaraman, C. Bastard, L. P. B. Guerzoni, Y. Kittel, R. Vinokur, N. Born, T. Haraszti, L. De Laporte, *Adv. Sci.* **2022**, *9*, 2103554.

[108] J. C. Rose, M. Cámara-Torres, K. Rahimi, J. Köhler, M. Möller, L. De Laporte, *Nano Lett.* **2017**, *17*, 3782.

[109] J. Kim, Y. P. Kong, S. M. Niedzielski, R. K. Singh, A. J. Putnam, A. Shikanov, *Soft Matter* **2016**, *12*, 2076.

[110] T. Kirila, A. Smirnova, A. Razina, A. Tenkovtsev, A. Filippov, *Polymers (Basel).* **2020**, *12*, 800.

[111] Z. Ye, R. Subramanian, *Can. J. Chem. Eng.* **2023**, *101*, 5162.

[112] X. Lang, W. R. Lenart, J. E. P. Sun, B. Hammouda, M. J. A. Hore, *Macromolecules* **2017**, *50*, 2145.

[113] P. G. de Gennes, *Macromolecules* **1980**, *13*, 1069.

[114] S. Alexander, *J Phys* **1977**, *38*, 983.

[115] M. Daoud, J. P. Cotton, *J. Phys. Paris* **1982**, *43*, 531.

[116] A. Jusufi, C. N. Likos, *Rev. Mod. Phys.* **2009**, *81*, 1753.

[117] D. Dukes, Y. Li, S. Lewis, B. Benicewicz, L. Schadler, S. K. Kumar, *Macromolecules* **2010**, *43*, 1564.

[118] J. P. Flory, *Principles of Polymer Chemistry*, Cornell University Press, Ithaca, New York, **1953**.

[119] P. G. de Gennes, *Scaling Concepts in Polymer Physics*, Cornell University Press, Ithaca, New York, **1979**.

[120] J. C. Rose, D. B. Gehlen, T. Haraszti, J. Köhler, C. J. Licht, L. De Laporte, *Biomaterials* **2018**, *163*, 128.

[121] S. Qiong Liu, Q. Tian, L. Wang, J. L. Hedrick, J. H. Po Hui, Y. Yan Yang, P. L. R. Ee, *Macromol. Rapid Commun.* **2010**, *31*, 1148.

[122] K. Goodarzi, R. Lane, S. S. Rao, *J. Biomed. Mater. Res. - Part A* **2023**, 1.

[123] E. M. Ahmed, *J. Adv. Res.* **2015**, *6*, 105.

[124] E. Caló, V. V. Khutoryanskiy, *Eur. Polym. J.* **2015**, *65*, 252.

[125] O. Erol, A. Pantula, W. Liu, D. H. Gracias, *Adv. Mater. Technol.* **2019**, *4*, 1900043.

[126] J. C. Rose, L. De Laporte, *Adv. Healthc. Mater.* **2018**, *7*, 1701067.

[127] J. J. Rice, M. M. Martino, L. De Laporte, F. Tortelli, P. S. Briquez, J. A. Hubbell, *Adv. Healthc. Mater.* **2013**, *2*, 57.

[128] Pich, *Polym Int* **2006**, *55*, 961.

[129] F. Sanchez, K. Sobolev, *Constr. Build. Mater.* **2010**, *24*, 2060.

[130] G. Guisbiers, S. Mejía-Rosales, F. Leonard Deepak, *J. Nanomater.* **2012**, 2012.

[131] A. J. D. Krüger, J. Köhler, S. Cichosz, J. C. Rose, D. B. Gehlen, T. Haraszti, M. Möller, L. De Laporte, *Chem. Commun.* **2018**, *54*, 6943.

[132] L. M. T. Martinez, O. V. Kharissova, B. I. Kharisov, in *Handbook of Ecomaterials*, ed. M. Ahumada, E. Jacques, C. Calderon, F. Martínez-Gómez, Springer-Verlag, Berlin, Heidelberg, **2017**, pp. 1-20.

[133] M. Chan, A. Almutairi, *Mater. Horizons* **2016**, *3*, 21.

[134] J. Zhu, W. Sun, J. Zhang, Y. Zhou, M. Shen, C. Peng, X. Shi, *Bioconjug. Chem.* **2017**, *28*, 2692.

[135] V. Keskar, N. W. Marion, J. J. Mao, R. A. Gemeinhart, *Tissue Eng. - Part A* **2009**, *15*, 1695.

[136] J. Sun, D. Wei, Y. Zhu, M. Zhong, Y. Zuo, H. Fan, X. Zhang, *Biomaterials* **2014**, *35*, 4759.

[137] H. Wang, S. C. Heilshorn, *Adv. Mater.* **2015**, *27*, 3717.

[138] M. J. Webber, P. Y. W. Dankers, *Macromol. Biosci.* **2019**, *19*, 1800452.

[139] M. Diba, S. Spaans, S. I. S. Hendrikse, M. M. C. Bastings, M. J. G. Schotman, J. F. van Sprang, D. J. Wu, F. J. M. Hoeben, H. M. Janssen, P. Y. W. Dankers, *Adv. Mater.* **2021**, *33*, 2008111.

[140] D. Seliktar, **2012**, *336*, 1124.

[141] A. Vashist, A. K. Kaushik,S. Ahmad and M. Nair, *Nanogels for Biomedical Applications*, Royal Society of Chemistry, Cambridge, **2018**.

[142] M. H. Chen, J. J. Chung, J. E. Mealy, S. Zaman, E. C. Li, M. F. Arisi, P. Atluri, J. A. Burdick, *Macromol. Biosci.* **2019**, *19*, 1800248.

[143] D. F. Emerich, C. G. Thanos, *Expert Opin. Biol. Ther.* **2003**, *3*, 655.

[144] E. Mauri, S. M. Giannitelli, M. Trombetta, A. Rainer, *Gels* **2021**, *7*, 36.

[145] Y. Bin Hamzah, S. Hashim, W. A. W. A. Rahman, *J. Polym. Res.* **2017**, *24*, 134.

[146] D. Suzuki, K. Horigome, T. Kureha, S. Matsui, T. Watanabe, *Polym. J.* **2017**, *49*, 695.

[147] M. Karg, A. Pich, T. Hellweg, T. Hoare, L. A. Lyon, J. J. Crassous, D. Suzuki, R. A. Gumerov, S. Schneider, I. I. Potemkin, W. Richtering, *Langmuir* **2019**, *35*, 6231.

[148] N. M. B. Smeets, T. Hoare, *J. Polym. Sci. Part A Polym. Chem.* **2013**, *51*, 3027.

[149] S. Seiffert, *Angew. Chemie - Int. Ed.* **2013**, *52*, 11462.

[150] Y. Hertle, T. Hellweg, *J. Mater. Chem. B* **2013**, *1*, 5874.

[151] C. Echeverria, S. Fernandes, M. Godinho, J. Borges, P. Soares, *Gels* **2018**, *4*, 54.

[152] R. Pelton, *Adv. Colloid Interface Sci.* **2000**, *85*, 1.

[153] P. Saha, R. Ganguly, X. Li, R. Das, N. K. Singha, A. Pich, *Macromol. Rapid Commun.* **2021**, *42*, 2100112.

[154] S. Singh, M. Möller, A. Pich, *J. Polym. Sci. Part A Polym. Chem.* **2013**, *51*, 3044.

[155] S. Saxena, C. E. Hansen, L. A. Lyon, *Acc. Chem. Res.* **2014**, *47*, 2426.

[156] F. A. Plamper, W. Richtering, *Acc. Chem. Res.* **2017**, *50*, 131.

[157] T. Kamperman, M. Karperien, S. Le Gac, J. Leijten, *Trends Biotechnol.* **2018**, *36*, 850.

[158] W. Jiang, M. Li, Z. Chen, K. W. Leong, *Lab Chip* **2016**, *16*, 4482.

[159] S. Kühn, J. Sievers, A. Stoppa, N. Träber, R. Zimmermann, P. B. Welzel, C. Werner, *Adv. Funct. Mater.* **2020**, *30*,1908857.

[160] B. Stawicki, T. Schacher, H. Cho, *Gels* **2021**, *7*, 63.

[161] V. Baskar, I. Salim Meeran, A. Subramani, Sruthi, A. Jawahar. T. K. Shabeer, *Int. J. Pharm. Pharm. Sci.* **2018**, *10*, 1.

[162] A. J. Sivaram, P. Rajitha, S. Maya, R. Jayakumar, M. Sabitha, *Wiley Interdiscip. Rev. Nanomedicine Nanobiotechnology* **2015**, *7*, 509.

[163] S. S. Das, P. Bharadwaj, M. Bilal, M. Barani, A. Rahdar, P. Taboada, S. Bungau, G. Z. Kyzas, *Polymers (Basel).* **2020**, *12*, 1397.

[164] Y. Jiang, J. Chen, C. Deng, E. J. Suuronen, Z. Zhong, *Biomaterials* **2014**, *35*, 4969.

[165] M. A. Grimaudo, A. Concheiro, C. Alvarez-Lorenzo, *J. Control. Release* **2019**, *313*, 148.

[166] A. C. Daly, L. Riley, T. Segura, J. A. Burdick, *Nat. Rev. Mater.* **2020**, *5*, 20.

[167] M. D. Neto, M. B. Oliveira, J. F. Mano, *Trends Biotechnol.* **2019**, *37*, 1011.

[168] J. M. Anderson, *Polym. Sci. A Compr. Ref.* **2012**, *9*, 363.

[169] S. Naahidi, M. Jafari, M. Logan, Y. Wang, Y. Yuan, H. Bae, B. Dixon, P. Chen, *Biotechnol. Adv.* **2017**, *35*, 530.

[170] K. Xue, X. Wang, P. W. Yong, D. J. Young, Y.-L. Wu, Z. Li, X. J. Loh, *Adv. Ther.* **2019**, *2*, 1800088.

[171] M. D. Swartzlander, C. A. Barnes, A. K. Blakney, J. L. Kaar, T. R. Kyriakides, S. J. Bryant, *Biomaterials* **2015**, *41*, 26.

[172] P. J. LeValley, R. Neelarapu, B. P. Sutherland, S. Dasgupta, C. J. Kloxin, A. M. Kloxin, *J. Am. Chem. Soc.* **2020**, *142*, 4671.

[173] V. K. Garripelli, J. K. Kim, R. Namgung, W. J. Kim, M. A. Repka, S. Jo, *Acta Biomater.* **2010**, *6*, 477.

[174] J. Hu, Y. Chen, Y. Li, Z. Zhou, Y. Cheng, *Biomaterials* **2017**, *112*, 133.

[175] S. Pradhan, K. A. Keller, J. L. Sperduto, J. H. Slater, *Adv. Healthc. Mater.* **2017**, *6*, 1700681.

[176] F. Alexis, E. Pridgen, L. K. Molnar, O. C. Farokhzad, *Mol. Pharm.* **2008**, *5*, 505.

[177] M. B. Browning, S. N. Cereceres, P. T. Luong, E. M. Cosgriff-Hernandez, *J. Biomed. Mater. Res. - Part A* **2014**, *102*, 4244.

[178] M. B. Browning, E. Cosgriff-Hernandez, *Biomacromolecules* **2012**, *13*, 779.

[179] D. Y. Lee, K. Choe, Y. J. Jeong, J. Yoo, S. M. Lee, J. H. Park, P. Kim, Y. C. Kim, *RSC Adv.* **2015**, *5*, 14482.

[180] R. Luxenhofer, M. Bezen, R. Jordan, *Macromol. Rapid Commun.* **2008**, *29*, 1509.

[181] S. M. Grayson, W. T. Godbey, *J. Drug Target.* **2008**, *16*, 329.

[182] C. X. Wang, S. Utech, J. D. Gopez, M. F. J. Mabesoone, C. J. Hawker, D. Klinger, *ACS Appl. Mater. Interfaces* **2016**, *8*, 16914.

[183] Y. Chen, N. Ballard, S. A. F. Bon, *Polym. Chem.* **2013**, *4*, 387.

[184] Y. Azuma, T. Terashima, M. Sawamoto, *Macromolecules* **2017**, *50*, 587.

[185] F. García, M. M. J. Smulders, *J. Polym. Sci. Part A Polym. Chem.* **2016**, *54*, 3551.

[186] A. C. Brown, S. E. Stabenfeldt, B. Ahn, R. T. Hannan, K. S. Dhada, E. S. Herman, V. Stefanelli, N. Guzzetta, A. Alexeev, W. A. Lam, et al., *Nat. Mater.* **2014**, *13*, 1108.

[187] H. Bachman, A. C. Brown, K. C. Clarke, K. S. Dhada, A. Douglas, C. E. Hansen, E.

Herman, J. S. Hyatt, P. Kodlekere, Z. Meng, et al., *Soft Matter* **2015**, *11*, 2018.

[188] J. Liu, Y. Pang, S. Zhang, C. Cleveland, X. Yin, L. Booth, J. Lin, Y. A. Lucy Lee, H. Mazdiyasni, S. Saxton, et al., *Nat. Commun.* **2017**, *8*, 124.

[189] C. B. Rodell, J. W. MacArthur, S. M. Dorsey, R. J. Wade, L. L. Wang, Y. J. Woo, J. A. Burdick, *Adv Funct Mater* **2015**, *25 (4)*, 636.

[190] H. K. S. Yadav, N. Anwar, A. Halabi, G. A. Alsalloum, *Insight Pharma Res.* **2017**, *1*, 5.

[191] J. S. Varghese, N. Chellappa, N. N. Fathima, *Colloids Surfaces B Biointerfaces* **2014**, *113*, 346.

[192] S. Allazetta, M. P. Lutolf, *Curr. Opin. Biotechnol.* **2015**, *35*, 86.

[193] Q. Feng, D. Li, Q. Li, X. Cao, H. Dong, *Bioact. Mater.* **2021**, *9*, 105.

[194] K. H. Bae, L. S. Wang, M. Kurisawa, *J. Mater. Chem. B* **2013**, *1*, 5371.

[195] M. Alvarado-Velez, S. B. Pai, R. V. Bellamkonda, *IEEE Trans. Biomed. Eng.* **2014**, *61*, 1474.

[196] A. Singh, N. A. Peppas, *Adv. Mater.* **2014**, *26*, 6530.

[197] Towards advanced cell therapies. *Nat Biomed Eng* **2**, 339–340 (2018). https://doi.org/10.1038/s41551-018-0256-4

[198] V. F. M. Segers, R. T. Lee, *Nature* **2008**, *451*, 937.

[199] Waage et al., *Physiol. Behav.* **2017**, *176*, 139.

[200] G. Choe, S. W. Kim, J. Park, J. Park, S. Kim, Y. S. Kim, Y. Ahn, D. W. Jung, D. R. Williams, J. Y. Lee, *Biomaterials* **2019**, *225*, 119513.

[201] A. S. Mao, J. W. Shin, S. Utech, H. Wang, O. Uzun, W. Li, M. Cooper, Y. Hu, L. Zhang, D. A. Weitz, et al., *Nat. Mater.* **2017**, *16*, 236.

[202] D. R. Griffin, W. M. Weaver, P. Scumpia, D. Di Carlo, T. Segura, *Nat. Mater.* **2015**, *14*, 737.

[203] Caliari, *Ecol. Austral* **2016**, *26*, 72.

[204] T. Kamperman, S. Henke, A. van den Berg, S. R. Shin, A. Tamayol, A. Khademhosseini, M. Karperien, J. Leijten, *Adv. Healthc. Mater.* **2017**, *6*, 1600913.

[205] D. Husman, P. B. Welzel, S. Vogler, L. J. Bray, N. Träber, J. Friedrichs, V. Körber, M. V. Tsurkan, U. Freudenberg, J. Thiele, et al., *Biomater. Sci.* **2020**, *8*, 101.

[206] J. Maitra, V. K. Shukla, *Am. J. Polym. Sci.* **2014**, *4*, 25.

[207] D. Crespy, K. Landfester, *Beilstein J. Org. Chem.* **2010**, *6*, 1132.

[208] T. Tadros, in *Encyclopedia of Colloid and Interface Science*, ed. T. Tadros, Springer-Verlag, Berlin, Heidelberg, **2013**, ch. M, pp. 685-731.

[209] S. Kawaguchi, K. Ito, *Adv. Polym. Sci.* **2005**, *175*, 299.

[210] V. Chaudhary, S. Sharma, *J. Polym. Res.* **2019**, *26*, 102.

[211] A. Pich and W. Richtering, *Chemical Design of Responsive Microgels*, Springer-Verlag, Berlin, Heidelberg, vol. 234, **2010**.

[212] R. Tiwari, T. Heuser, E. Weyandt, B. Wang, A. Walther, *Soft Matter* **2015**, *11*, 8342.

[213] K. T. M. Tran, T. D. Nguyen, *J. Sci. Adv. Mater. Devices* **2017**, *2*, 1.

[214] H. Zhang, J. K. Nunes, S. E. A. Gratton, K. P. Herlihy, P. D. Pohlhaus, J. M. DeSimone, *New J. Phys.* **2009**, *11*, 075018.

[215] J. C. Rose, M. Cámara-Torres, K. Rahimi, J. Köhler, M. Möller, L. De Laporte, *Nano Lett.* **2017**, *17*, 3782.

[216] D. Liu, H. Zhang, F. Fontana, J. T. Hirvonen, H. A. Santos, *Adv. Drug Deliv. Rev.* **2018**, *128*, 54.

[217] T. Heida, O. Otto, D. Biedenweg, N. Hauck, J. Thiele, *Polymers (Basel).* **2020**, *12*, 1760.

[218] L. P. B. Guerzoni, J. Bohl, A. Jans, J. C. Rose, J. Koehler, A. J. C. Kuehne, L. De Laporte, *Biomater. Sci.* **2017**, *5*, 1549.

[219] D. Hovermann, T. Rossow, R. J. Gübeli, S. Seiffert, W. Weber, *Macromol. Biosci.*, **2014**, *14*, 1730.

[220] D. Steinhilber, T. Rossow, S. Wedepohl, F. Paulus, S. Seiffert, R. Haag, *Angew. Chemie - Int. Ed.* **2013**, *52*, 13538.

[221] E. Stengelin, A. Kuzmina, G. L. Beltramo, M. F. Koziol, L. Besch, R. Schröder, R. E. Unger, W. Tremel, S. Seiffert, *Adv. Healthc. Mater.* **2020**, *9*, 1901820.

[222] K. W. Bong, J. Lee, P. S. Doyle, *Lab Chip* **2014**, *14*, 4680.

[223] J. Guan, N. Ferrell, L. James Lee, D. J. Hansford, *Biomaterials* **2006**, *27*, 4034.

[224] Y. Hu, Q. Wang, J. Wang, J. Zhu, H. Wang, Y. Yang, *Biomicrofluidics* **2012**, *6*, 026502.

[225] J. R. Tumbleston, D. Shirvanyants, N. Ermoshkin, R. Janusziewicz, A. R. Johnson, D. Kelly, K. Chen, R. Pinschmidt, J. P. Rolland, A. Ermoshkin, et al., *Science (80-).* **2015**, *347*, 1349.

[226] D. Dendukuri, S. S. Gu, D. C. Pregibon, T. A. Hatton, P. S. Doyle, *Lab Chip* **2007**, *7*, 818.

[227] Y. Nishizawa, S. Matsui, K. Urayama, T. Kureha, M. Shibayama, T. Uchihashi, D. Suzuki, *Angew. Chemie - Int. Ed.* **2019**, *58*, 8809.

[228] A. Mourran, Y. Wu, R. A. Gumerov, A. A. Rudov, I. I. Potemkin, A. Pich, M. Möller, *Langmuir* **2016**, *32*, 723.

[229] N. Sanson, J. Rieger, *Polym. Chem.* **2010**, *1*, 965.

[230] M. Suhail, J. M. Rosenholm, M. U. Minhas, S. F. Badshah, A. Naeem, K. U. Khan,

M. Fahad, *Ther. Deliv.* **2019**, *10*, 697.

[231] P. Boisseau, B. Loubaton, *Comptes Rendus Phys.* **2011**, *12*, 620.

[232] S. Sinjari, J. S. Freitag, C. Herold, O. Otto, D. M. Smith, H. D. H. Stöver, *J. Polym. Sci.* **2020**, *58*, 2317.

[233] S. Girardo, N. Träber, K. Wagner, G. Cojoc, C. Herold, R. Goswami, R. Schlüßler, S. Abuhattum, A. Taubenberger, F. Reichel, et al., *J. Mater. Chem. B* **2018**, *6*, 6245.

[234] R. Schlüßler, K. Kim, M. Nötzel, A. Taubenberger, S. Abuhattum, T. Beck, P. Müller, S. Maharana, G. Cojoc, A. Hermann, et al., *bioRxiv* **2020**, 2020.10.30.361808.

[235] N. Hauck, N. Seixas, S. P. Centeno, R. Schlüßler, G. Cojoc, P. Müller, J. Guck, D. Wöll, L. A. Wessjohann, J. Thiele, *Polymers (Basel).* **2018**, *10*, 1055.

[236] T. G. F. Souza, V. S. T. Ciminelli, N. D. S. Mohallem, *J. Phys. Conf. Ser.* **2016**, *733*, 012039.

[237] T. Kureha, H. Minato, D. Suzuki, K. Urayama, M. Shibayama, *Soft Matter* **2019**, *15*, 5390.

[238] R. K. Nicholas Dias, Yung Peng, *Anal Biochem.* **2016**, *501*, 4.

[239] S. Bhattacharjee, *J. Control. Release* **2016**, *235*, 337.

[240] K. Horigome, T. Ueki, D. Suzuki, *Polym. J.* **2016**, *48*, 273.

[241] M. Koch, M. K. Włodarczyk-Biegun, *Bioprinting* **2020**, *20*, e00098.

[242] R. Cui, Z. Zhang, J. Nie, B. Du, *Colloid Polym. Sci.* **2017**, *295*, 665.

[243] B. Krug, N. Koukourakis, J. W. Czarske, *Opt. Express* **2019**, *27*, 26910.

[244] R. Macháň, Y. H. Foo, T. Wohland, *Biophys. J.* **2016**, *111*, 152.

[245] B. L. Sprague, J. G. McNally, *Trends Cell Biol.* **2005**, *15*, 84.

[246] A. Balaceanu, D. E. Demco, M. Möller, A. Pich, *Macromolecules* **2011**, *212*, 2161.

[247] A. Balaceanu, D. E. Demco, M. Möller, A. Pich, *Macromol. Chem. Phys.* **2011**, *212*, 2467.

[248] G. Aguirre, A. Khoukh, K. Chougrani, V. Alard, L. Billon, *Polym. Chem.* **2018**, *9*, 757.

[249] B. Sierra-Martín, M. S. Romero-Cano, T. Cosgrove, B. Vincent, A. Fernández-Barbero, *Colloids Surfaces A Physicochem. Eng. Asp.* **2005**, *270–271*, 296.

[250] M. Kappl, H. J. Butt, *Part. Part. Syst. Charact.* **2002**, *19*, 129.

[251] A. Mark, N. Helfricht, A. Rauh, M. Karg, G. Papastavrou, *Small* **2019**, *15*, 1902976.

[252] A. Aufderhorst-Roberts, D. Baker, R. J. Foster, O. Cayre, J. Mattsson, S. D. Connell, *Nanoscale* **2018**, *10*, 16050.

[253] A. D. Levin, E. A. Shmytkova, B. N. Khlebtsov, *J. Phys. Chem. C* **2017**, *121*, 3070.

[254] E. Siemes, O. Nevskyi, D. Sysoiev, S. K. Turnhoff, A. Oppermann, T. Huhn, W. Richtering, D. Wöll, *Angew. Chemie - Int. Ed.* **2018**, *57*, 12280.

[255] L. L. E. Mears, E. R. Draper, A. M. Castilla, H. Su, Zhuola, B. Dietrich, M. C. Nolan, G. N. Smith, J. Doutch, S. Rogers, et al., *Biomacromolecules* **2017**, *18*, 3531.

[256] M. Serna, *Front. Mol. Biosci.* **2019**, *6*, 33.

[257] T. Nakane, A. Kotecha, A. Sente, G. McMullan, S. Masiulis, P. M. G. E. Brown, I. T. Grigoras, L. Malinauskaite, T. Malinauskas, J. Miehling, et al., *Nature* **2020**, *587*, 152.

[258] D. K. Baby, in *Rheology of Polymer Blends and Nanocomposites*, ed. S. Thomas, C. Sarathchandran, N, Chandran, Elsevier Inc., **2019**, ch. 9, pp. 193-204.

[259] K. Rehmann, Skeens, Kharkar, Ford, Maverakis, Lee, *Physiol. Behav.* **2017**, *176*, 139.

[260] S. Wang, X. Wang, F. G. Draenert, O. Albert, H. C. Schröder, V. Mailänder, G. Mitov, W. E. G. Müller, *Bone* **2014**, *67*, 292.

[261] N. Jalili, K. Laxminarayana, *Mechatronics* **2004**, *14*, 907.

[262] C. Yu, J. Liu, G. Lu, Y. Xie, Y. Sun, Q. Wang, J. Liang, Y. Fan, X. Zhang, *J. Mater. Chem. B* **2018**, *6*, 5164.

[263] M. M. Villone, J. K. Nunes, Y. Li, H. A. Stone, P. L. Maffettone, *Soft Matter* **2019**, *15*, 880.

[264] L. Nyström, R. Nordström, J. Bramhill, B. R. Saunders, R. Álvarez-Asencio, M. W. Rutland, M. Malmsten, *Biomacromolecules* **2016**, *17*, 669.

[265] J. Friedrichs, J. M. Torkko, J. Helenius, T. P. Teräväinen, J. Füllekrug, D. J. Muller, K. Simons, A. Manninen, *J. Biol. Chem.* **2007**, *282*, 29375.

[266] M. Mokbel, D. Mokbel, A. Mietke, N. Träber, S. Girardo, O. Otto, J. Guck, S. Aland, *ACS Biomater. Sci. Eng.* **2017**, *3*, 2962.

[267] P. Daniel Harris, BA, Lynn McNicoll, MD, Gary Epstein-Lubow, MD, and Kali S. Thomas, *Physiol. Behav.* **2017**, *176*, 139.

[268] G. Agrawal, R. Agrawal, *Small* **2018**, *14*, 1801724.

[269] I. Neamtu, A. G. Rusu, A. Diaconu, L. E. Nita, A. P. Chiriac, *Drug Deliv.* **2017**, *24*, 539.

[270] W. Sun, J. Zhang, C. Zhang, P. Wang, C. Peng, M. Shen, X. Shi, *ACS Macro Lett.* **2018**, *7*, 137.

[271] H. Cho, U. Jammalamadaka, K. Tappa, *Materials (Basel).* **2018**, *11*, 302.

[272] F. Sultana, Manirujjaman, Imran-Ul-Haque, M. Arafat, S. Sharmin, *J. Appl. Pharm. Sci.* **2013**, *3*, 95.

[273] N. S. Zarekar, V. J. Lingayat, V. V Pande, *Nanosci. Nanotechnol. Res. Vol. 4, 2017,*

Pages 25-31 **2017**, *4*, 25.

[274] X. Huang, C. S. Brazel, *J. Control. Release* **2001**, *73*, 121.

[275] J. Yoo, Y. Y. Won, *ACS Biomater. Sci. Eng.* **2020**, *6*, 6053.

[276] A. J. Thote, J. T. Chappell, R. B. Gupta, R. Kumar, *Drug Dev. Ind. Pharm.* **2005**, *31*, 43.

[277] M. C. García and J. C. Cuggino, in *Stimulus-responsive Polymeric nanocarriers for Drug Delivery Applications - Types and Triggers,* ed. A. S. H. Makhlouf and N. Y. Abu-Thabit, Elsevier, Amsterdam, **2018**, vol. 1, ch. 12, pp. 321-338.

[278] L. Zha, B. Banik, F. Alexis, *Soft Matter* **2011**, *7*, 5908.

[279] J. G. Visser, A. D. P. Van Staden, C. Smith, *Front. Pharmacol.* **2019**, *10*, 22.

[280] Z. Li, J. Huang, J. Wu, *Biomater. Sci.* **2021**, *9*, 574.

[281] J. Karnoosh-Yamchi, M. Mobasseri, A. Akbarzadeh, S. Davaran, A. R. Ostad-Rahimi, H. Hamishehkar, R. Salehi, Z. Bahmani, K. Nejati-Koshki, A. Darbin, et al., *Mol. Biol. Rep.* **2014**, *41*, 6705.

[282] W. Gao, J. Chan, O. C. Farokhzad, *Bone* **2010**, *7*, 1913.

[283] G. Yang, X. Wang, S. Fu, R. Tang, J. Wang, *Acta Biomater.* **2017**, *60*, 232.

[284] Y. Zhao, C. Simon, M. Daoud Attieh, K. Haupt, A. Falcimaigne-Cordin, *RSC Adv.* **2020**, *10*, 5978.

[285] M. P. Gamcsik, M. S. Kasibhatla, S. D. Teeter, O. M. Colvin, *Biomarkers* **2012**, *17*, 671.

[286] X. Liu, J. Wang, W. Xu, J. Ding, B. Shi, K. Huang, X. Zhuang, X. Chen, *Int. J. Nanomedicine* **2015**, *10*, 6587.

[287] L. Massi, A. Najer, R. Chapman, C. D. Spicer, V. Nele, J. Che, M. A. Booth, J. J. Doutch, M. M. Stevens, *J. Mater. Chem. B* **2020**, *8*, 8894.

[288] Y. Wang, Y. Luo, Q. Zhao, Z. Wang, Z. Xu, X. Jia, *ACS Appl. Mater. Interfaces* **2016**, *8*, 19899.

[289] Q. Guo, X. Zhang, *J. Biomater. Sci. Polym. Ed.* **2019**, *30*, 815.

[290] M. Vicario-de-la-Torre, J. Forcada, *Gels* **2017**, *3*, 16.

[291] X. Wang, D. Niu, P. Li, Q. Wu, X. Bo, B. Liu, S. Bao, T. Su, H. Xu, Q. Wang, *ACS Nano* **2015**, *9*, 5646.

[292] D. C. Leite, S. Kakorin, Y. Hertle, T. Hellweg, N. P. da Silveira, *Langmuir* **2018**, *34*, 10943.

[293] Z. Zhang, H. Li, S. Kasmi, S. Van Herck, K. Deswarte, B. N. Lambrecht, R. Hoogenboom, L. Nuhn, B. G. De Geest, *Angew. Chemie - Int. Ed.* **2019**, *58*, 7866.

[294] M. Ohshio, K. Ishihara, A. Maruyama, N. Shimada, S. I. Yusa, *Langmuir* **2019**, *35*, 7261.

[295] Y. Kotsuchibashi, *Polym. J.* **2020**, *52*, 681.

[296] N. Shimada, T. Sasaki, T. Kawano, A. Maruyama, *Biomacromolecules* **2018**, *19*, 4133.

[297] A. Fujihara, K. Itsuki, N. Shimada, A. Maruyama, N. Sagawa, T. Shikata, S. I. Yusa, *J. Polym. Sci. Part A Polym. Chem.* **2016**, *54*, 2845.

[298] R. Rajan, K. Matsumura, *Macromol. Rapid Commun.* **2017**, *38*, 1700478.

[299] R. Rajan, K. Matsumura, *J. Mater. Chem. B* **2015**, *3*, 5683.

[300] M. Seuss, W. Schmolke, A. Drechsler, A. Fery, S. Seiffert, *ACS Appl. Mater. Interfaces* **2016**, *8*, 16317.

[301] C. G. Lopez, T. Lohmeier, J. E. Wong, W. Richtering, *J. Colloid Interface Sci.* **2019**, *558*, 200.

[302] C. Hu, W. Xu, C. M. Conrads, J. Wu, A. Pich, *J. Colloid Interface Sci.* **2021**, *582*, 1075.

[303] C. Echeverria, C. Mijangos, *Langmuir* **2011**, *27*, 8027.

[304] A. M. Schmidt, *Colloid Polym. Sci.* **2007**, *285*, 953.

[305] S. Chen, Q. Bian, P. Wang, X. Zheng, L. Lv, Z. Dang, G. Wang, *Polym. Chem.* **2017**, *8*, 6150.

[306] J. Yeo, Y. M. Lee, J. Lee, D. Park, K. Kim, J. Kim, J. Park, W. J. Kim, *Nano Lett.* **2019**, *19*, 6716.

[307] J. Yeo, J. Lee, S. Yoon, W. J. Kim, *Biomater. Sci.* **2020**, *8*, 1148.

[308] S. Kumar, S. Sharma, N. Vasudeva, *Chin. J. Integr. Med.* **2017**, 1.

[309] A. Jans, R. R. Rosencrantz, A. D. Mandić, N. Anwar, S. Boesveld, C. Trautwein, M. Moeller, G. Sellge, L. Elling, A. J. C. Kuehne, *Biomacromolecules* **2017**, *18*, 1460.

[310] S. Das, P. Angsantikul, C. Le, D. Bao, Y. Miyamoto, W. Gao, L. Zhang, L. Eckmann, *PLOS Negl. Trop. Dis.* **2018**, e0006266.

[311] D. D. Zomer-Van Ommen, A. V. Pukin, O. Fu, L. H. C. Quarles Van Ufford, H. M. Janssens, J. M. Beekman, R. J. Pieters, *J. Med. Chem.* **2016**, *59*, 6968.

[312] T. J. Paul, S. Rübel, M. Hildebrandt, A. K. Strzelczyk, C. Spormann, T. K. Lindhorst, S. Schmidt, *ACS Appl. Mater. Interfaces* **2019**, *11*, 26674.

[313] H. Wang, Q. Chen, S. Zhou, *Chem. Soc. Rev.* **2018**, *47*, 4198.

[314] M. Tsintou, C. Wang, K. Dalamagkas, D. Weng, Y. N. Zhang and W. Niu, in *Nanobiomaterials Science, Development and Evaluation*, ed. M. Razavi and A. Thakor, Elsevier, Amsterdam, **2017**, ch. 5, pp. 87-124.

[315] W. Zhou, G. Yang, X. Ni, S. Diao, C. Xie, Q. Fan, *Polymers (Basel).* **2020**, *12*, 1902.

[316] K. T. Nguyen, J. L. West, *Biomaterials* **2002**, *23*, 4307.

[317] A. Sivashanmugam, R. Arun Kumar, M. Vishnu Priya, S. V. Nair, R. Jayakumar, *Eur. Polym. J.* **2015**, *72*, 543.

[318] A. Al-Abboodi, J. Fu, P. M. Doran, T. T. Y. Tan, P. P. Y. Chan, *Adv. Healthc. Mater.* **2014**, *3*, 725.

[319] J. Kim, M. J. Yaszemski, L. Lu, *Tissue Eng. - Part C Methods* **2009**, *15*, 583.

[320] N. Huebsch, E. Lippens, K. Lee, M. Mehta, S. T. Koshy, M. C. Darnell, R. M. Desai, C. M. Madl, M. Xu, X. Zhao, et al., *Nat. Mater.* **2015**, *14*, 1269.

[321] A. Marrella, A. Lagazzo, E. Dellacasa, C. Pasquini, E. Finocchio, F. Barberis, L. Pastorino, P. Giannoni, S. Scaglione, *Polymers (Basel).* **2018**, *10*, 380.

[322] E. Sideris, D. R. Griffin, Y. Ding, S. Li, W. M. Weaver, D. Di Carlo, T. Hsiai, T. Segura, *ACS Biomater. Sci. Eng.* **2016**, *2*, 2034.

[323] J. M. de Rutte, J. Koh, D. Di Carlo, *Adv. Funct. Mater.* **2019**, *29*, 1900071.

[324] L. Pruett, R. Ellis, M. McDermott, C. Roosa, D. Griffin, *J. Mater. Chem. B* **2021**, *9*, 7132.

[325] N. F. Truong, E. Kurt, N. Tahmizyan, S. C. Lesher-Pérez, M. Chen, N. J. Darling, W. Xi, T. Segura, *Acta Biomater.* **2019**, *94*, 160.

[326] J. Fang, J. Koh, Q. Fang, H. Qiu, M. M. Archang, M. M. Hasani-Sadrabadi, H. Miwa, X. Zhong, R. Sievers, D. W. Gao, et al., *Adv. Funct. Mater.* **2020**, *30*, 2004307.

[327] L. J. Pruett, C. H. Jenkins, N. S. Singh, K. J. Catallo, D. R. Griffin, *Adv. Funct. Mater.* **2021**, 2104337.

[328] J. Koh, D. R. Griffin, M. M. Archang, A. C. Feng, T. Horn, M. Margolis, D. Zalazar, T. Segura, P. O. Scumpia, D. Di Carlo, *Small* **2019**, *15*, 1903147.

[329] R. S. Hsu, P. Y. Chen, J. H. Fang, Y. Y. Chen, C. W. Chang, Y. J. Lu, S. H. Hu, *Adv. Sci.* **2019**, *6*, 1900520.

[330] A. J. Seymour, S. Shin, S. C. Heilshorn, *Adv. Healthc. Mater.* **2021**, 2100644.

[331] N. J. Darling, W. Xi, E. Sideris, A. R. Anderson, C. Pong, S. T. Carmichael, T. Segura, *Adv. Healthc. Mater.* **2020**, *9*, 1901391.

[332] B. N. Pfaff, L. J. Pruett, N. J. Cornell, J. De Rutte, D. Di Carlo and B. Christopher, *ACS Biomater. Sci. Eng.*, 2021, **7**, 2, 422-427.

[333] D. R. Griffin, M. M. Archang, C. H. Kuan, W. M. Weaver, J. S. Weinstein, A. C. Feng, A. Ruccia, E. Sideris, V. Ragkousis, J. Koh, et al., *Nat. Mater.* **2021**, *20*, 560.

[334] N. F. Truong, S. C. Lesher-Pérez, E. Kurt, T. Segura, *Bioconjug. Chem.* **2019**, *30*, 476.

[335] C. M. Dumont, M. A. Carlson, M. K. Munsell, A. J. Ciciriello, K. Strnadova, J. Park, B. J. Cummings, A. J. Anderson, L. D. Shea, *Acta Biomater.* **2019**, *86*, 312.

[336] Z. Hu, C. Ma, X. Rong, S. Zou, X. Liu, *ACS Appl. Mater. Interfaces* **2018**, *10*, 2377.

[337] A. S. Caldwell, V. V. Rao, A. C. Golden, D. J. Bell, J. C. Grim, K. S. Anseth, *Bioeng. Transl. Med.* **2021**, *6*, e10217.

[338] J. C. Rose, M. Fölster, L. Kivilip, J. L. Gerardo-Nava, E. E. Jaekel, D. B. Gehlen, W. Rohlfs, L. De Laporte, *Polym. Chem.* **2020**, *11*, 496.

[339] J. C. Rose, D. B. Gehlen, A. Omidinia-Anarkoli, M. Fölster, T. Haraszti, E. E. Jaekel, L. De Laporte, *Adv. Healthc. Mater.* **2020**, 2000886.

[340] C. Licht, J. C. Rose, A. O. Anarkoli, D. Blondel, M. Roccio, T. Haraszti, D. B. Gehlen, J. A. Hubbell, M. P. Lutolf, L. De Laporte, *Biomacromolecules* **2019**, *20*, 4075.

[341] M. M. Martino, J. A. Hubbell, *FASEB J.* **2010**, *24*, 4711.

[342] T. Bliss, R. Guzman, M. Daadi, G. K. Steinberg, *Stroke* **2007**, *38*, 817.

[343] P. Assinck, G. J. Duncan, B. J. Hilton, J. R. Plemel, W. Tetzlaff, *Nat. Neurosci.* **2017**, *20*, 637.

[344] S. Rafii, D. Lyden, *Nat. Med.* **2003**, *9*, 702.

[345] L. P. B. Guerzoni, Y. Tsukamoto, D. B. Gehlen, D. Rommel, T. Haraszti, M. Akashi, L. De Laporte, *Biomacromolecules* **2019**, *20*, 3746.

[346] S. Babu, F. Albertino, A. Omidinia Anarkoli, L. De Laporte, *Adv. Healthc. Mater.* **2021**, *10*, 2002221.

[347] A. Mandal, J. R. Clegg, A. C. Anselmo, S. Mitragotri, *Bioeng. Transl. Med.* **2020**, *5*, e10158.

[348] R.-M. Lu, Y.-C. Hwang, I.-J. Liu, C.-C. Lee, H.-Z. Tsai, H.-J. Li, H.-C. Wu, *J. Biomed. Sci.* **2020**, *27*, 1.

[349] T. Bongartz, A. J. Sutton, M. J. Sweeting, I. Buchan, E. L. Matteson, V. Montori, *J. Am. Med. Assoc.* **2006**, *295*, 2275.

[350] S. Minozzi, S. Bonovas, T. Lytras, V. Pecoraro, M. González-Lorenzo, A. J. Bastiampillai, E. M. Gabrielli, A. C. Lonati, L. Moja, M. Cinquini, et al., *Expert Opin. Drug Saf.* **2016**, *15*, 11.

[351] J. W. Myerson, P. N. Patel, K. M. Rubey, M. E. Zamora, M. H. Zaleski, N. Habibi, L. R. Walsh, Y. W. Lee, D. C. Luther, L. T. Ferguson, et al., *Nat. Nanotechnol.* **2022**, *17*, 86.

[352] C. T. Jiang, K. G. Chen, A. Liu, H. Huang, Y. N. Fan, D. K. Zhao, Q. N. Ye, H. B. Zhang, C. F. Xu, S. Shen, et al., *Nat. Commun.* **2021**, *12*, 1359.

[353] W. J. Smith, G. Wang, H. Gaikwad, V. P. Vu, E. Groman, D. W. A. Bourne, D. Simberg, *ACS Nano* **2018**, *12*, 12523.

[354] M. E. Wechsler, R. E. Stephenson, A. C. Murphy, H. F. Oldenkamp, A. Singh, N. A. Peppas, *Biomed. Microdevices* **2019**, *21*, 31.

[355] Y. Kittel, A. J. C. Kuehne, L. De Laporte, *Adv. Healthc. Mater.* **2022**, *11*, 2101989.

[356] J. Kim, D. M. Francis, L. F. Sestito, P. A. Archer, M. P. Manspeaker, M. J. O'Melia, S. N. Thomas, *Nat. Commun.* **2022**, *13*, 1479.

[357] R. Miura, Y. Tahara, S. Sawada, Y. Sasaki, K. Akiyoshi, *Sci. Rep.* **2018**, *8*, 16464.

[358] X. Ma, Z. Zhao, H. Wang, Y. Liu, Y. Xu, J. Zhang, B. Chen, L. Li, Y. Zhao, *Adv. Healthc. Mater.* **2019**, *8*, 1900136.

[359] A. Seyfoori, S. A. Seyyed Ebrahimi, E. Samiei, M. Akbari, *ACS Appl. Mater. Interfaces* **2019**, *11*, 24945.

[360] J. C. Cuggino, E. R. O. Blanco, L. M. Gugliotta, C. I. Alvarez Igarzabal, M. Calderón, *J. Control. Release* **2019**, *307*, 221.

[361] H. Onishi, Y. Ikeuchi-Takahashi, K. Kawano, Y. Hattori, *Biol. Pharm. Bull.* **2019**, *42*, 1155.

[362] Y. Yuan, Y. Liu, Y. He, B. Zhang, L. Zhao, S. Tian, Q. Wang, S. Chen, Z. Li, S. Liang, et al., *Biomaterials* **2022**, *287*, 121613.

[363] P. H. Kim, H. G. Yim, Y. J. Choi, B. J. Kang, J. Kim, S. M. Kwon, B. S. Kim, N. S. Hwang, J. Y. Cho, *J. Control. Release* **2014**, *187*, 1.

[364] A. S. Sonzogni, G. Yealland, M. Kar, S. Wedepohl, L. M. Gugliotta, V. D. G. Gonzalez, S. Hedtrich, M. Calderón, R. J. Minari, *Biomacromolecules* **2018**, *19*, 4607.

[365] S. Singh, N. Drude, L. Blank, P. B. Desai, H. Königs, S. Rütten, K. J. Langen, M. Möller, F. M. Mottaghy, A. Morgenroth, *Adv. Healthc. Mater.* **2021**, *10*, 2100812.

[366] R. Noth, E. Stüber, R. Häsler, S. Nikolaus, T. Kühbacher, J. Hampe, B. Bewig, S. Schreiber, A. Arlt, *J. Crohn's Colitis* **2012**, *6*, 464.

[367] J. Scott Crowe, K. J. Roberts, T. M. Carlton, L. Maggiore, M. F. Cubitt, S. Clare, K. Harcourt, J. Reckless, T. T. MacDonald, K. P. Ray, et al., *Sci. Rep.* **2018**, *8*, 4941.

[368] M. E. Pedersen, R. M. S. Haegebaert, J. Østergaard, H. Jensen, *Sci. Rep.* **2021**, *11*, 4754.

[369] B. G. Amsden, *Macromolecules* **2022**, *55*, 8399.

[370] J. M. de Rutte, J. Koh, D. Di Carlo, *Adv. Funct. Mater.* **2019**, *29*, 1900071.

[371] J. J. Kim, M. S. Shajib, M. M. Manocha, W. I. Khan, *J. Vis. Exp.* **2012**, e3678.

[372] Y. J. Liu, B. Tang, F. C. Wang, L. Tang, Y. Y. Lei, Y. Luo, S. J. Huang, M. Yang, L. Y. Wu, W. Wang, et al., *Theranostics* **2020**, *10*, 5225.

[373] K. Truong, M. Ikura, *Curr. Opin. Struct. Biol.* **2001**, *11*, 573.

[374] M. Y. Berezin, S. Achilefu, *Chem. Rev.* **2010**, *110*, 2641.

[375] J. H. Chi, Y. H. Kim, D. H. Sohn, G. S. Seo, S. H. Lee, *Biomed. Pharmacother.* **2018**, *108*, 1767.

[376] J. H. Chi, G. S. Seo, S. H. Lee, *Int. Immunopharmacol.* **2018**, *59*, 134.

[377] M. Bartneck, K. H. Heffels, Y. Pan, M. Bovi, G. Zwadlo-Klarwasser, J. Groll, *Biomaterials* **2012**, *33*, 4136.

[378] M. Bartneck, F. M. Peters, K. T. Warzecha, M. Bienert, L. van Bloois, C. Trautwein, T. Lammers, F. Tacke, *Nanomedicine Nanotechnology, Biol. Med.* **2014**, *10*, 1209.

[379] E. Migliorini, P. Horn, T. Haraszti, S. V. Wegner, C. Hiepen, P. Knaus, R. P. Richter, E. A. Cavalcanti-Adam, *Adv. Biosyst.* **2017**, *1*, 1600041.

[380] D. Xu, T. Harvey, E. Begiristain, C. Domínguez, L. Sánchez-Abella, M. Browne, R. B. Cook, *J. Mech. Behav. Biomed. Mater.* **2022**, *133*, 105329.

[381] M. Bartneck, H. A. Keul, S. Singh, K. Czaja, J. Bornemann, M. Bockstaller, M. Moeller, G. Zwadlo-Klarwasser, J. Groll, *ACS Nano* **2010**, *4*, 3073.

[382] T. Pelaseyed, J. H. Bergström, J. K. Gustafsson, A. Ermund, G. M. H. Birchenough, A. Schütte, S. van der Post, F. Svensson, A. M. Rodríguez-Piñeiro, E. E. L. Nyström, et al., *Immunol. Rev.* **2014**, *260*, 8.

[383] W. W. Sun, E. S. Krystofiak, A. Leo-Macias, R. Cui, A. Sesso, R. Weigert, S. Ebrahim, B. Kachar, *Commun. Biol.* **2020**, *3*, 5.

[384] B. Deplancke, H. R. Gaskins, *Am. J. Clin. Nutr.* **2001**, *73*, 1131S.

[385] L. Sardelli, D. P. Pacheco, A. Ziccarelli, M. Tunesi, O. Caspani, A. Fusari, F. Briatico Vangosa, C. Giordano, P. Petrini, *RSC Adv.* **2019**, *9*, 15887.

[386] A. M. Duraj-Thatte, N. M. D. Courchesne, P. Praveschotinunt, J. Rutledge, Y. Lee, J. M. Karp, N. S. Joshi, *Adv. Mater.* **2019**, *31*, e1901826.

[387] H. Liu, Z. Cai, F. Wang, L. Hong, L. Deng, J. Zhong, Z. Wang, W. Cui, *Adv. Sci.* **2021**, *8*, 2101619.

[388] Y. Lee, K. Sugihara, M. G. G. Iii, S. Jon, N. Kamada, J. J. Moon, *Nat. Mater.* **2020**, *19*, 118.

[389] M. Ozawa, Y. Ichikawa, Y. W. Zheng, T. Oshima, H. Miyata, K. Nakazawa, H. B. Guan, M. Shiozawa, M. Akaike, K. Watanabe, et al., *Br. J. Cancer* **2014**, *111*, 365.

[390] A. Pramanik, Z. Xu, N. Ingram, P. L. Coletta, P. A. Millner, A. I. I. Tyler, T. A. Hughes, *Mol. Pharm.* **2022**, *19*, 4601.

[391] M. Xavier, L. García-Hevia, I. R. Amado, L. Pastrana, C. Gonçalves, *Int. J. Nanomedicine* **2019**, *14*, 9077.

[392] J. Du, J. Zhu, R. Wu, S. Xu, Y. Tan, J. Wang, *RSC Adv.* **2015**, *5*, 60152.

[393] C. Yan, D. J. Pochan, *Chem. Soc. Rev.* **2010**, *39*, 3528.

[394] E. Kutálková, J. Hrnčiřík, R. Witasek, M. Ingr, *Carbohydr. Polym.* **2020**, *234*, 115919.

[395] S. Boesveld, Y. Kittel, Y. Luo, A. Jans, B. Oezcifci, M. Bartneck, C. Preisinger, D. Rommel, T. Haraszti, S. P. Centeno, et al., *Adv. Healthc. Mater.* **2023**, *12*, 2300695.

[396] M. Zhong, R. Wang, K. Kawamoto, B. D. Olsen, J. A. Johnson, *Science (80).* **2016**, *353*, 1264.

[397] L. De Keer, K. I. Kilic, P. H. M. Van Steenberge, L. Daelemans, D. Kodura, H. Frisch, K. De Clerck, M. F. Reyniers, C. Barner-Kowollik, R. H. Dauskardt, et al., *Nat. Mater.* **2021**, *20*, 1422.

[398] O. Yom-Tov, D. Seliktar, H. Bianco-Peled, *Eur. Polym. J.* **2016**, *74*, 1.

[399] C. R. Nuttelman, M. A. Rice, A. E. Rydholm, C. N. Salinas, D. N. Shah, K. S. Anseth, *Prog. Polym. Sci.* **2008**, *33*, 167.

[400] R. A. Meurer, S. Kemper, S. Knopp, T. Eichert, F. Jakob, H. E. Goldbach, U. Schwaneberg, A. Pich, *Angew. Chemie - Int. Ed.* **2017**, *56*, 7380.

[401] Y. Tsuji, X. Li, M. Shibayama, *Gels* **2018**, *4*, 50.

[402] V. Hagel, T. Haraszti, H. Boehm, *Biointerphases* **2013**, *8*, 36.

[403] T. Yang, M. Malkoch, A. Hult, *J. Polym. Sci. Part A Polym. Chem.* **2013**, *51*, 1378.

[404] S. P. Zustiak, H. Boukari, J. B. Leach, *Soft Matter* **2010**, *6*, 3609.

[405] M. S. Rehmann, K. M. Skeens, P. M. Kharkar, E. M. Ford, E. Maverakis, K. H. Lee, A. M. Kloxin, *Biomacromolecules* **2017**, *18*, 3131.

[406] M. E. Hwang, P. J. Black, C. D. Elliston, B. A. Wolthuis, D. R. Smith, C. C. Wu, S. Wenske, I. Deutsch, *Radiat. Oncol.* **2018**, 13:192.

[407] A. D. Rao, Z. Feng, E. J. Shin, J. He, K. M. Waters, S. Coquia, R. DeJong, L. M. Rosati, L. Su, D. Li, et al., *Int. J. Radiat. Oncol. Biol. Phys.* **2017**, *99*, 1111.

[408] S. Vaggers, B. P. Rai, E. C. P. Chedgy, A. de la Taille, B. K. Somani, *World J. Urol.* **2020**, *39*, 1769.

[409] S. Lee, X. Tong, F. Yang, *Biomater. Sci.* **2016**, *4*, 405.

[410] K. H. Son, J. W. Lee, *Materials (Basel).* **2016**, *9*, 854.

[411] A. C. Suturin, A. J. D. Krüger, K. Neidig, N. Klos, N. Dolfen, M. Bund, T. Gronemann, R. Sebers, A. Manukanc, G. Yazdani, et al., *Adv. Healthc. Mater.* **2022**, *11*, 2200989.

[412] D. L. Braunmiller, S. Babu, D. B. Gehlen, M. Seuß, T. Haraszti, A. Falkenstein, J. Eigen, L. De Laporte, J. J. Crassous, *Adv. Funct. Mater.* **2022**, 2202430.

[413] Z. Zhang, A. Loebus, G. De Vicente, F. Ren, M. Arafeh, Z. Ouyang, M. C. Lensen, *Polymers (Basel).* **2018**, *10*, 970.

[414] Y. Fukumori, H. Takeuchi, Y. Ando (**2018**) *Structural Control of Nanoparticles*. In Nogi, K., Naitō, M., Yokoyama, T., Hosokawa, M. (eds) Nanoparticle technology handbook. Elsevier, Amsterdam, Netherlands.

[415] C. Fernández-Rico, T. Sai, A. Sicher, R. W. Style, E. R. Dufresne, *JACS Au* **2022**, *2*, 66.

[416] F. Wang, L. Ratke, H. Zhang, P. Altschuh, B. Nestler, *J. Sol-Gel Sci. Technol.* **2020**, *94*, 356.

[417] R. W. Style, T. Sai, N. Fanelli, M. Ijavi, K. Smith-Mannschott, Q. Xu, L. A. Wilen, E. R. Dufresne, *Phys. Rev. X* **2018**, *8*, 11028.

[418] Z. Tang, L. Jiang, *Giant* **2022**, *12*, 100131.

[419] S. Seiffert, *Polym. Chem.* **2017**, *8*, 4472.

[420] V. P. Swapna, V. S. Abhisha, R. Stephen (**2020**) *Polymer/Polyhedral Oligomeric Silsesquioxane Nanocomposite Membranes for Pervaporation*. In Sabu, T., George, S. C., Jose, T., (eds) Polymer Nanocomposite Membranes for Pervaporation. Elsevier, Amsterdam, Netherlands.

[421] S. M. Fica-Contreras, D. J. Hoffman, J. Pan, C. Liang, M. D. Fayer, *J. Am. Chem. Soc.* **2021**, *143*, 3583.

[422] J. Pacułt, M. Rams-Baron, B. Chrząszcz, R. Jachowicz, M. Paluch, *Mol. Pharm.* **2018**, *15*, 2807.

[423] X. Han, J. Gao, T. Chen, L. Qian, H. Xiong, Z. Chen, *Nanomaterials* **2022**, *12*, 4161.

[424] G. Scarcelli, W. J. Polacheck, H. T. Nia, K. Patel, A. J. Grodzinsky, R. D. Kamm, S. H. Yun, *Nat. Methods* **2015**, *12*, 1132.

[425] R. Prevedel, A. Diz-Muñoz, G. Ruocco, G. Antonacci, *Nat. Methods* **2019**, *16*, 969.

[426] R. Schlüßler, K. Kim, M. Nötzel, A. Taubenberger, S. Abuhattum, T. Beck, P. Müller, S. Maharana, G. Cojoc, S. Girardo, et al., *Elife* **2022**, *11*, e68490.

[427] A. J. Traverso, J. V. Thompson, Z. A. Steelman, Z. Meng, M. O. Scully, V. V. Yakovlev, *Anal. Chem.* **2015**, *87*, 7519.

[428] M. Bailey, M. Alunni-Cardinali, N. Correa, S. Caponi, T. Holsgrove, H. Barr, N. Stone, C. P. Winlove, D. Fioretto, F. Palombo, *Sci. Adv.* **2020**, *6*, eabc1937.

[429] N. Hauck, T. Beck, G. Cojoc, R. Schlüßler, S. Ahmed, I. Raguzin, M. Mayer, J. Schubert, P. Müller, J. Guck, et al., *Mater. Adv.* **2022**, *3*, 6179.

[430] R. Barer, *Nature* **1952**, *169*, 366.

[431] R. Sunyer, A. J. Jin, R. Nossal, D. L. Sackett, *PLoS One* **2012**, *7*, e46107.

[432] Y. Chandorkar, A. Castro Nava, S. Schweizerhof, M. Van Dongen, T. Haraszti, J. Köhler, H. Zhang, R. Windoffer, A. Mourran, M. Möller, et al., *Nat. Commun.* **2019**, *10*, 4027.

[433] Y. Chandorkar, C. Bastard, J. Di Russo, T. Haraszti, L. De Laporte, *Appl. Mater. Today* **2022**, *27*, 101492.

[434] A. Das, R. S. Fischer, D. Pan, C. M. Waterman, *J. Biol. Chem.* **2016**, *291*, 6096.

[435] D. Missirlis, J. P. Spatz, *Biomacromolecules* **2014**, *15*, 195.

[436] E. E. Charrier, K. Pogoda, R. G. Wells, P. A. Janmey, *Nat. Commun.* **2018**, *9*, 449.

[437] E. Migliorini, P. Horn, T. Haraszti, S. V. Wegner, C. Hiepen, P. Knaus, R. P. Richter, E. A. Cavalcanti-Adam, *Adv. Biosyst.* **2017**, *1*, 1600041.

[438] T. T. Tsay, K. A. Jacobson, *Biophys. J.* **1991**, *60*, 360.

[439] N. Otsu, *Czas. Stomatol.* **1979**, *9*, 62.

[440] K. Kim, J. Guck, *Biophys. J.* **2020**, *119*, 1946.

[441] E. Cuche, P. Marquet, C. Depeursinge, *Appl. Opt.* **2000**, *39*, 4070.

[442] Y. Sung, W. Choi, C. Fang-Yen, K. Badizadegan, R. R. Dasari, M. S. Feld, *Opt. InfoBase Conf. Pap.* **2009**, *17*, 1977.

[443] E. Wolf, *Opt. Commun.* **1969**, *1*, 153.

[444] K. Kim, H. Yoon, M. Diez-Silva, M. Dao, R. R. Dasari, Y. Park, *J. Biomed. Opt.* **2014**, *19*, 011005.

[445] R. Schlüßler, S. Möllmert, S. Abuhattum, G. Cojoc, P. Müller, K. Kim, C. Möckel, C. Zimmermann, J. Czarske, J. Guck, *Biophys. J.* **2018**, *115*, 911.

[446] L. Iliopoulou, G. Kollias, *Mucosal Immunol.* **2022**, *15*, 10.

[447] S. A. Hirota, V. Iablokov, S. E. Tulk, L. P. Schenck, H. Becker, J. Nguyen, S. Al Bashir, T. C. Dingle, A. Laing, J. Liu, et al., *Infect. Immun.* **2012**, *80*, 4474.

[448] B. Chassaing, J. D. Aitken, M. Malleshappa, M. Kumar-Vijay, *Curr. Protoc. Immunol.* **2014**, 15.25.1.

[449] L. M. Keubler, M. Buettner, C. Häger, A. Bleich, *Inflamm. Bowel Dis.* **2015**, *21*, 1967.

[450] N. Khuu, S. Kheiri, E. Kumacheva, *Trends Chem.* **2021**, *3*, 1002.

[451] K. Akiyoshi, S. Kobayashi, S. Shichibe, D. Mix, M. Baudys, S. Wan Kim, J. Sunamoto, *J. Control. Release* **1998**, *54*, 313.

[452] S. V. Vinogradov, T. K. Bronich, A. V. Kabanov, *Adv. Drug Deliv. Rev.* **2002**, *54*, 135.

[453] S. V. Vinogradov, E. V. Batrakova, A. V. Kabanov, *Bioconjug. Chem.* **2004**, *15*, 50.

[454] J. P. Rolland, B. W. Maynor, L. E. Euliss, A. E. Exner, G. M. Denison, J. M. DeSimone, *J. Am. Chem. Soc.* **2005**, *127*, 10096.

[455] S. Xu, Z. Nie, M. Seo, P. Lewis, E. Kumacheva, H. A. Stone, P. Garstecki, D. B. Weibel, I. Gitlin, G. M. Whitesides, *Angew. Chemie - Int. Ed.* **2005**, *44*, 724.

[456] D. Dendukuri, K. Tsoi, T. A. Hatton, P. S. Doyle, *Langmuir* **2005**, *21*, 2113.

[457] U. Hasegawa, S. I. M. Nomura, S. C. Kaul, T. Hirano, K. Akiyoshi, *Biochem. Biophys. Res. Commun.* **2005**, *331*, 917.

[458] S. Kitano, S. Kageyama, Y. Nagata, Y. Miyahara, A. Hiasa, H. Naota, S. Okumura, H. Imai, T. Shiraishi, M. Masuya, et al., *Clin. Cancer Res.* **2006**, *12*, 7397.

[459] B. S. Chandrashekha, M. Anitha, M. Ruparelia, P. Vaidya, R. Aamir, S. Shah, S. Thilak, S. Aurangabadkar, S. Pal, A. Saraswat, et al., *J. Clin. Diagnostic Res.* **2015**, *9*, WC04.

[460] A. Omidinia-Anarkoli, S. Boesveld, U. Tuvshindorj, J. C. Rose, T. Haraszti, L. De Laporte, *Small* **2017**, *13*, 1702207.

List of Abbreviations

AF	Alexa Fluor
AFM	Atomic force microscopy
ANOVA	Analysis of variance
AMF	Alternating magnetic field
AMB	Amphotericin B
Au	Gold
BBB	Blood-brain barrier
BSA	Bovine serum albumin
CBQCA	3-(4-Carboxybenzoyl)quinoline-2-carboxaldehyde
C. diff.	Clostridium difficile
ChitoMA	Chitosan oligomer methacrylate
CLSM	Confocal laser scanning microscopy
CMC	Critical micelle concentration
ConA	Concanavalin A
COX-II	Cyclooxygenase-II
CT	Cholera toxin
D	Diffusion coefficient
DAPI	4',6-Diamidino-2-phenylindole
DC	Daoud and Cotton
DCM	Dichloromethane
DDS	Drug delivery system
DIC	Differential interference contract
DLS	Dynamic light scattering

DMA	Dynamic mechanical analysis
DMEM	Dulbecco's modified eagle's medium
DNA	Deoxyribonucleic acid
DoS	Degree of substitution
DOSY-NMR	Diffusion ordered spectroscopy-NMR
DOX	Doxorubicin
DSS	Dextran sulfate sodium
E. coli	Escherichia coli
ECM	Extracellular matrix
EcN	*E. coli* Nissle
EGDMA	Ethylene glycol dimethacrylate
E_{eff}	Effective Young's modulus
ELISA	Enzyme-linked immunosorbent assay
EMA	European medicines agency
eq.	Equivalents
FBS	Fetal bovine serum
Fc	Fragment crystallizable
FCS	Fluorescence correlation spectroscopy
FDA	Food and Drug Administration
FITC	Fluorescein isothiocyanate
FRAP	Fluorescence recovery after photobleaching
FRET	Förster resonance energy transfer
FLIM	Fluorescence-lifetime imaging microscopy
G'	Storage modulus
G''	Loss modulus

Gal	β-D-galactopyranoside
GC	Glycol chitosan
GelMA	Gelatin-methacryloyl
GI	Gastrointestinal
GMA	Glycidyl methacrylate
GRGDS-PC	H-Gly-Arg-Gly-Asp-Ser-Pro-Cys-OH
H_2O_2	Hydrogen peroxide
HA	Hyaluronic acid
HA-Ac	HA-acrylate
HEMP	2-Hydroxy-4′-(2-hydroxyethoxy)-2-methylpropiophenone
hMSC	Human mesenchymal stem cell
HRP	Horseradish peroxidase
HRSEM	High resolution SEM
HRTEM	High resolution TEM
HT29	Human colon adenocarcinoma cell line
IBD	Inflammatory bowel disease
IgG	Immunoglobin G
IKVAV	Ile-Lys-Val-ala-Val
IL	Interleukin
IR	Infrared
IUPAC	International union of pure and applied chemistry
LAP	Lithium phenyl(2,4,6-trimethylbenzoyl)phosphinate
LCST	Lower critical solution temperature
LED	Light-emitting diode
LPS	Lipopolysaccharide

LVE	Linear viscoelasticity
Man	α-D-mannopyranoside
MAP	Microporous annealed particle
MASCS	methacrylated succinyl-chitosan
MRI	Magnetic resonance imaging
M_W	Molecular weight
µG	Microgel
N_2	Nitrogen
N/C	Nitrogen-to-carbon
NIPAM	N-Isopropylacrylamid
NMR	Nuclear magnetic resonance
NO	Nitric oxide
NOCCL	NO-cleavable crosslinker
NOESY-NMR	Nuclear overhauser enhancement spectroscopy-NMR
NP	Nanoparticle
$O2^-$	Superoxide anions
ODT	Optical imaging tomography
OEAM	Diacrylamide containing ortho ester
$OH^.$	Hydroxyl radicals
PAA	Poly(acrylic acid)
PBS	Phosphate-buffered saline
p_c	Cloud point
Pd	Palladium
PDMS	Polydimethylsiloxane
PEG	Poly(ethylene glycol)

PEG-Ac	PEG-acrylate
PEG-DA	PEG-diacrylate
PEG-DAA	PEG diacrylamide
PET	Positron emission tomography
PFA	Paraformaldehyde
PFPE	Perfluoropolyether
PGGA	Poly(L-glutmate-*co*-*N*-3-L-glutamylphenylboronic acid
PLGA	Poly(lactic-co-glycolic acid)
PolyBPLP	Photoluminescent polymer
PRINT	Particle replication in nonwetting templates
Pt	Platinum
RA	Rheumatoid arthritis
RGD	Arg-Gly-Asp (Arginyl-glycyl-aspartic acid)
R_h	Hydrodynamic radius
RI	Refractive index
ROI	Region of interest
ROS	Reactive oxygen species
RPMI	Roswell Park Memorial Institute
RT-DC	Real-time deformability cytometry
RT-PCR	Real time-polymerase chain reaction
SA	Sodium alginate
SANS	Small-angle neutron scattering
SAOS	Small amplitude oscillatory shear
SC	Schwann cell
SEM	Scanning electron microscopy

SFL	Stop-flow lithography
SLS	Static light scattering
SMD HyD	Single molecule detection hybrid detector
SPB	Sulfobetaine
sPEG	Star-shaped PEG
STED	Stimulated emission depletion
TA	Tannic acid
TC7	Human colon adenocarcinoma cell line
TCSPC	Time-correlated single photon counting
TEM	Transmission electron microscopy
t_{gel}	Gelation time
TNFα	Tumour necrosis factor α
UCST	Upper critical solution temperature
US	Ultrasound
UV	Ultraviolet
VIPA	Virtually imaged phase array
w/o	water-in-oil
w/o/w	water-in-oil-in-water
XPS	X-ray photoelectron spectroscopy
YAP	Yes-associated protein

Acknowledgement

Curriculum Vitae

PERSONAL DATA

Name	Yonca Kittel (née Kayku)
Date/Place of Birth	07.08.1996/Stolberg (Rhld.)
Family	married
Contact	Lilienweg 4, 52457 Aldenhoven, Germany
Email	yonca.kayku@gmx.de
Phone	+49 17657811659

EDUCATION

11/2019 – present	Doctoral studies at DWI – Leibniz Institute for Interactive Materials e. V., Germany; **Microfluidic synthesis of multifunctional microgels for treatment of inflammatory bowel syndrome**; Supervisor: Prof. Dr.-Ing. Laura De Laporte; Functional Microgels and Microgel Systems SFB 985 (Project C3) from DFG (Deutsche Forschungsgemeinschaft) • Engineering of microgels for the treatment of required functions for the treatment of IBD • Production of microgels via microfluidics • Characterization of microgels
10/2017 – 08/2019	Master studies (M. Sc.) at RWTH Aachen University, Germany in Chemistry: Grade: 1.5
10/2014 – 08/2017	Bachelor studies (B. Sc.) at RWTH Aachen University, Germany in Chemistry: Grade: 2.3

RESEARCH PROJECTS

02/2019 – 08/2019	Master thesis at Institute of Technical and Macromolecular Chemistry, RWTH Aachen, Germany Studies: *Catalytic processes for an access to diols from sorbitol*

| 10/2018 – 02/2019 | Research Internship at DWI – Leibniz Institute for Interactive Materials e. V., Germany |

Studies: *On-chip production of soft PEG-DA/star-PEG-A microgels via microfluidics*

| 03/2018 – 06/2018 | Research Internship at Institute of Technical and Macromolecular Chemistry, RWTH Aachen, Germany |

Studies: Studies and investigation of supported catalysts of the organic hydrogen carrier perhydro-dibenzyl-toluene (PDBT)

| 10/2017 – 01/2018 | Research Internship at DWI – Leibniz Institute for Interactive Materials e. V., Germany |

Studies: *pH-sensitive PVCL/VIm-microgels and their incorporation in biocompatible electrospun PLA-microfibres*

| 04/2017 – 07/2017 | Bachelor thesis at ITA Group International Centre for Sustainable Textiles, RWTH Aachen, Germany |

Studies: *Synthesis of alumina aerogel fibres via sol-gel process*

PUBLICATIONS

1. **Yonca Kittel**, Alexander J. C. Kuehne, Laura De Laporte: Translating Therapeutic Microgels into Clinical Applications, Adv. Healthc. Mater., 2022, 11, 2101989.

2. Sarah Boesveld*, **Yonca Kittel***, Yizhao Luo, Alexander Jans, Bural Oezcifci, Matthias Bartneck, Christian Preisinger, Dirk Rommel, Tamás Haraszti, Silvia P. Centeno, Arnold J. Boersma, Laura De Laporte, Christian Trautwein, Alexander J. C. Kuehne, Pavel Strnad, Microgels as Platforms for Antibody-Mediated Cytokine Scavenging, Adv. Healthc. Mater., 2023, 12, 2300695.

3. **Yonca Kittel**, Luis P. B. Guerzoni, Carolina Itzin, Dirk Rommel, Matthias Mork, Céline Bastard, Bernhard Häßel, Abdolrahman Omidinia-Anarkoli, Silvia P. Centeno, Tamás Haraszti, Kyoohyun Kim, Jochen Guck, Alexander J. C. Kuehne, Laura De Laporte, Varying the Stiffness and Diffusivity of Rod-Shaped Microgels Independently through Their Molecular Building Blocks, Angew. Chem. Int. Ed., 2023, 62, e202309779.

* Equal contribution.

SCIENTIFIC PRESENTATIONS

1. Gave a talk at International Summer School on Microgels (SFB 985 Functional Microgels and Microgel Systems) in Monschau (Aachen) Germany in September 2022
2. Gave a talk in Colloquium at the Institute for Applied Medical Engineering (AME) in Aachen, Germany in April 2023
3. Presented a poster at Gordon Research Conference Biomaterials and Tissue Engineering in Holderness, New Hampshire, USA in July 2023

SKILLS

Microfluidics, Photolithography, Free radical polymerization, Synthesis and engineering of hydrogels and microgels, UV-Vis, Rheology, Atomic force microscopy, Nanoindentation, Raman spectroscopy, Confocal microscopy, Fluorescence recovery after photobleaching (FRAP), 2D cell culture, Immunofluorescent staining

ImageJ, Origin, GraphPad, Microsoft Office

LANGUAGES

German: Native speaker

Turkish: Native speaker

English: Fluent

French: Good

Yonca Kittel

21.02.2024, Aachen